Université catholique de Louvain
École Polytechnique de Louvain
Institute of mechanics, materials and civil engineering

Contributions to nonlinear micromechanical modeling of composite and porous materials under small and large deformation

Marieme Imene El Ghezal

Thesis submitted in fulfillment of the requirements for the Ph. D. degree in Engineering Sciences

Jury Members

Prof. **I. Doghri**, Supervisor, Université catholique de Louvain
Prof. **L. Delannay**, Université catholique de Louvain
Prof. **T. Pardoen**, Université catholique de Louvain
Prof. **D. Kondo**, Université Pierre et Marie Curie, Paris
Prof. **H. Böhm**, Technische Universität Wien
Prof. **K. Danas**, École polytechnique, Paris
Prof. **R. Ronsse**, Chair, Université catholique de Louvain

February 2018

Acknowledgements

Undertaking this Ph.D. has been a truly life-changing experience for me and it would not have been possible to do without the guidance and support that I have received from many people.

I would like to express my heartfelt gratitude to my Ph.D. advisor and mentor Professor Issam Doghri for his guidance throughout this long journey. I would like to thank him for his invaluable advices in all aspects related not only to my research but also life, his trust in me and most of all his patience toward my sceptical attitude in research.

My heartfelt appreciation also extends to Professor Djimedo Kondo who made my stay at UPMC an enriching and great experience. Being in his team was an extraordinary opportunity to discover a new subject enriching my background in micromechanics.

My special thanks go to Professor Laurent Delannay and Professor Thomas Pardoen for their attention to my work since I started my thesis. Their helpful comments and suggestions incentivized me to widen my research from various perspectives.

I gratefully thank Professor Kostas Danas and Professor Helmut Böhm who have kindly accepted to review my thesis as well as for valuable feedback and insightful questions they provided which made this research work better. I am thankful to Professor Renaud Ronsse for accepting with enthusiasm to be the president of my thesis committee.

I owe my passion in learning to many inspiring professors and teachers I had during my studies. My thoughts and prayers go to many of them who are already gone.

I have been lucky to join MEMA and the joyful people in Euler who made the atmosphere friendly. The list of people who made my stay at Euler enjoyable is very long.

Words cannot express my gratitude to my family: my parents and my brothers Bessem and Adam for their unconditional love and support and their moral strength throughout my ventures. I am forever indebted to them.

To the sparkling eyes that fill me everyday with love, to the two men of my life
Saiff & Anass: simply, thank you!

Marieme Imene

Contents

Introduction

All industries (automotive, aerospace, consumer electronics, biomedical, etc.) have been positively impacted and enriched by the rapid growing field of composite materials. [1] Nowadays, almost all engineered materials are heterogeneous on one scale or the other. In most of engineering applications, the heterogeneity is added by a sophisticated process as a means of upgrading the material behavior. In fact, it has been found, since thousands of years, that combining different materials or different states of the same material can greatly improve some particular properties and allows to achieve performance that could not be attained with a single material. A wide variety of heterogeneous media has been then ushered and the technological advancements of the last decades boosted the expansion of this field.

An important class of composite materials widely used in modern industry in the context of lightweight design is the fiber reinforced polymers (see Fig.1). This class includes a wide range of materials depending on the type of polymeric matrix (e.g. thermoplastic or thermoset), on the fiber's type (e.g. short fibers and continuous fibers) and on the distribution of the reinforcements from random to perfectly arranged. The strengthening effect of reinforcements is tightly influenced by the microstructural disposition of the two phases, the size, shape and spatial distribution of the fibers and their respective interfaces. Another class of industrially used heterogeneous materials consists in metal matrix composites. Those materials combine low density with improved strength, together with sufficient amount of ductility and stiffness. Some examples of metal matrix composites microstructures are shown in Fig.2. The effect of the microstructural morphology and properties on the macroscopic behavior of those materials has been established and extensively investigated. Other multi-phase materials that have been gaining attention since the last two decades are metal and polymer foams. Those materials combine lightweight with superior material properties (e.g. high energy absorption, sound absorption efficiency etc.) which are also highly micro-structural- dependent.

Understanding the physical behaviour and predicting accurately the effective properties of heterogeneous materials is essential in order to control and take full advantage of their functionalities according to the destined application. Approaches with predictive capabilities are thus needed .

To address this challenge, multi-scale modeling approaches have been developed. In continuum mechanics, those methods rely on a separation of scales. Commonly, they assume that the material configuration can be regarded as homogeneous at the macroscale and heterogeneous (consisting of different components with different properties) microscopically. Their key objective is to derive relationships bridging those different length scales and to predict the effective properties[2] of those heterogeneous materials. In particular, micromechanical approaches which derive equivalent material properties of multi-phase materials while taking into account the microstructural characteristics and the constitutive behavior of each phase are relevant candidates.

[1] The term composite must be considered here in a broad sense: i.e. an heterogeneous material made of two or more different constituents that do not merge and thus it covers a wide class of materials.

[2] In this work we are concerned only with the effective mechanical properties of a class of heterogeneous materials, nevertheless approaches similar to the ones that will be discussed apply for predicting other physical properties such as thermal expansion, heat conduction and electromagnetic properties.

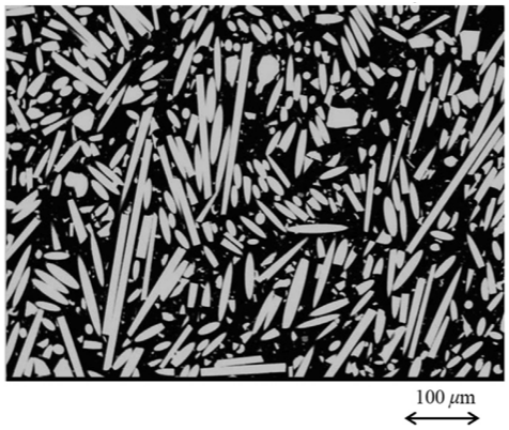

Figure 1: Typical micrograph of short glass fibre reinforced plastic. Sawada and Kusaka (2017)

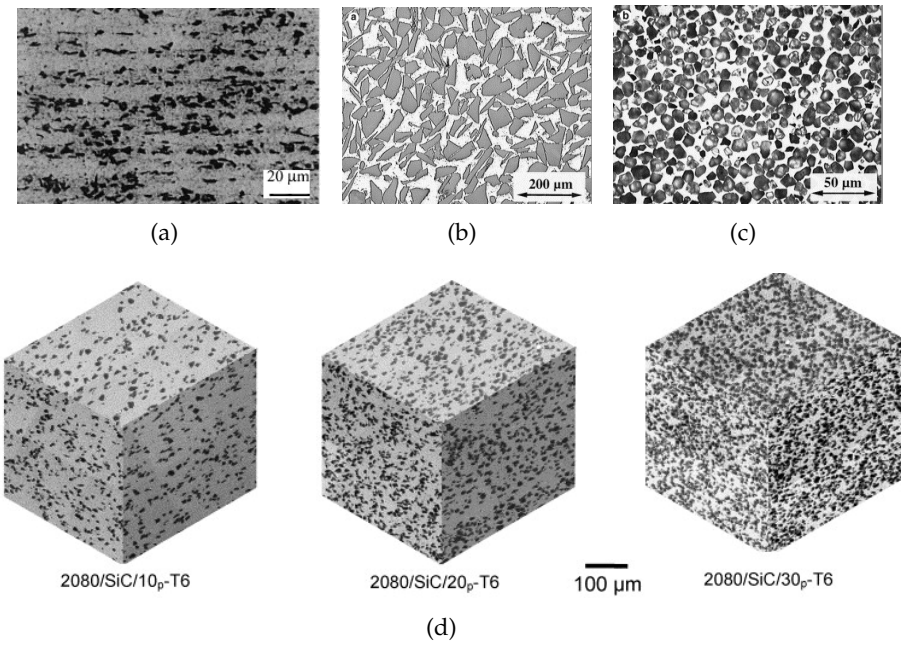

Figure 2: Examples of typical microstructures of metal matrix composites (a) microstructure of Al(6061)/SiC (10%) Soppa et al. (1999) (b) a microstructure of B_4C reinforced composite,(c): polygonal Al_2O_3 reinforced composite with volume fraction of ceramic particles (in dark) ranging between 50% and 60% Miserez et al. (2004), (d): microstructures of $Al/SiCp$ composites for three volume fractions: 10%, 20% and 30% respectively Chawla et al. (2006).

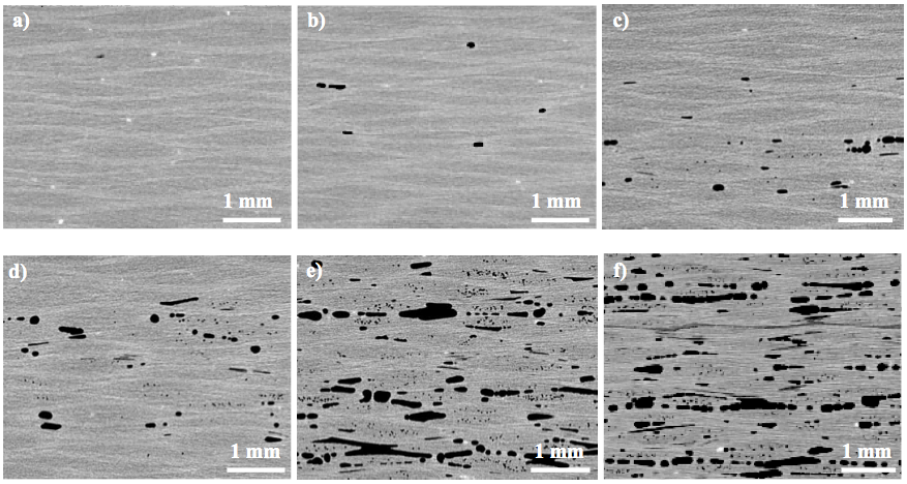

Figure 3: Computed tomography cross-sectional images of typical carbon reinforced composite samples showing different porosity volume fractions: a) ~ 0%, b) ~ 0.15%, c) ~ 0.39%, d) ~ 0.9%, e) ~ 4.5%, f) ~ 10%. Kastner et al. (2010).

In this context, this dissertation is dedicated to the homogenization of two classes of materials: composite materials and porous solids. While the subjects may seem different, the two classes of materials present a common feature: both are multi-phase materials and porous materials can be seen as a special case for which one constituent shows vanishing stiffness. Also, materials with at least three distinct phases: matrix, solid inclusions and cavities and which can be viewed as porous composites or reinforced porous materials do exist in practice. Figure 3 shows cross-sectional computed tomography images of carbon reinforced composite samples containing voids with different porosity values (between 0% and 10%). Indeed, it has been shown that in fiber reinforced composites, voids are formed "because of entrapment of air in the compounding and melt flow processing steps and as a result of uneven shrinkage due to temperature gradients involved in the solidification step by cooling". The experimental results suggest that "voids nucleate at fiber ends, and their content depends on the processing method and processing conditions, on fiber concentration, and on fiber length"Vaxman et al. (2011). In metal matrix composites, matrix voids form during eutectic solidification and grow further by elasto-plastic flow of the matrix during cooling Schöbel et al. (2014). Moreover, voids may nucleate at inclusions by particle-matrix interface decohesion, by particle cracking, or also by particle fragmentation for elongated inclusions loaded along their length (e.g. Beremin (1981); Roy et al. (1981); Babout et al. (2004)).

Several multi-scale modelling strategies have been proposed over the years. They can be classified into two typical methodological categories. The first category covers full-field methods. First, there is the direct finite element (FE) analysis of representative volume elements (RVEs). If periodic microstructure is assumed, unit cell method with periodic boundary conditions could be considered. This method provides valuable information on the local microstructural fields and computes the global response by averaging microscopic stress-strain fields over the representative unit cell. However, this method is computationally expensive and difficulties in generating good meshes for

complex microstructures may arise requiring additional effort. The second sub-categorie is the method of cells and subcells (which is related to the transformation field analysis), the RVE or unit cell is discretized with pixels (2D) or voxels (3D). The method is thus particularly suitable for analyses of digital images from real and eventually complex microstructures (e.g. obtained by 3D microtomography techniques). The boundary-value problem could be solved using different approaches. If periodic boundary conditions are considered, fast Fourier transform (FFT) based formulation originally proposed by Moulinec and Suquet (1998), Michel et al. (1999) could be used to solve the problem in the Fourier space. The method of cells proved to be efficient even when dealing with billions of voxels because FFT solutions are obtained at much lower computational cost compared to FE simulations. The macroscopic response is accurately predicted by the cells method, however, artificial stress concentrations are introduced in the vicinity of multi-materials interfaces due to the imposed rectangular shape of the subcells. Third, there is the asymptotic or mathematical theory of homogenization for periodic media documented in Bensoussan et al. (1978), which ends up with problems on a unit cell which need to be solved with FE or voxel methods.

The second category comprises mean-field homogenization (MFH) which is restricted to microstructures such that multiple phases of solid inclusions or cavities which are supposed to have an ellipsoidal shape are embedded in a continuum matrix. MFH essentially relies on assumed relations between the mean values (volume averages) of strain or stress fields in each phase, and unlike the former category, it is not direct and it does not solve for the detailed micro fields. Compared to the direct full-field methods, MFH is more restricted both in terms of microstructures that it can handle and the results it can deliver, however it is much easier to use and its computing time is several orders of magnitude smaller than that of direct scale-bridging methods, especially in the nonlinear regime.

Early developments of MFH methods were established by Voigt (1889) and later Reuss (1929) leading to simple models based on the rule of mixtures and thus takes on consideration only one microstructural information i.e. the volume fraction of the constituents. More sophisticated MFH methods are based on the fundamental linear elastic solution developed by Eshelby (1957) for an ellipsoidal subdomain of an infinite matrix undergoing a uniform eigen or transformation strain. In linear elasticity, successful MFH models have been developed based on an approximate use of Eshelby's solution, typical examples being the Mori and Tanaka (1973) model, the self-consistent scheme (Kröner (1958); Hill (1965a)) and Generalized Self Consistent Method (Christensen (1990),Christensen and Lo (1979), Christensen (1979)). Alongside with Eshelby based models, variational bounding methods (Hashin (1962) and Hashin and Shtrikman (1963) provide tighter upper and lower bounds for the overall composite properties. They rely on suitable variational (minimum energy) principles.

For linear composites, MFH techniques are well-established and provide accurate predictions of the effective overall properties. However, for high contrasts between the properties of different phases such as porous materials further investigations are needed.

For nonlinear composites, a significant research effort has been devoted to extending MFH to the nonlinear regime. First attempts date from the pioneer works of Kröner (1961) and Hill (1965b). The major difficulty is that for nonlinear composites, even if each

phase's material is homogeneous, the instantaneous stiffness operators are not uniform per phase. Consequently, Eshelby's results and MFH models cannot be extended directly from linear elasticity to the nonlinear realm, and in order to circumvent this difficulty, several methods each based on its own assumptions and approximations have been proposed. The unifying feature of those methods is the definition of a linear comparison composite (LCC) whose response approximates that of the nonlinear composite.

On the other hand, variational approaches were extended to nonlinear media by Talbot and Willis (1985) using a homogeneous linear comparison medium having a uniform stiffness and subjected to some polarization stress field. Ponte Castañeda (1991) extended the method by introducing the concept of an heterogeneous comparison medium (a linear comparison composite: LCC) having the same microstructure distribution as the real nonlinear one. For finite strain hyperelastic composites, several MFH formulations based on variational formulations and including field fluctuations have been proposed over the years by Ponte Castañeda, Suquet and their co-workers, reaching a high degree of accuracy, see for instance Ponte Castañeda and Tiberio (2000), Ponte Castañeda and Suquet (2002), Ponte Castañeda (2002) and Idiart et al. (2006).

For finite strain elasto(visco)plastic heterogeneous materials, most MFH methods rely on local (micro) constitutive models which are based on an additive decomposition of the rate of deformation tensor onto elastic and inelastic parts, and a hypoelastic stress-strain relation. Representative MFH proposals based on such assumptions include, for polycrystalline metals: Nemat-Nasser and Obata (1986) and Segurado et al. (2012), for porous materials: Danas and Aravas (2012) and Aravas and Ponte Castañeda (2004), for solid propellants: Xu et al. (2008) and for metal-matrix composites: Pettermann et al. (2010).

However, it is well known that such assumptions are acceptable if the elastic strains are small, which is typical of metals. This is not the case for polymer materials, for which a better formulation is based on a multiplicative decomposition of the deformation gradient onto elastic and inelastic parts, and a hyperelastic stress strain relation. Other models suited for such materials are thus required.

In another context related to the ductile fracture, porous ductile metallic materials were studied in the later 1960s by McClintock (1968) and Rice and Tracey (1969). Few years later, Gurson (1977) paved the way for a better micromechanical modeling of the plasticity of porous materials. Continuous efforts have been devoted to extend his model in several directions in order to enhance its predictions or to make it suitable for broader range of materials. Several thorough reviews on the different extensions of the Gurson model can be found in Pineau and Pardoen (2007), Benzerga and Leblond (2010) and Pineau et al. (2016).

Despite the vast literature on the homogenization methods, a lot of questions still remain. In this thesis, we investigate several issues related to the homogenization of composite or porous materials and try to answer some of the remaining questions via both analytical and numerical approaches. We adopt MFH approach and full-field FE technique will serve as a tool for evaluating and verifying homogenization models that will be developed.

Concretely, we aim at adressing the following issues that are still open in the literature:

- To which extent are MFH models able to predict effective behavior of highly porous

and cellular solids in linear elasticity and viscoelaticity?

- Is it possible to derive a macroscopic yield function accounting for interactions between voids and thus enhance the original Gurson's model predictions for moderate to high porosities without adding fitting parameters?
- For an anisotropic porous matrix material, is there an alternative to the existing literature on analytical derivation of macroscopic yield criterion?
- How does the matrix anisotropy affect the macroscopic yield surface?
- How to generalize mean-field homogenization schemes from linear elasticity to finite strain elastoplasticity?

In order to answer those questions, this thesis is organized into four chapters. Each chapter is structured to be independent of the others. In each chapter, one or several modelling strategies are presented to tackle one or another issue. The titles of the chapters are the following:

- Chapter 1: Porous materials in linear elasticity and viscoelasticity
- Chapter 2: Porous plasticity: predictive second moment homogenization models coupled with Gurson's solution
- Chapter 3: Porous plasticity: Static limit analysis and strength of porous solids with Hill orthotropic matrix
- Chapter 4: Composite materials at finite strains

The first chapter is concerned with the mechanical properties for elastic and viscoelastic porous materials over the full range of possible porosities. In one hand, for small porosities, several mean-field models used for predicting the overall composite properties in terms of the constituent properties and distributions of phases could be particularized for the case of porous solids. Solutions of linear elasticity are extended to visco-elasticty by making use of the correspondence principle. In the other hand, finite element results obtained on representative volume elements of different microstructures serve as a reference to verify the accordance of the different predictions. For low density materials (called cellular solids), open cell foams are idealized by perfectly periodic space filling Kelvin cells (see Fig.4). Existing analytical beam theory models are compared in linear elasticity and making use of Laplace Carson transform the solutions were extended to linear viscoelasticity. Predictions were confronted to FE simulations carried on tetrakaidecahedral unit cells.

The second chapter deals with the modeling of the plastic behavior of porous materials. The most widely known model based on homogenization theory for porous ductile materials was developped by Gurson (1977) through limit-analysis of a hollow sphere made of a rigid-ideal-plastic material and subjected to axisymmetric loadings. The original model of Gurson does not incorporate interaction effects between multiple voids in real materials and thus was enriched heuristically by adding additional parameters

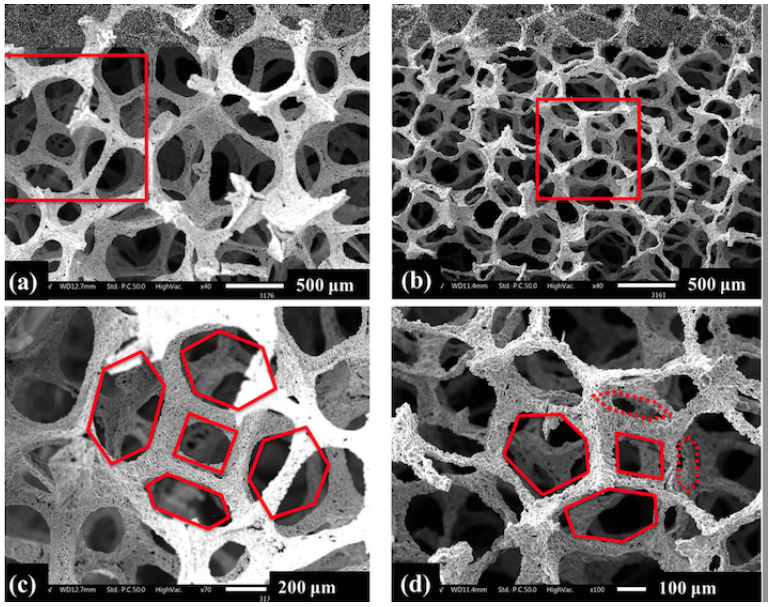

Figure 4: Scanning Electron Microscope (SEM) images of two different polyurethane foams (relative densities are respectively 2% and 3.5%) showing a representative tetrakaidecahedron unit-cell shape. Zhai et al. (2018)

Tvergaard (1981). On the other hand, mean field models often fail to predict the effective response of a perfectly plastic matrix containing voids for high stress triaxialities. In this chapter, we propose an original and rather simple coupling between mean-field homogenization and Gurson's solution allowing to account for multiple cavities. The actual porous microstructure is modeled alternatively as spherical rigid plastic inclusions in a homogenized Gurson matrix phase and the volume fractions are determined from a maximum packing argument.

The third chapter deals with the plastic anisotropy of porous solids. In fact, initial anisotropy may be either naturally present in various engineering materials or induced by the deformation during forming processes: e.g rolling, drawing and extrusion (see Fig. 5). Therefore, plastic anisotropy should be incorporated into the macroscopic constitutive model of porous ductile metals. Extension of Gurson's model to plastically anisotropic matrix was performed by Benzerga and Besson (2001) who used a simplified description of matrix anisotropy, by using the Hill quadratic yield criterion. In this chapter, we use a stress variational limit analysis approach, initially developped by Cheng et al. (2014) for isotropic materials, and derive a quasi-lower bound model for ductile porous materials incorporating plastic anisotropy by considering a Hill type matrix.

In the fourth chapter, we are concerned with the mechanical effective behavior of nonlinear two-phase composites subjected to finite deformations. For linear composites, successful MFH models have been developed based on an approximate use of Eshelby's solution. A significant research effort has been devoted to extending MFH to the nonlinear regime and several methods each based on its own assumptions and approximations have been proposed. The unifying feature of those methods is the definition of a linear comparison composite (LCC) whose response approximates that of the nonlinear composite.

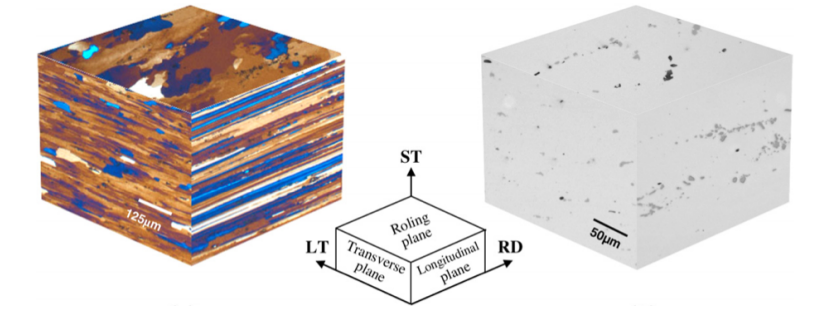

(a)

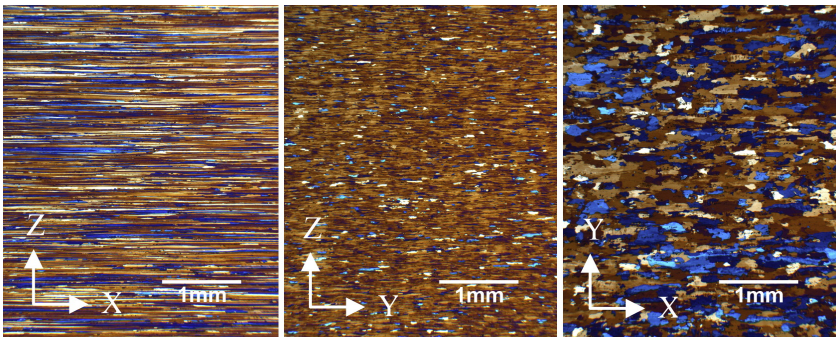

(b)

Figure 5: (a) Tri-planar optical micrographs along the three orthogonal directions of the rolled plate illustrating the grain structure and the particle distribution of the AA7075-T651 aluminium alloy. (b)Microstructure of AA7075-T651 where X designates the rolling direction, Y the transverse direction and Z the thickness direction of the plate. The figures show a "complex and non-recrystallized grain structure with flat, elongated grains in the rolling plane. The rolling process also implies a strong crystallographic texture, which leads to anisotropic characteristics" Brvik et al. (2010), Fourmeau et al. (2011).

In this chapter, we propose two models which also rely on the definition of a LCC. Local constitutive equations of each solid phase are based on a multiplicative decomposition of the deformation gradient onto elastic and inelastic parts and hyperelastic-plastic stress-strain relations. In the first part, an incremental approach is presented which is based on a rate formulation of the constitutive equations. The formulation builds on the earlier finite strain homogenization framework of Nemat-Nasser (1999). The latter showed how to generalize Eshelby's results as well as mean field homogenization schemes, provided that we consider tangent operators which are uniform per phase. In the second part of the chapter, we present a second approach based on the incremental secant formulation El Ghezal et al. (in preparation) , initially formulated by Wu et al. (2013a) for infinitesimal strains. This homogenisation scheme allows to evaluate the residual stress and strain states in each phase by applying a fictitious elastic unloading step. The LCC is then subjected to a strain increment deduced from the residual state. The finite strain problem is reformulated in a similar way than the infinitesimal one involving elastic left Cauchy-Green strain and Kirchhoff stress (see Simo (1992)).

Finally, we summarise the main conclusions obtained from the work presented in this dissertation, and we highlight its contribution. Some ideas for possible future research directions are also presented.

Supporting publications:

- El Ghezal M.I., Maalej Y., Doghri I., (2013) Micromechanical models for porous and cellular materials in linear elasticity and viscoelasticity, *Computational Materials Science*, 70: 51–70.
- El Ghezal M. I., Doghri I., (2013) Micromechanical Modeling of Porous Solids, *Poromechanics V: Proceedings of the Fifth Biot Conference on Poromechanics*.
- Doghri I., El Ghezal M. I., Adam L., (2016) Finite strain mean-field homogenization of composite materials with hyperelastic-plastic constituents, *International Journal of Plasticity*, 81: 40–62.
- El Ghezal M. I., Doghri I., Kondo D., (2017) Static limit analysis and strength of porous solids with Hill orthotropic matrix, *International Journal of Solids and Structures*, 109: 63–71.
- El Ghezal M. I., Doghri I., Porous plasticity: predictive second moment homogenization models coupled with Gurson's solution, *Under review*.
- El Ghezal M. I., Wu L., Doghri I., Noels L., A finite strain incremental-secant homogenization model for elasto-plastic composites. *in preparation*.

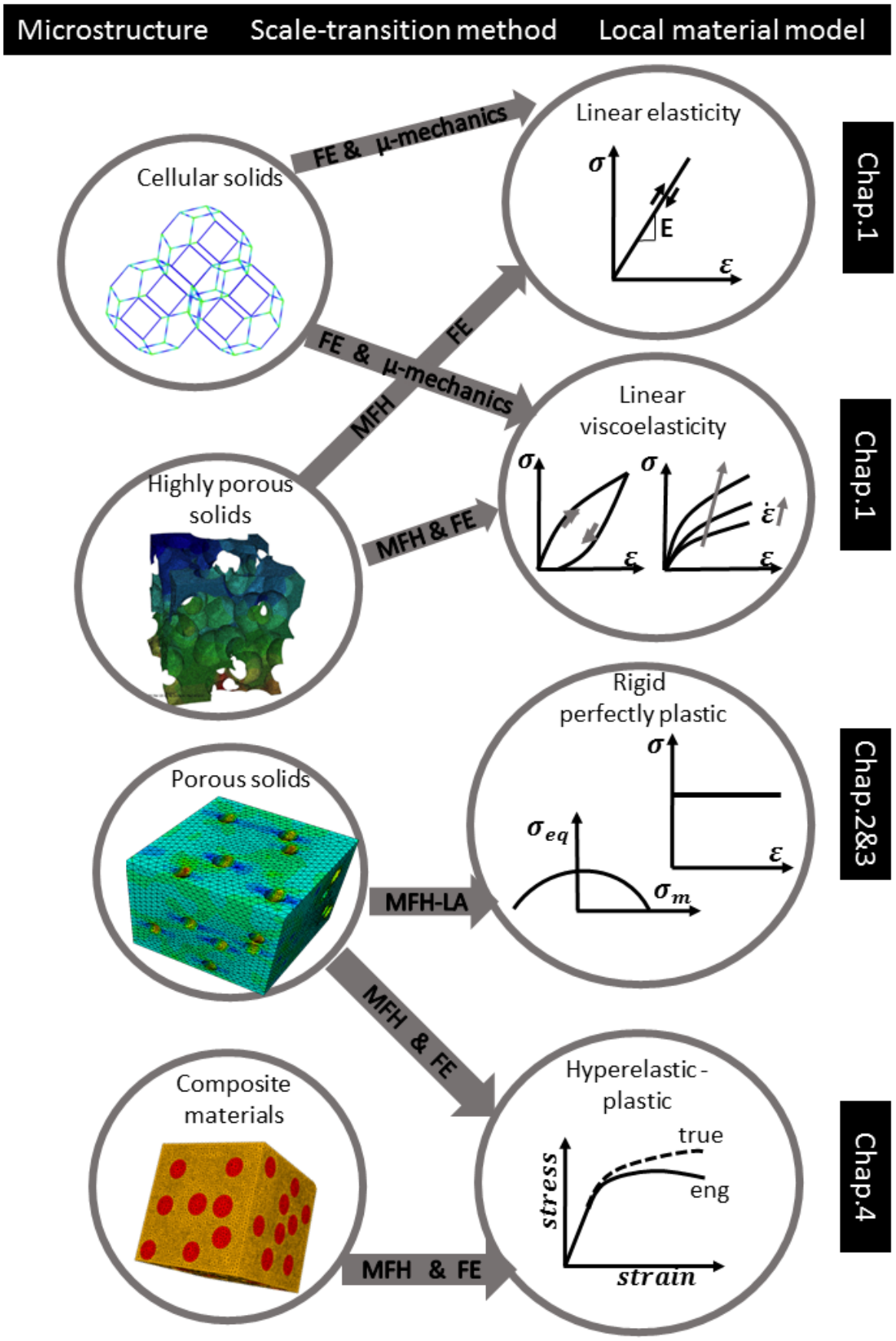

LA = limit analysis, MFH = mean field homogenization, FE = finite element

CHAPTER 1

Porous materials in linear elasticity and viscoelasticity

Summary

Due to their interesting properties and diverse applications, porous solids and cellular materials are the focus of many researches. This chapter deals with the prediction of the macroscopic elastic and linear viscoelastic properties of these materials based on their microstructure. Hence, a comparative study of several micromechanical models is conducted for both porous solids and open cell foams. Analytical beam theory models based on tetrakaidecahedron representation of the microstructure are studied for cellular materials. The applicability of common Mean Field (MF) theoretical models is examined and compared for porous solids in the whole range of porosity. The linear viscoelastic behavior is deduced from elastic results using the correspondence principle for both cellular and porous solids. Finite Element (FE) analyses are carried out in order to assess the quality of analytical solutions in elasticity and viscoelasticity. Unit cell FE models under periodic boundary conditions were developed for cellular materials and Representative Volume Elements (RVE) were generated to represent the porous solids. Finally, the potential of MF models suitable for highly porous solids to predict the response of cellular materials is investigated.

keywords

Porous solids, homogenization, elasticity, linear viscoelasticity, Finite elements, RVE

Present Chapter corresponds to the published research paper El Ghezal et al. (2013).
A self-consistent notation is adopted.

In this first chapter we are concerned with the effective behavior of linear elastic and viscoelastic porous materials for the entire range of porosity. The main objective is to develop and validate Mean-Field models (MF) for porous materials and then to see to what extent MF models validated for highly porous materials can or cannot predict the effective response of cellular materials. It is assumed that the reader is familiar with MF approach. An extensive description of the MF homogenization methods can be found in the book of Nemat-Nasser and Hori (1999). Moreover, a thorough introduction to cellular solids can be found in the book of Gibson and Ashby (1999).

1.1 Introduction

Foams and porous solids are characterized by their ability to combine good properties with light weight. They are used in diverse areas of application such as thermal insulation (taking advantage of their low thermal mass), energy absorption, buoyancy and sound-proofing, but they also exist as biomaterials. The literature describing the microstructure of cellular solids is vast. As regards modeling, the three dimensional networks of cellular materials were modeled by both open and closed cells. The standard cell shapes used as an idealization of the cells in foams are the rhombic dodecahedron Plateau (1873) and the tetrakaidecahedron structure Zhu et al. (1997),Li et al. (2003), while other simplified models of foams use cubic cells Gibson and Ashby (1999),Gibson (2005) and Roberts and Garboczi (2002). The effective mechanical behavior of cellular solids (especially open cell solids) was studied in the literature in elasticity and viscoelasticity. This was achieved by homogenizing the heterogeneous structure of the material using several approaches such as the theory of beams (e.g Dement'ev and Tarakanov (1970a),Dement'ev and Tarakanov (1970b),Zhu et al. (1997),Li et al. (2003) for elastic behavior and Mills (2006), Zhu and Mills (1999) for linear viscoelasticity) and the semi-empirical method with fitting parameters (e.g Gibson and Ashby (1999), Huang and Gibson (1991) for both elasticity and viscoelasticity).

On the other hand, porous solids can be seen as composites made of a solid matrix material and cavities or voids. In this sense, the application of the well-known Mean Field Eshelby-based homogenization methods (MF) is possible. Numerous models were developed in the field of composite materials. Among them, the Generalized Self Consistent Method (GSCM, Christensen (1990),Christensen and Lo (1979), Christensen (1979)), Composite Sphere Model (CSM,Hashin (1962)), Mori-Tanaka Model (M-T,Mori and Tanaka (1973), Benveniste (1987)) and Differential methodNorris (1985). Using MF approach, one can consider isotropic porous solids as a particular case of a two phase composite where the second phase (the inclusions) is replaced by a random distribution of spherical voids. The effective elastic moduli can be derived from the citetd MF homogenization schemes as a function of both the moduli of the matrix and the porosity (proportion of voids).Ramakrishnan and Arunachalam (1990) tuned the CSM to the case of porous solids. Other studies use empirical scaling models (named generalized means) for averaging the elastic properties of porous solids (e.g Pabst et al. (2006), Ji (2004), Ji et al. (2006)). In practice, the semi empirical approach is not fully predictive as it is experiment dependent.

There is abundant literature on cellular solids and on composite materials. However, the

governing tendency is to treat these materials separately. There are few works which investigate the link between the predictions of micromechanical models used for porous materials on the one hand, and those for cellular solids on the other hand.

The aims of this study are the following. Firstly, to predict the macroscopic behavior of porous solids and open cell foams in linear elasticity and viscoelasticity as a function of their microstructure using several models from the literature. FE computations are conducted on a unit cell for cellular solids and on Representative Volume Elements (RVE) for porous materials. The various models are confronted to FE analyses in order to choose those which provide the best match against FE predictions. Secondly, to test whether solids with high porosity and cellular materials are within the prediction range of MF homogenization models. A major motivation for this is that the extension of MF models to nonlinear behavior (e.g., elasto(visco)plasticity) is both well mastered in the literature and computationally cheap, to the contrary to micromechanical models for cellular materials. However, this raises some issues which will be discussed in section 1.5.

This study has the following outline. In section 1.2, we study cellular solids, especially open cell foams. We focus on analytical homogenization models in elasticity, and FE simulations are performed on unit cells. The predictions of different analytical models are compared to FE results. A second part of this section is dedicated to extending the study to viscoelasticity. For cellular solids, stress relaxation and strain creep functions are related to solid relaxation modulus and geometric properties using the correspondence principle. Predicted results are then compared to FE simulations. In section 1.3, we analyse porous solids. Different MF models are applied to determine the effective elastic properties. FE simulations are carried out on RVE containing various concentrations of voids, up to 65%. Analytical results are compared to FE ones. Elastic models are extended to linear viscoelasticity and verified by FE creep and relaxation tests. In section 1.4, the link between the predictions of models for highly porous materials and foams is discussed. The ability of some MF models to predict results for cellular solids will be illustrated in both elasticity and viscoelasticity. Conclusions are drawn in section 1.5.

List of acronyms
MF: Mean Field, FE: Finite Element, RVE: Representative Volume Element, GSCM: Generalized Self Consistent Method, CSM: Composite Spherical Model, M-T: Mori-Tanaka, DM: Differential Method, BCC: Body Centered Cubic, PU: Polyurethane, LCT: Laplace Carson Transform, R-A: Ramakrishnan-Arunachalam, BC: Boundary Condition, 3PE: Three Point Estimates.

1.2 Cellular solids

1.2.1 Elasticity

1.2.1.1 Micromechanical models

Many studies tried to find a link between microscopic and macroscopic properties of foams and this by making use of beam models, (e.g.Gibson (2005)Dement'ev and

Tarakanov (1970a),Dement'ev and Tarakanov (1970b),Zhu et al. (1997),Kim and Al-Hassani (2001),Warren and Kraynik (1988),Warren and Kraynik (1997) and Li et al. (2003)). In contrast, since these models are based on beam theory, they are valid only for low density cellular solids. We will focus hereafter on the model of tetrakaidecahedron cells packed in a Body Centered Cubic (BCC) lattice. Our choice is motivated by the fact that this lattice model was found to be a good model for isotropic open cell foams whereas other models (close-packed hexagonal and face-centered cubic) are highly anisotropic Ko (1965),Huber and Gibson (1988). As illustrated in figure 1.1, the tetrakaidecahedral cell has eight regular hexagonal faces and six square faces. It possesses cubic orthotropy and could be periodically extended in the three orthogonal directions. All the struts of the tetrakaidecahedral cell are assumed to be uniform beams satisfying the classical beam theory. The relative density R is defined as the density of the cellular material divided by that of the solid from which the cell walls are made .

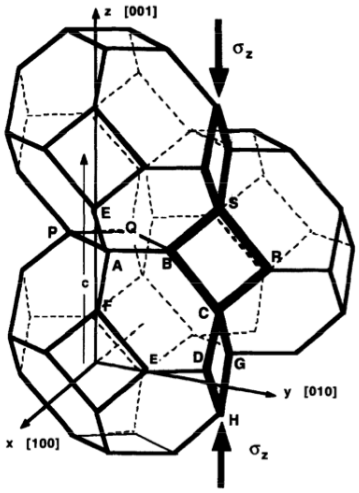

Figure 1.1: Tetrakaidecahedral model. Zhu et al. (1997)

By taking L the length of an edge (e.g [BC] in figure 1.1) and A its cross section area, the relative density of an open cell foam with regular tetrakaidecahedral cells is:

$$R = \frac{3A}{2\sqrt{2}L^2} \tag{1.1}$$

Many authors used this kind of cells for the modeling of cellular structures. We will review a selection of analytical models studied by Zhu et al. (1997) and Li et al. (2003), based on beam theory.

Zhu et al. model

The model of Zhu et al. (1997) is based on the following assumptions:

- There are three modes of deformation: bending, stretching and torsion of edges

- There is no rotation of joints and only the edges have the ability to deform

Zhu et al. defined for each mechanical test (tensile and shear) an associated *structure cell* which consists on only a part of the lattice bounded by mirror planes. Using the symmetry of the RVE and energy methods, the three mechanical constants of the cellular material are given by:

$$\bar{E} = \frac{6\sqrt{2}EI}{L^4(1+\frac{12I}{AL^2})},\ \bar{\nu} = 0.5\frac{AL^2-12I}{AL^2+12I},\ \frac{1}{\bar{\mu}} = \frac{2\sqrt{2}L^2}{EA} + \frac{\sqrt{2}L^4}{6EI}\frac{8EI+\mu I_p}{5EI+\mu I_p} \tag{1.2}$$

where A, I and I_p are respectively: the cross sectional area, the second moment of area and the polar second moment of area of each edge. Their values depend on the shape of the edge's section. Elastic constants can be re-expressed as a function of the relative density R. For square sections, they are respectively:

$$\bar{E} = \frac{0.629R^2E}{1+0.943R},\ \bar{\nu} = 0.5\frac{1-0.943R}{1+0.943R},\ \bar{\mu} = \frac{0.207R^2E}{1+0.62R} \tag{1.3}$$

For other section shapes and more details we refer to Zhu et al. (1997). In order to examine the anisotropy of the tetrakaidecahedral model, Zhu et al. (1997) evaluated Zener's anisotropy factor for the foam ζ given by:

$$\zeta = \frac{2(1+\bar{\nu}_{12})\bar{\mu}_{12}}{\bar{E}_{[100]}}$$

where $\bar{E}_{[100]}$ and $\bar{\nu}_{12}$ are the Young's modulus and Poisson's ratio for a tensile test along [100] axis and $\bar{\mu}_{12}$ is the shear modulus measured in the cube lattice axes.

They found ζ to be close to unity (which correspond to isotropic materials). They concluded that the elastic response is isotropic. Similar results were proved in Warren and Kraynik (1997). We obtained the same expression of effective Young's modulus as equation (1.2) using the homogenization procedure proposed by Onck (2008) (see Appendix A).

Li et al. model

Li et al. (2003) used Castigliano's energy theorem to develop their 3D cell model (the same as in figure 1.1). The analysis is performed on a tetrakaidecahedral unit cell under the following hypotheses:

- All the vertices (where the four edges meet) are rigid joints
- The deformation modes are: bending, stretching and shearing

The expressions of Young's modulus and Poisson's ratio are respectively:

$$\begin{aligned}\bar{E} &= \frac{cER^2}{0.07872 + (1.171875 + 1.21875k(1+\nu))cR} \\ \bar{\nu} &= \frac{0.342105 + 0.297729(1+6(1+\nu)k)cR}{1+0.595458(25+26(1+\nu)k)cR}\end{aligned} \tag{1.4}$$

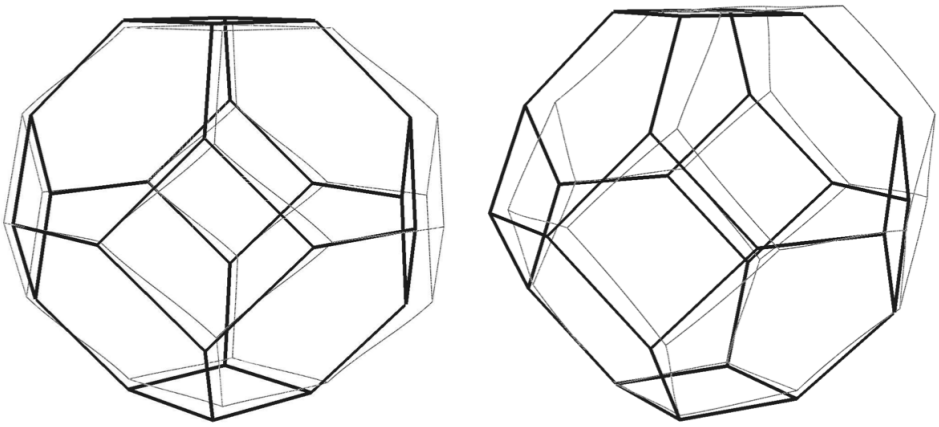

(a) (b)

Figure 1.2: FE Model of tetrakaidecahedral unit cell. The thin lines show the deformed shape (a) under a tensile test, (b) under a shear test.

Where two geometric parameters c and k are $c = I/A^2$ and k is the transverse shear factor. For square sections, $c = 0.0833$ and $k = 1.2$.
These formulae show explicitly the dependence of the effective mechanical properties on the foam density (R), the cross section shape and the elastic properties of the constitutive material. Differing from the result of Zhu et al. (1997), the expression of the effective Poisson's ratio incorporates the Poisson's ratio of the strut material.

Li et al. (2003) didn't compute the shear modulus to verify the isotropy of the foam model. Nevertheless, in section 1.2.1.3, a shear modulus computed using the isotropy hypothesis will be confronted against FE simulations and other analytical results to check the validity of the assumption.

1.2.1.2 FE simulations

As seen in the previous section, three-dimensional open cell foams can be modeled by regular tetrakaidecahedral cells sitting on a BCC lattice. Since the microstructure is periodic along the three directions, a unit cell is sufficient to provide the information needed to compute the effective properties at the macroscopic scale provided that periodic boundary conditions are imposed Michel et al. (1999), Bornert et al. (2001). FE Simulations are therefore performed on a tetrakaidecahedral unit cell (figure3.1) generated by Abaqus software. The struts are modeled by Timoshenko beam elements (Abaqus type B31) having square cross sections. The tetrakaidecahedral cell's mesh contains 7200 elements (each strut is meshed with 200 elements) and 14425 nodes.

Periodic boundary conditions

In order to apply periodic boundary conditions, we placed the unit cell in a fictitious cube of dimensions L so that the six square faces of the tetrakaidecahedral are tangent to the faces of the cube. The origin of the coordinate system (o, x, y, z) is placed in the

center of the cube. Next, we added a set of master ($M(-0.5L, -0.5L, -0.5L)$)and slave nodes (S1, S2 and S3 respectively of coordinates $(0.5L, -0.5L, -0.5L)$, $(-0.5L, 0.5L, -0.5L)$ and $(-0.5L, -0.5L, 0.5L)$).
The displacement fields obey the following conditions:

$$\begin{aligned} u_i(M) - u_i(S_1) &= u_i(nodes \in face\ x = -L/2) - u_i(nodes \in face\ x = +L/2), \quad i \in [1,3] \\ u_i(M) - u_i(S_2) &= u_i(nodes \in face\ y = -L/2) - u_i(nodes \in face\ y = +L/2), \quad i \in [1,3] \\ u_i(M) - u_i(S_3) &= u_i(nodes \in face\ z = -L/2) - u_i(nodes \in face\ z = +L/2), \quad i \in [1,3] \end{aligned} \tag{1.5}$$

where u designates the displacement vector imposed as :

$$\begin{aligned} &M\ is\ a\ fixed\ node: && u_i(M) = 0, \quad i \in [1,3] \\ &No\ rotation\ around\ x: && u_3(S_2) = 0 \\ &No\ rotation\ around\ y: && u_1(S_3) = 0 \\ &No\ rotation\ around\ z: && u_2(S_1) = 0 \end{aligned} \tag{1.6}$$

Furthermore, depending on the test to be performed, a displacement is applied to the appropriate slave node. The macroscopic stress is computed from the external tractions at the master and slave nodes and the strain from displacement components of these nodes (details in Kouznetsova (2004)). In the case of cubic symmetry, only three independent elastic constants need to be computed. Both the effective Young's modulus and Poisson's ratio can be derived from a tensile test applied along one of the cube axes. The shear modulus is directly obtained from a shear test. In this work, tensile tests were conducted along three orthogonal directions parallel to the axes of the BCC lattice and simple shear tests were also simulated in order to obtain effective shear moduli. Besides, hydrostatic tensile tests were performed for a proper evaluation of the effective bulk modulus.

1.2.1.3 Analysis of results: application to polymeric foams

In this section, the predictions of the analytical tetrakaidecahedral models are compared to results from FE simulations on the unit cell. For the previously presented analytical models and FE computations, the estimate of the relative density of the foam neglects the multiple volumes at overlapping beams meeting in the vertices of the tetrakaidecahedral cell. The formula of equation (1.1) supposes the entire volume of each strut to be considered, whereas for the real foam, for given cross section and beam length, the real relative density is lower than the theoretical one. The error due to the overlap is insignificant for low relative densities, but becomes non negligible for higher values of R. We computed the overlap volume using Autocad software and developed a relationship matching the theoretical relative density used in Abaqus and in analytical models with the corresponding real one. The details of the formulation are given in Appendix B and the variation of the real relative density of the foam is plotted against the theoretical one in figure 1.20. The variation of the effective elastic constants versus relative density will be presented in figures including both densities in horizontal axes.
Consider a polymeric open cell foam (made of Polyurethane (PU)) as an application to compare different predictions of elastic constants. The constitutive material of the solid skeleton behaves like an isotropic solid characterized by Young's modulus $E = 100$ MPa

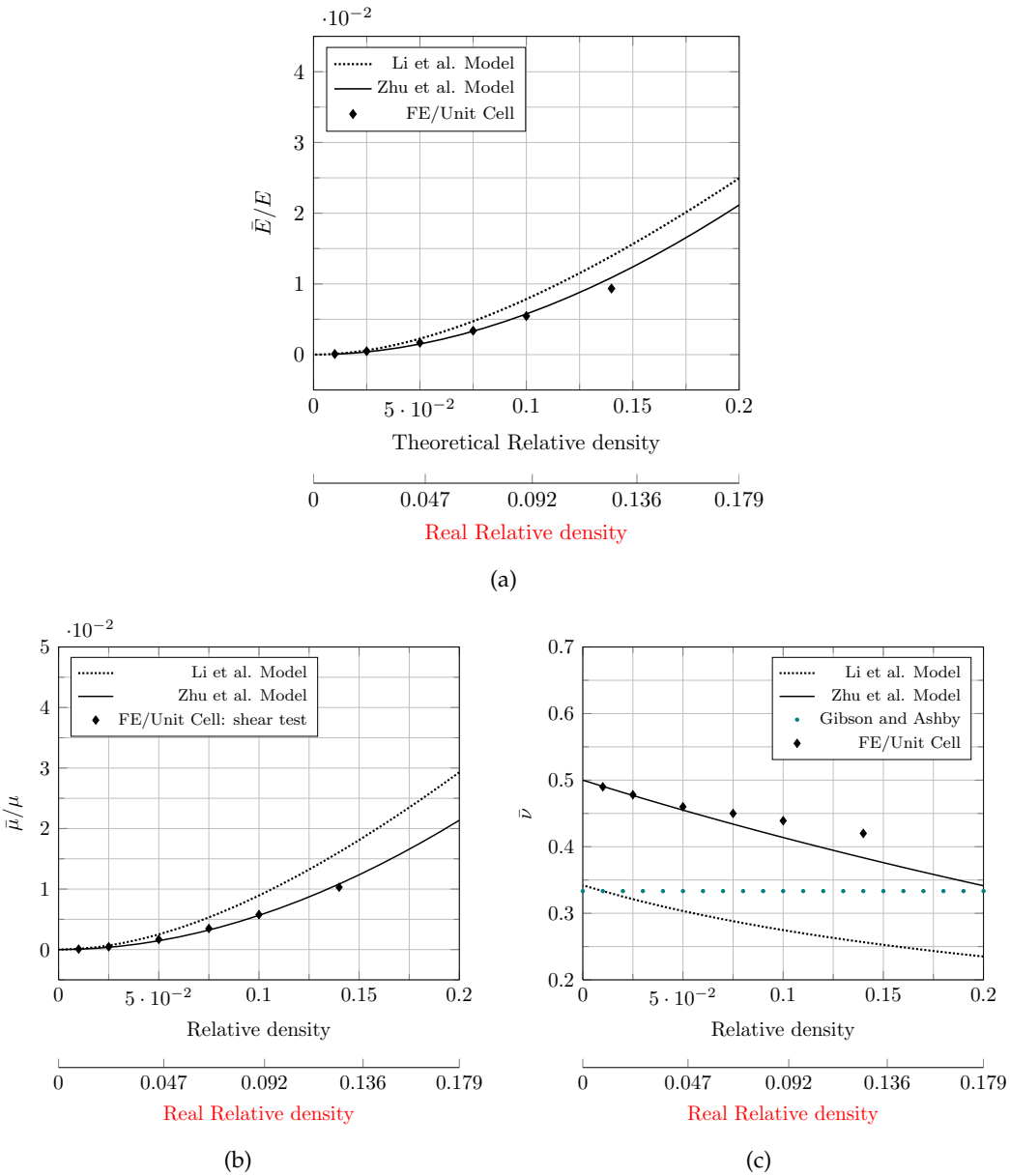

Figure 1.3: Variation of the effective properties of a foam with the relative density: (a) normalized Young's modulus, (b) normalized shear modulus and (c) Poisson's ratio.

Table 1.1: Zener's anisotropy factor for the unit cell as a function of relative density

Theoretical Relative density R	0.01	0.025	0.05	0.075	0.1	0.14
Real Relative density R	0.0097	0.0240	0.0473	0.0701	0.0925	0.1277
Anisotropy factor ζ	0.96	0.97	1.005	1.03	1.04	1.08

and Poisson's ratio $\nu = 0.45$. The foam's Young's moduli computed with FE method from the tensile tests in the lattice vector directions [100], [010] and [001] are found to be almost equal (with a fluctuation less than 2%), which is a property of the cubic symmetry. The variation of the elastic constants predicted by the homogenization models with relative density is plotted in figure 1.3, along with FE results. It is seen in figure 1.3(a) that at low relative densities, all predictions of Young's modulus are close. For higher densities, Zhu et al. model gives a good agreement with FE and the difference between Li et al. model and Zhu et al. predictions increases with relative density.
As shown in figure 1.3(c), despite the fact that the models of Zhu et al. and Li et al. emanate from the same geometry, there is an unexpected difference between the Poisson's ratios predicted by each one. For lower relative densities, Poisson's ratio predicted by Zhu et al. comes close to 0.5 and therefore, an incompressible behavior. This result agrees well with that obtained by FE simulations. However, the predictions of Li et al. approached the average experimental value ($\bar{\nu} = 1/3$) proposed by Gibson and Ashby (1999).

The results of shear simulations are plotted in figure 1.3(b) and the dimensionless Zener's anisotropy factor ζ is computed from FE results for different relative densities. The output is reported in table 1.1. The computed values of ζ are found to be close to unity which means that the effective behavior approaches macroscopic isotropy.

The effective shear modulus $\bar{\mu}$ was not provided by Li et al. model, yet, we approximated it using the isotropic relationship with Young's modulus and Poisson's ratio. These predictions and those of Zhu et al. model are both compared with FE results in figure 1.3(b). The figure shows that the values of $\bar{\mu}$ predicted by Zhu et al. fit the FE results well. However, the approximation of $\bar{\mu}$ from Li et al. model tends to overestimate FE results as the relative density increases.

It is worth mentioning that while we modeled open cell cellular solids by a periodic model of tetrakaidecahedral cell, the real material is random and its microstructure is more complex. The limitation of the previously discussed models is that they do not account for the natural irregularities due to imperfect geometry or/and irregular arrangement of cells. This is out of the scope of the current study; for a thorough analysis of the effect of cell irregularities on the overall mechanical behavior refer for instance to Li et al. (2006), Zhu et al. (2000) andLuxner et al. (2007).

1.2.2 Viscoelasticity

In this section, we will employ the elastic solutions for solving linear viscoelastic problems, by taking advantage of the correspondence principle. The macroscopic viscoelastic behavior of cellular materials will be defined in terms of effective relaxation moduli and

equivalently creep compliances using the microscopic ones and the geometric properties. For a homogeneous linear viscoelastic solid, the three dimensional constitutive equation is given by Boltzmann's superposition principle as follows:

$$\boldsymbol{\sigma}(t) = \int_{-\infty}^{t} \boldsymbol{C}(t-\tau) : \dot{\boldsymbol{\varepsilon}}(\tau)\, d\tau \tag{1.7}$$

where $\boldsymbol{C}(t)$ is the fourth order viscoelastic relaxation tensor and $\dot{\boldsymbol{\varepsilon}}$ is the second order strain rate.

Assuming the material to be isotropic, the relaxation tensor can be decomposed into deviatoric and volumetric parts $\boldsymbol{C}(t) = (2\mu(t), 3K(t))$ where $\mu(t)$ and $K(t)$ are the shear and bulk relaxation moduli, respectively. Similarly to equation (1.7), it is possible to relate the strain to the stress history via the creep compliance tensor $\boldsymbol{J}(t)$. In fact, when this function is slowly varying with time it can be deduced from the relaxation function by the approximation $\boldsymbol{J}(t) \cong \boldsymbol{C}^{-1}(t)$ (Wineman and Rajagopal (2000), Salençon (1983)).
The viscoelastic material's stress relaxation data can be approximated by a set of Maxwell elements (spring and viscous damper connected in series) assembled in parallel plus a single spring (a long term elastic element). Then the relaxation moduli are given by a Prony series:

$$\begin{cases} \mu(t) = \mu_0[1 - \sum_{i=1}^{n} \mu_i\,(1 - exp(-t/\tau_i^{\mu}))] \\ K(t) = K_0[1 - \sum_{i=1}^{m} k_i\,(1 - exp(-t/\tau_i^{K}))] \end{cases} \tag{1.8}$$

where μ_0 and K_0 are the instantaneous shear and bulk moduli, μ_i and k_i are the dimensionless shear and bulk moduli associated with relaxation times τ_i^{μ} and τ_i^{K}, respectively.

1.2.2.1 Analytical predictions obtained from elastic solutions

The Laplace Carson Transform (LCT) allows to generalize the elastic constitutive equations to the linear viscoelastic behavior. As a matter of fact, the viscoelastic response can be written as the elastic solution when a change of variables is made. The following correspondence relates the elastic constants to the relaxation functions in the Laplace Carson domain Wineman and Rajagopal (2000):

$$\begin{cases} E \leftrightarrow s\, E_R(s) \\ K \leftrightarrow s\, K_R(s) \\ \mu \leftrightarrow s\, \mu_R(s) \end{cases} \tag{1.9}$$

The inverse of LCT is then required to obtain the time dependent creep or relaxation functions. This inversion can be solved by numerical techniques if needed. Hereafter, we apply the correspondence principle to extend the effective elastic moduli obtained in section 1.2.1.1 from different homogenization schemes to linear viscoelastic behavior and to express the effective relaxation and creep functions. The application is found in the case of isotropic porous solids and cellular materials to be simple (although the model of Li et al. is Poisson's ratio dependent, we suppose that the latter is constant), hence, we will limit our illustration to only one example taken from Zhu et al. model:

The solution of the elastic problem is given by equation (1.2). As we apply the correspondence principle, we have in Laplace-Carson domain:

$$s\,\bar{E_R}(s) = \frac{6\sqrt{2}\,s\,E_R(s)\,I}{L^4(1+\frac{12I}{AL^2})} = \alpha\,s\,E_R(s) \tag{1.10}$$

where α is the geometric constant. Applying the inverse Laplace transform:

$$d\bar{E_R}(t) = \alpha\,d\,E_R(t) \tag{1.11}$$

$$\Longrightarrow \int_0^t d\bar{E_R}(\tau) = \alpha \int_0^t d\,E_R(\tau) \tag{1.12}$$

It was assumed that the material has been stress free for times anterior to zero. Considering that $\bar{E_R}(+\infty) = \bar{E}$ and using the relationship between $\bar{E}$ and E, we obtain:

$$\bar{E_R}(t) = \alpha\,E_R(t) \tag{1.13}$$

This implies that the foam's relaxation is linearly related to the one of the constitutive solid and that it is sufficient to replace the elastic modulus by the time-dependent relaxation function. It means that the stress relaxation (or respectively the creep strain) of the foam is simply that of the solid multiplied by the ratio of the elastic stiffnesses. The same result was found by Huang and Gibson (1991) who, starting from the proportionality between the elastic constants of the open cell foams and an empirical equation describing the viscoelastic behavior of solid polymer, ended with a relative creep compliance of the foam ($\frac{\bar{J}(t)}{J(t)} = \frac{E}{\bar{E}}$).

1.2.2.2 Verification of the analytical predictions against FE analysis: application to PU foams

At small strains, many solid polymers have a linear viscoelastic response. In other words, creep strains are proportional to the stress under a constant load at any given time. We will use for this analysis (as an application) the experimental data obtained by Zhu and Mills (1999) on solid PU and look for the overall behavior of the PU foams for various relative densities applying some analytical models extended to linear viscoelasticity, and FE simulations. The relaxation Young's modulus of the solid Bulpren PU was approximated by:

$$E_R(t) = E_\infty + \sum_{i=1}^{n} E_i\,exp(-t/\tau_i) \tag{1.14}$$

With eight relaxation times: $0.01, 0.1, 1, \cdots 10^5$ and moduli $E_i = 9.3$ MPa for $i = 1$ to 8 and $E_\infty = 28$ MPa. The experimental data provided only the relaxation Young's modulus. We calculated the bulk and the shear moduli of the solid assuming Poisson's ratio to be constant and set to 0.45 following Mills (2006). Similarly to the elastic analysis, we conducted FE computations on different unit cells of cellular solids with varying relative

density (by adjusting the beam section).

The unit cell is described in section 1.2.1.2. In this test the polymer foam undergoes uniaxial compression creep (the applied stress σ_0 = 1kPa). The FE effective relaxation modulus can be deduced using the approximation $\bar{E}_R(t) \cong 1/\bar{J}(t)$, where $\bar{J}(t) = \bar{\varepsilon}(t)/\sigma_0$ and $\bar{\varepsilon}(t)$ is the resulting macroscopic strain. The predictions of the micromechanical foam models of Li et al. and Zhu et al. generalized to linear viscoelasticity (by means of LCT) are compared with FE simulations and Huang and Gibson viscoelastic model Huang and Gibson (1991) .

Figures 1.4(a) and 1.4(b) show the superposition of the predictions by different methods for polymer foams of relative density 0.05 and 0.025 respectively. The FE results are bounded by the extended Li et al. and Zhu et al. predictions.

1.3 Porous solids

1.3.1 Elasticity

1.3.1.1 Micromechanical models

In this section we consider porous solids as a specific case of a two-phase composite material. All inclusions are voids having spherical shape and a random arrangement, embedded in a continuum matrix. We define the volume fraction f_i of a phase i which occupies a region Ω_i as: f_i=v(Ω_i)/v(Ω), where v(Ω_i) and v(Ω) represent respectively the volume of region Ω_i and that of the RVE. The matrix parameters will not be indexed; however, index i will be attributed to the second phase (i.e E is the matrix Young's modulus and E_i refers to the inclusion's modulus). From now on, we will denote the volume fraction of the void phase by porosity p. Assuming isotropic behavior, the effective stiffness of the homogenized composite can be decomposed into deviatoric and volumetric parts such that :

$$\bar{C} = (2\bar{\mu}, 3\bar{K}) \tag{1.15}$$

where $\bar{K}$ and $\bar{\mu}$ are respectively the unknown effective bulk and shear moduli, and our objective is to compute them in terms of the matrix properties and the porosity. We compare hereafter the validity of some analytical homogenization schemes using FE calculations based on different RVEs for a large range of porosity [0-65%].

Composite sphere model (CSM)

The Composite Sphere Model (CSM) was introduced by Hashin (1962). The model postulates that the composite can be modeled by an assemblage of concentric composite spheres of various sizes. Each sphere is imagined to be composed of a core comprised of the inclusion material and surrounded by a shell of the matrix phase. The size distribution has a particular characteristic, that is the ratio of radius a (internal sphere) by b (external sphere) is constant regardless of the size of the composite sphere, such that $(\frac{a}{b})^3 = f$,

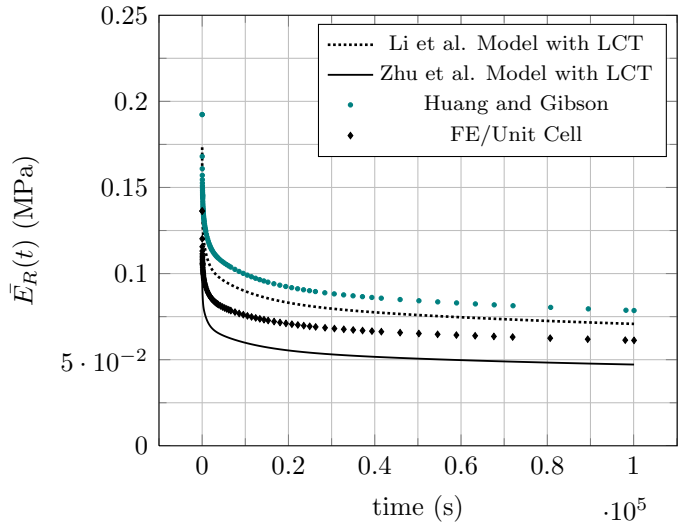

(a)

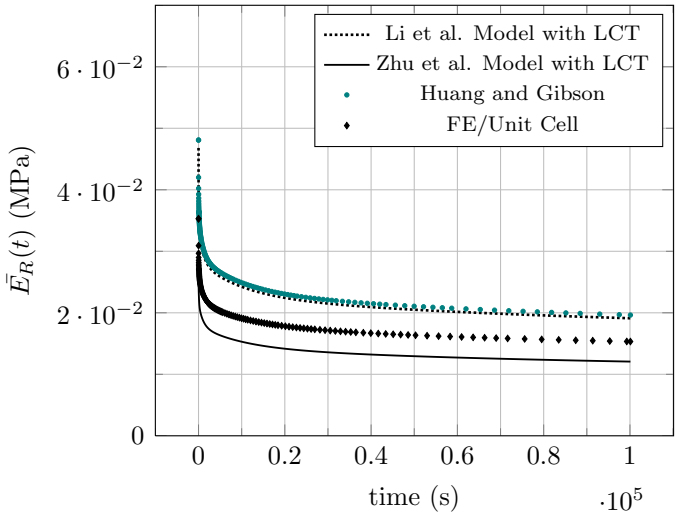

(b)

Figure 1.4: Effective relaxation modulus predictions of polymer foams. The FE computations are performed on unit cells as described in section 1.2.1.2. (a) Polymer foam of relative density 0.05, (b) Polymer foam of relative density 0.025.

where f is the volume fraction of the inclusions in the entire composite. To fill the entire space of the composite by spheres, there must be very small ones. Quite obviously, such a model is not appropriate for a composite with single size particles. Transposing the model to the particular case of porous solid, the CSM yields an exact solution of the bulk modulus and only bounds for the shear modulus.

$$\frac{\bar{K}}{K} = \frac{(1-p)(2-4\nu)}{(2-4\nu)+(1+\nu)p} \tag{1.16}$$

Though the upper and lower bounds are close for a two-phase composite, they diverge widely when extended to the case of porous solids given the very high contrast between the properties of the matrix and the pore. However, at very small and very large volume concentrations, it is found that both upper and lower bound expressions of the shear modulus coincide and are reduced to :

$$\frac{\bar{\mu}}{\mu} = \frac{(7-5\nu)(1-p)}{15(1-\nu)} \; ; p \mapsto 1 \tag{1.17}$$

$$\frac{\bar{\mu}}{\mu} = 1 - \frac{15(1-\nu)p}{7-5\nu} \; ; p \mapsto 0 \tag{1.18}$$

Generalized self consistent model (GSCM)

This model as described by (Christensen and Lo (1979), Christensen (1979)) consists of a composite sphere, made of concentric matrix and inclusion spheres such that the ratio of the internal and external radii respects the prescribed volume fraction. The composite sphere is embedded in an infinite equivalent homogeneous medium having the unknown effective properties and subjected to uniform strain $\bar{\varepsilon}$. Christensen (1998) examined this model in the case of spherical voids ($k_i = \mu_i = 0$) and found the effective bulk modulus to be expressed as a function of porosity as:

$$\frac{\bar{K}}{K} = 1 - \frac{p}{1 - \dfrac{(1-p)(1+\nu)}{3(1-\nu)}} \tag{1.19}$$

The shear modulus is the positive solution of the quadratic equation:

$$A(\frac{\bar{\mu}}{\mu})^2 + 2B(\frac{\bar{\mu}}{\mu}) + C = 0 \tag{1.20}$$

Where the constants A, B and C depend on the porosity and the Poisson's ratio of the matrix. As concluded in Christensen (1998), the outcome of the comparison between GSCM and CSM is that the two models give the same bulk modulus but diverge on the effective shear modulus. In fact, GSCM yields an equivalent shear modulus independent of Poisson's ratio in the case of concentrated range (for $p \mapsto 1$), which is unexpected.

Ramakrishnan-Arunachalam (R-A) Model

Ramakrishnan and Arunachalam (1990) revisited the CSM of Hashin and transposed all the computations to the case of porous solids. Their study was conducted first on a single hollow sphere then generalized to the whole porous material introducing a "correction factor". In fact, in contrast to Hashin's approximation (Hashin (1962)) assuming that the pressure applied on the composite material is the same as the one exerted on the single composite sphere, Ramakrishnan and Arunachalam established a "Correction factor", in the case where the inner pressure inside each void is zero. They also introduced a model of variation of the effective Poisson's ratio as a function of porosity:

- for $p = 1$, $\bar{\nu}$: $constant = \ c \ = 0.25$ (from experimental results) $\forall$ the material,
- if $\nu = c$, $\bar{\nu}(p) = c \ \forall \ p$.

The effective elastic constants can be expressed in the form:

$$\frac{\bar{K}}{K} = \frac{(1-p)^2}{(1+\alpha_k p)}, \ \ \frac{\bar{\mu}}{\mu} = \frac{(1-p)^2}{1+\alpha_\mu p} \tag{1.21}$$

Where :

$$\alpha_k = \frac{(1+\nu)}{2(1-2\nu)}, \ \ \alpha_\mu = \frac{11-19\nu}{4(1+\nu)} \tag{1.22}$$

Mori-Tanaka (M-T) Model

This model was originally proposed by Mori and Tanaka (1973), and later, Benveniste (1987) published a simple interpretation of it. In the case of porous material with spherical voids, the model assumes that each cavity behaves as if it were isolated in an infinite body made of the matrix material and seeing as strain at infinity the average strain in the matrix of the actual composite. The result is based on the well-known Eshelby's solution Eshelby (1957) and superposition principle. The effective constants are found to be:

$$\frac{\bar{K}}{K} = \frac{2(1-p)(1-2\nu)}{2(1-2\nu)+p(1+\nu)}, \ \ \frac{\bar{\mu}}{\mu} = \frac{(1-p)(7-5\nu)}{7-5\nu+8p-10\nu p} \tag{1.23}$$

The Mori-Tanaka model yields estimates corresponding to Hashin's upper bound.

Differential Method (DM)

In the Differential Method (DM) Norris (1985) the composite's effective response is approximated by an iterative (or incremental or differential) scheme. At each iteration, the inclusions are added in dilute concentration to a homogeneous matrix material -which changes from one iteration to the next- until obtaining the requested final concentration. Initially one considers a volume V of a homogeneous isotropic material (matrix). Next, a low volume fraction of isotropic inclusions is embedded into this material such that the total volume V remains unchanged. Then, the obtained composite is homogenized. The effective properties of this composite are then affected to the matrix phase of the next iteration and an other portion of inclusions is added. The process is repeated up to the

final inclusions concentration value. We used a numerical procedure based on the M-T model at each iteration to compute the effective moduli of porous solids for the whole range of porosity. We could have used also the dilute inclusions model at each iteration. The following figure illustrates the iterative process adapted.

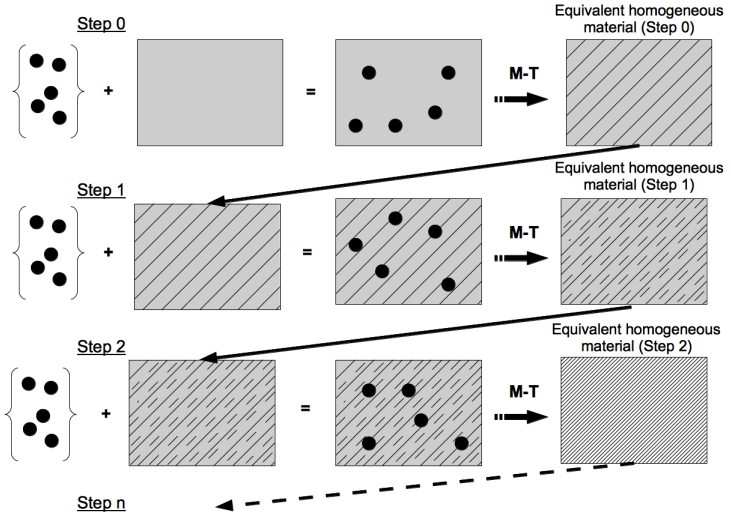

Figure 1.5: Schematic illustration of the iterative Differential Method

Some authors (e.g. Roscoe (1973) and Norris (1985)) argue that the DM scheme is only applicable to a microstructure containing a wide range of inclusion sizes. Their argument is that if the smaller inclusions are added first, then newly inserted larger inclusions would see the matrix with a concentration of smaller inclusions as a "homogeneous medium". According to this viewpoint, considering equal-size inclusions or cavities in DM would violate a basic tenet of homogenization. However, Hashin (1988) pointed out that " the requirements of infinitesimality of inclusion volume increment, large numbers of inclusions and increasing order of magnitude of inclusion size are mutually contradictory". Besides, as the inclusion size does not enter neither into the equations nor in the implementation of the scheme, there is no explicit influence of the inclusion size on the result.
In this work, we have a purely numerical view of DM, and we make no attempt at justifying it on physical grounds. At each iteration, we suppose a *homogeneous* matrix to which we add a *small* concentration of cavities. We can neither claim that this iterative numerical process is physically justified nor that the effective stiffness that is computed at the final iteration is an accurate approximation of the real composite's stiffness. The only certainty is that the real volume fraction of cavities (or inclusions) is reached at the end.
Now, there are two reasons which could explain good DM predictions. The first one is that the stiffness of the (fictitious -except at initialization) matrix at each iteration is computed from the homogenization of a two-phase medium at the previous iteration. Therefore

some "memory" is built-in from one iteration to the next, until the final concentration is reached. The second argument in favor of DM is the fact that at each iteration one profits from the accuracy of the homogenization models for dilute composites. A final high concentration of inclusions can be thus reached.

1.3.1.2 FE Simulations

The microstructure of isotropic porous solids was idealized by a continuum matrix containing a random distribution of spherical voids. In this study we considered three different microstructure geometries. The first consists of impenetrable spherical voids having equal size with a porosity ranging from 5% to 40%. The second microgeometry consists of identical overlapping spherical cavities. The inter-penetration between pores enabled us to model a porosity up to 65%. The third microgeometry is made up of a uniform distribution of void sizes. This type of microstructure involves a combination of a wide range of spherical void sizes varying from 0.05 to 0.3 (these values correspond to the diameter of the spherical void knowing that the length of the cubic cell is unity) and the porosity varying from 5% to 60%. The inter-penetration option was activated starting from 40%. The number of spherical voids (and the size distribution) were adapted in each case with the porosity in order to guarantee a suitable and sufficient number to obtain a representative cell (RVE). In addition, periodic geometry was generated in order to apply periodic boundary conditions (BCs) which provide the best estimate of the overall properties among the class of BCs. Indeed, it was verified by Terada et al. (2000) that convergence of the apparent properties to the effective values with increasing size of the RVE is reached faster with periodic BCs. The microstructure is generated using FE Digimat (2011) and meshed using modified quadratic tetrahedra elements (C3D10M) in Abaqus (2014). In average, around 2×10^5 elements and 4.8×10^5 nodes are generated for each RVE with the two first microstructures, and ranging from 2×10^5 to 10^6 elements for the third one. Figure 1.6 illustrates the mesh of two representative cells containing 65% of porosity for the second microstructure, and 60% for the third one. The periodic BCs are applied following the same criteria as described in section 1.2.1.2.

1.3.1.3 Results

In this section, the analytical mean field (MF) predictions of the macroscopic behavior are compared to reference results from FE computations. The PU polymer considered in the previous case of cellular solids is used as a matrix material. Various computations were realized varying the porosity from 5% up to 65%. For each porosity level, the effective moduli presented in the following were obtained by averaging three simulations over cells with statistically equivalent topologies for the two first microstructure types and over one random generation for the third type. The moduli fluctuation between the three different random generations (for the first two microgeometries) was found to be less than 3%. For each RVE, five tests were carried out, namely, three tensile tests (in order to extract both effective Young's modulus and Poisson's ratio and to check the isotropy of the RVE), simple shear test and hydrostatic tensile test. Figures 1.7 -1.8 show the predictions of macroscopic elastic constants obtained from various homogenization models confronted to FE computations. An exponential decay of the effective bulk modulus is

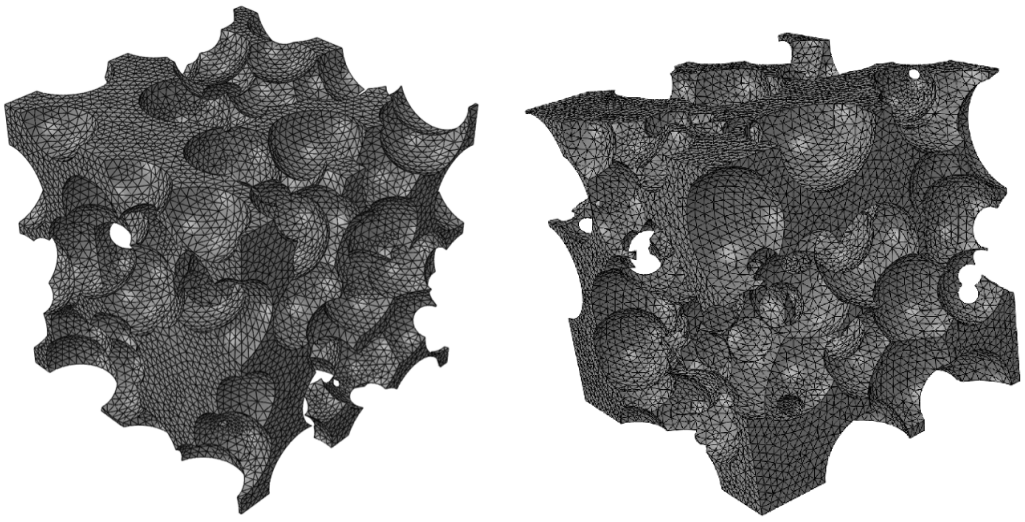

(a) (b)

Figure 1.6: (a): A representative cell of microstructure type 2 comprising 126 equal-size overlapping spherical pores with volume fraction of 65%. (b) RVE of microstructure type 3 containing 180 overlapping spherical voids with a uniform distribution of sizes [0.05 − 0.3] and porosity = 60%.

observed when examining its variation with porosity (figure 1.7(a)). At only 20% of voids, $\bar{K}$ is reduced to 30% of its initial value, which indicates a high sensitivity to porosity of the resistance to uniform compression. On the contrary, the shear modulus does not exhibit similar behavior (figure 1.7(b)).

As expected from equations (1.23), (1.19) and (1.16), M-T model, GSCM and CSM yield the same bulk modulus but discrepancy is observed for the effective shear modulus. As seen in figure 1.7, all predictions are close for low porosities but the difference between DM, R-A model and the other MF models for higher values of porosity become significant. The results obtained numerically by DM based on M-T model are identical to Zimmerman's Zimmerman (1991) equations derived using the differential approach for solids containing spherical pores. However, it is important to note for the CSM, that for the effective shear modulus, the two limits ($\mu_i \mapsto 0$ and $p \mapsto 1$) are not interchangeable. In order to find equation (1.17), one sets $p \mapsto 1$, then $\mu_i \mapsto 0$. It is then found that the two CSM bounds coincide. However, if one sets $\mu_i \mapsto 0$, then $p \mapsto 1$, the two bounds do not converge. This is illustrated in figure 1.7(b). The same issue was discussed in Christensen (1998) .
The variation of the effective Poisson's ratio with porosity given by different theoretical models is depicted in figure 1.8. GSCM, M-T and DM Poisson's ratios were estimated using the relationship with bulk and shear moduli. R-A model yields a theoretical expression:

$$\bar{\nu} = \frac{1}{4}\frac{4\nu + 3p - 7\nu p}{1 + 2p - 3\nu p} \tag{1.24}$$

Both DM and R-A results converge also to a constant when $p \mapsto 1$ independently from ν. Figure 1.9 shows this convergence for different values of ν(0.1, 0.2, 0.3, 0.4 and

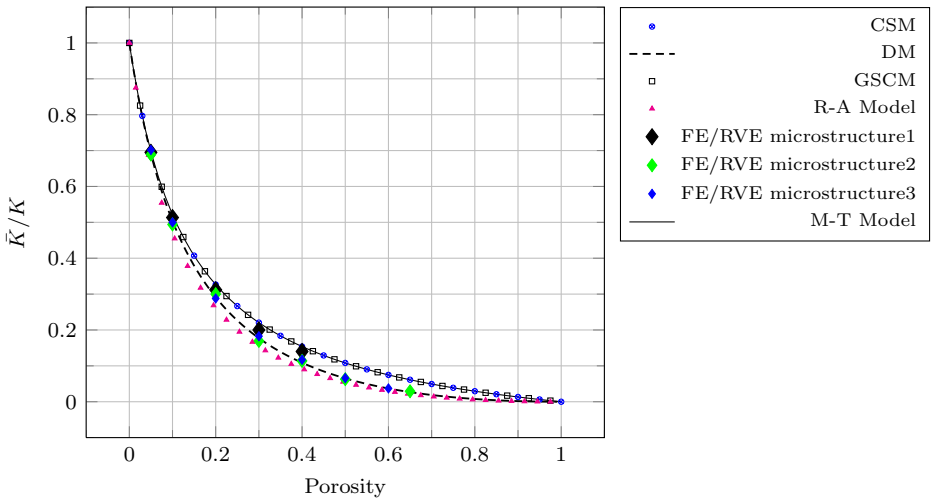

(a)

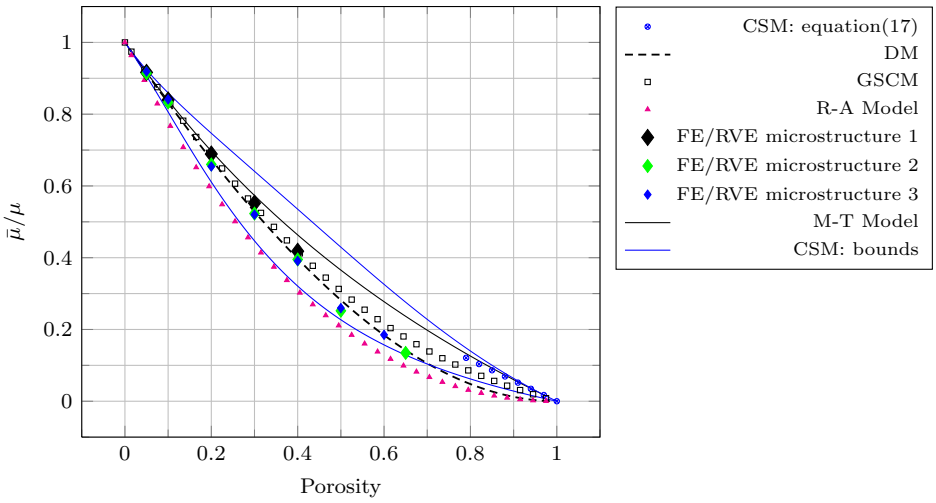

(b)

Figure 1.7: Effective normalized elastic moduli of a porous material. (a) bulk modulus, (b) shear modulus.

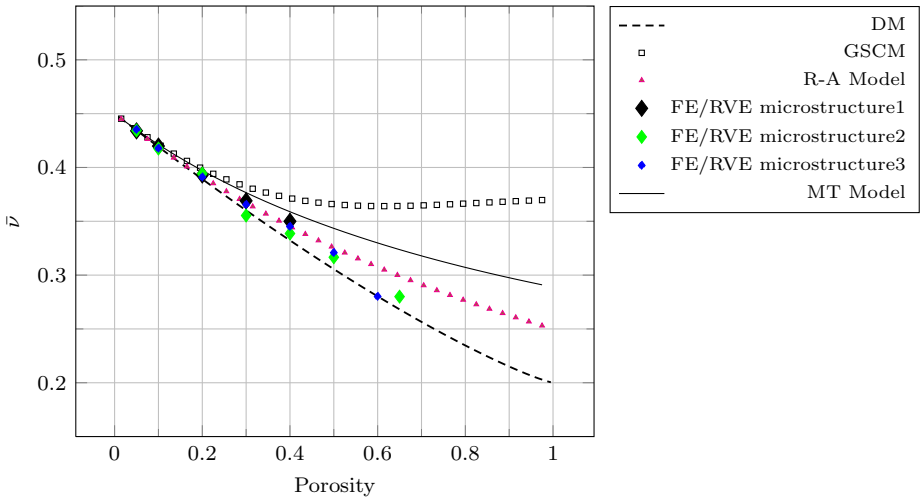

Figure 1.8: Poisson's ratio for a porous material.

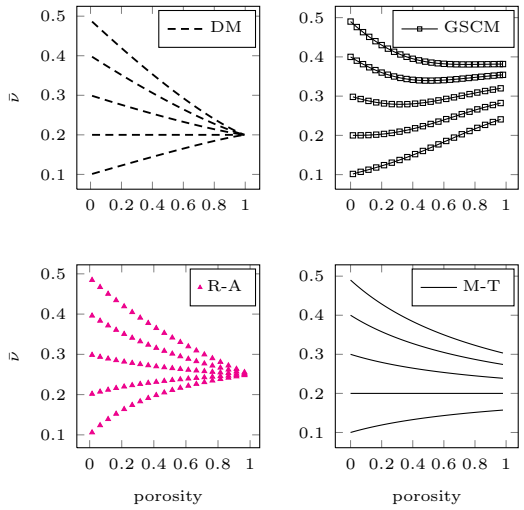

Figure 1.9: Variation of effective Poisson's ratio with porosity for different values of ν_0.

0.5). Unlike them, the effective Poisson's ratio provided by GSCM converges to a matrix Poisson's ratio dependent expression Christensen (1998):

$$\bar{\nu} = \frac{1+3\nu}{5+3\nu}\ ;\ p \mapsto 1 \tag{1.25}$$

Comparing the MF estimates with FE results, we can notice as a general trend that M-T (which estimates coincide with the upper Hashin-Shtrikman bound), GSCM and CSM overestimate (with different levels) the elastic moduli whereas R-A model underestimates them. However, the discrepancy between FE results and MF models estimates is closely related to the morphology of the porous solid. The FE results show an influence of the microstructure of the pores (for a given porosity) on the effective response.
For the first microstructure, as the pores are isolated and have low-to-moderate volume fractions [0.05-0.4], several MF models namely (M-T, GSCM and DM) provide good predictions of the effective bulk and shear modulus. MF models are insensitive to cavity sizes. However, FE results show that for a porosity of 10% the bulk modulus of isolated identical spherical cavities is about 2.5% higher than that corresponding to polydisperse ones. The relative difference is more significant when increasing porosity and reaches 16% for $p = 40\%$. The shear modulus shows less sensitivity and the highest difference between the two morphologies is around 6.4% only. Although CSM and R-A model are by construction better suited for polydisperse inclusions (pores), the size of inclusions does not enter into the equations and the only parameter that matters is the ratio of radii which is in correlation with the volume fraction. A similar comment can be made in the case of DM as discussed in section 1.3.1.1.

Another geometrical parameter, is the interpenetration of the holes. Void interaction is not explicitly described by MF models which account (with different degrees) only for collective interactions between inhomogeneities (voids). This reason can justify the increasing discrepancy between FE and the different MF models (except DM) with increasing porosity when void interaction becomes dominant (microstructure 2 and p$\geq$ 40% for the third microstructure). As shown in figures 1.7(a) and 1.7(b), the elastic moduli in the case of overlapping cavities (microstructure 2) are lower than those pertaining to isolated pores given the same porosity. The reduction of the bulk modulus is around 3.7% at $p = 10\%$ and becomes more pronounced when increasing porosity (the relative difference is about 18% for $p = 40\%$) . This discrepancy is less significant for the shear modulus which is reduced by about 5.5% for $p = 40\%$. However, as a general observation, the differential scheme (DM) fits the FE results very well for overlapping spheres for the whole range of porosity. Recently, Miled et al. (2011) performed a similar comparative study on polystyrene (EPS) concrete for porosity ranging in [0%-56%] and validated MF predictions against experimental data. The outcome of their study, is that among the MF schemes studied, only DM fits well the experimental data for relatively high porosity. Roberts and Garboczi (2000) also compared several models to FE data for porous ceramics and found that DM performs well for overlapping spherical pores model (as well as overlapping oblate ellipsoidal pores) over a porosity range of [0-50%]. Moreover, Zimmerman (1996) found that the DM worked well for predicting the conductivity of a 2D medium containing overlapping circular holes, for porosities up to almost 50%.

Table 1.2: Bulk moduli of porous solids in two different microstructures: identical overlapping spheres and identical impenetrable (hard) spheres.

$\frac{\bar{K}}{K}$					
		Identical overlapping spheres		Identical hard spheres	
Porosity	DM	FE	3 PE	FE	3 PE
0.05	0.688	0.689	0.687	0.692	0.693
0.1	0.501	0.494	0.499	0.513	0.514
0.2	0.288	0.300	0.285	0.311	0.312
0.3	0.175	0.169	0.170	0.200	0.204
0.4	0.107	0.113	0.105	0.140	0.138

Table 1.3: Shear moduli of porous solids in two different microstructures: identical overlapping spheres and identical impenetrable (hard) spheres.

$\frac{\bar{\mu}}{\mu}$					
		Identical overlapping spheres		Identical hard spheres	
Porosity	DM	FE	3 PE	FE	3 PE
0.05	0.913	0.914	0.913	0.916	0.914
0.1	0.828	0.833	0.828	0.839	0.833
0.2	0.668	0.660	0.666	0.688	0.680
0.3	0.527	0.523	0.518	0.552	0.544
0.4	0.395	0.395	0.388	0.418	0.424

Comparison between DM predictions and Torquato's Three-Point Estimates (3PE)

It is worthwhile to compare DM estimates to those given by Torquato's Three Point Estimates (3PE), Torquato (2002) and Torquato (1998). The latter take into account the three point correlation function representing the statistical distribution and morphology of the phases of realistic microstructures. The 3PE parameters differentiate (for the same volume fraction and inclusion shape) between the cases of identical interpenetrating inclusions, identical "hard" (impenetrable) inclusions and polydisperse ones. Results of the theoretical calculations and FE simulations are shown in Tables 1.2 and 1.3. The expressions of Torquato 's 3PE are given byTorquato (1998) for three dimensional dispersions and the statistical parameters were evaluated using the expression given respectively by Torquato et al. (1985) for distributions of identical overlapping spheres, by relations (22.30) and (22.54) from Torquato (2002) for identical hard spheres and from relations (22.33) and (22.57) in Torquato (2002) for polydispersed hard spheres. A similarity between DM estimates and those of 3PE is witnessed in the case of identical overlapping spheres. Details of a comparison between these two models for several composites involving high elastic contrast and three different microstructures are presented in Appendix C. A discussion and further comparisons between several MF models and Torquato's 3PE for the effective thermoelastic moduli of particle and fiber reinforced composites can be found in Böhm (2012).

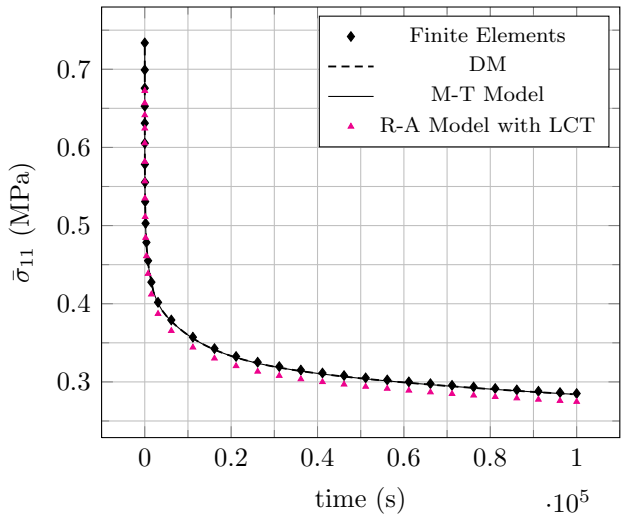

Figure 1.10: Porous polymer (10 % porosity) under uniaxial relaxation test

1.3.2 Viscoelasticity

For porous solids, we performed numerical simulations with the Mori-Tanaka (M-T) model and with DM based iteratively on M-T. These estimates together with the analytical elastic solution of R-A model extended to linear viscoelasticity by the use of LCT, were confronted to FE computations on Abaqus. For this test (uniaxial relaxation), the RVE was loaded at a constant strain rate ($10^{-2}s^{-1}$) in one second, then the strain was maintained constant for up to $10^5 s$. The corresponding stress relaxation for a porous polymer with 10% porosity is represented in figure 1.10, which shows that the MF results are in good agreement with the FE ones.

We report in figure 1.11 the different predictions of the effective relaxation modulus from different models confronted to FE computations on RVEs for porous polymers having respectively 20%(microstructure 1), 40% and 65% (microstructure 2) of porosity. As depicted in figure 1.11 , M-T model gives good results up to 20% of porosity. However, R-A model when extended to linear viscoelasticity fits better the FE results for higher porosities. In fact, this is similar to and a consequence of the elastic results. Using DM, we take advantage of the accuracy of M-T model in low porosity to get much better results for higher concentrations of voids.

1.4 Link between porous and cellular solids

Where both cellular and porous solids were studied separately in the previous sections, in the following we will look for a link between these two kinds of materials. Indeed, a cellular material can be seen as a highly porous solid. At high porosity attained by a large number of overlapping spherical cavities, the microgeometry of a porous solid presents a certain resemblance to that of a cellular one (of high to moderate relative density). The pores are three dimensionally interconnected and the solid phase (matrix) -which remains

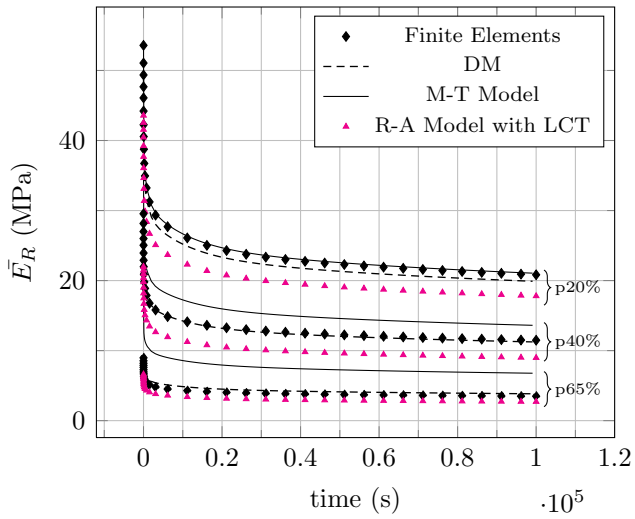

Figure 1.11: Variation of the effective relaxation mudulus with time and porosity.

connected- is reduced to walls and edges (to a varying degree of thickness), see figure 1.12. This morphology is obviously not exactly the same as what is observed in real foams (such as trabecular bone, polymer or metallic foams). However, even the cellular solid models are not an exact representation of actual foams. A more accurate modeling of real foam microstructures is the combination of FE analysis with imaging techniques (such as computed tomography). Hereafter, we will assess to what extent some MF models (which provided reasonable estimates of effective moduli of highly porous solids) can or cannot predict the effective response of cellular solids, especially open cell ones.

Christensen (1998) compared GSCM and CSM for solids containing a large fraction of spherical voids. He showed a linear dependence of modulus upon $(1-p)$ and estimated this case to represent an idealization of closed cell foams. As reported in section 1.3.1.3 for porous materials, and by comparison with FE computations on RVE, the differential scheme (DM) provided good estimates of the elastic constants in the $[5\% - 65\%]$ porosity range especially for overlapping spheres. R-A model underestimated moduli in low and intermediate porosity ranges, but its predictions improved with increasing porosity. The present investigation will focus on the applicability of models for porous solids (namely DM and R-A models) in the case of cellular solids and this by using the FE computations as benchmark. In figure 1.13 we make a zoom on the range of large concentration and we report only the DM and R-A model results as well as those of the models dedicated to cellular materials. For the latter models, "porosity" in the horizontal axes was computed from the real relative density ($Porosity = 1 - R_{real}$) which is discussed in section 1.2.1.3 and Appendix B. For high porosity it is clearly observed that R-A model is in good agreement with the FE computations on the unit cells of the tetrakaidecahedral for both Young's and shear moduli. DM overestimated the effective shear and Young's moduli for cellular solids, nevertheless its estimates are in the same range as those of Gibson and Ashby for cellular solids. In fact, we can note the proportional relationship (on approximation for

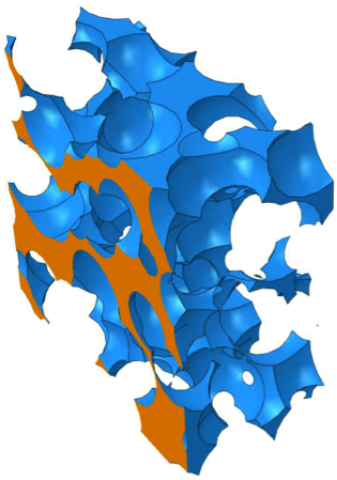

Figure 1.12: A view cut of a porous RVE containing 80% of overlapping spherical cavities.

$p \mapsto 1$) between the effective moduli given by R-A model and the matrix moduli with a factor of $(1-p)^2$. This factor was proposed by Gibson and Ashby (1999) for cellular solids by fitting empirical data. The same observation was made by Mondal et al. (2007) who checked the validity of some analytical equations of porous solids (among them the CSM and R-A model) in the case of closed cell aluminum foams by comparing them with experimental data. They conclude that the R-A model is capable of expressing with reasonable accuracy the moduli of closed cell aluminum foams for the entire range of porosity. Earlier, R Ramakrishnan and Arunachalam (1993) compared the validity of some theoretical MF models on ceramic materials using FE analysis and experimental data. They derived the same conclusions.
All the predictions for the bulk modulus (figure 1.13(b)) underestimate the FE computations and this can be explained by the fact that the bulk modulus is very affected by the variation of Poisson's ratio. The latter was estimated with high scatter between the different theoretical equations. Figure 1.14 illustrates the different predictions. The FE computations as well as Zhu et al. model predict an incompressible behavior for porosity of 1. The value of 1/3 proposed by Gibson et al. is a mean of experimental values. The intriguing point is the fact that cellular models (Zhu et al. and Li et al.) and FE computations on cellular unit cells all predict decreasing values of effective Poisson's ratio as the relative density $R = 1 - p$ increases, counter to the models issued from porous solids (MF and FE, figures 1.14 and 1.8).

The link between porous and cellular solids was also studied in linear viscoelasticity. The uniaxial relaxation test described in section 1.3.2 performed on porous solids was also applied to open cell polymer foams. In this test, we compare the results obtained by DM and R-A model generalized to viscoelasticity with micromechanical models dedicated to foams (namely Zhu et al. and Li et al. models) extended to viscoelasticity by means of LCT, the viscoelastic model proposed by Huang and Gibson (1991) and FE computations on unit foam cells. In figures 1.15(a) and 1.15(b) we superposed the effective relaxation

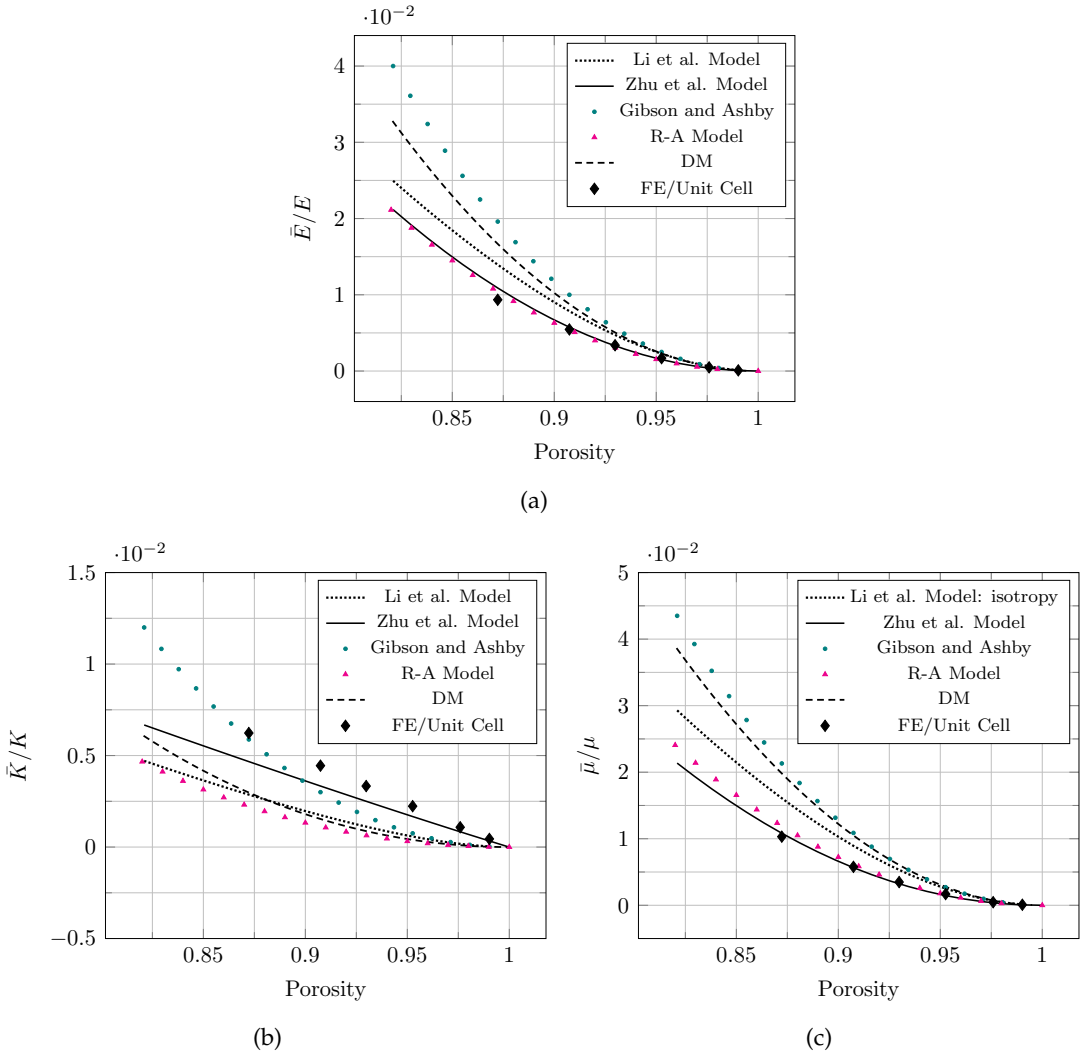

Figure 1.13: Effective normalized elastic moduli with different models for highly porous materials (Differential Method, Ramakrishnan et al. model) and open cell solids (Zhu et al. , Li et al., Gibson et al. models and FE results) (a) Young's modulus, (b) Bulk modulus and (c) Shear modulus

.

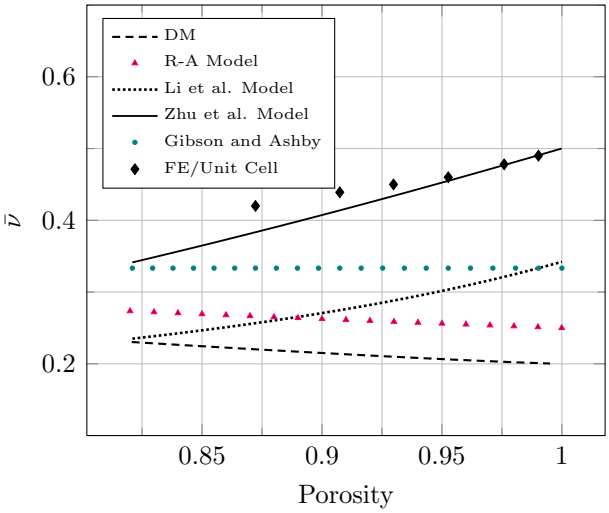

Figure 1.14: Variation of Poisson's ratio with porosity: comparison between different micromechanical models

modulus obtained by the named methods of polymeric foams having relative densities of 0.05 and 0.025 respectively (which correspond respectively to a porosity of 95% and 97.5%) .

The differential scheme (DM) yields relatively good predictions similar to Huang et al. model Huang and Gibson (1991). R-A and Zhu et al. models give almost identical predictions, and they both underestimate the effective relaxation modulus; this is compatible with the elastic results. Analysis of these results leads to the conclusion that as long as the elastic model is accurate, the derived viscoelastic predictions will be.

1.5 Conclusion

The present study for open cell foams and porous solids was conducted in linear elasticity and viscoelasticity. Elastic solutions were extended to linear viscoelasticity via LCT. The macroscopic relaxation (respectively creep) function was found to be proportional to the relaxation (respectively creep) function of the solid skeleton or matrix. This proportionality depends on the porosity (for isotropic porous solids) and on both the shape of edges and the relative density for foams. The analytical results have been validated against FE computations.

In the first part of this chapter (section 1.2), several micromechanical models (namely Li et al., Zhu et al., Gibson and Ashby and Huang and Gibson models) for the prediction of the properties of open cell solids were studied and assessed by comparing them to FE computations on unit cells under periodic boundary conditions. It was found that for low relative density (R), the analytical predictions of Young's and shear moduli were close to those of FE but discrepancy was observed with increasing R and for the estimation of Poisson's ratio. Zhu et al. model provided good agreement with FE simulations. Li et al. model overestimated the response of the foam (except for Poisson's ratio) and then overestimated the viscoelastic relaxation modulus.

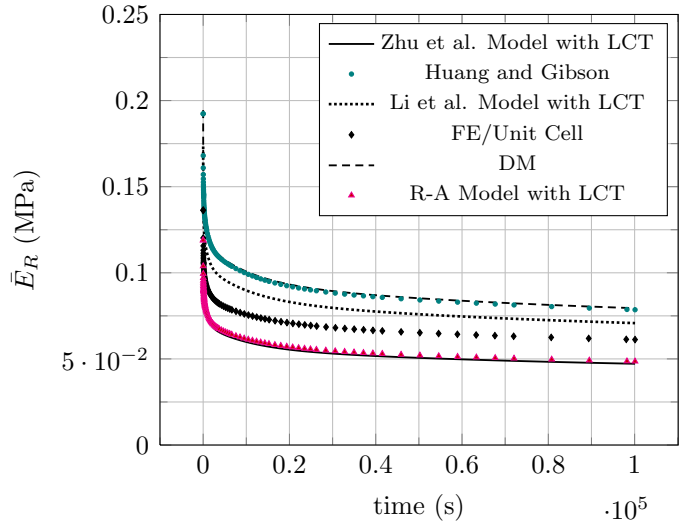

(a)

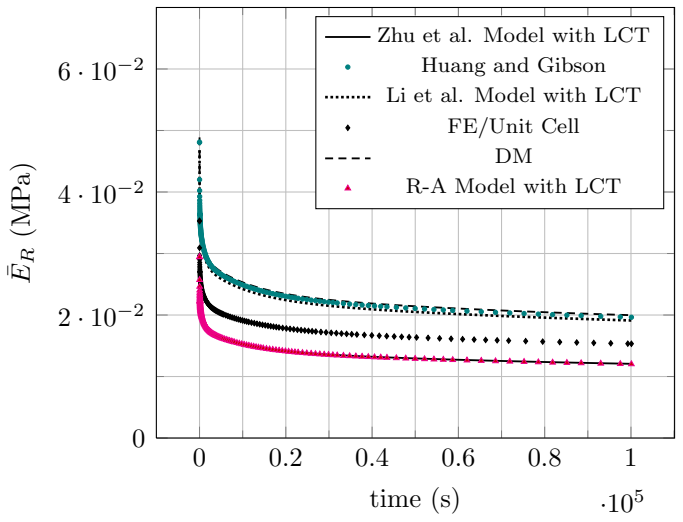

(b)

Figure 1.15: The effective relaxation modulus predictions of polymer foams: (a) relative density 0.05, (b) relative density 0.025. Comparison between various homogenization schemes predictions and FE computations performed on foam unit cells.

In a second part (section 1.3), we examined some MF models (namely CSM, GSCM, R-A, M-T and DM) for the homogenization of porous solids and we confronted them to FE simulations made on numerous RVEs. From this study, several conclusions can be made. For low concentration of dispersed impenetrable spherical voids (microstructure 1), MF models yield good predictions. But when increasing the porosity and the pores become macroscopically interconnected (microstructure 2 and microstructure 3 for p≥ 40%) only the differential scheme (DM) based on M-T model at each iteration succeeded to follow the variation of the effective elastic moduli for the entire range of porosity. R-A model

underestimated the behavior for the low and the intermediate ranges of porosity but came closer to the FE results for larger values. We also tested Torquato's Three Point Estimates (3PE). Their estimates are close to FE results for porous solids involving both microgeometries of "hard" and overlapping spherical cavities and to DM predictions for the latter morphology.
In a third part of the study (section 1.4), we explored the link between cellular and porous solids. We tested the adequacy of some MF models (namely DM and R-A models) to reproduce the behavior of low density open cell solids. It was concluded that these two MF models give results comparable to those of beam theory models devoted to cellular solids in elasticity and viscoelasticity.
For future work, the suitability (or not) of DM and R-A models to predict the effective response of closed cell foams can be investigated. Also, it would be interesting to extend the two MF models (DM and R-A) to nonlinear behavior (e.g., elasto(visco) plasticity). The potential of MF models developed for highly porous solids to model the effective elasto(visco) plastic response of open and closed cell foams will then be investigated. However, the application of MF models to highly porous solids faces some delicate issues such as considerable changes in size and shape of the voids even under moderate macro-strains (e.g., Ponte Castañeda and Zaidman (1994) and Garajeu et al. (2000)). MF models are able to predict the change of shape of cavities under two main conditions. First, the MF formulation needs to be developed for finite or large transformations. There are several papers in the literature about MF in large deformations, in particular numerous papers by Ponte Castaneda et al., such as Aravas and Ponte Castañeda (2004) for elasto(visco) plastic porous materials. Essentially, using a MF model one computes the average deformation gradient to be applied to the cavities, which can then change shape, for instance from initially spherical to ellipsoidal. This leads us to the second condition, that is the initial and deformed cavity shapes are assumed to be ellipsoidal. The reason for that is that MF models in the nonlinear regime always end up defining (step-by-step and iteratively) a linear comparison composite (LCC) where Eshelby's solution for the single inclusion problem in linear elasticity can be used. It is this solution which makes MF models computationally much cheaper than direct (e.g. FE) methods. The restriction to ellipsoids is not too problematic if they can capture in good approximation the deformed shape of a cavity. One can consider for this purpose general ellipsoids, which are not of revolution (in this case, the linear Eshelby solution is still valid, but integrals defining Eshelby's tensors need to be integrated numerically). However, for compressive loading, initially spherical pores may evolve into shapes which are not approximated correctly by ellipsoids e.g., Segurado et al. (2002).
Now, as regards the application of MF models to cellular materials, the former cannot be expected to capture aspects such as considerable changes of shape or buckling of cell struts or walls under compression. However, our main objective is to develop and validate a couple of MF models for highly porous materials and then to see to what extent they can or cannot predict the effective response of cellular materials. This is what we tried to do in the present study for linear elastic and viscoleastic behavior, and what we intend to investigate in the future in elasto-(visco)plasticity. The results might show that some MF models are able to predict the effective response of elasto(visco)plastic cellular materials quite well under tension (and some other loadings to be found) but fail to do so

for other loadings such as compression.

Appendix A

Prediction of a foam's Young's modulus using a general homogenization scheme

The purpose of these calculations is to find the effective Young's modulus $\bar{E}$ of a foam using continuum mechanical theory with static boundary conditions. Our calculations are based on the general method presented inOnck (2008). Each material point of the macroscopic continuum body is seen as the center of a RVE (volume V) made of a cellular material (figure 1.16). The macroscopic stress σ_{ij} is transmitted to the cellular RVE through

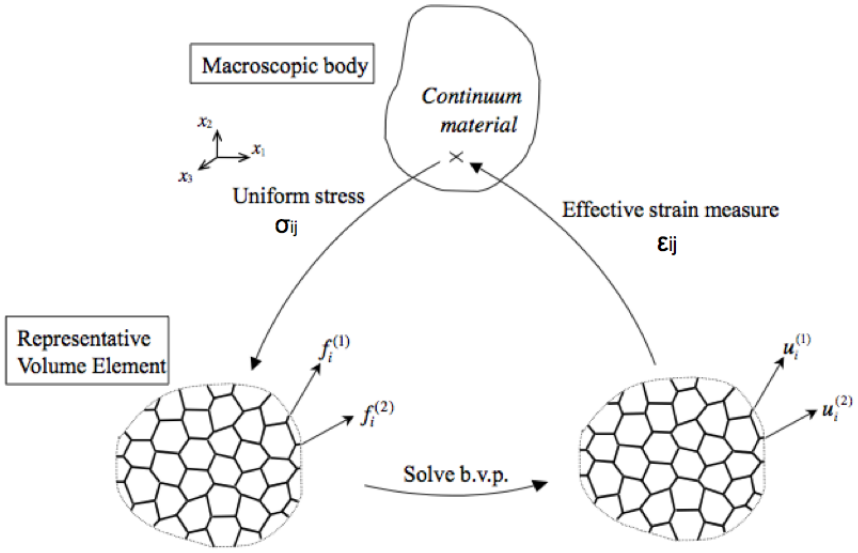

Figure 1.16: Homogenization procedure with static boundary conditions; after Onck (2008).

local forces at the RVE's boundary:

$$f_i^{(k)} = \sigma_{ij} n_j^{(k)} ds^{(k)} \tag{1.26}$$

where $f_i^{(k)}$ is the force acting on node (k) associated with surface area $ds^{(k)}$. We solve the equilibrium problem on a micromechanical scale by determining displacements. The computation of equivalent macroscopic deformation uses the equivalence between the average external work on the discrete material sample ($\overline{W} = \frac{1}{V} \sum_K f_i^{(k)} u_i^{(k)}$) and the strain energy density in the macroscopic material point ($W = 1/2 \sigma_{ml} \epsilon_{ml}$). $u^{(k)}$ is the displacement due to $f_i^{(k)}$ and $n_j^{(k)}$ is the unit vector normal to surface $ds^{(k)}$. Then, the effective macroscopic strain measure can be identified as :

$$\epsilon_{ij} = \frac{1}{V} \sum_k \frac{1}{2} (n_j^{(k)} u_i^{(k)} + n_i^{(k)} u_j^{(k)}) ds^{(k)} \tag{1.27}$$

Open-cell foam structure is modeled by regular tetrakaidecahedra sitting on a body-centered cubic (BCC) lattice as shown in figure1.17.

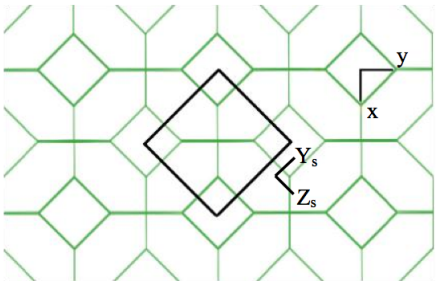

(a) Projection of the foam structure (with RVE in bold lines) on the xy plane

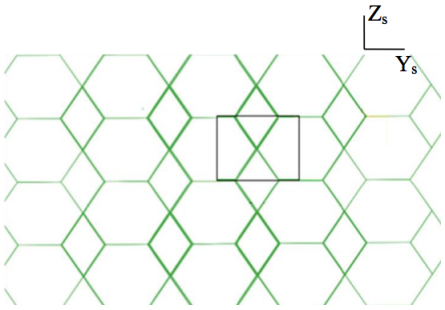

(b) Projection of the foam structure onto the Y_s, Z_s plane

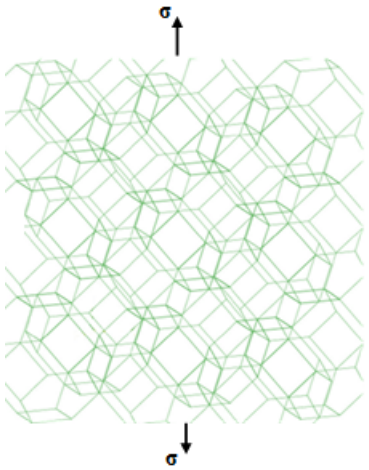

(c) Open Cell foam structure under tensile test

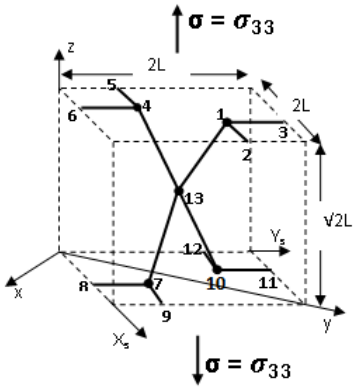

(d) The RVE under tensile stress. After Zhu et al. (1997)

Figure 1.17: Choice of RVE of tetrakaidecahedral open cell solid.

We define three coordinate systems:

- xyz: axes of Body-Centered Cubic lattice
- XYZ: Coordinate system of edge with unit vectors (i, j, k)
- $X_sY_sZ_s$: Coordinate system of cell structure

Unit vectors of edge coordinate system $(i, j, k)_{XYZ}$ are related to unit vectors of the BCC lattice $(e_1, e_2, e_3)_{xyz}$ by:
$i = e_1$, $j = \frac{1}{\sqrt{2}}e_2 - \frac{1}{\sqrt{2}}e_3$, $K = \frac{1}{\sqrt{2}}e_2 + \frac{1}{\sqrt{2}}e_3$

To calculate the Young's modulus, a pair of tensile stress σ is applied in the z-direction as shown in figure1.17(d). It is assumed that the strut material is linearly elastic and

isotropic of Young's modulus E. Also, all the edges are taken to be uniform slender beams having the same length L and a constant cross-sectional area A. It will be assumed in this calculation that there is no vertex distortion (this is realistic in the case that web radius at the junction between edges is large). The Young's modulus of the foam in direction z, $\overline{E}_{zz}$ is defined by:

$\overline{E}_{zz} = \overline{E}_{33} = \frac{\sigma}{\epsilon_{33}}$, so we need to calculate the effective macroscopic strain ϵ_{33}. Using the notation of figure 1.17(d):

$$\epsilon_{33} = \frac{1}{V}\sum_{k}(n_3^{(k)}u_3^{(k)}ds^{(k)}) \tag{1.28}$$

We choose to attach to each node (k) an elementary surface area $ds^{(k)}$ with respect to the force equilibrium (1.26) :

$$ds^{(1)} = ds^{(4)} = ds^{(7)} = ds^{(10)} = 2L^2 \tag{1.29}$$

This gives:

$$\epsilon_{33} = \frac{1}{4\sqrt{2}L}(8u_3^{(1)}) \tag{1.30}$$

So, the displacement component $u_3^{(1)}$ needs to be determined. Using the force equilibrium we have:

$$f_i^{(k)} = \sigma_{ij}n_j^{(k)}ds^{(k)} \tag{1.31}$$

Substituting (1.29) in (1.31) yields :

$$f_3^{(1)} = \sigma_{33}n_3^{(1)}ds^{(1)} = 2\sigma L^2 \tag{1.32}$$

Projecting this force into the different coordinate systems gives :

$$f^{(1)} = \begin{pmatrix} 0 \\ 0 \\ 2\sigma L^2 \end{pmatrix}_{X_sY_sZ_s} = \begin{pmatrix} 0 \\ 0 \\ 2\sigma L^2 \end{pmatrix}_{xyz} = \begin{pmatrix} 0 \\ -\frac{2\sigma L^2}{\sqrt{2}} \\ \frac{2\sigma L^2}{\sqrt{2}} \end{pmatrix}_{XYZ} = \begin{pmatrix} 0 \\ F_Y \\ F_Z \end{pmatrix}_{XYZ} \tag{1.33}$$

As we suppose that the rotation of node 1 relative to node 13 about the X axis is zero, it follows from equilibrium of moments that :

$$\frac{M_X L}{EI} + \frac{F_Z L^2}{2EI} = 0 \;\Rightarrow\; M_X = -\frac{F_Z L}{2} \tag{1.34}$$

Where I is the second moment of area. Then we calculate the displacement of node 1 relative to node 13 using the principle of superposition (figure1.18):

$$u^{(1)} = \begin{pmatrix} 0 \\ \frac{F_Y L}{AE} \\ \frac{F_Z L^3}{3EI} - \frac{F_Z L^3}{4EI} \end{pmatrix}_{XYZ} \tag{1.35}$$

Substituting (1.33) in (1.35) and projecting into coordinate system (xyz) we obtain the displacement of node (1) in the z direction:

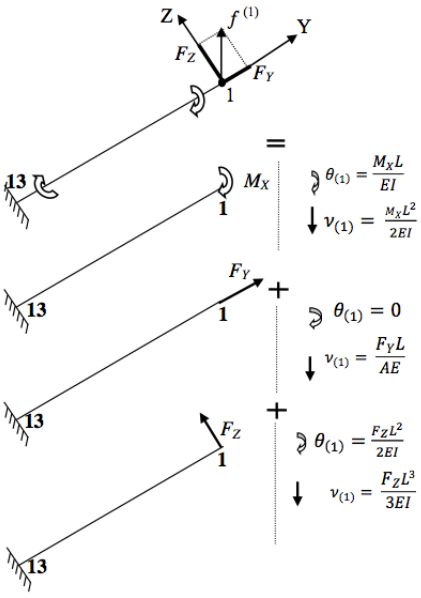

Figure 1.18: Superposition principle. M_X: bending moment, $\theta_{(1)}$: rotation of node (1) and $v_{(1)}$: displacement of node (1) .

$$u_3^{(1)} = \sigma(\frac{L^3}{AE} + \frac{L^5}{12AE}) \tag{1.36}$$

Using (1.30) we obtain the homogenized Young's modulus in the z direction $\overline{E}_{zz}$:

$$\overline{E} = \overline{E}_{zz} = \frac{\sigma}{\epsilon_{33}} = \frac{6\sqrt{2}EI}{(L^4(1 + \frac{12I}{AL^2})} \tag{1.37}$$

This result is identical to that of equation(1.2) obtained by Zhu et al. using another method.

Appendix B

Computation of foam's real relative density

In this appendix we explain how to compute the volume of overlap in the vertices of a tetracaidecahedron. This will enable the computation of the real value of the volume and consequently the real relative density of the foam. This need arises from the fact that both the FE code Abaqus and analytical formulae are overestimating the foam volume as overlap is not accounted for. Indeed, the real volume corresponds to the volume of the *union* of the struts and not to the sum as supposed in Abaqus and in the analytical formula of relative density. For the purpose of computing overlap we consider a vertex formed by the intersection of 3 half beams (see figure 1.19). This choice is motivated by the fact that the whole structure of the tetracaidecahedron could be seen as a repetition of the same shape after applying some rotations. In fact, this shape could be called a generating form. The Autocad software will be useful to compute the volume of the union of the three half beams. Let's consider a first case study of a foam with regular struts:

$$\begin{cases} \frac{l}{2} = 0.17677 \\ a_1 = 0.1285 \end{cases}$$

Where l is the length of the strut and a_1 is the side length of the square cross section. These values yield on an analytical density $R_{1analyt} = \frac{3a_1^2}{2\sqrt{2}l^2} = 0.14$. The length l corresponds to that of the FE model and is computed such that the fictitious cube containing the cell has a side of unit length. We define the *correction volume* V_c as:

$$V_c = V(B1) + V(B2) + V(B3) - V(B1 \cup B2 \cup B3) \tag{1.38}$$

where Bi refers to beam i. The corresponding *correction volume* is V_{c1}=1.025e-03. We consider now a second case study where the beam length l is kept fixed and only the section dimension a_2 changes: $a_2 = 0.10857$. This corresponds to an analytical relative density $R_{2analyt} = 0.10$. The correction volume of the corresponding vertex is V_{c2}=6.18e-04. We will try now to establish a correlation between the correction volume and the relative density in order to develop a formula relating these two variables. We introduce a parameter f that will be called the size factor:

$$f = \frac{a_2}{a_1} = 0.8449$$

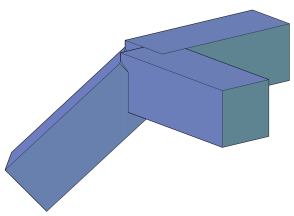

Figure 1.19: Three half beams meeting in a vertex. Owing to geometric symmetries, only this shape will be considered for the computation of overlap volume.

We also introduce a volume correction factor f_c :

$$f_c = \frac{V_{c2}}{V_{c1}} = 0.6029$$

It is easy to notice that $f_c = f^3$.

More generally for a fixed length l we have $\left(\frac{a_2}{a_1}\right)^3 = \frac{V_{c2}}{V_{c1}}$
This will yield:

$$\frac{V_{c2}}{V_{c1}} = \left(\frac{R_{2analyt}}{R_{1analyt}}\right)^{\frac{3}{2}} \tag{1.39}$$

The general expression of the real relative density R_{Real} is:

$$\begin{aligned} R_{Real} &= \frac{Real\ solid\ volume}{Total\ Cell\ volume} \\ &= \frac{\sum^* Volume\ of\ 12\ beams - \sum^* correction\ volume\ of\ 6\ vertices}{Total\ Cell\ volume} \end{aligned} \tag{1.40}$$

$*$ In fact, the structure of the tetracaidecahedron has 36 beams shared between 3 cells and 24 vertices shared between 4 cells.
At the end we have:

$$R_{Real} = R_{analyt}(\text{ also } R_{Abaqus}) - \frac{6V_c}{Total\ Cell\ volume} \tag{1.41}$$

For any tetracaidecahedral foam with square section, its real relative density is:

$$\begin{aligned} R_{2Real} &= R_{2analyt} - \frac{6V_{c1}(\frac{R_{2analyt}}{R_{1analyt}})^{\frac{3}{2}}}{8\sqrt{(2)}l^3} \\ &= R_{2analyt} - 6\left(\frac{1}{12}\left(\frac{2\sqrt{2}}{3}\right)^{\frac{1}{2}}\frac{V_{c1}}{a_1^3}\right)R_{2analyt}^{\frac{3}{2}} \\ &= R_{2analyt} - 0.23454\ R_{2analyt}^{\frac{3}{2}} \end{aligned} \tag{1.42}$$

This formula enables to compute the real relative density of any tetrakaidecahedral foam having square section and analytical relative density $R_{2analyt}$ using a unique measure of *correction volume* V_{c1} (corresponding to a relative density $R_{1analyt}$). This expression was verified using several examples.

Let's consider for example a case study of a foam with regular struts:

$$\begin{cases} \frac{l}{2} = 0.17677 \\ a = 0.06425 \end{cases}$$

Where l is the length of the strut and a is the dimension of the square cross section. This example yields on an analytical density $R_{analyt} = \frac{3a^2}{2\sqrt{2}l^2} = 0.035$. We computed with Autocad the volume of the union of the three half struts meeting in the vertex.

$$V_R(B_1 \cup B_2 \cup B_3) = 0.0020611$$

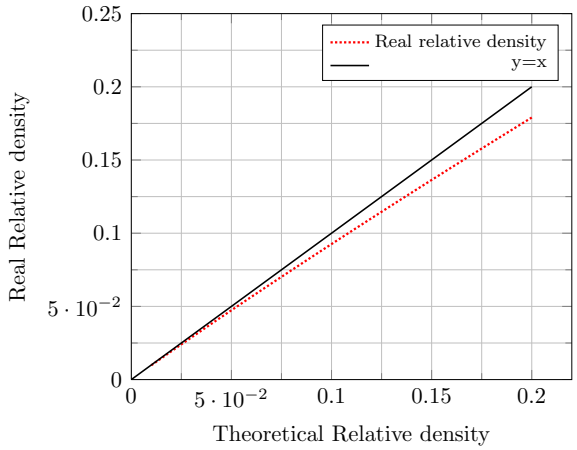

Figure 1.20: Real relative density as function of theoretical relative density. For increasing values of R, the gap becomes significant and should not be neglected.

Hence the real volume of the solid skeleton would be $V = 24V_R$ as 24 is the number of vertices on a single cell. At the end, the real density of the corresponding foam will be :

$$R_{Real} = \frac{8V_R}{8\sqrt{2}l^3} = 0.033$$

In the numerator 8 corresponds to 24/3 as a single cell will have 24 vertices and every strut is shared between 3 cells.

On the other hand, when applying formula (1.42), we have:

$$R_{Real} = 0.035 - 0.23454 \times 0.035^{\frac{3}{2}} = 0.033$$

The variation of the real relative density of the foam (having square cross section) with the analytical relative density is plotted in figure 1.20 and compared with the expression $y = x$. The curves show that for low relative density, the error due to the neglected overlap is small but it becomes significant for increasing R. We limited our study here to the case of square section beams, nevertheless, the same methodology could be followed for any other shape.

Appendix C

Torquato's three point estimates

In this appendix we compare the effective shear and bulk moduli predicted by Torquato's three point estimates (3PE) and those of MF models. Consider a first case in which the dispersed phase consists of spherical cavities ($K_2 = \mu_2 = 0$) and the matrix is such that $\mu_1/K_1 = 1/2$. We compare hereafter DM and 3PE for three different morphologies whose parameters were evaluated using the expression given by Torquato et al. Torquato et al. (1985) for distributions of identical overlapping spheres, by relations (22.30) and (22.54) from Torquato (2002) for identical "hard" (impenetrable) spheres and from relations (22.33) and (22.57) in Torquato (2002) for polydispersed hard spheres. We report in figure 1.21 the dimensionless effective bulk and shear moduli versus porosity . The 3PEs for identical overlapping spheres and the DM predictions are remarkably close until $p = 0.6$. For larger porosities, a small difference occurs. However, 3PEs for identical "hard" spheres are higher than those for overlapping ones and the relative difference is increasing with porosity. For a porosity of 60% the effective bulk modulus pertaining to identical hard pores is about 34% higher than that related to overlapping cavities.

We now consider the material of our study, namely the polymeric porous composite. The matrix phase has the following properties: $K_1 = 341.33$ MPa and $\mu_1 = 35.31$MPa. We superimpose in figure 1.22 Torquato's 3PEs for the different morphologies to those given by MF methods. The results of DM and Torquato's 3PEs coincide for the case of overlapping spheres for both the effective bulk and shear moduli, with a small difference in the prediction of $\bar{\mu}$ which occurs for a porosity higher than 0.6 . However 3PEs show a morphology-dependent variation of the effective response which the MF models are unable to predict.

Two other cases of particulate composites of high elastic contrast are studied and presented in the figures below. The first composite consists of stiff spherical inclusions ($E_2 = 5$GPa, $\nu_2 = 0.2$) dispersed in a matrix ($E_1 = 100$MPa, $\nu_1 = 0.3$). The stiffness ratio is ($E_2/E_1 = 50$). Figure 1.23 shows the predictions of macro bulk and shear moduli obtained with both DM and Torquato's 3PE. A good agreement is found between DM predictions and those of 3PE for identical overlapping particles.

The second particulate composite consists of a polymer matrix made of epoxy (E_1 =3.16 GPa, $\nu_1 = 0.35$) reinforced with spherical silica inclusions ($E_2 = 73.1$GPa, $\nu_2 = 0.18$) (material data from Pierard et al. (2004)). The stiffness ratio is ($E_2/E_1 = 23.13$). In figure 1.24 we compare DM estimates and Torquato's 3PE. Similar conclusions to those for Fig 1.23 can be made.

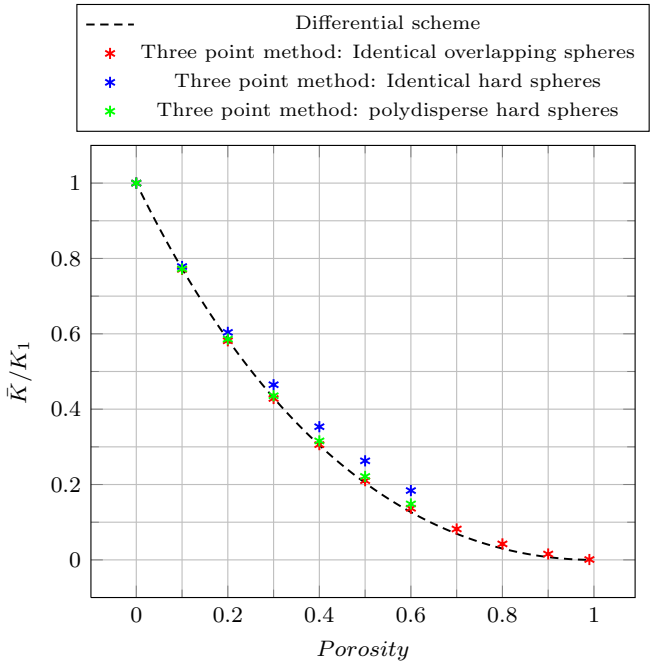

(a)

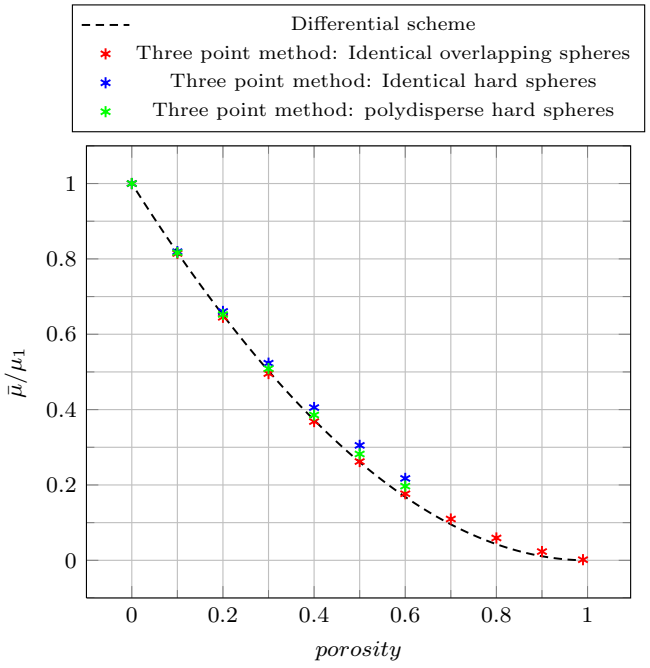

(b)

Figure 1.21: Effective response of a porous solid with $\mu_1/K_1 = 0.5$. Comparison between Torquato's and DM predictions.

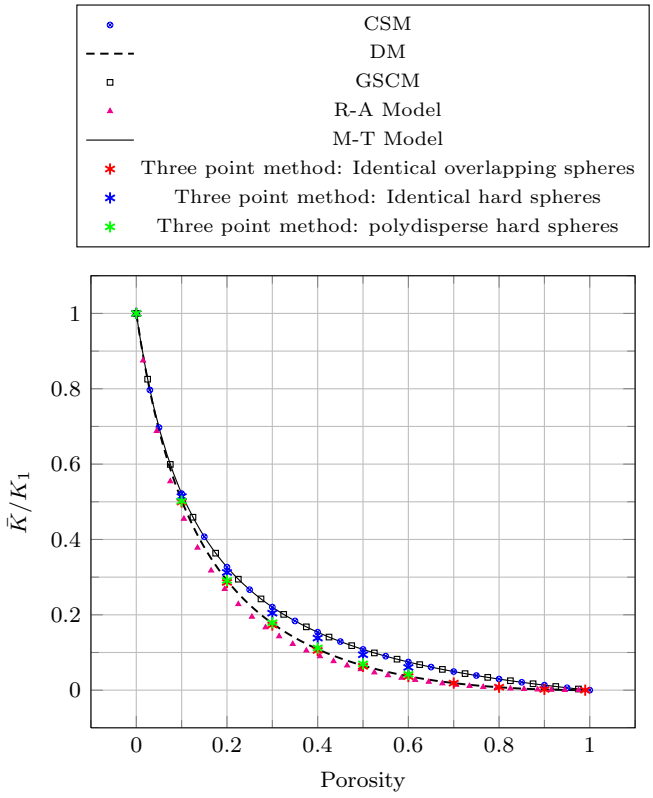

(a)

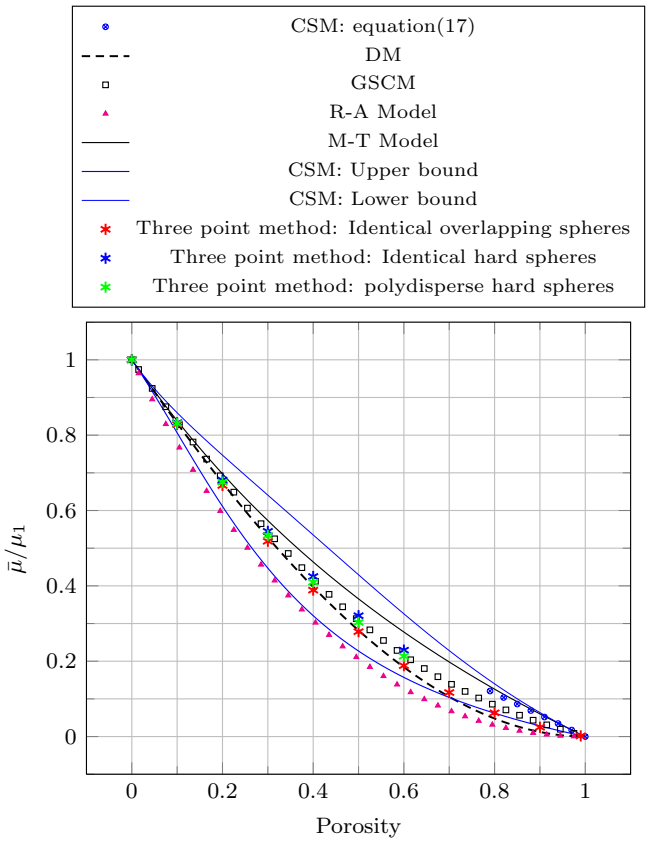

(b)

Figure 1.22: Effective normalized elastic moduli of a polymeric porous material. Comparison between Torquato's and several mean-field models (a) bulk modulus, (b) shear modulus.

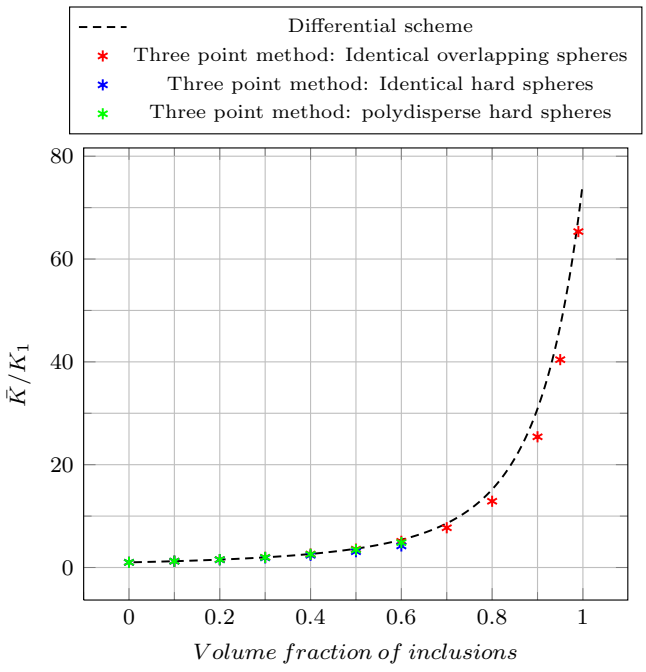

(a)

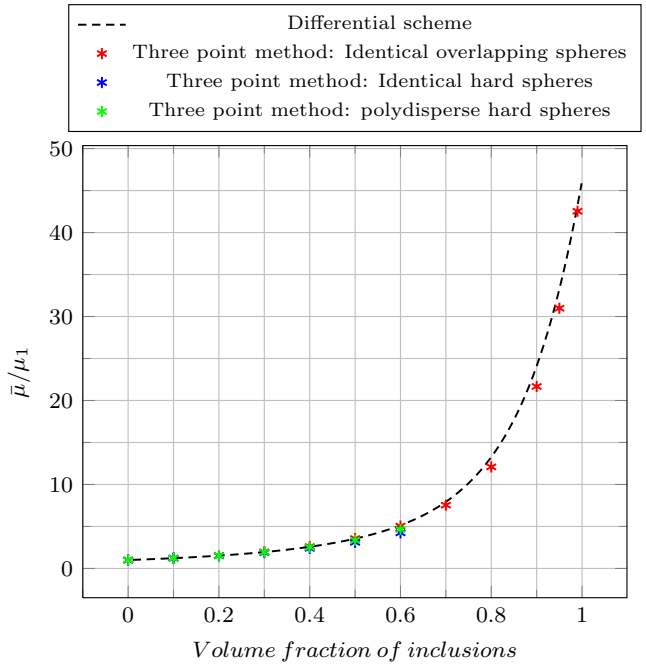

(b)

Figure 1.23: Effective normalized elastic moduli of a particulate composite with $E_2/E_1 = 50$. Comparison between Torquato's and DM (a) bulk modulus, (b) shear modulus.

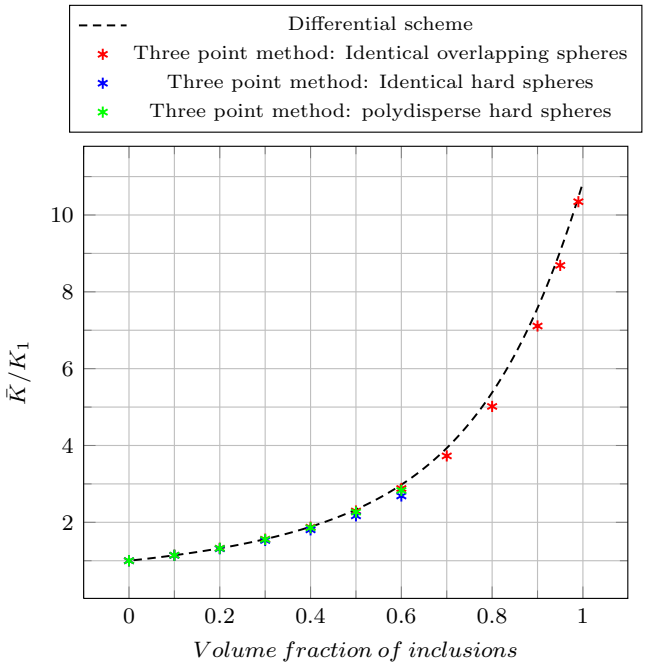

(a)

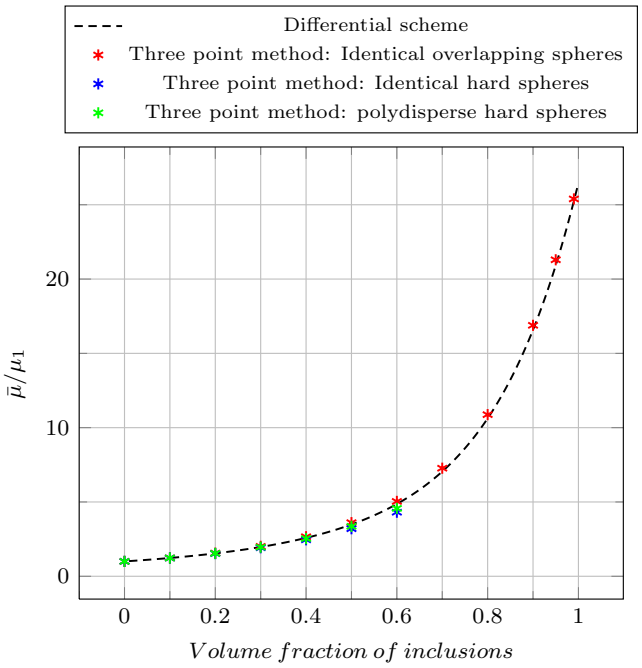

(b)

Figure 1.24: Effective response of a polymer matrix made of epoxy reinforced with spherical silica inclusions with $E_2/E_1 = 23.13$.

CHAPTER 2

Porous plasticity: predictive second moment homogenization models coupled with Gurson's solution

Summary

For a single spherical cavity in a rigid plastic von Mises matrix subjected to linear velocities on the boundary, the homogenized response is given by Gurson's solution. For multiple cavities, we propose an original and rather simple coupling between mean-field homogenization and Gurson's solution. The actual porous microstructure is modeled alternatively as spherical rigid plastic inclusions in a homogenized Gurson matrix phase and the volume fractions are determined from a maximum packing argument. The alternative microstructures are homogenized with the Generalized self-consistent (GSC) and Mori-Tanaka (MT) models which are formulated with the secant method and second statistical moments of per phase strain fields. The mean accumulated plastic strain rate in the incompressible material of the original microstructure is computed. Numerical predictions of effective yield envelopes in the plane of hydrostatic and von Mises stresses are verified against full-field finite element results for a large range of porosities. No fitting or empirical parameters are used. It is found that the GSC model gives excellent predictions, except when both the porosity and the stress triaxiality are small.

keywords

Porous plasticity, micromechanics, homogenization, Gurson's solution.

Present Chapter corresponds to the submitted research paper El Ghezal and Doghri (Under review). A self-consistent notation is adopted.

The first chapter focused on the scale transition methods for porous solids in linear elasticity and viscoelasticity. Particular attention was drawn to MFH approaches and their applicability to highly porous solids. In this chapter we are concerned with the plastic behavior of porous materials. As a first attempt, the authors considered MF models developed within our research group and which proved to be successful for elasto-plastic composites (namely the incremental tangent model Doghri and Ouaar (2003), Pierard and Doghri (2006), the variational model Brassart et al. (2011) and the incremental secant model Wu et al. (2013a)) and tried to apply them to porous plastic materials by taking the stiffness of the solid inclusions vanishingly small. However, it turns out that those MF models are not able in their current status to predict pressure sensitivity of the macroscopic response which is an important feature of porous materials. Also, since those models extensively rely on the J2 plasticity model, considering other constitutive models with different flow rules for the matrix phase is not a straightforward modification. In addition, for perfectly plastic porous matrix, first order estimates of the MF models lead systematically to a macroscopic equivalent stress proportional to the one of the matrix phase which in this specific case remains constant for all the loading conditions. Therefore, MF models are not reliable for predicting yield surfaces of plastic porous materials. In a second attempt, we try to build on the well known Gurson's solution while MF approach will serve as a second layer to allow to take into account the void interaction effect not considered in the original model of Gurson.

2.1 Introduction

In his seminal work, Gurson (1977) solved the problem of a single spherical cavity in a rigid von Mises plastic matrix subjected to linear velocities at the boundary corresponding to a macroscopic rate of deformation D_{ij}. Using limit analysis [1], he found an estimate of the effective (macro) yield condition of the homogenized material which depends on both von Mises equivalent stress and hydrostatic stress:

$$\left(\frac{\Sigma_{eq}}{\sigma_0}\right)^2 + 2f\cosh\left(\frac{1}{2}\frac{\Sigma_{ll}}{\sigma_0}\right) - 1 - f^2 = 0, \tag{2.1}$$

where f is the porosity, σ_0 the yield stress of the matrix material, Σ_{ll} the trace of the stress and Σ_{eq} the von Mises equivalent stress

$$\Sigma_{ll} = \sum_{i=1}^{3} \Sigma_{ii}, \quad \Sigma_{eq} = \sqrt{\frac{3}{2}\Sigma'_{ij}\Sigma'_{ji}} \tag{2.2}$$

where Σ'_{ij} is the deviatoric part of Σ_{ij}. The summation convention over a repeated index is used throughout unless otherwise indicated. Garajeu (1995) used a sophisticated velocity field consisting in an exact solution for a hollow elastic sphere subjected to an arbitrary loading, and found a Gurson-like effective yield criterion. His model led to the following

[1] The interested reader can find an overview of the limit analysis framework in which the classical Gurson approach has been developped in Appendix B.

Gurson-like form:

$$q(f)(\frac{\Sigma_{eq}}{\sigma_0})^2 + 2f\cosh(\frac{1}{2}\frac{\Sigma_l l}{\sigma_0}) - 1 - f^2 = 0 \tag{2.3}$$

with

$$q(f) = \frac{1-f}{1-5f\dfrac{16+19f^{7/3}}{(3+2f)(16+19f^{7/3})+168f(1-f^{2/3})^2}} \tag{2.4}$$

Monchiet et al. (2011) considered the exact Eshelby (1957) solution for the ellipsoidal inclusion problem in an infinite elastic matrix, and obtained a non-elliptic macroscopic criterion.

For multiple cavities in a rigid plastic matrix, different approaches exist. Tvergaard (1981) suggested an empirical extension of Gurson's solution that accounts for the interaction effect between multiple voids by introducing an empirical factor multiplying the porosity:

$$\left(\frac{\Sigma_{eq}}{\sigma_0}\right)^2 + 2qf\cosh\left(\frac{1}{2}\frac{\Sigma_{ll}}{\sigma_0}\right) - 1 - q^2f^2 = 0, \tag{2.5}$$

where q, is an empirical parameter fitted against full-field simulations (e.g., finite elements) on porous volumes or experimental data. Perrin and Leblond (1990) performed an analytical derivation of parameter q by using a self-consistent approach. The model consists in a central spherical cavity embedded in a porous matrix satisfying a simplified version of Gurson-Tvergaard-Needleman (GTN) criterion and loaded hydrostatically. They obtained $q = 4/e$ which is close to the value suggested by Tvergaard ($q = 1.5$) from numerical simulations of plastic porous media.

A second approach for porous plastic materials is to carry out full-field analyses. Several references dealt with void cell calculations based on two- dimensional finite element (FE) simulations. The seminal papers of Needleman (1972a) and Needleman (1972b) addressed square array of circular cylindrical voids in an isotropic matrix under plane-strain conditions. Later,Tvergaard (1982) and Koplik and Needleman (1988) considered transverse isotropic distribution of spherical voids in an isotropic matrix.
In earlier works, Hom and McMeeking (1989), Worswick and Pick (1990) and Richelsen and Tvergaard (1994) investigated three-dimensional representative volume elements (RVEs) with cubic patterns of spherical voids. All the cited works idealize the material's microstructure by considering periodically distributed voids.
Multi-pore models that take into account the nonuniform distribution of the voids were considered by Huang (1993),Thomson et al. (2003). Fast Fourier Transformation (FFT) method was also used by Bilger et al. (2005) and Bilger et al. (2007) to investigate the effect of porosity fluctuation inside the RVE on the overall yield surface of the voided materials. More recent FE analyses of Fritzen et al. (2012) and Bourih et al. (2017) consider three-dimensional RVEs having random microstructures.
When done properly, the full-field analyses are extremely accurate, but their computational cost is prohibitive. However, they provide reference results for much faster (semi)analytical micromechanical models built on simplifying assumptions.

A third modeling approach is to develop mean-field (MF) homogenization models. First, it is noticed that in principle it is possible to consider MF models which proved to be successful for elasto-plastic composites and apply them to porous plastic materials by taking the stiffness of the solid inclusions vanishingly small. However, in the case of pure hydrostatic stress, MF models often fail to predict plasticity in a incompressible plastic matrix, even if these models include second statistical moments of strain or stress fields in the plastic matrix phase; e.g. the incremental-tangent method of Doghri et al. (2011), the variational formulation of Brassart et al. (2011) and the incremental-secant procedure of Wu et al. (2015). Therefore MF models appropriate for porous plasticity are needed.

The Hashin-Shtrikman (HS) variational approach was initially proposed by Willis (1983) in the context of linear composites. Later, Talbot and Willis (1985) extended this variational principle to nonlinear media using a homogeneous linear comparison medium having a uniform stiffness and subjected to some polarization stress field. Ponte Castañeda (1991) extended the method by introducing the concept of an heterogeneous comparison medium (a linear comparison composite: LCC) having the same microstructure distribution as the real nonlinear one. Independently, Michel and Suquet (1992) proposed a similar variational formulation for nonlinear viscous porous media and obtained the same upper bound. They studied the problem of a single cavity in a porous material, and for multiple cavities, they used self-consistent and differential homogenization schemes.

The obtained bound improves on Gursons criterion at low stress triaxiality. However, it overestimates the strength for high stress triaxialities especially at low porosities. Later, Ponte Castañeda (2002) improved the variational approach with a sophisticated second order linear comparison homogenization method by using generalized secant moduli and incorporating second moment information. Subsequently, Danas and Ponte Castañeda (2009b) prescribed a reference stress tensor for the computation of the potential in the LCC that allows the "second-order" estimate to coincide with the analytical spherical shell result in the hydrostatic limit and thus their model retrieves the same hydrostatic point as Gurson's model. More recently, an iterative homogenization strategy was proposed by Ponte Castañeda (2012) allowing to correct the hydrostatic point without any ad hoc modification.

Garajeu and Suquet (1997) considered a microstructure made of multiple cavities and rigid inclusions embedded in a rigid plastic material. They proposed a homogenization approach for rigid inclusions in GTN-type matrix. Later, Tekoglu and Pardoen (2010) combined a ductile model based on the Gologanu-Leblond-Devaux constitutive behaviour with a non linear mean field homogenization scheme in order to account for the particles' effect on the overall ductility of composite materials. Bilger et al. (2007) considered multiple spherical cavities in a rigid plastic material, and supposed that each cavity is coated with multiple layers (typically 20 to 30) of the matrix material. A second-moment secant formulation is used and each layer has its own secant moduli. Recently, Dormieux et al. (2017) proposed a homogenization approach based on a secant formulation and where the actual microstructure is replaced by another one consisting of homogenized Gurson spheres embedded in a solid rigid plastic matrix. However, no numerical predictions on actual porous plastic materials were presented.

Finally, we mention a different approach developed by Pastor et al. (2013) which

is based on limit state analysis with kinematic and static formulations and provides numerical lower and upper bounds for porous plastic materials.

The present chapter proposes a MF homogenization approach for a rigid plastic von Mises matrix containing multiple spherical cavities. Although some ingredients in our approach are found in other references, e.g. Michel and Suquet (1992), Garajeu and Suquet (1997), Bilger et al. (2007) and Dormieux et al. (2017), the proposal as a whole is original. Moreover, it is verified against full-field FE results on a full range of porosities, from low (1%) to high (50%). The chapter is organized as follows. In Sect. 2.2, the secant formulation of Gurson's single cavity stress-strain solution is presented and special cases are studied. In Sect. 2.3, we present the proposed MF homogenization approach coupled with Gurson's solution. Alternative microstructures are defined and homogenized with secant versions of two MF models: generalized self-consistent Christensen and Lo (1979) and Mori-Tanaka Mori and Tanaka (1973). Sect. 2.4 presents MF homogenization based on the secant formulation and second statistical moments of per-phase strain fields. In Sect. 2.5, the computation of the mean accumulated plastic strain rate in the rigid plastic matrix of the original RVE is developed. In Sect. 2.6, the predictions of the proposed MF models for a large set of porosities are verified against full-field FE simulations. Conclusions are drawn in Sect. 2.7, and the chapter ends with an appendix.

Acronyms and abbreviations: FE : finite element, GSC: generalized self-consistent, MF: mean-field, MFH: MF homogenization, MT: Mori-Tanaka, RVE: representative volume element, w.r.t.: with respect to.

2.2 Gurson's stress-strain solution and its secant formulation

2.2.1 Gurson's stress-strain solution

Consider again the problem of a single spherical cavity in a rigid von Mises plastic matrix, with linear velocities at the boundary corresponding to a macro rate of deformation D_{ij}. Gurson's effective yield condition of the homogenized material -eq. (2.1)- is extremely well-known and used in the literature. However, for the purpose of this study, we make use of another Gurson solution which relates the effective (homogenized) Cauchy stress Σ_{ij} to D_{ij},

$$\Sigma_{ij} = \frac{2}{3}\sigma_0 \left[\left(\operatorname{argsinh} \frac{\lambda}{f} - \operatorname{argsinh} \lambda \right) \delta_{ij} + \frac{D'_{ij}}{D_{eq}} \left(\sqrt{1+\lambda^2} - \sqrt{f^2+\lambda^2} \right) \right] \tag{2.6}$$

where σ_0 is the matrix material's yield stress, D'_{ij} is the deviatoric part of D_{ij}, δ_{ij} is Kronecker's symbol, f is the porosity (volume fraction of the spherical cavity), D_{eq} is the von Mises measure of D_{ij} and λ measures the triaxiality of D_{ij},

$$\lambda = \frac{2D_{ll}}{3D_{eq}}; \quad D_{eq} = \sqrt{\frac{2}{3} D'_{ij} D'_{ji}} \tag{2.7}$$

The derivation of this last equation is provided in Appendix B. Since the present contribution is restricted to small strains, we shall consider in the remainder displacement instead of velocity boundary conditions and infinitesimal strains ϵ_{ij} instead of D_{ij}.

2.2.2 Secant formulation of Gurson's solution and special cases

For an isotropic material, the secant formulation (valid under monotonic and radial loadings) gives the following stress-strain relation using the secant bulk (κ_s) and shear (μ_s) moduli:

$$\sigma_{ij} = \kappa_s \epsilon_{ll} \delta_{ij} + 2\mu_s \epsilon'_{ij} \tag{2.8}$$

This enables to define the secant moduli as

$$\kappa_s = \frac{\sigma_{ii}}{3\epsilon_{ll}}; \;\; \mu_s = \frac{\sigma_{eq}}{3\epsilon_{eq}} \tag{2.9}$$

where the von Mises measures of stress and strain are given by:

$$\sigma_{eq} = \sqrt{\frac{3}{2}\sigma'_{ij}\sigma'_{ji}}; \;\; \epsilon_{eq} = \sqrt{\frac{2}{3}\epsilon'_{ij}\epsilon'_{ji}} \tag{2.10}$$

Applying these formulae to the homogenized Gurson material gives its secant moduli as follows:

$$\begin{aligned} \kappa_{sG} &= \frac{2\sigma_0}{3\epsilon_{ll}} \left(\operatorname{argsinh} \frac{\lambda}{f} - \operatorname{argsinh} \lambda \right), \\ \mu_{sG} &= \frac{\sigma_0}{3\epsilon_{eq}} \left(\sqrt{1+\lambda^2} - \sqrt{f^2+\lambda^2} \right) \end{aligned} \tag{2.11}$$

These secant moduli present some special cases which are addressed hereafter.

• **Case 1:** $\epsilon_{ll} \longrightarrow 0$ in κ_{sG}. A priori, κ_{sG} is indeterminate ($\kappa_{sG} \longrightarrow \frac{0}{0}$). After using L'Hôpital's rule several times, a second-order Taylor expansion gives:

$$3\kappa_{sG} \approx \frac{4}{3}\frac{\sigma_0}{\epsilon_{eq}}\left(\frac{1}{f}-1\right)\left[1 - \frac{2}{3}\left(1+\frac{1}{f}+\frac{1}{f^2}\right)\left(\frac{\epsilon_{ll}}{3\epsilon_{eq}}\right)^2\right], \;\; \text{if } |\frac{\epsilon_{ll}}{\epsilon_{eq}}| \ll 1 \tag{2.12}$$

• **Case 2:** $\epsilon_{ll} \longrightarrow 0$ in μ_{sG}. A second-order Taylor expansion gives:

$$\mu_{sG} \approx \sigma_0 \frac{(1-f)}{3\epsilon_{eq}}\left[1 - \frac{2}{f}\left(\frac{\epsilon_{ll}}{3\epsilon_{eq}}\right)^2\right], \;\; \text{if } |\frac{\epsilon_{ll}}{\epsilon_{eq}}| \ll 1 \tag{2.13}$$

• **Case 3:** $\epsilon_{eq} \longrightarrow 0$ in κ_{sG}. A second-order Taylor expansion leads to:

$$3\kappa_{sG} \approx -2\frac{\sigma_0}{\epsilon_{ll}} \ln f + \frac{\sigma_0}{8\epsilon_{ll}}(f^2-1)\left(\frac{3\epsilon_{eq}}{\epsilon_{ll}}\right)^2, \;\; \text{if } |\frac{\epsilon_{eq}}{\epsilon_{ll}}| \ll 1 \tag{2.14}$$

• **Case 4:** $\epsilon_{eq} \longrightarrow 0$ in μ_{sG}. A priori, the latter modulus is indeterminate. Using L'Hôpital's rule, the following limit is found:

$$\mu_{sG} \longrightarrow \frac{\sigma_0}{4|\epsilon_{ll}|}(1-f^2), \;\; \text{if } \frac{\epsilon_{eq}}{\epsilon_{ll}} \longrightarrow 0 \tag{2.15}$$

2.3 Mean-field homogenization (MF) coupled with Gurson's solution

In this section, we propose two alternative representations of the actual porous microstructure, and each is homogenized with a mean-field (MF) model coupled with Gurson's single cavity solution: either the generalized self-consistent (GSC) or the Mori-Tanaka (MT) models. The section ends with MF results common to both models.

2.3.1 Coupling Gurson's solution with generalized self-consistent model (GSC)

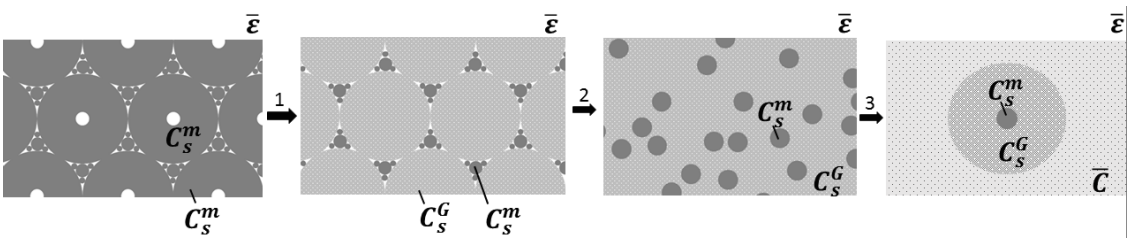

Figure 2.1: Coupling Gurson's solution and generalized self-consistent (GSC) model using secant formulation (index "s"). Left: original microstructure: multiple cavities in rigid plastic material (m). Step 1: each cavity coated with (m) is replaced with a solid sphere with homogeneous Gurson material (G). Maximum packing concentration of spheres (G) is assumed. Step 2: alternative microstructure with rigid plastic inclusions (m) in matrix phase (G). Step 3: homogenization with GSC.

In Fig.2.1 we consider a rigid plastic von Mises matrix (m) containing multiple spherical cavities. We assume that each cavity of radius R_i is coated with material (m) of thickness $(R_e - R_i)$. Each coated cavity is then homogenized using the secant version of Gurson's solution, thus obtaining homogeneous solid spheres of material (G) and radius R_e such that they correspond to a maximum packing concentration for regularly placed equal-size spheres, Fig.2.1-step 1. Next, we view the microstructure as made of solid spherical inclusions of material (m) embedded in a matrix phase of material (G), Fig.2.1-step 2. Finally, this microstructure is homogenized using the secant version of the generalized self-consistent (GSC) model of Christensen and Lo (1979). The latter supposes that each solid sphere (m) is coated with (G) and embedded in a fictitious matrix which has the effective properties of the composite and is subjected to the macroscopic strain at the boundary, Fig.2.1-step 3.

The linear elastic GSC model considers a coated solid sphere with inner and outer radii (R_i) and (R_e), resp., which is embedded in a fictitious medium having the composite's effective bulk and shear moduli $\overline{\kappa}$ and $\overline{\mu}$, resp. The constituents' bulk and shear moduli are κ_i and μ_i for the inner sphere and κ_e and μ_e for the coating. It is found that $\overline{\mu}$ is the solution of the following quadratic equation (Christensen, 1979):

$$A\left(\frac{\overline{\mu}}{\mu_e}\right)^2 + 2B\frac{\overline{\mu}}{\mu_e} + C = 0 \tag{2.16}$$

where the lengthy expressions of coefficients A, B and C are given in Appendix A for completeness.

The homogenized bulk modulus is given by Christensen and Lo (1979):

$$\frac{\overline{\kappa}-\kappa_e}{\kappa_i-\kappa_e}=\frac{c}{1+(1-c)\dfrac{\kappa_i-\kappa_e}{\kappa_e+\dfrac{4}{3}\mu_e}};\quad c\equiv\left(\frac{R_i}{R_e}\right)^3 \tag{2.17}$$

In the secant formulation, κ_e and μ_e are replaced with the secant moduli of (G), κ_{sG} and μ_{sG}, κ_i and μ_i with the secant moduli of (m), κ_{sm} and μ_{sm}. Moreover, κ_{sm} is infinitely large, therefore the effective secant bulk modulus becomes:

$$\overline{\kappa}_s\longrightarrow\frac{1}{1-c}\left(\kappa_{sG}+\frac{4}{3}c\mu_{sG}\right) \tag{2.18}$$

2.3.2 Coupling Gurson's solution with Mori-Tanaka (MT) model

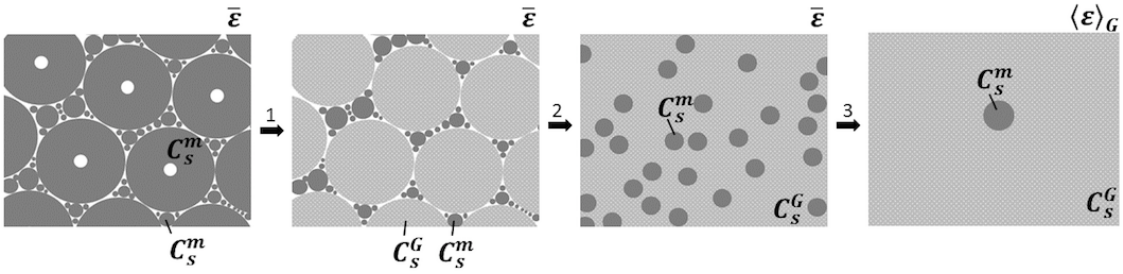

Figure 2.2: Coupling Gurson's solution and Mori-Tanaka (MT) model using secant formulation (index "s"). Left: original microstructure: multiple cavities in rigid plastic material (m). Steps 1 and 2 are similar to those of Fig. 2.1. Step 3: homogenization with MT.

In Fig.2.2-left we consider the actual porous microstructure. Steps 1 and 2 in Fig. 2.2 are similar to those of Fig.2.1, except that maximum packing of randomly dispersed equal-size spheres is supposed here. Step 3 however is different: the alternative microstructure made of rigid plastic spheres (m) embedded in matrix phase (G) is homogenized using the secant version of Mori-Tanaka (MT) model. The latter supposes that each solid sphere (m) is embedded in an infinite medium of material (G) which is subjected at the boundary to linear displacements corresponding to the volume mean of the strain field inside the matrix phase of the microstructure of Fig.2.2- step 2.
We first recall the linear elastic Mori-Tanaka results for a matrix phase (subscript 0) with embedded spherical inclusions (subscript 1). The volume fractions are v_0 and $v_1=1-v_0$. The materials' properties are κ_i (bulk moduli), and μ_i (shear moduli), with ($i=0;1$). On the RVE's boundary, linear displacements corresponding to a macro strain are imposed. The Mori-Tanaka estimates of the macro bulk modulus $\overline{\kappa}$ and shear modulus $\overline{\mu}$ are the following:

$$\frac{\overline{\kappa}}{\kappa_0}=\frac{v_1\frac{\kappa_1}{\kappa_0}+(1-v_1)\left(1+3\kappa_E(\frac{\kappa_1}{\kappa_0}-1)\right)}{v_1+(1-v_1)\left(1+3\kappa_E(\frac{\kappa_1}{\kappa_0}-1)\right)}, \tag{2.19}$$

$$\frac{\overline{\mu}}{\mu_0}=\frac{v_1\frac{\mu_1}{\mu_0}+(1-v_1)\left(1+2\mu_E(\frac{\mu_1}{\mu_0}-1)\right)}{v_1+(1-v_1)\left(1+2\mu_E(\frac{\mu_1}{\mu_0}-1)\right)}, \tag{2.20}$$

where κ_E and μ_E are bulk and shear parts of Eshelby's tensor:

$$\kappa_E = \frac{\kappa_0}{3\kappa_0 + 4\mu_0}; \quad \mu_E = \frac{3(\kappa_0 + 2\mu_0)}{5(3\kappa_0 + 4\mu_0)} \tag{2.21}$$

In the context of porous plasticity with the secant formulation, matrix (0) refers to the homogenized Gurson material (G), inclusions (1) to the rigid plastic material (m), and the elastic moduli are replaced with the secant ones. Moreover, material (m) is incompressible, therefore its secant bulk modulus is infinitely large. The effective secant bulk modulus is then given by:

$$\frac{\overline{\kappa}_s}{\kappa_{sG}} \longrightarrow 1 + \frac{v_m}{3v_G\kappa_E} \tag{2.22}$$

2.3.3 Common mean-field (MF) results

In this section, we present some volume averaging results which are common to GSC and MT models, since the alternative microstructures for both is a Gurson matrix phase (G) with embedded inclusions of the incompressible material (m). The volume fractions are v_G and $v_m = 1 - v_G$. With $\overline{\epsilon}_{ij}$ the imposed macro strain and $\overline{\sigma}_{ij}$ the estimated macro stress, the following identities hold:

$$\overline{\epsilon}_{ij} = v_G\overline{\epsilon}_{(ij)G} + v_m\overline{\epsilon}_{(ij)m}; \quad \overline{\sigma}_{ij} = v_G\overline{\sigma}_{(ij)G} + v_m\overline{\sigma}_{(ij)m} \tag{2.23}$$

where $\overline{\epsilon}_{(ij)r}$ and $\overline{\sigma}_{(ij)r}$ are mean values over phase $r = G, m$. Since (m) is incompressible, the trace of $\overline{\epsilon}_{(ij)G}$ is simply

$$\overline{\epsilon}_{(ll)G} = \frac{\overline{\epsilon}_{ll}}{v_G} \tag{2.24}$$

As for the deviatoric parts, they are related by:

$$\overline{\epsilon}'_{ij} = v_G\overline{\epsilon}'_{(ij)G} + v_m\overline{\epsilon}'_{(ij)m}; \quad \overline{\mu}_s\overline{\epsilon}'_{ij} = v_G\mu_{sG}\overline{\epsilon}'_{(ij)G} + v_m\mu_{sm}\overline{\epsilon}'_{(ij)m} \tag{2.25}$$

where $\overline{\mu}_s$ and μ_{sr} ($r = G, m$) are macro and per-phase secant shear moduli, resp., which are computed with the method of second statistical moments of Sect. 2.4.

From eqs. (2.25), the mean deviatoric strains in the phases are given by:

$$\overline{\epsilon}'_{(ij)G} = \frac{(\overline{\mu}_s - \mu_{sm})}{v_G(\mu_{sG} - \mu_{sm})}\overline{\epsilon}'_{ij}; \quad \overline{\epsilon}'_{(ij)m} = \frac{(\overline{\mu}_s - \mu_{sG})}{v_m(\mu_{sm} - \mu_{sG})}\overline{\epsilon}'_{ij} \tag{2.26}$$

from which the following von Mises measures are found:

$$\overline{\epsilon}_{(eq)G} = \frac{1}{v_G}\left|\frac{\overline{\mu}_s - \mu_{sm}}{\mu_{sG} - \mu_{sm}}\right|\overline{\epsilon}_{eq}; \quad \overline{\epsilon}_{(eq)m} = \frac{1}{v_m}\left|\frac{\overline{\mu}_s - \mu_{sG}}{\mu_{sm} - \mu_{sG}}\right|\overline{\epsilon}_{eq} \tag{2.27}$$

Physically, one expects that $\mu_{sm} > \overline{\mu}_s > \mu_{sG}$, and the absolute values could be removed.

2.4 Homogenization with secant formulation and second statistical moments

The secant formulation for the homogenized Gurson material (G) was discussed in Sect.2.2. For the incompressible material (m), the secant bulk modulus is infinitely large and the secant shear modulus is simply given by:

$$\mu_{sm} = \frac{\sigma_0}{3\epsilon_{eq}} \tag{2.28}$$

Within a first statistical moment MFH, the secant moduli are computed with the volume average values of the strain field in each phase, (m) or (G), that is with $< \epsilon_{ij} >_{\omega_m}$ in eq. (2.28) and $< \epsilon_{ij} >_{\omega_G}$ in eq. (2.11).

In the present work, the secant moduli are computed with the second statistical moments of per phase strain fields, that is $< \epsilon_{ij}\epsilon_{kl} >_{\omega_m}$ and $< \epsilon_{ij}\epsilon_{kl} >_{\omega_G}$, or equivalently, because of micro and macro isotropy, $< (\epsilon_{eq})^2 >_{\omega_m}$, $< (\epsilon_{eq})^2 >_{\omega_G}$ and $< (\epsilon_{ll})^2 >_{\omega_G}$. Therefore, the variance of the per phase strain fields influences the computation of the secant moduli. The second moment homogenization is outlined hereafter.

The Hill-Mandel compatibility condition gives (mean values taken over all the volume element):

$$< \sigma_{ij}\epsilon_{ij} >=< \sigma_{ij} >< \epsilon_{ij} > \tag{2.29}$$

Assume that the composite as well as the material of each phase (r) are isotropic and linear elastic. The previous equation becomes:

$$\sum_r v_r \left[\kappa_r < (\epsilon_{ll})^2 >_{\omega_r} + 3\mu_r < (\epsilon_{eq})^2 >_{\omega_r}\right] = \overline{\kappa}(\overline{\epsilon}_{ll})^2 + 3\overline{\mu}(\overline{\epsilon}_{eq})^2 \tag{2.30}$$

Perturbing μ_r in one phase (r) under constant macro strain $\overline{\epsilon}_{ij}$ leads to:

$$< (\epsilon_{eq})^2 >_{\omega_r} = \frac{1}{3v_r}\left[\frac{\partial\overline{\kappa}}{\partial\mu_r}(\overline{\epsilon}_{ll})^2 + 3\frac{\partial\overline{\mu}}{\partial\mu_r}(\overline{\epsilon}_{eq})^2\right] \tag{2.31}$$

Similarly, perturbing κ_r in one phase (r) under constant $\overline{\epsilon}_{ij}$ leads to:

$$< (\epsilon_{ll})^2 >_{\omega_r} = \frac{1}{v_r}\left[\frac{\partial\overline{\kappa}}{\partial\kappa_r}(\overline{\epsilon}_{ll})^2 + 3\frac{\partial\overline{\mu}}{\partial\kappa_r}(\overline{\epsilon}_{eq})^2\right] \tag{2.32}$$

The previous results are known in the literature Bobeth and Diener (1987). In the present contribution, phases (r) correspond to (m) (rigid plastic incompressible material) and (G) (homogenized Gurson material), and the elastic moduli are replaced with the secant ones. The latter are computed from eqs. (2.11) and (2.28) with:

$$\epsilon_G^{eq} = \sqrt{< (\epsilon_{eq})^2 >_{\omega_G}};\quad \epsilon_{(ll)G} = (\pm 1)\sqrt{< (\epsilon_{ll})^2 >_{\omega_G}};\quad \epsilon_m^{eq} = \sqrt{< (\epsilon_{eq})^2 >_{\omega_m}} \tag{2.33}$$

where the sign is initialized with that of $\overline{\epsilon}_{ll}$. Also, the effective moduli in eqs. (2.31) and (2.32) correspond to the overall secant moduli $\overline{\kappa}_s$ and $\overline{\mu}_s$ which are computed using either GSC (Sect. 2.3.1) or MT (Sect. 2.3.2) homogenization models. Since the secant material models are nonlinear, a numerical algorithm is needed to compute the per phase and effective responses corresponding to a macro strain $\overline{\epsilon}_{ij}$. A simple iterative fixed point algorithm was implemented.

2.5 Mean accumulated plastic strain rate in the rigid plastic incompressible matrix

In addition to estimating the macro stress, it is shown in this section that MF enables also to compute the mean accumulated plastic strain rate in the rigid plastic incompressible matrix of the original RVE. The result is not exploited in the present study, but it might be in the future within ductile failure modeling for instance.

Consider the original porous RVE. The Hill-Mandell lemma gives (a superposed dot designates the material time derivative $\frac{D}{Dt}$):

$$\overline{\sigma}_{ij}\dot{\overline{\epsilon}}_{ij} = v_0 < \sigma_{ij}\dot{\epsilon}_{ij} >_{\omega_0} \tag{2.34}$$

where index 0 refers to the rigid J_2 plastic incompressible matrix phase (whose volume fraction is $v_0 = 1 - f$, where f is the actual porosity). Using the normality rule, the following local relation in ω_0 is found:

$$\sigma_{ij}\dot{\epsilon}_{ij} = \sigma_0\dot{\epsilon}^p_{eq} \tag{2.35}$$

where $\dot{\epsilon}^p_{eq}$ is the accumulated plastic strain rate, i.e. the von Mises measure of $\dot{\epsilon}^p_{ij} = \dot{\epsilon}_{ij}$. Taking the volume average over ω_0 gives:

$$\overline{\sigma}_{ij}\dot{\overline{\epsilon}}_{ij} = v_0\sigma_0 < \dot{\epsilon}^p_{eq} >_{\omega_0} \tag{2.36}$$

In order to compute the mean value of $\dot{\epsilon}^p_{eq}$ we use a perturbation method similar to the one which enables to compute the second statistical moments of per-phase strain fields in Sect. 2.4. We pertub σ_0 -which is the only material property- at $\dot{\overline{\epsilon}}_{ij}$ constant, thus obtaining:

$$(\delta\overline{\sigma}_{ij})\dot{\overline{\epsilon}}_{ij} = v_0(\delta\sigma_0) < \dot{\epsilon}^p_{eq} >_{\omega_0} + v_0\sigma_0 < \delta\dot{\epsilon}^p_{eq} >_{\omega_0} \tag{2.37}$$

Using again the normality rule of the rigid J_2 plastic incompressible material gives the local relation:

$$\sigma_0(\delta\dot{\epsilon}^p_{eq}) = \sigma_{ij}(\delta\dot{\epsilon}_{ij}) \tag{2.38}$$

Taking the mean value over ω_0 and using the Hill-Mandel lemma again leads to:

$$v_0 < \sigma_{ij}(\delta\dot{\epsilon}_{ij}) >_{\omega_0} = \overline{\sigma}_{ij}(\delta\dot{\overline{\epsilon}}_{ij}) = 0 \tag{2.39}$$

because the perturbation of σ_0 is carried out at constant $\dot{\overline{\epsilon}}_{ij}$. Replacing this last result into eq. (2.37) gives:

$$< \dot{\epsilon}^p_{eq} >_{\omega_0} = \frac{1}{v_0}\frac{\partial\overline{\sigma}_{ij}}{\partial\sigma_0}\dot{\overline{\epsilon}}_{ij} \tag{2.40}$$

An estimate of the macro stress $\overline{\sigma}_{ij}$ is given by the secant formulation using the macro bulk and shear moduli $\overline{\kappa}_s$ and $\overline{\mu}_s$ computed with one of the MF models proposed for the alternative microstructures: GSC (Sect. 2.3.1) or MT (Sect. 2.3.2). Therefore an estimate of the partial derivative of $\overline{\sigma}_{ij}$ w.r.t. σ_0 reads:

$$\frac{\partial\overline{\sigma}_{ij}}{\partial\sigma_0} = \frac{\partial\overline{\kappa}_s}{\partial\sigma_0}\overline{\epsilon}_{ll}\delta_{ij} + 2\frac{\partial\overline{\mu}_s}{\partial\sigma_0}\overline{\epsilon}'_{ij} \tag{2.41}$$

Plugging this expression in eq. (2.40) gives after simplification the mean value of the accumulated plastic strain rate in the matrix as:

$$< \dot{\epsilon}^p_{eq} >_{\omega_0} = \frac{1}{2v_0}\left(\frac{\partial \overline{\kappa}_s}{\partial \sigma_0}\frac{D}{Dt}(\overline{\epsilon}_{ll})^2 + 3\frac{\partial \overline{\mu}_s}{\partial \sigma_0}\frac{D}{Dt}(\overline{\epsilon}_{eq})^2\right) \tag{2.42}$$

The partial derivatives of the macro secant moduli $\overline{\kappa}_s$ and $\overline{\mu}_s$ w.r.t. σ_0 are estimated from the MF model. For instance, for GSC, eq. (2.18) gives

$$\frac{\partial \overline{\kappa}_s}{\partial \sigma_0} = \frac{1}{1-c}\left(\frac{\partial \kappa_{sG}}{\partial \sigma_0} + \frac{4}{3}c\frac{\partial \mu_{sG}}{\partial \sigma_0}\right) \tag{2.43}$$

where the partial derivatives of the Gurson secant moduli κ_{sG} and μ_{sG} w.r.t. σ_0 can be computed from eqs. (2.11), (2.7), (2.31) and (2.32). The computation and exploitation of the results is left for a future work.

2.6 Numerical simulations

In this section, the predictions of generalized self-consistent (GSC) and Mori-Tanaka (MT) models coupled with Gurson' solution as described above are verified against full-field FE results of RVEs due to Bourih et al. (2017) and Fritzen et al. (2012). They are also compared to the Gurson single cavity solution, the Hashin-Shtrikman (HS) upper bound Michel and Suquet (1992), and to the analytical estimates of Garajeu (1995), Danas and Ponte Castañeda (2009b) and Ponte Castañeda (2012).

Under imposed macro strain $\overline{\epsilon}_{ij}$, the macro secant moduli $\overline{\kappa}_s$ and $\overline{\mu}_s$ are estimated with GSC or MT based on second statistical moments (Sect. 2.4), and the macro von Mises stress (Σ_{eq}) and hydrostatic stress (Σ_m) are computed as follows and reported in the figures

$$\Sigma_{eq} = 3\overline{\mu}_s\overline{\epsilon}_{eq}; \quad \Sigma_m = \frac{\Sigma_{ii}}{3} = \overline{\kappa}_s\overline{\epsilon}_{jj}$$

2.6.1 Numerical results with generalized self-consistent (GSC) model

The coupling of Gurson's solution with GSC homogenization model is depicted in Fig.2.1. In Fig.2.1-step 1, the solid spheres having the homogenized Gurson material (G) are assumed to follow a dense regular packing of equal size spheres, which gives their volume fraction as $v_G = 74\%$, and that of solid rigid plastic spheres (m) in Fig. 2.1-step 2 as $v_m = 26\%$. These values are kept for all the GSC predictions presented in Figs. 2.3-2.9, and no fitting or empirical parameter is used.

Figs. 2.3-2.6 show that for porosities ranging from 50% to 20% the GSC predictions are rather excellent and much better than other analytical models. For a porosity of 10% the GSC predictions are also very good, Fig. 2.7. However, for lower porosities (5% and 1%) Figs. 2.8 and 2.9 show that the GSC predictions are excellent for high values of the triaxiality ratio Σ_m/Σ_{eq}, but deteriorate considerably for lower triaxialities. One explanation is that even at very small porosities, the GSC predictions do not tend towards the single cavity Gurson solution, because in the present version a fixed concentration of rigid plastic incompressible material (m) is always assumed (26%) due to the maximum

packing argument of spheres (G).
At this point, one noteworthy point should be commented. The numerical results obtained from finite element computations on RVEs deviate from Gurson's solution even for low porosities (see for example Fig. 2.9). At this low level of porosity, interaction effects are very small and could not explain on their own the observed difference. Moreover, the Gurson solution has been shown to be a rigorous bound for any isotropic porosity. One possible reason of such discrepancy, is the microstructure under consideration. Indeed, Gurson's model consider the spherical shell which corresponds to a composite sphere assemblage microstructure. Such microstructure involves many different (i.e. poly-disperse) cavities' sizes. However, in both FE results and our coupled MF-Gurson model, the microstructure involves monodisperse voids.

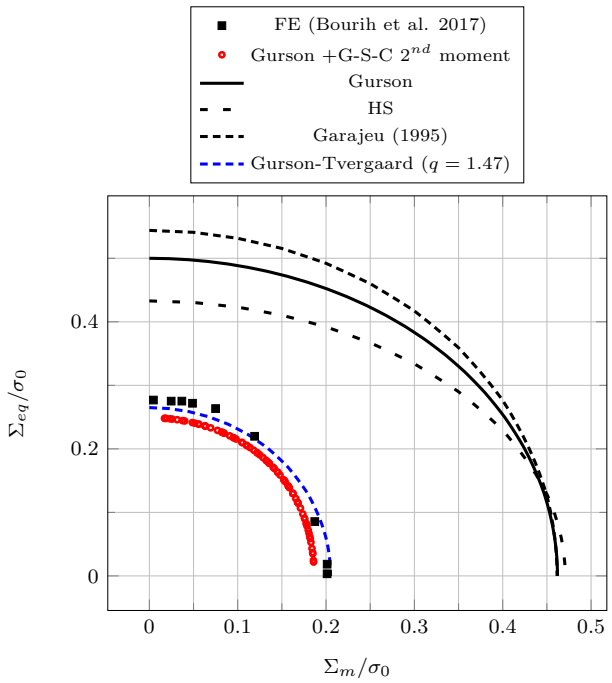

Figure 2.3: Predictions with the second moment generalized self consistent (GSC) model for 50% porosity. Verification against full-field finite element (FE) results on representative volume elements and 3 analytical models.

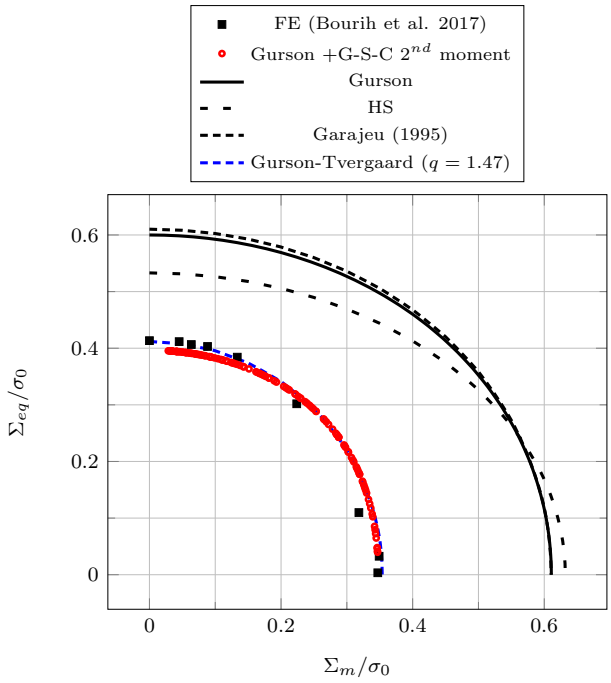

Figure 2.4: Predictions with the second moment generalized self consistent (GSC) model for 40% porosity.

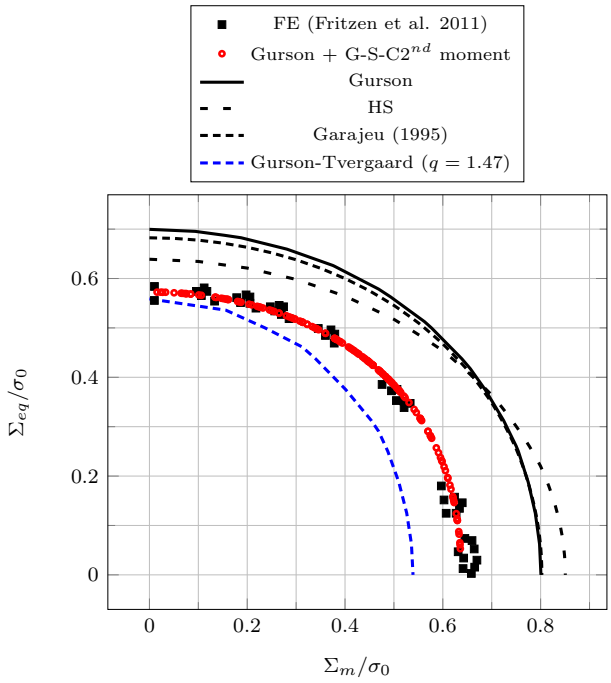

Figure 2.5: Predictions with the second moment generalized self consistent (GSC) model for 30% porosity.

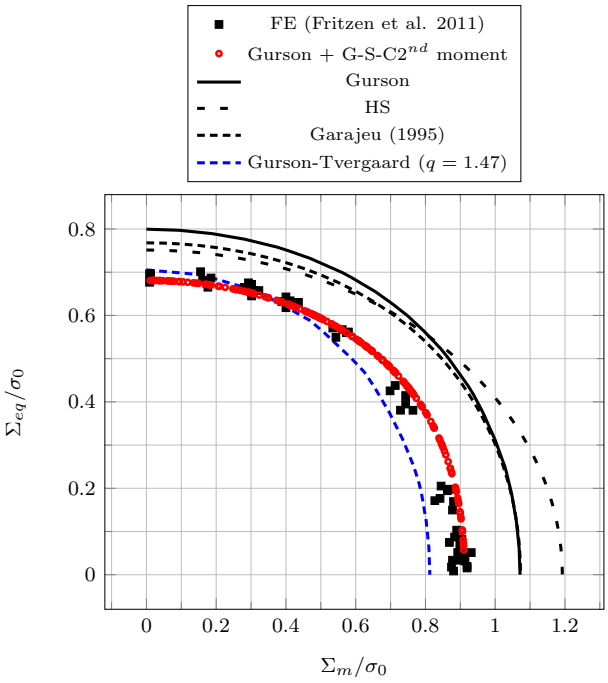

Figure 2.6: Predictions with the second moment generalized self consistent (GSC) model for 20% porosity.

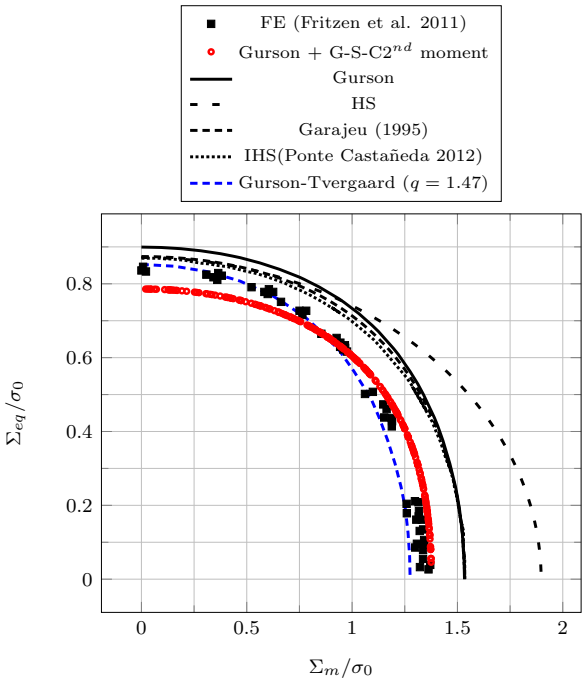

Figure 2.7: Predictions with the second moment generalized self consistent (GSC) model for 10% porosity.

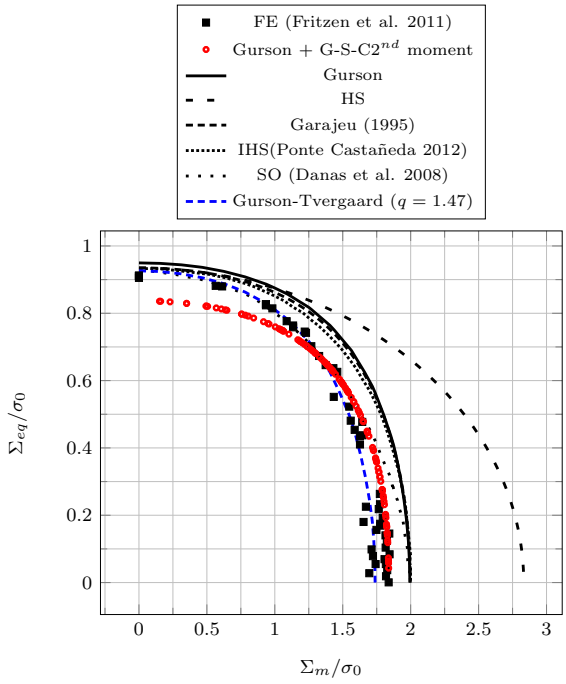

Figure 2.8: Predictions with the second moment generalized self consistent (GSC) model for 5% porosity.

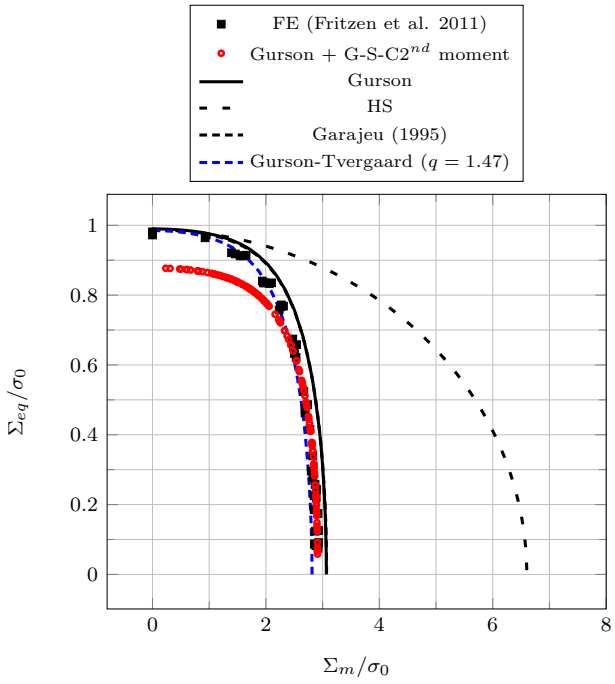

Figure 2.9: Predictions with the second moment generalized self consistent (GSC) model for 1% porosity.

2.6.2 Numerical results with Mori-Tanaka (MT) model

The coupling of Gurson's solution with MT homogenization model is depicted in Fig.2.2. In Fig. 2.2-step 1, the solid spheres having the homogenized Gurson material (G) are assumed to follow an irregular packing of randomly dispersed equal size spheres, which gives their volume fraction as v_G = 64%, and that of solid rigid plastic incompressible spheres (m) in Fig. 2.2-step 2 as v_m = 36%. These values are kept for all the MT predictions presented in Figs. 2.10-2.15, and no fitting or empirical parameter is used.

For high porosities, the MT predictions are either rather excellent (for 50%, Fig. 2.10) and much better than other analytical models. For 30% porosity, the MT predictions (Fig. 2.11) are very good, except for low triaxialities. For 20% (Fig. 2.12) the quality of MT predictions is acceptable for high stress triaxialities, but deteriorates for low triaxialities. For 10% porositiy, the MT predictions (Fig. 2.13) are inaccurate but the high stress triaxiality results are slightly better than for other analytical models. For low porosities (5% and 1%) the MT predictions do not improve at all the Gurson results (Figs. 2.14-2.15).

One possible explanation for the lower quality of MT predictions as compared to the GSC ones is that for MT, the strain field inside the solid inclusions (m) is supposed to be uniform (see Fig. 2.2-step 3) therefore the second moment formulation is unable to improve the predictions in the inclusions by comparaison with a first moment method, and this affects the quality of the overall properties.

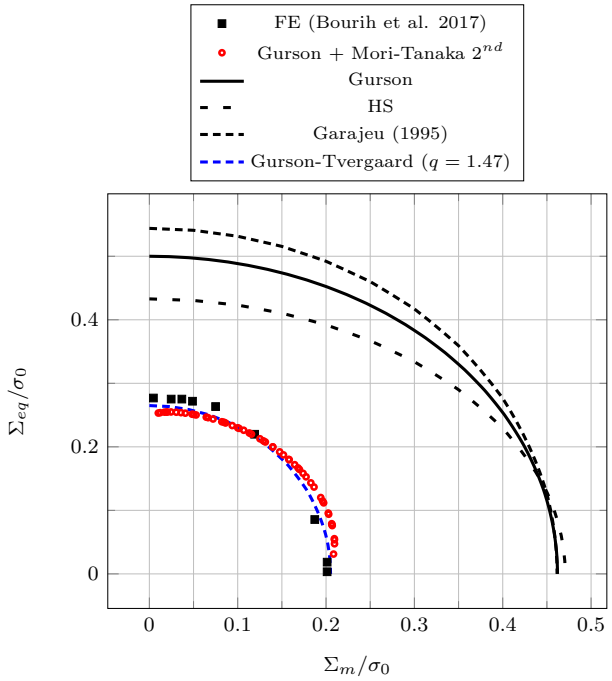

Figure 2.10: Predictions with the second moment Mori-Tanaka (MT) model for 50% porosity. Verification against full-field finite element (FE) results on representative volume elements and 3 analytical models.

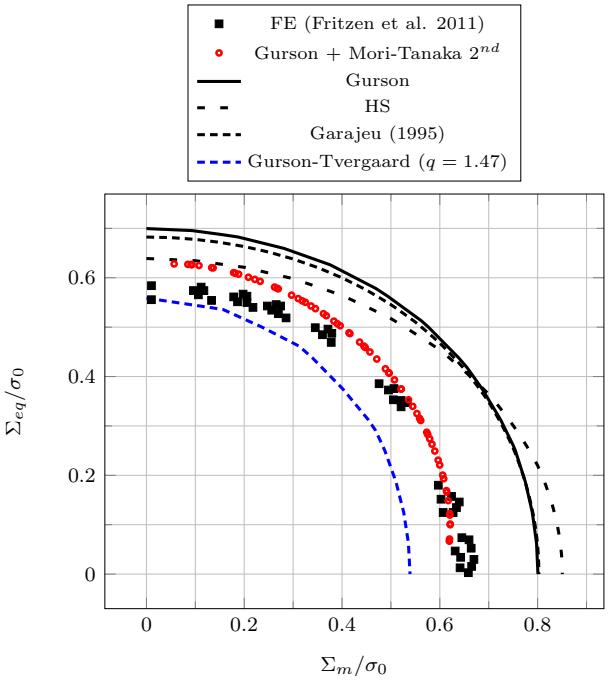

Figure 2.11: Predictions with the second moment Mori-Tanaka (MT) model for 30% porosity.

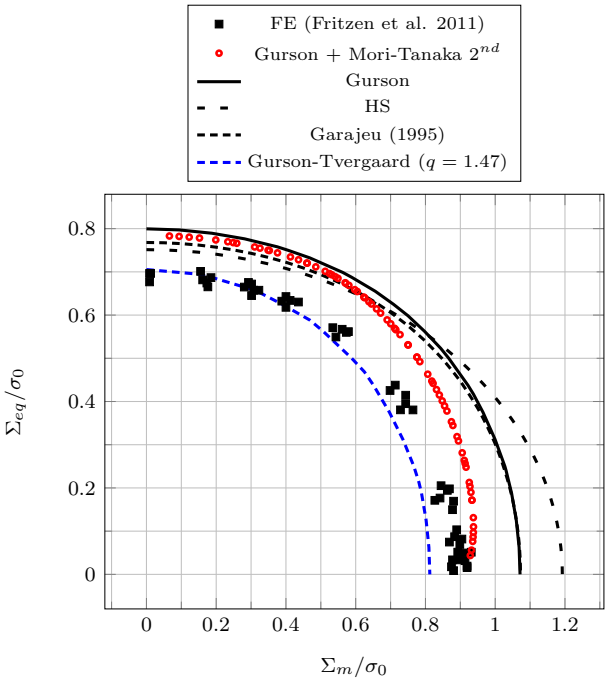

Figure 2.12: Predictions with the second moment Mori-Tanaka (MT) model for 20% porosity.

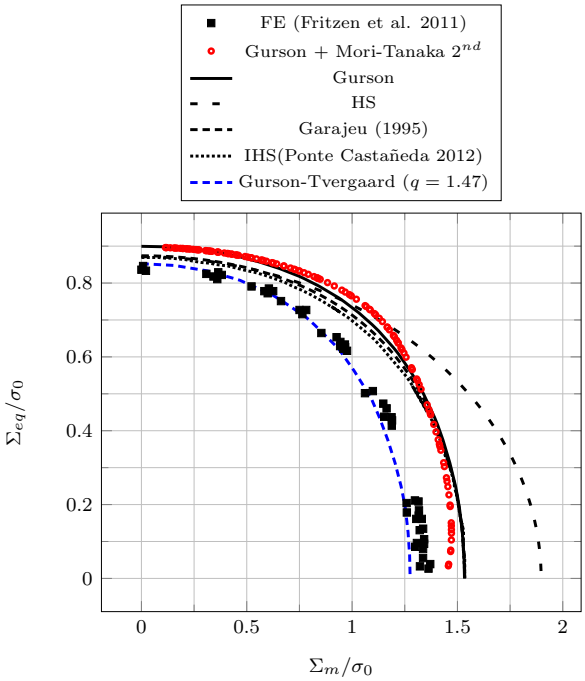

Figure 2.13: Predictions with the second moment Mori-Tanaka (MT) model for 10% porosity.

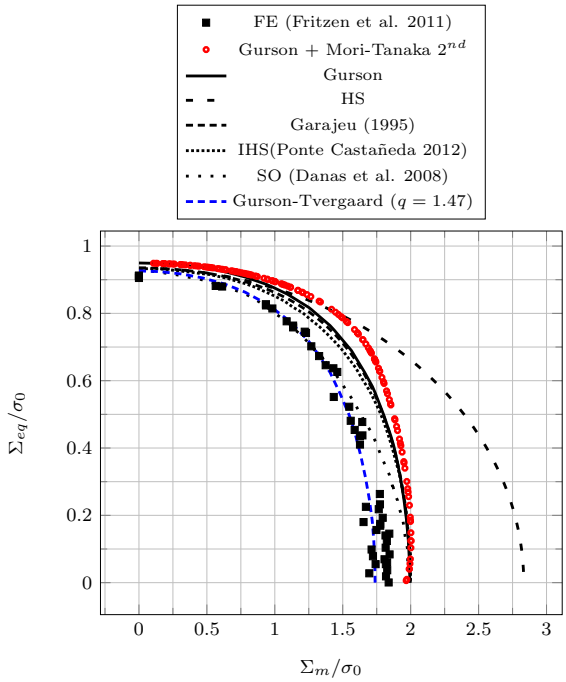

Figure 2.14: Predictions with the second moment Mori-Tanaka (MT) model for 5% porosity.

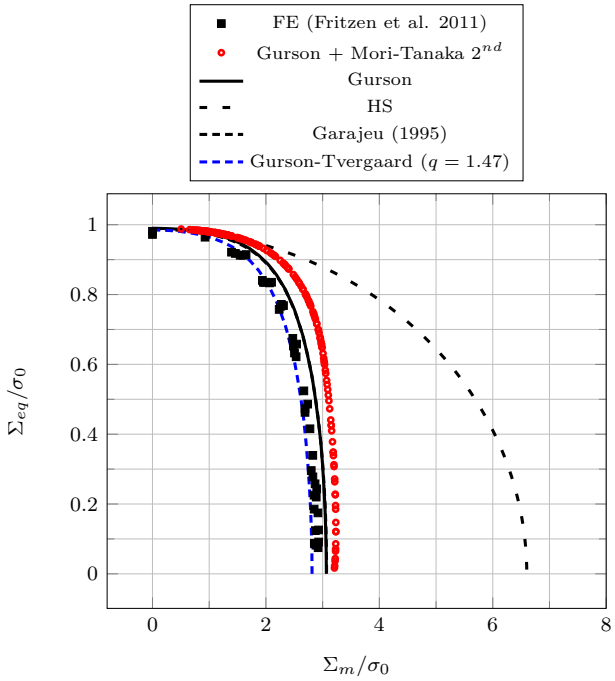

Figure 2.15: Predictions with the second moment Mori-Tanaka (MT) model for 1% porosity.

2.7 Conclusions

A micromechanical modeling approach was proposed for a rigid plastic von Mises matrix material (m) containing multiple spherical cavities. Each single cavity with surrounding matrix is homogenized using Gurson's stress-strain solution, thus obtaining a solid sphere of material (G). Maximum packing concentration is supposed for solid spheres (G). Next, an alternative microstructural representation for the actual porous material is defined such that solid spherical inclusions (m) are embedded in a matrix phase (G). This microstructue is homogenized using the generalized self consistent (GSC) or the Mori-Tanaka (MT) models based on secant formulations of materials (G) and (m). Second statistical moment versions of secant GSC and MT are developed, which enable to take into account the variance of the strain fields in each phase. Additionally, the mean value of the accumulated plastic strain rate in the incompressible rigid plastic material of the original RVE was computed. The result was not exploited but might be in the future in connection with ductile failure modeling for instance.

Numerical predictions of effective yield envelopes in the plane of hydrostatic- von Mises stresses were compared against full-field finite element (FE) results and several analytical models for various porosity levels. No fitting or empirical parameters were used. It was found that the GSC model gives rather excellent predictions, except when both the porosity and the stress triaxiality are small. For the MT model, some predictions are good, especially at high porosities, while some others are not, especially at low porosities. The shortcomings of GSC and MT predictions were partially discussed in Sect.2.6.1 and 2.6.2, although a complete understanding of the issues is lacking at the moment.

It can be concluded that the GSC model is recommended for high or moderate porosities, but its predictions need to be improved for low porosities.

It is possible with further work to generalize the present contribution to other cases. One would be a rigid plastic von Mises matrix with ellipsoidal cavities Gologanu et al. (1993), another would be a rigid plastic orthotropic Hill matrix with cavities (Benzerga and Besson (2001), El Ghezal et al. (2017)) and a third one would be a porous elasto-plastic hardening matrix. In the latter case, the single cavity problem could be solved by an approximate extension of Gurson's solution Leblond et al. (1995) or more accurately with a full-field analysis. The latter procedure would then be comparable to the one proposed in Brassart et al. (2010) for an elasto-plastic matrix reinforced with elastic solid inclusions, where the single inclusion problem was solved with FE and coupled with a MF model for the homogenization of the multiple inclusions RVE.

Appendix A

Coefficients of the Generalized Self-Consistent model

Consider a coated solid sphere with inner and outer radii R_i and R_e, resp. In the following, $c = (R_i/R_e)^3$ and indices (i) and (e) refer to the properties of the inner sphere and the coating, resp., with μ_i and μ_e designating the shear moduli and ν_i and ν_e the Poisson's ratios. Coefficients A, B and C of the GSC model for isotropic linear elastic materials -eq. (2.16)- are given by Christensen (1979) as follows

$$\begin{aligned} A &= 8\left(\frac{\mu_i}{\mu_e}-1\right)(4-5\nu_e)\eta_1 c^{\frac{10}{3}} - 2\left[63\left(\frac{\mu_i}{\mu_e}-1\right)\eta_2 + 2\eta_1\eta_3\right]c^{\frac{7}{3}} \\ &+ 252\left(\frac{\mu_i}{\mu_e}-1\right)\eta_2 c^{\frac{5}{3}} - 50\left(\frac{\mu_i}{\mu_e}-1\right)\left(7-12\nu_e+8\nu_e^2\right)\eta_2 c \\ &+ 4(7-10\nu_e)\eta_2\eta_3 \end{aligned} \tag{2.44}$$

$$\begin{aligned} B &= -2\left(\frac{\mu_i}{\mu_e}-1\right)(1-5\nu_e)\eta_1 c^{\frac{10}{3}} + 2\left[63\left(\frac{\mu_i}{\mu_e}-1\right)\eta_2 + 2\eta_1\eta_3\right]c^{\frac{7}{3}} \\ &- 252\left(\frac{\mu_i}{\mu_e}-1\right)\eta_2 c^{\frac{5}{3}} + 75\left(\frac{\mu_i}{\mu_e}-1\right)(3-\nu_e)\eta_2\nu_e c \\ &+ \frac{3}{2}(15\nu_e-7)\eta_2\eta_3 \end{aligned} \tag{2.45}$$

$$\begin{aligned} C &= 4\left(\frac{\mu_i}{\mu_e}-1\right)(5\nu_e-7)\eta_1 c^{\frac{10}{3}} - 2\left[63\left(\frac{\mu_i}{\mu_e}-1\right)\eta_2 + 2\eta_1\eta_3\right]c^{\frac{7}{3}} \\ &+ 252\left(\frac{\mu_i}{\mu_e}-1\right)\eta_2 c^{\frac{5}{3}} + 25\left(\frac{\mu_i}{\mu_e}-1\right)(\nu_e^2-7)\eta_2 c \\ &- (7+5\nu_e)\eta_2\eta_3 \end{aligned} \tag{2.46}$$

with

$$\begin{aligned} \eta_1 &= (49-50\nu_i\nu_e)\left(\frac{\mu_i}{\mu_e}-1\right) + 35\frac{\mu_i}{\mu_e}(\nu_i-2\nu_e) + 35(2\nu_i-\nu_e) \\ \eta_2 &= 5\nu_i\left(\frac{\mu_i}{\mu_e}-8\right) + 7\left(\frac{\mu_i}{\mu_e}+4\right) \\ \eta_3 &= \frac{\mu_i}{\mu_e}(8-10\nu_e) + (7-5\nu_e) \end{aligned} \tag{2.47}$$

Appendix B
Limit analysis: a brief recall of bounding theorems and application to ductile porous materials

Introduction

The present thesis uses several notions of limit analysis. The purpose of this appendix is to recall some basic principles of the limit analysis theory and its framework with emphasis on the upper and lower bound theorems. For a complete information about the classical limit analysis, see the reference books of Salençon (1983) and Save et al. (1997). Limit analysis theory has been used most significantly as a tool for the design and safety evaluation of engineering structures. It provides, based on its bounding theorems, estimates of the maximum strength and collapse load of a given structural model.
In the context of this thesis, the derivation of the well known Gurson model referred to in the second and third chapters, as well as the stress-based variational model proposed by Cheng et al. (2014) on which relies the developed strength criterion in the third chapter, are based respectively on the kinematic and static limit analysis approaches. The two limit theorems were first presented by Gvozdev (1938) and were established independently later by Hill (1950) for rigid-perfectly-plastic materials and by Drucker et al. (1952) for elastic-perfectly-plastic materials. They enable to bound the solution of a given plasticity problem by choosing in a class of admissible stress and displacement fields those that maximize, and respectively minimize, an associated functional. In the following, the general forms of the theorems of limit analysis are first recalled. The combination of limit analysis with the homogenization theory applied in the context of porous ductile solids is also briefly exposed following Leblond (2003). Finally, a brief outline of the Gurson's model is presented as well as the derivation of the effective stress used in the second chapter.

Some definitions

Consider a solid body Ω subjected to imposed stress vector $\mathbf{t}$ on a part $\partial\Omega_t$ of its boundary and imposed rate of displacements $\mathbf{v^d}$ on the remaining part $\partial\Omega_v$.
We can define a statically admissible (SA) stress field as being:

- satisfying the static equilibrium equation: div $\sigma = 0$ in Ω
- satisfying the given boundary conditions: $\sigma.\mathbf{n} = \mathbf{t}$ on $\partial\Omega_t$

A plastically admissible (PA) stress field does not exceed the yield limit anywhere in the domain.
A stress field both statically and plastically admissible is called licit.

The set $\kappa(\mathbf{v}(x))$ of kinematically and plastically admissible and incompressible velocity fields is defined by:

$$\kappa(\mathbf{v}(x)) = \{\mathbf{v}(x) = \mathbf{v^d} \text{ on } \partial\Omega_v \text{ and } d_{kk} = 0 \text{ with } \mathbf{d} = \frac{1}{2}(\nabla(\mathbf{v}) + \nabla^T(\mathbf{v}))\}$$

Lower-bound theorem or statical theorem

In a class of licit stress fields, the one closest to the solution is that which maximizes the functional of the power of external forces:

$$\int_{\partial\Omega_v} \mathbf{v^d}.\mathbf{t}^* \, dS \leqslant \int_{\partial\Omega_v} \mathbf{v^d}.\mathbf{t} \, dS$$

where $\mathbf{t}^*$ and $\mathbf{t}$ are respectively the surface intensities of forces of the admissible field and the real field.

Upper-bound theorem or kinematical theorem

In a class of admissible velocity fields, the field closest to the solution is the one which minimizes the functional difference between the power of internal forces and the power of external forces corresponding to the given forces:

$$\int_\Omega \sigma : \mathbf{d} \, dV - \int_{\partial\Omega_t} \mathbf{v^d}.\mathbf{t} \, dS \leqslant \int_\Omega \boldsymbol{\sigma}^* : \mathbf{d}^* \, dV - \int_{\partial\Omega_t} \mathbf{v}^*.\mathbf{t} \, dS$$

where v^* denotes the admissible field and $\boldsymbol{\sigma}^*$ is related to $\mathbf{d}^*$ by a constitutive equation.

Kinematic limit analysis method applied to ductile porous materials

In this section, the kinematic limit analysis method applied to ductile porous materials is briefly summarized. Consider now a representative volume element RVE (Ω) of a porous ductile solid consisting in voids (with domain ω) embedded in a matrix. The porosity f is thus given by $\frac{|\omega|}{|\Omega|}$. The matrix is supposed to be incompressible, rigid-ideal plastic and obeying a yield criterion with an associated flow rule.
Suppose now that the RVE is subjected to a uniform rate of deformation $\mathbf{D}$ on its boundary $\partial\Omega$. Let $\mathbf{v}$ be a kinematically admissible (KA) velocity field and $\boldsymbol{\sigma}$ a statically admissible stress field. Hill-Mandel Lemma (Hill (1967)) states that:

$$\boldsymbol{\Sigma} : \mathbf{D} = \frac{1}{|\Omega|} \int_\Omega \boldsymbol{\sigma} : \mathbf{d} \, dV \tag{2.48}$$

with $\boldsymbol{\Sigma}$ and $\mathbf{D}$ being the macroscopic stress and rate of deformation and corresponding to the volume averages of their microscopic counterparts.

The microscopic rate of plastic dissipation associated with the matrix deformation rate $\mathbf{d}$ is given by:

$$\pi(\mathbf{d}) = \max_{\sigma \in C} \boldsymbol{\sigma} : \mathbf{d} \tag{2.49}$$

where C is the convex of plastic admissible stress tensors.
The macroscopic plastic dissipation associated with $\mathbf{D}$ is defined as:

$$\Pi(\mathbf{D}) = \inf_{\mathbf{d} \in \kappa(\mathbf{D})} < \pi(\mathbf{d}) >_{\Omega} = \inf_{\mathbf{d} \in \kappa(\mathbf{D})} (1 - f) < \pi(\mathbf{d}) >_{\Omega - \omega} \tag{2.50}$$

where $\kappa(\mathbf{D})$ is the set of kinematically admissible microscopic deformations with a uniform strain rate boundary condition $\mathbf{D}$:

$$\kappa(\mathbf{D}) = \{\mathbf{d} \; s.t. \; \mathbf{v}(x) = \mathbf{D}.\mathbf{x} \text{ on } \partial\Omega_v \text{ and } d_{kk} = 0 \text{ with } \mathbf{d} = \frac{1}{2}(\nabla(\mathbf{v}) + \nabla^T(\mathbf{v}))\} \tag{2.51}$$

Consider now a stress field $\boldsymbol{\sigma}$ that is statically admissible with $\boldsymbol{\Sigma}$ and plastically admissible, it follows from the Hill-Mandel lemma and the definitions (2.49) and (2.50) that:

$$\boldsymbol{\Sigma} : \mathbf{D} \leq \Pi(\mathbf{D}), \; \forall \boldsymbol{\Sigma} \text{ s.t. } \exists \, \boldsymbol{\sigma} \text{ SA with } \boldsymbol{\Sigma} \text{ and PA}, \; \forall \mathbf{D} \tag{2.52}$$

It follows from (2.52) that the set of potentially sustainable macroscopic stresses (i.e, s.t. $\exists \; \boldsymbol{\sigma}$ SA with $\boldsymbol{\Sigma}$ and PA) lies in the intersection of the semi-spaces dependant on the parameter $\mathbf{D}$ and defined by equation $\boldsymbol{\Sigma} : \mathbf{D} \leq \Pi(\mathbf{D})$. The boundary of this set can be identified as the boundary of a macroscopic domain of elasticity and has a parametric equation given by (see Leblond (2003) for a discussion and a demonstration):

$$\boldsymbol{\Sigma} = \frac{\partial \Pi}{\partial \mathbf{D}}(\mathbf{D}) \tag{2.53}$$

This last equation defines the macroscopic yield surface of the porous ductile material. In practice, the computation of the macroscopic plastic dissipation $\Pi(\mathbf{D})$ is done by partial minimization over a limited set of KA velocity fields. Thus, the corresponding boundary defined by (2.53) lies outside the effective yield surface. Figure 2.16 illustrates the difference between the kinematic and static approaches called respectively "approche par l'extérieur" and "approche par l'intérieur".

The Gurson model

Hereafter we recall the main steps yielding to the approximation (upper bound) of a yield criterion for porous solids developed by Gurson (1977). The simplified model used by Gurson consists in a hollow sphere of uniform wall thickness with external and internal radii b and a respectively such that the void volume fraction f (porosity) is given by $f = (\frac{a}{b})^3$. The matrix material is idealized as rigid-perfectly plastic obeying the Von Mises yield criterion.
The macroscopic plastic dissipation defined by (2.50) is estimated by constructing approximate velocity fields. In order to meet the requirements of the kinematic approach,

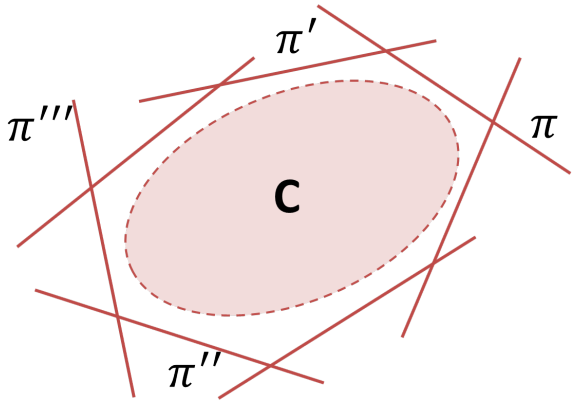

(a)

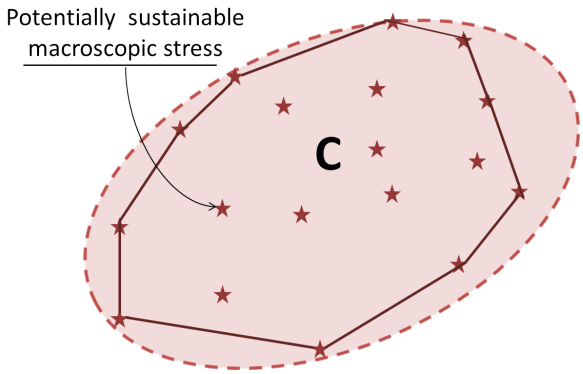

(b)

Figure 2.16: Illustration of the kinematic (a) and static (b) limit analysis approaches.

the velocity fields must be kinematically admissible with the prescribed macroscopic rate of deformation **D** on the outer surface of the sphere S such that:

$$v_i|_S = D_{ij}x_j|_S \tag{2.54}$$

Where x_i is the position of a material point in the Cartesian coordinates. A second constraint on the velocity field is to maintain the matrix incompressibility (*i.e.*$d_{kk} = 0$) while allowing void expansion. The approximate microscopic velocity field in the matrix proposed by Gurson can be broken up into two parts:

$$\mathbf{v} = \mathbf{v^s} + \mathbf{v^v} \tag{2.55}$$

Where $\mathbf{v^s}$ describes the shape change of the cavity with a constant volume and $\mathbf{v^v}$ characterizes the volume change of the cavity. Following this idea, the boundary condition can also be separated as follows:

$$\begin{aligned} D_{ij} &= D'_{ij} + \tfrac{1}{3}D_{nn}\delta_{ij} \\ v_i^s|_S &= D'_{ij}x_j|_S \\ v_i^v|_S &= \tfrac{1}{3}D_{nn}x_i|_S \end{aligned} \tag{2.56}$$

A simple approximation of the shape changing part of the velocity is to use the deviatoric part D'_{ij} which clearly satisfies the incompressibility such that:

$$v_i^s = D'_{ij}x_j \tag{2.57}$$

It can be deduced by prescribing incompressibility and applying the boundary conditions that:

$$\mathbf{v^v} = \frac{b^3}{r^2}D_m\mathbf{e_r} \tag{2.58}$$

with $D_m = \dfrac{1}{3}D_{nn}$ and $\mathbf{e_r}$ is the spherical unit vector. The microscopic strain rate can be written in the form:

$$d_{ij} = D'_{ij} + \frac{1}{3}D_{nn}\,h_{ij} \tag{2.59}$$

where, in spherical coordinates:

$$h_{rr} = -2(\frac{b}{r})^3,\ h_{\phi\phi} = h_{\theta\theta} = (\frac{b}{r})^3,\ h_{ij}|_{i\neq j} = 0, \tag{2.60}$$

and in Cartesian coordinates:

$$h_{ij} = (\delta_{ij} - \frac{3x_ix_j}{r^2})(\frac{b}{r})^3 = (\delta_{ij} - 3n_in_j)(\frac{b}{r})^3 \tag{2.61}$$

where $n_i = \dfrac{x_i}{r}$ are Cartesian components of the normal to a sphere of radius r.
The use of the variational principle (eq. 2.50) with this velocity field yields an upper bound for the macroscopic dissipation (noted as $\Pi^+(\mathbf{D})$):

$$\Pi^+(\mathbf{D}) = (1-f) < \pi(\mathbf{d}(x)) >_{\Omega-\omega} = \frac{\sigma_0^Y}{\Omega}\int_0^{2\pi}\int_0^{\pi}\int_a^b d_{eq}r^2\,\sin\theta dr d\theta d\phi \tag{2.62}$$

where eq.(2.49) was used for the microscopic dissipation in the matrix and σ_0^Y and d_{eq} are respectively the yield stress of the matrix and the equivalent strain rate.
The inequality of Cauchy-Schwartz yields:

$$\Pi^{+}(\mathbf{D}) \leq \Pi^{++}(\mathbf{D}) = \frac{\sigma_0^Y}{\Omega} \int_a^b 4\pi r^2 [\frac{1}{4\pi r^2} \int_0^{2\pi} \int_0^{\pi} d_{eq}^2 \, r^2 \sin\theta d\theta d\phi]^{1/2} dr \tag{2.63}$$

Computing d_{eq}^2, one finally gets:

$$\Pi^{++}(\mathbf{D}) = \frac{\sigma_0^Y}{\Omega} \int_a^b (4D_m^2 \frac{b^6}{r^6} + D_{eq}^2)^{1/2} \, 4\pi r^2 \, dr \tag{2.64}$$

The yield surface associated to the upper macroscopic dissipation is defined by:

$$\Sigma = \frac{\partial \Pi^{++}(\mathbf{D})}{\partial \mathbf{D}} \tag{2.65}$$

which after integrating eq.(2.64) and making explicit the partial derivatives of $\Pi^{++}(\mathbf{D})$ provides the well known Gurson strength criterion:

$$(\frac{\Sigma_{eq}}{\sigma_0^Y})^2 + 2f \cosh(\frac{3}{2}\frac{\Sigma_m}{\sigma_0^Y}) - 1 - f^2 = 0 \tag{2.66}$$

Approximate (upper bound) macroscopic stress

Resolving the integrals given by eq.(2.64) (see Leblond (2003) for details), one gets the upper bound of the macroscopic plastic dissipation:

$$\Pi^{++}(\mathbf{D}) = \sigma_0^Y \left[2D_m \, \operatorname{arg\,sinh}(\frac{2D_m x}{D_{eq}}) - \sqrt{4D_m^2 + D_{eq}^2/x^2} \right]_{x=1}^{x=1/f} \tag{2.67}$$

The approximate macroscopic stress (or limit state) can be computed from $\Sigma = \frac{\partial \Pi^{++}(\mathbf{D})}{\partial \mathbf{D}}$ which can be rewritten in the form:

$$\Sigma_{ij} = \frac{\delta_{ij}}{3} \frac{\partial \Pi^{++}}{\partial D_m} + \frac{2D'_{ij}}{3D_{eq}} \frac{\partial \Pi^{++}}{\partial D_{eq}} \tag{2.68}$$

which yields the following expression:

$$\Sigma_{ij} = \frac{2}{3}\sigma_0^Y [\delta_{ij}(\operatorname{arg\,sinh}(\frac{\lambda}{f}) - \operatorname{arg\,sinh}\lambda) + \frac{D'_{ij}}{D_{eq}}(\sqrt{1+\lambda^2} - \sqrt{f^2+\lambda^2})] \tag{2.69}$$

with $\lambda = \frac{D_m}{D_{eq}}$.

CHAPTER 3

Porous plasticity: Static limit analysis and strength of porous solids with Hill orthotropic matrix

Summary

The present study deals with a strength criterion for ductile porous materials consisting in a Hill type orthotropic matrix containing spherical voids. The originality of the study lies into an attempt to develop an approximate static Limit Analysis for this class of materials, based on the recent work of Cheng et al. (2014) initially proposed for isotropic von Mises matrix. To this end, we considered, in the framework of a statical limit analysis framework, a trial stress field complying with the boundary conditions of the homogenization problem. Interestingly, the proposed procedure delivers an anisotropic macroscopic criterion which is not only pressure dependent, but exhibits an original sensitivity to the sign of the third invariant of the stress deviator. The obtained results are discussed and compared to existing theoretical models, to numerical bounds and to recently available Finite Element results. Finally, we provide the plastic strain rate equations and the void evolution law which are crucial for formulating the failure of anisotropic ductile metals. The influence of the plastic anisotropy on these constitutive equations is illustrated.

keywords

Ductile porous materials; Hill orthotropic matrix; Statical limit analysis; Third stress invariant.

Present Chapter corresponds to the published research paper El Ghezal et al. (2017).
A self-consistent notation is adopted.

This chapter presents an original approximate lower bound for the macroscopic criterion of porous orthotropic plastic materials. Unlike the previous chapter where the proposed model is built upon Gurson's kinematic approach, this study explores a different approach based on the static limit analysis recently proposed by Cheng et al. (2014). The aim here is to extend the latter model by incorporating the plastic anisotropy effects analytically. The obtained criterion will be compared to its theoretical kinematic counterpart proposed by Benzerga and Besson (2001) as an extension of Gurson's model to plastically anisotropic matrix.

3.1 Introduction

The macroscopic yielding and plastic behavior of isotropic porous materials have been extensively studied following the pioneering kinematic approach proposed by Gurson (1977) who studied a hollow sphere and a hollow cylinder subjected to uniform strain rate boundary conditions. The considered matrix is made up of a rigid-perfectly plastic material obeying the von Mises criterion. Although Gurson's kinematic analysis involves several approximations, it has been shown later that the obtained result preserves the upper bound character of the macroscopic criterion (see for instance Perrin (1992)).
Still in the context of Kinematic Limit Analysis[1], the standard Gurson model was later extended by Tvergaard (1981) and subsequently by Perrin and Leblond (1990) in a theoretical approach by introducing additional parameters in order to better fit finite element (FE) unit cell computations and to account for the interaction between voids [2]. Other extensions accounting for void shape effects were further developed for spheroidal voids (e.g. prolate and oblate ellipsoidal cavities) by Gologanu et al. (1993) and Gologanu et al. (1994), Gologanu et al. (1997), Garajeu et al. (2000) and then Monchiet et al. (2014). Pardoen and Hutchinson (2000) integrated the extended model of Gologanu et al. (1997) into a heuristically enhanced void growth and coalescence model incorporating the effect of strain hardening. Studies concerning pressure-sensitive dilatant matrix have been also proposed by Guo et al. (2008) (see alsoCheng and Guo (2007), Chew et al. (2006), Jeong and Pan (1995) and Jeong (2002)) who used a Drucker-Prager yield criterion to describe the compressibility of the matrix.

All the above mentioned extensions concern an isotropic matrix. However, initial anisotropy may be either naturally present in various engineering materials or induced by the deformation during forming processes (e.g rolling, drawing and extrusion). That has motivated several studies dealing with ductile porous materials with plastically anisotropic matrix. Indeed, Benzerga and Besson (2001) extended the Gurson yield criterion to porous materials with Hill orthotropic matrix. This model has been extended by Monchiet et al. (2008) and then by Keralavarma and a.a. Benzerga (2010) who developed micromechanical models that couple both the matrix anisotropy and void shape effects by considering spheroidal voids. Recently, Morin et al. (2014) evaluated the above men-

[1] Another class of models for porous materials has been proposed in the literature based on variational non linear homogenization techniques (see for instance Ponte Castañeda (1991), Ponte Castañeda and Suquet (1997), Danas et al. (2008) and Danas and Ponte Castañeda (2012)).

[2] Note also the well-known computational results of Koplik and Needleman (1988).

tioned criteria using a new FE technique for numerical limit-analysis of Hill materials. Their method is based on the standard FE method. More completely, Pastor et al. (2012) provided numerical upper and lower bounds for the macroscopic criteria of orthotropic plastic materials using static and kinematic numerical limit analysis codes. The case of a Hill type matrix with arbitrary ellipsoidal voids has been very recently investigated by Morin et al. (2015). All the above models with matrix anisotropy have been derived from a kinematic limit analysis approach (except the numerical static bound of Pastor et al.) and thus yield upper bounds of the macroscopic yield criterion. Recently, Cheng et al. (2014) proposed an original statical limit analysis procedure for porous materials with isotropic von Mises solid matrix. Notable feature of the static-based model is the prediction of the third invariant in a rather easy way [3]. The ease of the derivation of the macroscopic criterion and the validity of the results obtained using this approach make it an attractive alternative to kinematics-based models.

In the present study, we are concerned with the anisotropic plastic behavior of ductile porous metals and provide a static-based limit analysis of a Hill-type anisotropic matrix containing spherical voids. This will lead to a fully explicit macroscopic criterion. The plastic strain rate equations and the void evolution law which are crucial for formulating the anisotropic plastic behavior of ductile porous metals will be also provided.

The outline of the chapter is as follows: The static limit analysis recently proposed by Cheng et al. (2014) is first briefly recalled in section 3.2. In section 3.3, an approximate criterion is developed by applying the statical approach to materials with anisotropic matrix and considering a new appropriate trial stress field. The obtained criterion is illustrated in section 3.4, while a comparison of the model predictions with those obtained from FE computations on unit cells (see Morin et al. (2014)) is presented. Numerical upper and lower bounds established by Pastor et al. (2012) are also considered for this comparison purpose. Finally, in section 3.6, we provide the void growth equations and illustrate the porosity evolution laws for different examples of materials anisotropy.

3.2 Basic principles of the static limit analysis approach of porous materials

In this section, general features of the statical limit analysis [4] of porous media presented by Cheng et al. (2014) are briefly recalled in the perspective of the extension that we will expose below for ductile materials with anisotropic matrix.

Scale transition from microscopic scale (typical size of a cavity) to the macroscopic one is performed in the context of standard uniform boundary conditions. The macroscopic stress $\mathbf{\Sigma}$ and strain rate $\mathbf{D}$ are then obtained from the volume averages of their microscopic counterparts σ and $\mathbf{d}$ over the considered Representative Volume Element (RVE) of the

[3] This work has been preceded by that performed in the context of kinematic approach of Limit Analysis by Cazacu et al. (2013) who had investigated the effect of the sign of the third invariant for a von Mises matrix.

[4] A thorough overview of the theory of limit analysis can be found in Benzerga and Leblond (2010) and Save et al. (1997)

porous material:

$$\mathbf{\Sigma} = \frac{1}{|\Omega|}\int_{\Omega-\omega} \boldsymbol{\sigma}\, dV, \quad \mathbf{D} = \frac{1}{|\Omega|}\int_{\Omega} \mathbf{d}\, dV \tag{3.1}$$

Ω refers to the domain occupied by the RVE, while $\Omega - \omega$ corresponds to that of the solid matrix.

Let us introduce the set $\kappa(V(x))$ of kinematically and plastically admissible and incompressible velocity fields:

$$\kappa(\mathbf{V}(x)) = \{\mathbf{V}(x) = \mathbf{D}.\mathbf{x} \text{ on } \partial\Omega \text{ and } d_{kk} = 0 \text{ with } \mathbf{d} = \frac{1}{2}(\nabla(\mathbf{V}) + \nabla^T(\mathbf{V}))\} \tag{3.2}$$

The set $\chi(\boldsymbol{\sigma})$ of statically admissible stress fields is given by:

$$\chi(\boldsymbol{\sigma}) = \{\boldsymbol{\sigma},\ \sigma_{ij} = \sigma_{ji},\ \text{div}\ \boldsymbol{\sigma} = 0,\ \boldsymbol{\sigma}.\mathbf{n} = 0 \text{ on } \partial\omega\} \tag{3.3}$$

Let us recall the Hill-Mandel Lemma (Hill (1967)) which states that the macroscopic work rate equals the average microscopic one and reads as follows:

$$\mathbf{\Sigma} : \mathbf{D} = \frac{1}{|\Omega|}\int_{\Omega-\omega} \boldsymbol{\sigma} : \mathbf{d}\, dV \tag{3.4}$$

in which $(\mathbf{V},\ \boldsymbol{\sigma})$ is an admissible couple. Moreover, the principle of maximum plastic work, introduced by Hill (1950), states that:

$$\forall \boldsymbol{\sigma}^* \in C,\ (\boldsymbol{\sigma}^* - \boldsymbol{\sigma}) : \mathbf{d} \leq 0, \tag{3.5}$$

where C is the convex set of plastic admissible stress fields (defined by the criterion $f(\boldsymbol{\sigma}) \leq 0$ where f is the considered yield function). Introducing the indicator function $\psi(\boldsymbol{\sigma})$ of the plastic domain, defined by:

$$\begin{cases} \psi(\boldsymbol{\sigma}) = 0 \Leftrightarrow \boldsymbol{\sigma} \in C \\ \psi(\boldsymbol{\sigma}) = +\infty \Leftrightarrow \boldsymbol{\sigma} \notin C \end{cases}, \tag{3.6}$$

the inequality (3.5) is reexpressed as:

$$\mathbf{d} \in \partial\psi(\boldsymbol{\sigma}) \tag{3.7}$$

where $\partial\psi(\boldsymbol{\sigma})$ is the subdifferential of ψ. Hill's variational principle Hill (1950) states that among the stress fields, the true one makes the functional:

$$\int_{\Omega-\omega} \psi(\boldsymbol{\sigma}) dV - \int_{\Gamma_{\mathbf{V}}} (\boldsymbol{\sigma}.\mathbf{n}).\mathbf{V}\, ds \tag{3.8}$$

an absolute minimum. In (3.8), $\mathbf{V}$ denotes the prescribed velocity on a part $\Gamma_{\mathbf{V}}$ of the boundary of the cell. An average functional Φ over the RVE, appropriate for the homogenization problem, is introduced such that:

$$\Phi = \min_{\boldsymbol{\sigma}\in\chi(\boldsymbol{\sigma})} \left(\frac{1}{|\Omega|}\int_{\Omega-\omega} \psi(\boldsymbol{\sigma})\, dV - \mathbf{\Sigma} : \mathbf{D}\right) \tag{3.9}$$

Since $\psi(\boldsymbol{\sigma})$ vanishes for licit $\boldsymbol{\sigma}$, this variational problem is equivalent to the following one:

$$\min_{\boldsymbol{\sigma}\in\chi_l(\boldsymbol{\sigma})} (-\boldsymbol{\Sigma} : \mathbf{D}), \tag{3.10}$$

where:

$$\chi_l(\boldsymbol{\sigma}) = \{\boldsymbol{\sigma} \in \chi(\boldsymbol{\sigma}),\ \ f(\boldsymbol{\sigma}) \leq 0\}, \tag{3.11}$$

The resulting minimization problem is solved using Lagrangian functional. By relaxing the yield criterion [5] and imposing the Lagrange multiplier to be uniform over the matrix, the resulting saddle-point problem takes the following simple form:

$$\max_{\dot{\lambda}\geq 0} \min_{\boldsymbol{\sigma}\in\chi_l(\boldsymbol{\sigma})} (L(\boldsymbol{\sigma}, \dot{\lambda}) = \dot{\lambda} \frac{1}{|\Omega|} \int_{\Omega-\omega} f(\boldsymbol{\sigma})\, dV - \boldsymbol{\Sigma} : \mathbf{D}) \tag{3.12}$$

The considered static limit analysis approach results into a stress variational model which is equivalent to minimizing the functional Φ under the condition:

$$F(\boldsymbol{\Sigma}) = \frac{1}{|\Omega|} \int_{\Omega-\omega} f(\boldsymbol{\sigma})\, dV = 0 \tag{3.13}$$

This equality condition on $\boldsymbol{\Sigma}$ is interpreted as the equation of the macroscopic yield function.
The crucial step to obtain $F(\boldsymbol{\Sigma})$ consists in finding a trial stress field $\boldsymbol{\sigma}$ satisfying both the equilibrium equations and the void boundary conditions and implementing it into (3.13). Once $F(\boldsymbol{\Sigma})$ determined, the macroscopic flow rule is obtained by performing the derivation of the Lagrangian functional $L(\sigma, \dot{\lambda})$ with respect to $\boldsymbol{\Sigma}$. This reads:

$$\mathbf{D} = \dot{\lambda} \frac{\partial F}{\partial \boldsymbol{\Sigma}}, \quad \dot{\lambda} \geq 0 \tag{3.14}$$

where $\dot{\lambda}$ can be interpreted as a plastic multiplier.

3.3 Formulation of the approximate yield criterion

3.3.1 The general procedure

Let us now consider as a cell corresponding to the RVE a hollow sphere having external and internal radii b and a, respectively such that the void volume fraction p (porosity) reads $p = (\frac{a}{b})^3$. This hollow sphere is subjected to linear velocities on $(r = b)$ corresponding to a uniform strain rate. The solid matrix material is assumed to be rigid-perfectly plastic and obeying Hill's Hill (1948) quadratic orthotropic criterion. With respect to a Cartesian coordinate system that coincides with the symmetry axes of the plastic anisotropic matrix, the criterion is classically expressed as:

$$f(\boldsymbol{\sigma}) = \sigma_e - \sigma_0 = \sqrt{\frac{3}{2}\, \boldsymbol{\sigma} : \mathbf{M} : \boldsymbol{\sigma}} - \sigma_0 \leq 0 \tag{3.15}$$

[5] Following the numerical works of Dang (1976), the yield criterion is satisfied only in an average sense.

where σ_0 is the yield stress of the material in a reference direction and $\mathbf{M}$ is a symmetric fourth-order orthotropy tensor ($M_{ijkl} = M_{jikl} = M_{ijlk}$). With respect to the symmetry axes, the fourth-order tensor $\mathbf{M}$ takes the following form in the standard Voigt notation (6×6 matrix), the stress tensor being given as a vector:

$$\mathbf{M} = \begin{bmatrix} H+G & -H & -G & 0 & 0 & 0 \\ -H & F+H & -F & 0 & 0 & 0 \\ -G & -F & F+G & 0 & 0 & 0 \\ 0 & 0 & 0 & 2L & 0 & 0 \\ 0 & 0 & 0 & 0 & 2M & 0 \\ 0 & 0 & 0 & 0 & 0 & 2N \end{bmatrix}; \quad \boldsymbol{\sigma} = \begin{bmatrix} \sigma_{11} \\ \sigma_{22} \\ \sigma_{33} \\ \sigma_{23} \\ \sigma_{13} \\ \sigma_{12} \end{bmatrix} \tag{3.16}$$

Note that the Hill criterion reduces to the isotropic von Mises one when the characteristic constants read $F = G = H = 1/3$ and $L = M = N = 1$.

For the tractability of the determination of $F(\sigma)$ from (3.13), and similarly to the choice made by Benzerga and Besson (2001) and then Monchiet et al. (2008) in the context of kinematic limit analysis, we will consider an isotropic trial stress field:

$$\boldsymbol{\sigma} = \boldsymbol{\sigma}^{(1)} + \boldsymbol{\sigma}^{(2)}, \tag{3.17}$$

where $\boldsymbol{\sigma}^{(1)}$ reads in spherical coordinates ($r, \theta \in [0, \pi], \phi \in [0, 2\pi]$):

$$\boldsymbol{\sigma}^{(1)} = -C_0 \left(\ln(\frac{a}{r})\mathbf{1} - \frac{1}{2}(\mathbf{e}_\theta \otimes \mathbf{e}_\theta + \mathbf{e}_\phi \otimes \mathbf{e}_\phi)\right), \tag{3.18}$$

C_0 is a constant to be determined and $\mathbf{1}$ denotes the second order identity tensor. $\boldsymbol{\sigma}^{(1)}$ corresponds to the exact stress field in the case of hydrostatic loading for an isotropic matrix. The second part $\boldsymbol{\sigma}^{(2)}$ is taken for capturing the shear stress effects. At the difference of Cheng et al. (2014) who consider an homogeneous stress field, $\boldsymbol{\sigma}^{(2)}$ is inspired here from the exact solution to linear elastic hollow sphere problem subjected to deviatoric loading (see Huang et al. (1996))[6]:

$$\begin{aligned} \sigma^{(2)}_{rr} &= [3\nu A_1 x^2 + A_2 - 2(5-\nu)A_3 x^{-3} - 12A_4 x^{-5}](1 + 3\cos 2\theta), \\ \sigma^{(2)}_{\theta\theta} &= [7(2+\nu)A_1 x^2 - A_2 + (1-2\nu)A_3 x^{-3} + 7A_4 x^{-5}](1 + 3\cos 2\theta) \\ &\quad + [-2(7-4\nu)A_1 x^2 + 2A_2 + 4(1-2\nu)A_3 x^{-3} - 4A_4 x^{-5}] \\ \sigma^{(2)}_{\phi\phi} &= [(7+11\nu)A_1 x^2 + 3(1-2\nu)A_3 x^{-3} + 5A_4 x^{-5}](1 + 3\cos 2\theta) \\ &\quad + [2(7-4\nu)A_1 x^2 - 2A_2 - 4(1-2\nu)A_3 x^{-3} + 4A_4 x^{-5}] \\ \sigma^{(2)}_{r\theta} &= 3[(7+2\nu)A_1 x^2 - A_2 - 2(1+\nu)A_3 x^{-3} - 8A_4 x^{-5}]\sin 2\theta \end{aligned} \tag{3.19}$$

in spherical coordinates. Where:

$$\begin{aligned} A_1 &= 5(p^{-5/3} - p^{-1})C_1/\Delta, \\ A_2 &= [(49 - 25\nu^2)p^{-10/3} + 126p^{-5/3} + 25(\nu^2 - 7)p^{-1}]C_1/6\Delta, \\ A_3 &= 5(7+5\nu)(p^{-10/3} - p^{-1})C_1/12\Delta, \\ A_4 &= -(7+5\nu)(p^{-10/3} - p^{-5/3})C_1/4\Delta \end{aligned} \tag{3.20}$$

[6]This idea is similar to that already used by Garajeu (1995) in the context of kinematics limit analysis of isotropic porous materials.

and $\Delta = [(49-25\nu^2)p^{-10/3} + 25(\nu^2-7)p^{-7/3} + 252p^{-5/3} + 25(\nu^2-7)p^{-1} + (49-25\nu^2)]$. C_1 is also a constant parameter, $x = \frac{r}{a}$ and ν is a free parameter which must be determined by minimizing the macroscopic potential. [7]
In contrast to the homogeneous deviatoric part taken in Cheng et al. (2014), the considered stress field $\boldsymbol{\sigma}^{(2)}$ satisfies not only the equilibrium equations but also the boundary conditions on the inner surface of the hollow sphere.

The microscopic equivalent stress in the matrix $\sigma_e = \sqrt{\frac{3}{2}\boldsymbol{\sigma} : \mathbf{M} : \boldsymbol{\sigma}}$ is computed in a straightforward manner and is found to be a function of both r,θ and ϕ that could be recast in the form:

$$\sigma_e = \sqrt{C_0^2 f_1(r,\theta,\phi) + C_1^2 f_2(r,\theta,\phi) + C_0 C_1 f_3(r,\theta,\phi)}, \tag{3.21}$$

where f_1, f_2 and f_3 are combinations of functions of r, θ and ϕ, whose expressions are long so they were omitted here for brevity. The computation of the axisymmetric macroscopic stress tensor using (3.1) yields:

$$\boldsymbol{\Sigma} = -\frac{C_0 \ln p}{3}\mathbf{1} - \frac{1}{3}C_1(\mathbf{e}_1 \otimes \mathbf{e}_1 + \mathbf{e}_2 \otimes \mathbf{e}_2 - 2\mathbf{e}_3 \otimes \mathbf{e}_3) \tag{3.22}$$

It follows that the macroscopic mean stress Σ_m, the macroscopic Hill equivalent stress Σ_e and the third invariant of the deviatoric part $\mathbf{S}$ of $\boldsymbol{\Sigma}$, noted J_3, are given by:

$$\Sigma_m = -\frac{C_0 \ln p}{3},\ \Sigma_e^2 = \frac{3}{2}\boldsymbol{\Sigma} : \mathbf{M} : \boldsymbol{\Sigma} = \frac{3}{2}(F+G)C_1^2,\ J_3 = \frac{tr(\mathbf{S}^3)}{3} = \frac{2}{27}C_1^3 \tag{3.23}$$

Note that in equation (3.23), the macroscopic Hill equivalent stress Σ_e depends only on coefficients F and G through their sum $F+G$. This is due to the axisymmetric character of the considered loadings. Anticipating on developments which will follow, we introduce the following alternative expressions [8]:

$$\tilde{\Sigma}_e = \frac{\Sigma_e}{\sqrt{\frac{3}{2}(F+G)}} = |C_1|\ ,\ \tilde{\Sigma}_m = -\frac{3\Sigma_m}{\ln p} = C_0\ ,\ \text{sign}(J_3) = \frac{27}{2}\frac{J_3}{\tilde{\Sigma}_e{}^3} = \text{sign}(C_1) \tag{3.24}$$

According to (3.13), the macroscopic yield surface is defined by:

$$F(\boldsymbol{\Sigma}) = \frac{1}{|\Omega|}\int_{\Omega-\omega} \sigma_e(r,\theta,\phi)\, r^2 \sin\theta\, d\theta\, d\phi\, dr - (1-p)\,\sigma_0 \tag{3.25}$$

where, taking into account (3.24), the microscopic equivalent stress (eq. 3.21) , can be

[7] Note that ν (which may not be interpreted here as an elastic coefficient) has been shown by optimization of $F = \frac{1}{|\Omega|}\int_{\Omega-\omega} f(\boldsymbol{\sigma})\, dV$ to be equal to 0.5

[8] Note that if Z is the tensile yield stress in the principal anisotropy direction z, then we have $F+G=\frac{1}{Z^2}$ which confirms the positiveness of $F+G$ and allows its use in the square root.

recast in the form:

$$\begin{aligned}\sigma_e = & \sqrt{f_1(r,\theta,\phi)\tilde{\Sigma}_m^2 + f_2(r,\theta,\phi)\tilde{\Sigma}_e^2 + f_3(r,\theta,\phi)\text{sign}(J_3)\tilde{\Sigma}_m\tilde{\Sigma}_e} \\ = & \sqrt{f_1(r,\theta,\phi)\frac{9\Sigma_m^2}{\ln^2 p} + f_2(r,\theta,\phi)\frac{\Sigma_e^2}{3/2(F+G)} - f_3(r,\theta,\phi)\text{sign}(J_3)\frac{\Sigma_e}{\sqrt{3/2(F+G)}}\frac{3\Sigma_m}{\ln p}}\end{aligned} \tag{3.26}$$

Due to presence of the functions f_1, f_2 and $f_3(r,\theta,\phi)$, a closed form expression of the macroscopic criterion $F(\mathbf{\Sigma})$ by combining (3.25) and (3.26) is out of reach; this has motivated the approximations described below.

3.3.2 Approximate criterion based on Cauchy-Schwarz inequality

A first approximation of the macroscopic criterion can be obtained by adopting the Cauchy-Schwarz inequality, as in several previous works including those on porous materials with Hill orthotropic matrix (see for instance Benzerga and Besson (2001) or Monchiet et al. (2008)). This easies the computation of the integral in (3.25) and leads to:

$$\begin{aligned}&\tfrac{1}{|\Omega|}\int_{\Omega-\omega}\sigma_e(r,\theta,\phi)\, r^2 sin\theta\, d\theta\, d\phi\, dr - (1-p)\,\sigma_0 \\ \leq\ &\tfrac{1}{|\Omega|}\sqrt{|\Omega-\omega|\int_{\Omega-\omega}\sigma_e^2(r,\theta,\phi)\, r^2 sin\theta\, d\theta\, d\phi\, dr} - (1-p)\,\sigma_0\end{aligned} \tag{3.27}$$

The macroscopic criterion is obtained in the form:

$$\sqrt{\alpha\tilde{\Sigma}_e^2 + \beta\tilde{\Sigma}_m^2 + \gamma\text{sign}(J_3)\tilde{\Sigma}_e\tilde{\Sigma}_m} - \sigma_0 \leq 0, \tag{3.28}$$

where α, β and γ are combinations of both the matrix anisotropy characteristics and the porosity p. A power series expansion of those quantities up to order 1 allows to get a simplified expression:

$$\begin{aligned}&\alpha = \tfrac{3}{2}(F+G) + [\tfrac{631}{189}(F+G) + \tfrac{40}{189}H + \tfrac{20}{189}N + \tfrac{25}{189}(L+M)]p + O(p^2), \\ &\beta = \tfrac{1}{20}[2(F+G+H) + L + M + N], \\ &\gamma = \tfrac{1}{21}[-(L+M) - 2(G+F-N) + 4H]p\ln p \\ &+(p-p^{\frac{5}{3}})[\tfrac{-32}{95}H + \tfrac{8}{95}(L+M) + \tfrac{16}{95}(F+G-N)] + O(p^2).\end{aligned} \tag{3.29}$$

which proved to be a good approximation of the exact expression for porosity values up to 0.15. The new criterion takes the following form:

$$\sqrt{\frac{\alpha}{\frac{3}{2}(F+G)}(\frac{\Sigma_e}{\sigma_0})^2 + \frac{9}{(\ln p)^2}\beta\,(\frac{\Sigma_m}{\sigma_0})^2 - \frac{3\gamma\text{sign}(J_3)}{\sqrt{\frac{3}{2}(F+G)}\ln p}\frac{\Sigma_e}{\sigma_0}\frac{\Sigma_m}{\sigma_0}} - 1 \leq 0 \tag{3.30}$$

In the limit of a vanishing porosity, one can check that since $\ln p \to -\infty$ and $\alpha \to \frac{3}{2}(F+G)$, the Hill quadratic criterion of the matrix is obviously retrieved. Interestingly, criterion (3.30) shows an influence of the sign of the third deviatoric stress invariant. Such

type of effect has been already pointed out in a recent kinematic-based limit analysis study by Cazacu et al. (2013) for von Mises matrix materials (see also Benallal et al. (2014) or Revil-Baudard and Cazacu (2014) for the effect of Lode angle) and by Cheng et al. (2014) in the context of the static approach (this result has been recently extended to the influence of Lode angle Cheng et al. (2015)). An originality of the present result is that the effect of the sign of the third deviatoric stress invariant is coupled with the matrix anisotropy. In the limit of isotropic matrix, the criterion reduces to:

$$\sqrt{(1+\frac{8}{3}p)(\frac{\Sigma_e}{\sigma_0})^2+\frac{9}{4(\ln p)^2}(\frac{\Sigma_m}{\sigma_0})^2}-1\leq 0 \tag{3.31}$$

Remark1: The obtained criterion (3.31) has the same shape as the approximate one obtained by Cheng et al. (2014) but differs from it by the factor multiplying Σ_e. Indeed, in the approximate criterion of Cheng et al. (2014) the pure deviatoric point corresponds to $\frac{\Sigma_e}{\sigma_0}=1-p$, which is the same as in the Gurson model and which corresponds to Voigt upper bound. This difference is obviously due to the choice of the trial stress field, the one considered here being more refined.

Remark2: It should be pointed out that for hydrostatic macroscopic stresses, as expected, the isotropic criterion (3.31) predicts the same yield loci as in Gurson model and in Cheng et al. (2014) and which corresponds to the exact solution of porous materials with a von Mises matrix: $\frac{\Sigma_m}{\sigma_0}=-\frac{2}{3}\ln p$. The pure deviatoric point corresponds to $\frac{\Sigma_e}{\sigma_0}=\frac{1}{\sqrt{1+\frac{8}{3}p}}$ which is, for $p\leq 0.15$, bounded below by the deviatoric point given by the elliptic criteria of Ponte Castañeda (1991) and Michel and Suquet (1992) (which correspond to $\frac{\Sigma_e}{\sigma_0}=\frac{1-p}{\sqrt{1+\frac{2}{3}p}}$) and bounded above by the one given by Gurson and the one given by Cheng et al. (2014).

Remark3: It can be noted that in the isotropic case, the effect of the third deviatoric stress disappears, this is due to the vanishing value of γ. This absence of the third stress deviator invariant contrasts with , the result established by Cheng et al. (2014) in the context of static limit analysis. This limitation may be obviously attributed to the use of the Cauchy-Schwarz inequality and has motivated an alternative approach presented in what follows.

3.3.3 Approximate criterion based on Taylor series expansion

Indeed, the microscopic equivalent stress σ_e may be put in the following form:

$$\sigma_e=\sqrt{f_1(r,\theta,\phi)\tilde{\Sigma}_m^2+f_2(r,\theta,\phi)\tilde{\Sigma}_e^2}\sqrt{1+\varrho(r,\theta,\phi)} \tag{3.32}$$

where

$$\varrho(r,\theta,\phi)=\frac{f_3(r,\theta,\phi)\text{sign}(J_3)\tilde{\Sigma}_m\tilde{\Sigma}_e}{f_1(r,\theta,\phi)\tilde{\Sigma}_m^2+f_2(r,\theta,\phi)\tilde{\Sigma}_e^2}$$

Assuming $\varrho(r,\theta,\phi)$ to be small, we adopt here an alternative approximation consisting in performing a Taylor series expansion of the expression $\sqrt{1+\varrho(r,\theta,\phi)}$ involved in (3.32) [9]:

$$\begin{aligned}\sigma_e \;\approx\; & \sqrt{<f_1>_{\Omega-\omega}\tilde{\Sigma}_m^2 + <f_2>_{\Omega-\omega}\tilde{\Sigma}_e^2}\left[1+\frac{1}{2}\frac{f_3(r,\theta,\phi)\mathrm{sign}(J_3)\tilde{\Sigma}_m\tilde{\Sigma}_e}{<f_1>_{\Omega-\omega}\tilde{\Sigma}_m^2 + <f_2>_{\Omega-\omega}\tilde{\Sigma}_e^2}\right.\\ & \left.-\frac{1}{8}\frac{f_3(r,\theta,\phi)^2\tilde{\Sigma}_m^2\tilde{\Sigma}_e^2}{(<f_1>_{\Omega-\omega}\tilde{\Sigma}_m^2 + <f_2>_{\Omega-\omega}\tilde{\Sigma}_e^2)^2}+\frac{1}{16}\frac{f_3(r,\theta,\phi)^3\mathrm{sign}(J_3)\tilde{\Sigma}_m^3\tilde{\Sigma}_e^3}{(<f_1>_{\Omega-\omega}\tilde{\Sigma}_m^2 + <f_2>_{\Omega-\omega}\tilde{\Sigma}_e^2)^3}\right]\end{aligned} \tag{3.33}$$

for which has been made a complementary approximation consisting in replacing $f_1(r,\theta,\phi)$ and $f_2(r,\theta,\phi)$ by their mean values in the matrix $<f_1>_{\Omega-\omega}$ and $<f_2>_{\Omega-\omega}$, respectively. One gets:

$$<f_1>_{\Omega-\omega}=\frac{1}{|\Omega-\omega|}\int_{\Omega-\omega}f_1 d\mathrm{v}=\beta\;;\; <f_2>_{\Omega-\omega}=\frac{1}{|\Omega-\omega|}\int_{\Omega-\omega}f_2 d\mathrm{v}=\alpha \tag{3.34}$$

The determination of the macroscopic criterion requires also the following integrations:

$$\begin{array}{l}\frac{1}{|\Omega-\omega|}\int_{\Omega-\omega}f_3 d\mathrm{v}=\gamma\\ \frac{1}{|\Omega-\omega|}\int_{\Omega-\omega}f_3^2 d\mathrm{v}=\xi\\ \frac{1}{|\Omega-\omega|}\int_{\Omega-\omega}f_3^3 d\mathrm{v}=\chi\end{array} \tag{3.35}$$

Let us draw the attention to the fact that α, β and γ are given by (3.29). The expressions of ξ and χ, which are functions of anisotropy parameters and porosity p are obtained as:

$$\begin{aligned}&\xi=\tfrac{3}{5}(F^2+G^2+FG),\\ &\chi=\frac{27}{640}\frac{(-32-323\pi)G^3+(685\pi-536)F^3+(11\pi-224)F^2G-(373\pi+32)G^2F}{\pi}.\end{aligned} \tag{3.36}$$

Finally, introducing (3.33), (3.34) and (3.35) into (3.25) yields the following general form of the macroscopic criterion:

$$\sqrt{\alpha\tilde{\Sigma}_e^2+\beta\tilde{\Sigma}_m^2}\left[1+\frac{\gamma}{2}\frac{\mathrm{sign}(J_3)\tilde{\Sigma}_m\tilde{\Sigma}_e}{\alpha\tilde{\Sigma}_e^2+\beta\tilde{\Sigma}_m^2}-\frac{\xi}{8}\frac{\tilde{\Sigma}_m^2\tilde{\Sigma}_e^2}{(\alpha\tilde{\Sigma}_e^2+\beta\tilde{\Sigma}_m^2)^2}+\frac{\chi}{16}\frac{\mathrm{sign}(J_3)\tilde{\Sigma}_m^3\tilde{\Sigma}_e^3}{(\alpha\tilde{\Sigma}_e^2+\beta\tilde{\Sigma}_m^2)^3}\right]-\sigma_0\leqslant 0 \tag{3.37}$$

for which it is recalled that $\tilde{\Sigma}_m$ and $\tilde{\Sigma}_e$ are defined in (3.24).
Note that (3.37) obviously reduces to the Hill quadratic criterion (of the matrix) in the limit $p\longrightarrow 0$.
It is worth noticing that in the particular case of the von Mises isotropic matrix, the parameter χ does not vanish and thus an effect of the third invariant in that case is obtained:

$$\sqrt{(1+\frac{8}{3}p)(\frac{\Sigma_e}{\sigma_0})^2+\frac{9}{4(\ln p)^2}(\frac{\Sigma_m}{\sigma_0})^2}\;\;\Pi(\mathrm{sign}(J_3),T,p)-1\leq 0, \tag{3.38}$$

[9] This follows an idea already implemented in the isotropic case by Leblond et al. (2014) who has revisited the Gurson kinematic limit analysis.

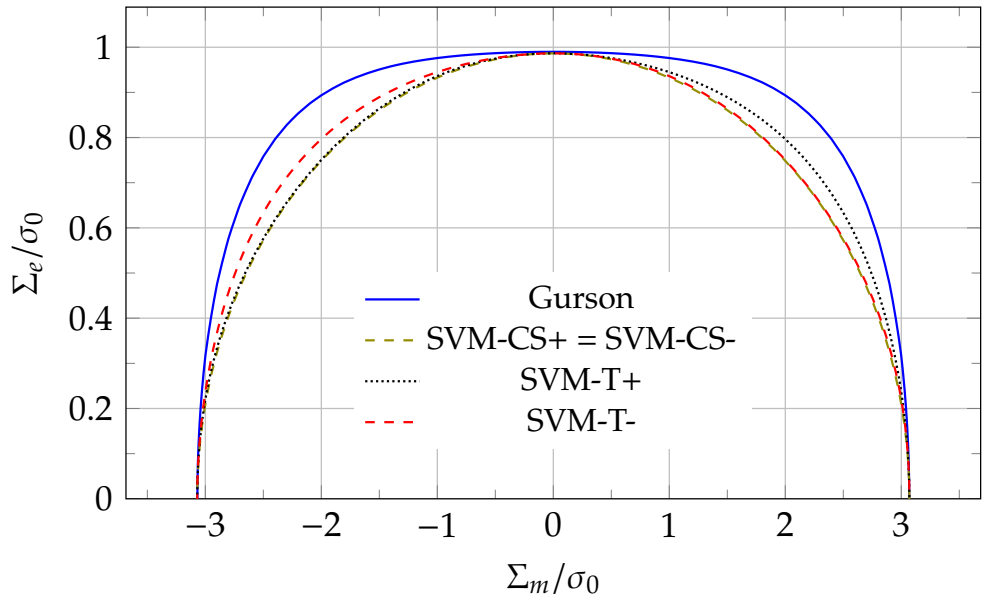

Figure 3.1: Yield surfaces of a metal matrix porous solid with 1% porosity given respectively by Gurson (1977) and by the proposed new criteria. Acronyms SVM-CS+ and SVM-CS- refer respectively to criterion (3.31) for $J_3 > 0$ and for $J_3 < 0$ and acronyms , SVM-T+ and SVM-T- refer respectively to criterion (3.38) for $J_3 > 0$ and for $J_3 < 0$.

with

$$\Pi(\text{sign}(J_3),T,p)=\left[1-\frac{1}{8}\frac{1}{5}\left(\frac{\frac{-3T}{\ln p}}{(1+\frac{8}{3}p)+\frac{9}{4(\ln p)^2}T^2}\right)^2-\frac{1}{16}\frac{103}{80\pi}\text{sign}(J_3)\left(\frac{\frac{-3T}{\ln p}}{(1+\frac{8}{3}p)+\frac{9}{4(\ln p)^2}T^2}\right)^3\right] \tag{3.39}$$

and T denotes the stress triaxiality $T=\Sigma_m/\Sigma_e$.

Remark 4: The criterion takes the same shape as in Cheng et al. (2014). Besides, the function $\Pi(\text{sign}(J_3),T,p)$ is smooth for $p\in[0,1]$ and $T\in\,]-\infty,+\infty[$ and takes values between 0.949 and 1.050; thus, as in Cheng et al. (2014), one can obtain an approximate criterion by taking $\Pi(\text{sign}(J_3),T,p)$ to be unity. However, it should be pointed out that in that case the influence of the third invariant J_3 is lost. Remarks 1-2 remain valid for this second criterion.

3.4 Illustration of the established macroscopic criterion

In this section, we aim at illustrating some salient features of the obtained criteria. The yield curve corresponding to the new criteria in the isotropic case and its comparison with Gurson model for a porosity p=0.01 are reported on Fig 3.1.

It is seen that the yield envelopes predicted by the new criteria stay inside the Gurson kinematic one as expected. It is recalled that for the isotropic case, the parameter γ

Table 3.1: Hill's coefficients considered for the different studied cases

Material's parameters	F	G	H	L	M	N
Isotropic: Fig 3.1	1/3	1/3	1/3	1	1	1
Set 1: Fig 3.2, Fig 3.8	0.332	0.332	0.999	1	1	2.333
Set 2: Fig 3.3, Fig 3.6	0.268	0.345	0.311	1.096	3.622	3.498
Set 3: Fig 3.4, Fig 3.7	0.331	0.402	0.168	3.669	1.141	2.2

vanishes and thus there is no effect of (J_3) predicted by the criterion (3.30) named SVM-CS. However, this effect is still present for the criterion obtained by Taylor series expansion (3.37) named SVM-T.
Let us consider now the anisotropic case for which the parameters chosen for every figure are indicated in table 3.1. In Figures 3.2(a) and 3.2(b) we compare the yield curves predicted by the new criteria (3.30) and (3.37) for $J_3 > 0$ and $J_3 < 0$ to those pertaining to Benzerga and Besson (2001) model; two porosity values, $p = 0.01$ and $p = 0.1$ are considered. It is observed that the obtained criteria display an asymmetry with respect to the axis $\Sigma_m = 0$ due to the sign of J_3. A zoom on appropriate portions of the figure reveals that the predicted macroscopic yield surface obtained by the Cauchy-Schwarz inequality (3.30) is within the one obtained by Taylor series expansion (3.37) and the effect of sign(J_3) is more pronounced for the latter.

3.5 Validation by comparison to FE estimate and to numerical bounds

For validation purposes, we provide two different comparisons. We first compare the obtained criteria (3.30) and (3.37) with FE limit-analysis results recently reported by Morin et al. (2014). The FE computations were conducted on hollow sphere subjected at its external boundary to homogeneous strain rate conditions. As in the theoretical model, axisymmetric strain rate loadings are considered such that: $\Sigma_{11} = \Sigma_{22} \neq 0$, $\Sigma_{33} \neq 0$ and $\Sigma_{ij} = 0$ for $i \neq j$. The porous solid is made up of an anisotropic aluminium alloy for which the parameters (reported in table 3.1) were experimentally obtained by Benzerga (2000). The corresponding macroscopic yield surfaces are presented in Fig3.3(a) for $p = 0.01$ and Fig 3.3(b) for $p = 0.1$. It is observed that the predicted envelope remains inside the yield envelopes obtained from the numerical FE results, as expected. However, one can note that the criterion obtained by Benzerga and Besson (2001), by using a kinematic approach provides closer upper bounds when compared to FE results. This fact may be explained by the fundamental difference between the kinematic and the static limit analysis approaches. More specifically, the difference with Benzerga criterion may be attributed to the relaxation of the yield condition in the matrix, this condition being enforced only in the mean and by assuming a uniform plastic multiplier. The same observation has been also made in the case of an isotropic matrix in Cheng et al. (2014).

A second assessment of the accuracy of the proposed criterion is performed by comparing the theoretical predictions to Pastor et al. (2012) upper and lower bounds of the macroscopic criterion for anisotropic materials. Those bounds are obtained using respectively static and kinematic FE approaches and based on the solution to the corresponding

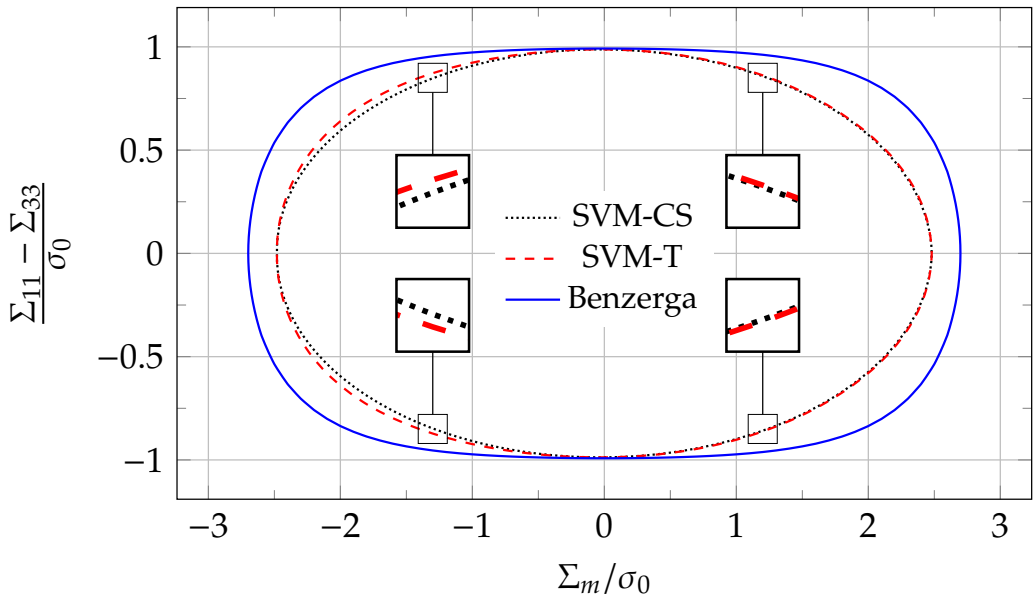

(a) porosity p=0.01

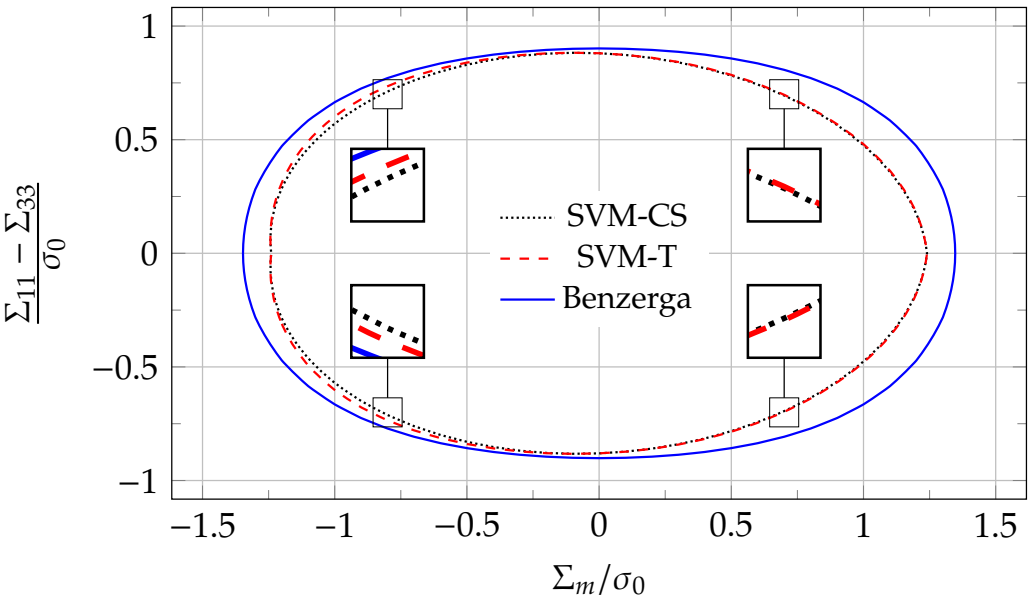

(b) porosity p=0.1

Figure 3.2: Hill matrix: comparaison of the yield surfaces given by the proposed new criteria given by eq (3.30) and eq(3.37) and that proposed by Benzerga and Besson (2001)

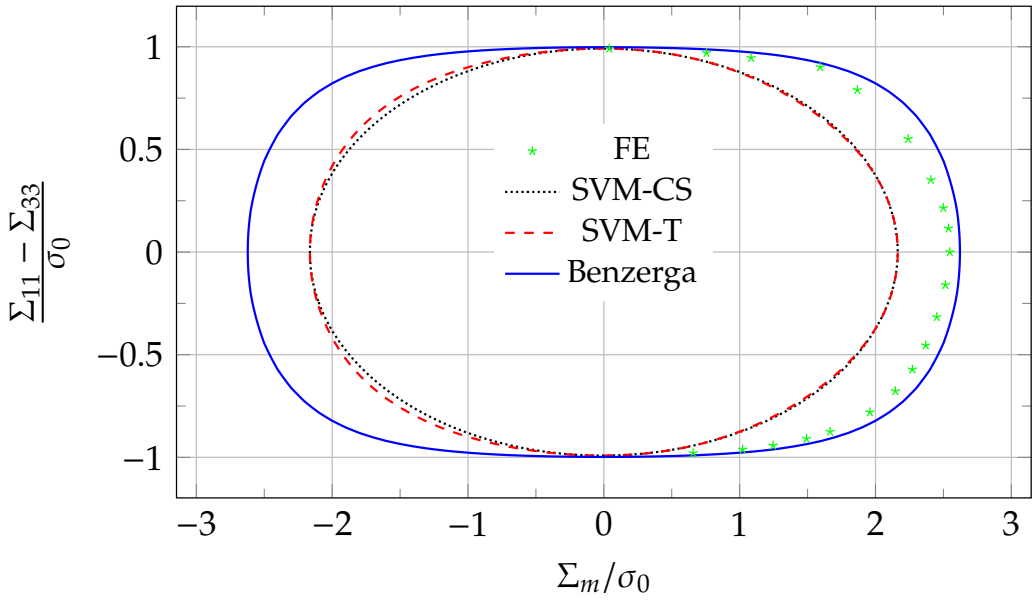

(a) porosity p=0.01

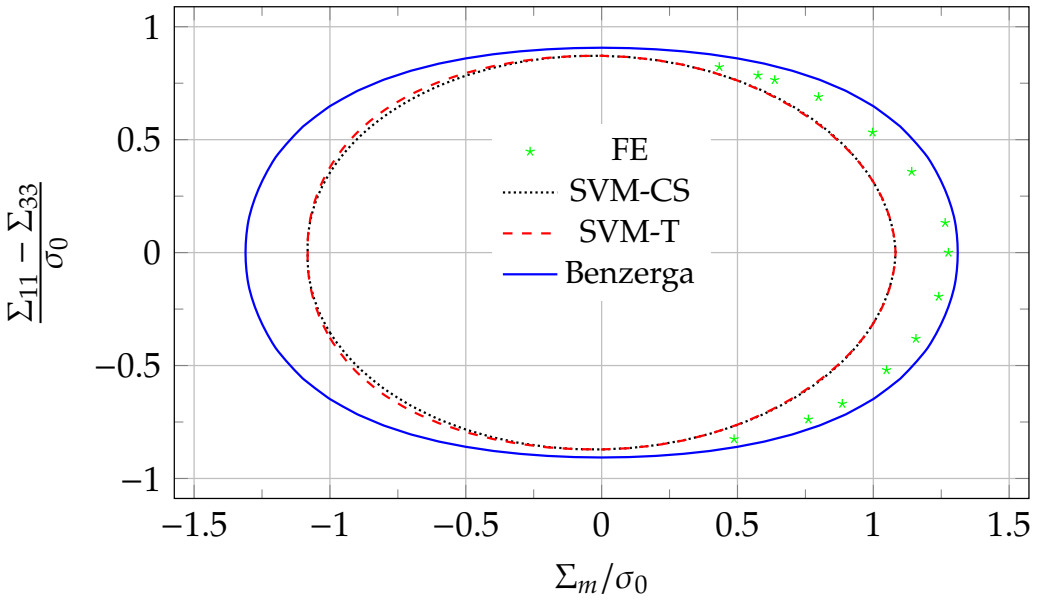

(b) porosity p=0.1

Figure 3.3: Hill matrix: comparaison of the yield surfaces given by the proposed new criterions eq(3.37)and eq(3.30) and by FE Morin et al. (2014)

conic programming problems[10]. In Fig 3.4 the yield surfaces projected in the plane $(\Sigma_{11}-\Sigma_{33}, \Sigma_m)$ corresponding to the established criteria (3.30) and (3.37) are compared to the bounds given by the static and kinematic codes from Pastor et al. (2012). In all quadrants, the theoretical criteria predict a macroscopic yield envelope inside the numerical lower bound. The discrepancy observed between the analytical model and the numerical results is probably due to the isotropic character of the used stress field which does not incorporate the anisotropy of the matrix. In particular, for hydrostatic loadings, the model does not predict the exact solution which can be estimated from the numerical upper and lower bounds. However, the accuracy is quite satisfactory when the stress triaxiality is low or moderate.
In summary, the assessment of the proposed model can be considered successful; moreover it must be emphasized that, to the best of our knowledge, it is the first criterion which accounts for the effect of the sign of J_3 in a context of ductile porous materials with an anisotropic matrix.

3.6 Plastic flow rule and void growth

The macroscopic plastic flow rule is obtained from the normality law already presented in (3.14). The macroscopic mean and deviatoric parts of the plastic deformation are readily obtained in the form :

$$\begin{aligned} D_m &= \frac{1}{3}\dot{\lambda}\frac{\partial F}{\partial \Sigma_m} = \frac{\dot{\lambda}}{6}\frac{\dfrac{18\beta}{(\ln p)^2}\dfrac{\Sigma_m}{\sigma_0^2} - \dfrac{3\Sigma_e\gamma\,\mathrm{sign}(J_3)}{\sigma_0^2\sqrt{3/2(F+G)}\ln p}}{A(\boldsymbol{\Sigma})}, \\ D_e &= \dot{\lambda}\frac{\partial F}{\partial \Sigma_e} = \frac{\dot{\lambda}}{2}\frac{\dfrac{2\alpha}{3/2(F+G)}\dfrac{\Sigma_e}{\sigma_0^2} - \dfrac{3\Sigma_m\gamma\,\mathrm{sign}(J_3)}{\sigma_0^2\sqrt{3/2(F+G)}\ln p}}{A(\boldsymbol{\Sigma})} \end{aligned} \tag{3.40}$$

in which have been introduced the following scalar quantity:

$$A(\boldsymbol{\Sigma}) = \sqrt{\frac{\alpha}{\frac{3}{2}(F+G)}\left(\frac{\Sigma_e}{\sigma_0}\right)^2 - \frac{3\gamma\,\mathrm{sign}(J_3)}{\sqrt{\frac{3}{2}(F+G)}\ln p}\frac{\Sigma_e}{\sigma_0}\frac{\Sigma_m}{\sigma_0} + 9\frac{\beta}{(\ln p)^2}\left(\frac{\Sigma_m}{\sigma_0}\right)^2}$$

Similarly, considering the macroscopic criterion obtained by Taylor series expansion (3.37), the corresponding macroscopic strain rates take the form:

$$\begin{aligned} D_m = \frac{1}{3}\dot{\lambda}\Bigg[&\frac{\partial D}{\partial \Sigma_m} + \frac{\gamma}{2}\mathrm{sign}(J_3)\left(\frac{\dfrac{\partial C}{\partial \Sigma_m}D - \dfrac{\partial D}{\partial \Sigma_m}C}{D^2}\right) - \frac{\xi}{8}\left(\frac{\dfrac{2CD\partial C}{\partial \Sigma_m} - 3C^2\dfrac{\partial D}{\partial \Sigma_m}}{D^4}\right) \\ &+ \frac{\chi}{16}\mathrm{sign}(J_3)\left(\frac{3DC^2\dfrac{\partial C}{\partial \Sigma_m} - 5C^3\dfrac{\partial D}{\partial \Sigma_m}}{D^8}\right)\Bigg] \end{aligned} \tag{3.41}$$

[10]The readers interested by this original numerical approach and its application to various porous materials can refer to Pastor et al. (2013).

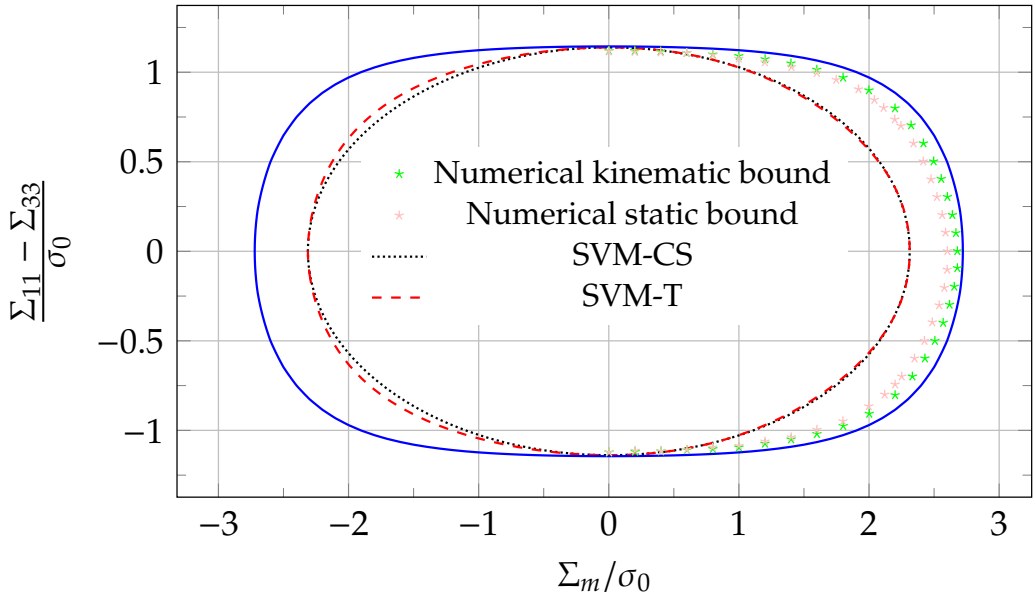

(a) porosity p=0.01

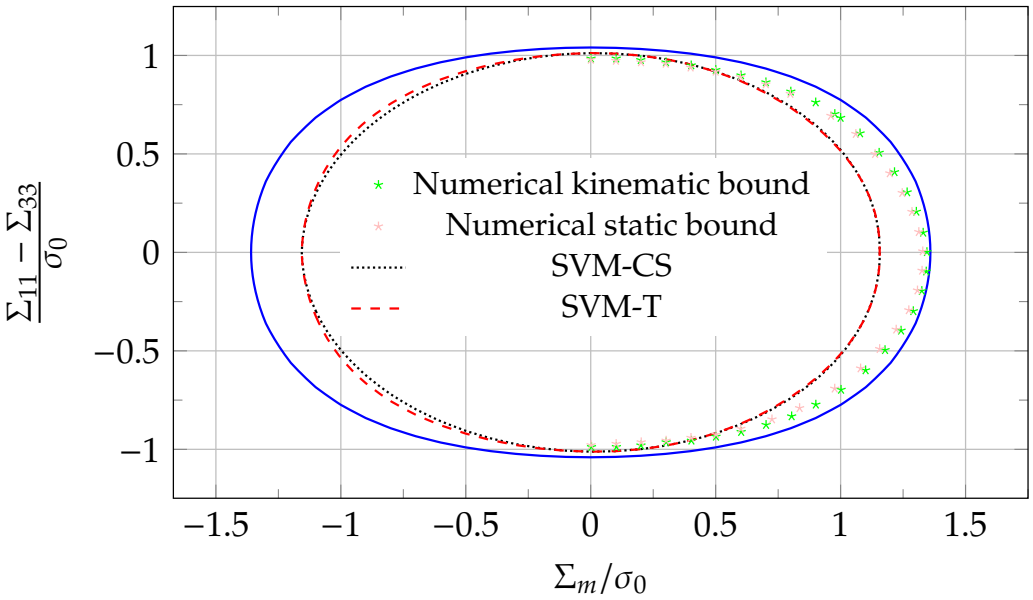

(b) porosity p=0.1

Figure 3.4: Comparison of the yield surfaces obtained from the established criteria (3.30) and (3.37) with numerical upper and lower bounds given by Pastor et al. (2012), porosity $p = 0.01$ and $p = 0.1$

$$D_e = \dot{\lambda}\Big[\frac{\partial D}{\partial \Sigma_e} + \frac{\gamma}{2}\text{sign}(J_3)(\frac{\frac{\partial C}{\partial \Sigma_e}D - \frac{\partial D}{\partial \Sigma_e}C}{D^2}) - \frac{\xi}{8}(\frac{\frac{2CD\partial C}{\partial \Sigma_e} - 3C^2\frac{\partial D}{\partial \Sigma_e}}{D^4}) + \frac{\chi}{16}\text{sign}(J_3)(\frac{3DC^2\frac{\partial C}{\partial \Sigma_e} - 5C^3\frac{\partial D}{\partial \Sigma_e}}{D^8}) \Big] \tag{3.42}$$

in which have been introduced the following scalar quantities:

$$\begin{aligned} &D(\boldsymbol{\Sigma}) = \sqrt{\alpha\tilde{\Sigma}_e^2 + \beta\tilde{\Sigma}_m^2} = \sqrt{\alpha(\frac{\Sigma_e}{\sqrt{3/2(F+G)}})^2 + \beta(-\frac{3\Sigma_m}{\ln p})^2}\,, \\ &\frac{\partial D}{\partial \Sigma_e} = \frac{\alpha\Sigma_e}{3/2(F+G)D}\,,\ \frac{\partial D}{\partial \Sigma_m} = \frac{9\beta\Sigma_m}{(\ln p)^2 D}, \\ &C(\boldsymbol{\Sigma}) = \tilde{\Sigma}_e\tilde{\Sigma}_m = -\frac{3\Sigma_m}{\ln p}\frac{\Sigma_e}{\sqrt{3/2(F+G)}}\,, \\ &\frac{\partial C}{\partial \Sigma_e} = -\frac{3\Sigma_m}{\ln p}\frac{1}{\sqrt{3/2(F+G)}}\,,\ \frac{\partial C}{\partial \Sigma_m} = -\frac{3}{\ln p}\frac{\Sigma_e}{\sqrt{3/2(F+G)}}. \end{aligned} \tag{3.43}$$

Owing to the plastic incompressibility of the matrix, the porosity evolution is obtained from the mass balance equation, as in the case of the Gurson model:

$$\dot{p} = 3(1-p)D_m \tag{3.44}$$

The difference with the predictions of the Gurson model obviously lies in the dependence of D_m not only on the stress triaxiality but also on the characteristics of the anisotropic matrix as well as on the sign of the third stress invariant. Figs 3.5, 3.6, 3.7 and 3.8 illustrate the normalized evolution of porosity given as function of stress triaxiality for initial porosity $p = 0.01$ and different parameters of anisotropy. We consider the range [0..4] for T which corresponds to stress triaxiality levels for most commonly specimens used in ductile fracture experiments Benzerga and Leblond (2010). For completeness, these figures also include the predictions of Gurson (1977) for the isotropic case and those of Benzerga and Besson (2001) model. The effect of the sign of the third invariant coupled to anisotropy parameters is much more pronounced for the porosity evolution than for the macroscopic criterion.

3.7 Conclusion

In this chapter, we presented a new macroscopic yield criterion for plastic anisotropic materials obeying Hill's quadratic criterion and containing spherical voids. Specifically, this criterion is derived by generalizing to an anisotropic matrix the statical limit analysis approach recently proposed by Cheng et al. (2014) for von Mises matrix. For the derivation of the macroscopic criterion, an appropriate statically admissible trial stress field has been considered. The obtained criteria are clearly impacted by the matrix anisotropy. A second interesting feature of the criterion obtained by a Taylor Series expansion is its dependence on the sign of the third invariant of the stress deviator, J_3, as well as on the two stress invariants Σ_m and Σ_e (Hill's equivalent stress). The criterion has been compared

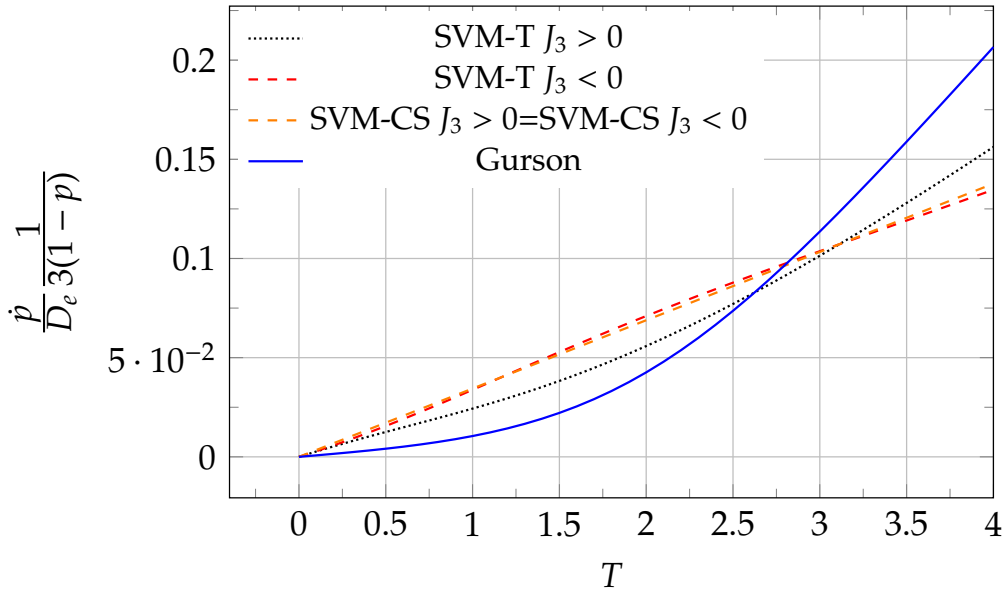

Figure 3.5: Evolution of porosity as function of the stress triaxiality for an isotropic matrix and for initial porosity p=0.01.

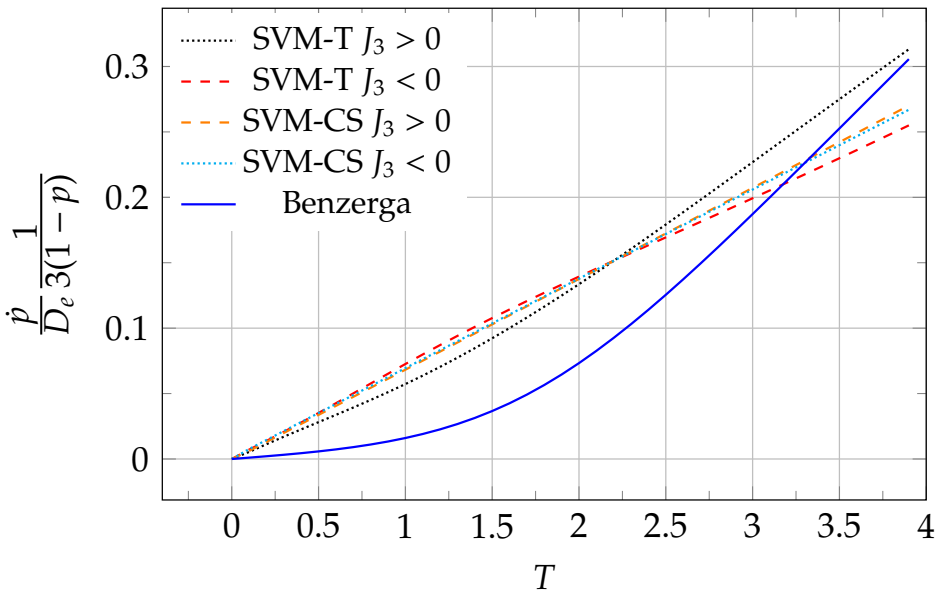

Figure 3.6: Evolution of porosity as function of the stress triaxiality for matrix parameters Set 2 in table 3.1 and for initial porosity p=0.01.

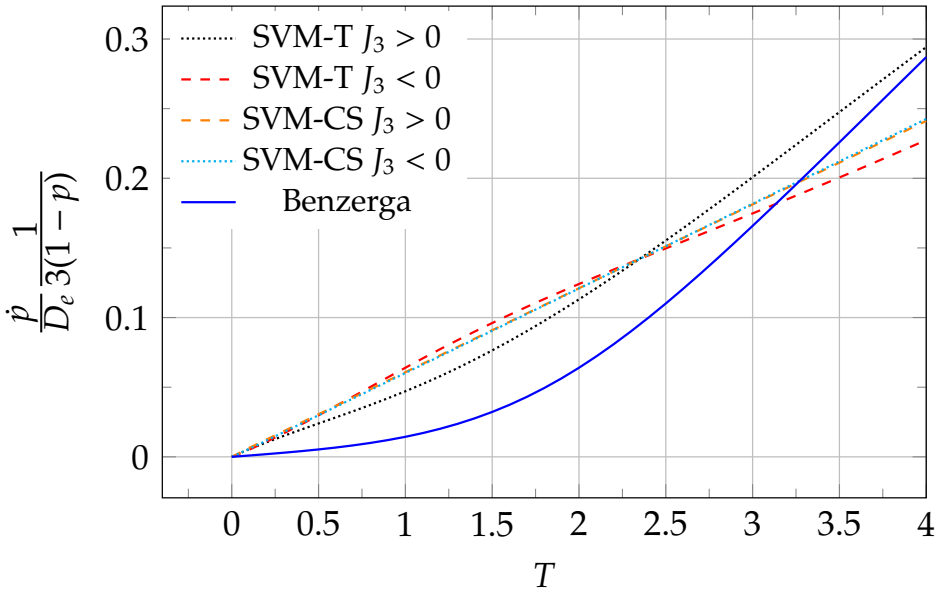

Figure 3.7: Evolution of porosity as function of the stress triaxiality for matrix parameters Set 3 in table 3.1 and for initial porosity p=0.01.

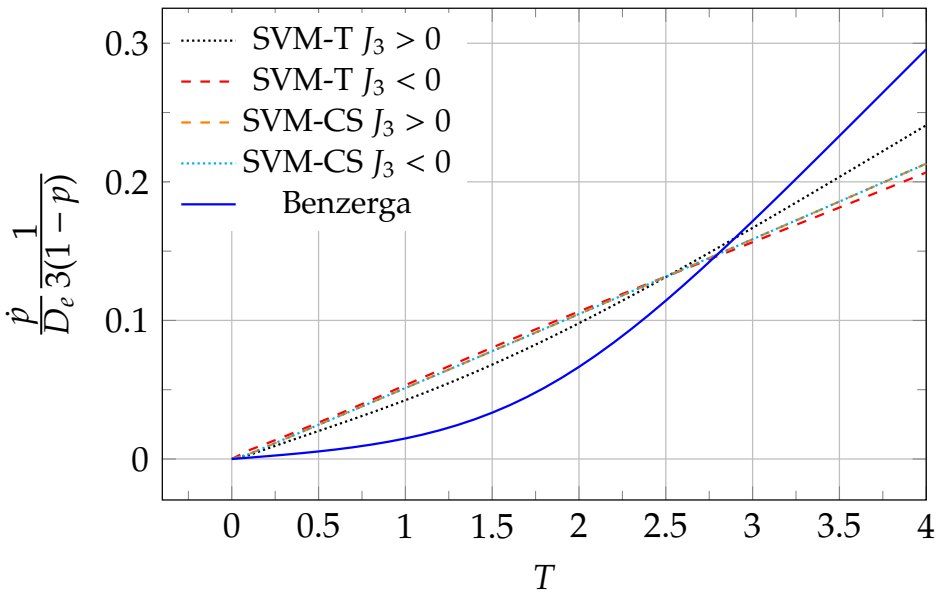

Figure 3.8: Evolution of porosity as function of the stress triaxiality for matrix parameters Set 1 in table 3.1 and for initial porosity p=0.01.

successfully to its theoretical kinematic counterpart proposed by Benzerga and Besson (2001) , to numerical data given by Pastor et al. (2012) and to recent FE results of Morin et al. (2014). For completeness, we also provided the plastic strain rate equations and the void evolution law derived from the new criterion. It turns out that the effect of the sign of J_3 is more pronounced on the porosity evolution.

CHAPTER 4

Composite materials at finite strains

Summary

This chapter presents two extensions of mean-field homogenization (MFH) formulations to the finite deformations. Both phases obey a finite strain elasto-plasticity model based on a multiplicative decomposition of the deformation gradient and hyperelastic constitutive equations. The two proposed formulations rely on the definition of a Linear Comparison Composite (LCC). In the first part, an incremental approach is presented which is based on a rate formulation of the constitutive equations Doghri et al. (2016). In the second formulation El Ghezal et al. (in preparation), we built on the incremental-secant MFH scheme of Wu et al. (2013a) initially formulated for infinitesimal strains. The corresponding numerical algorithms are presented and numerical simulations of different composite microstructures are verified against full-field finite element computations.

keywords

finite strain; MFH; incremental tangent scheme; incremental secant scheme; inhomogeneous materials; elastic-plastic materials; numerical algorithms.

The first formulation presented in this chapter is adapted from the published research paper Doghri et al. (2016).
The second formulation is the subject of the working paper El Ghezal et al. (in preparation).
A self-consistent notation is adopted.

4.1 Introduction

The prediction of the influence of the microstructure on the macroscopic or effective properties of heterogeneous materials is important both from scientific and engineering design viewpoints, and the aim of scale-transition methods is to understand and quantify this influence. In continuum mechanics, those methods rely on a separation of scales and belong to one of four categories (see for instance the reviews of Kanouté et al. (2009) and Geers et al. (2010) for references). First, there is the direct finite element (FE) analysis of representative volume elements (RVEs). Second, in the method of cells and subcells (which is related to the transformation field analysis), the RVE or unit cell is discretized with voxels (or pixels in 2D), and the boundary-value problem is solved using different approaches. Third, there is the asymptotic or mathematical theory of homogenization for periodic media, which ends up with problems on a unit cell which need to be solved with FE or voxel methods. The fourth and last category is mean-field homogenization (MFH) which is restricted to microstructures such that multiple phases of solid inclusions or cavities which are supposed to have an ellipsoidal shape are embedded in a continuum matrix. MFH is based on assumed relations between the mean values (volume averages) of strain or stress fields in each phase, and unlike the former three methods, it is not direct and it does not solve for the detailed micro fields. Compared to the three direct full-field methods, MFH is more restricted both in terms of microstructures that it can handle and the results it can deliver, however it is much easier to use and its computing time is several orders of magnitude smaller than that of direct scale-bridging methods, especially in the nonlinear regime.

MFH methods are based on the fundamental linear elastic solution developed by Eshelby (1957) for an ellipsoidal subdomain of an infinite matrix undergoing a uniform eigen or transformation strain. In linear elasticity, successful MFH models have been developed based on an approximate use of Eshelby's solution, typical examples being the Mori and Tanaka (1973) model and the self-consistent scheme (Kröner (1958); Hill (1965a)).

A significant research effort has been devoted to extending MFH to the nonlinear regime. The major difficulty is that for nonlinear composites, even if each phase's material is homogeneous, the instantaneous stiffness operators are not uniform per phase. Consequently, Eshelby's results and MFH models cannot be extended directly from linear elasticity to the nonlinear realm, and in order to circumvent this difficulty, several methods each based on its own assumptions and approximations have been proposed. The unifying feature of those methods is the definition of a linear comparison composite (LCC) whose response approximates that of the nonlinear composite. Recent research trends focus on achieving two goals. First, for history-dependent materials, be able to simulate general non-monotonic and non-radial loading histories. Second, construct LCCs where besides mean field values, field fluctuations are taken into account, typically via per-phase second statistical moments (which measure the variance). Such recent proposals for small strain elasto(visco)plastic composites include the incremental variational formulations of Brassart et al. (2011), Brassart et al. (2012) and Lahellec and Suquet (2013), the second-moment incremental tangent formulation of Doghri et al. (2011) and the second-moment incremental-secant formulation of Wu et al. (2015).

For finite strain elasto(visco)plastic heterogeneous materials, most MFH methods rely on local (micro) constitutive models which are based on the following two classical assumptions:

$$\boldsymbol{d} = \boldsymbol{d}^e + \boldsymbol{d}^p, \quad \overset{\nabla}{\boldsymbol{\tau}} = \boldsymbol{c}^e : \boldsymbol{d}^e, \tag{4.1}$$

i.e., an additive decomposition of the rate of deformation tensor $\boldsymbol{d}$ onto elastic and inelastic parts, and a hypoelastic stress-strain relation, where $\overset{\nabla}{\boldsymbol{\tau}}$ is an objective rate of the Kirchhoff stress $\boldsymbol{\tau}$ (e.g., Jaumann's, Green-Naghdi-Mc Innis, Lie, etc.) Representative MFH proposals based on eq. (4.1) include, for polycrystalline metals: Nemat-Nasser and Obata (1986) and Segurado et al. (2012), for porous materials: Danas and Aravas (2012) and Aravas and Ponte Castañeda (2004), for solid propellants: Xu et al. (2008) and for metal-matrix composites: Pettermann et al. (2010).

It is well known that assumptions (4.1) are acceptable if the elastic strains are small, which is typical of metals. However, this is not the case for polymer materials, for which a better formulation is based on the following assumptions:

$$\boldsymbol{F} = \boldsymbol{F}^e \cdot \boldsymbol{F}^p, \quad \boldsymbol{\tau} = 2\frac{\partial \psi}{\partial \boldsymbol{b}^e} \cdot \boldsymbol{b}^e, \tag{4.2}$$

i.e. a multiplicative decomposition of the deformation gradient $\boldsymbol{F}$ onto elastic and inelastic parts, and a hyperelastic stress strain relation between the Kirchhoff stress $\boldsymbol{\tau}$ and the elastic left Cauchy-Green strain $\boldsymbol{b}^e = \boldsymbol{F}^e \cdot (\boldsymbol{F}^e)^T$, derived from a specific free energy per unit reference volume ψ. Unless the elastic strains are small, eq. (4.1-a) cannot be deduced and is not compatible with eq. (4.2-a), see for instance Vladimirov et al. (2010). For heterogeneous materials with hyperelastic-viscoplastic constituents obeying to eqs.4.2, direct full-field homogenization methods have been proposed, e.g. Miehe et al. (1999) and Matous and Maniatty (2009) for polycrystals. However, the literature seems to lack finite strain MFH methods (e.g. extended Mori-Tanaka or self-consistent schemes) which are based locally on eqs.4.2.

For finite strain hyperelastic composites, several MFH formulations based on variational formulations and including field fluctuations have been proposed over the years by Ponte Castañeda, Suquet and their co-workers, reaching a high degree of accuracy, see for instance Ponte Castañeda and Tiberio (2000), Ponte Castañeda and Suquet (2002), Ponte Castañeda (2002) and Idiart et al. (2006).

The present chapter is concerned with the finite strain MFH of a class of composites where multiple phases of solid inclusions or cavities are embedded in a continuum matrix. Each solid phase obeys a hyperelastic-plastic material model built on the basic assumptions of eq.(4.2). We present two extensions of MFH formulation to the nonlinear regime and the corresponding numerical algorithms were developed and implemented for an extended Mori-Tanaka MFH model.

The first formulation builds on the earlier finite strain homogenization framework of Nemat-Nasser (1999). The latter showed how to generalize Eshelby's results as well as MFH schemes, provided that we consider tangent operators which are uniform per phase. This first formulation was implemented in the DIGIMAT software (Digimat (2014)) and extensively tested against direct FE simulations of unit cells and representative volume elements. Several numerical simulations will be presented.

However, one of the limitations of the incremental tangent method under small strains is its lack of accuracy for materials exhibiting strain softening. As explained in Wu et al. (2013b), for composites with elastic fibers and elasto-plasticity coupled with damage in the matrix phase, inclusions should see an elastic unloading during the softening stage. This motivated us to develop a second approach since in large deformations, the nominal stress (the transpose of the First Piola-Kirchhoff stress) can decrease with increasing strain, and even the true (Cauchy) stress can also (as for polymers). Therefore, in the second formulation we built on the incremental-secant MFH scheme of Wu et al. (2013a) initially formulated for infinitesimal strains. This homogenization scheme allows to evaluate the residual stress and strain states in each phase by applying a fictitious elastic unloading step. The LCC is then subjected to a strain increment deduced from the residual state. The idea behind this new formulation is to reformulate the finite strain problem in a similar way to the infinitesimal one involving logarithmic strains and Khirchhoff stresses.

The chapter is organized as follows. Sections 4.2 and 4.3 are common to the two formulations and present some basic results needed in all further developments. The incremental tangent formulation is considered in Section 4.4, wheras the second approach based on the incremental secant formulation is presented in Section 4.5. Along the chapter, Several numerical MFH predictions and their verification against direct FE simulations of RVEs or unit cells are presented and discussed.

Acronyms: FE : finite element, MF: mean-field, MFH: MF homogenization, RVE: representative volume element, VWT: virtual work theorem.

4.2 Kinematics of large deformations

In this section, we summarize some basic results needed in the remainder of this chapter. Throughout, boldface symbols designate tensors, the order of which is indicated by the context. Inner products over one and two indices are symbolized by a dot and a colon, resp. The summation convention over repeated indices is used unless indicated otherwise. The tensor (dyadic) product is designated by the symbol $\otimes$.

A solid body, which in this chapter designates a representative volume element (RVE) or a part of it, occupies a domain Ω_0 (boundary $\partial\Omega_0$) in the reference configuration and a domain ω_t (boundary $\partial\omega_t$) in the current configuration at time $t > 0$. A fixed Cartesian frame is considered. A material particle is determined by its position vectors $\boldsymbol{X}$ and $\boldsymbol{x}$ with respect to (w.r.t.) Ω_0 and ω_t so that for a motion $\boldsymbol{\varphi}(\boldsymbol{X}, t)$, we have:

$$\boldsymbol{x} = \boldsymbol{\varphi}(\boldsymbol{X}, t); \quad \boldsymbol{X} = (X_A); \quad \boldsymbol{x} = (x_i); \quad A, i = 1, 2, 3 \tag{4.3}$$

The convention of upper case indices for X_A and lower case for x_i will be used throughout.

A superposed dot designates a material time derivative. For instance, if the same field is expressed as: $\boldsymbol{K}(\boldsymbol{X}, t) = \boldsymbol{k}(\boldsymbol{x}, t)$, then its material time derivative is:

$$\dot{\boldsymbol{K}}(\boldsymbol{X}, t) = \frac{\partial \boldsymbol{K}}{\partial t}(\boldsymbol{X}, t) = \dot{\boldsymbol{k}}(\boldsymbol{x}, t) = \frac{\partial \boldsymbol{k}}{\partial t}(\boldsymbol{x}, t) + (\nabla \boldsymbol{k}) \cdot \boldsymbol{v}(\boldsymbol{x}, t), \tag{4.4}$$

where $\boldsymbol{v}(\boldsymbol{x}, t) = \dot{\boldsymbol{x}}$ is the velocity field, and $\nabla = \partial/\partial \boldsymbol{x}$. The velocity gradient is $\boldsymbol{l} = \nabla \boldsymbol{v}$, and its symmetric part is $\boldsymbol{d}$. In component form: $\boldsymbol{l} = (l_{ij})$ and $\boldsymbol{d} = (d_{ij})$ with $d_{ij} = d_{ji}$.

The deformation gradient and its determinant are defined as follows:

$$\boldsymbol{F}(\boldsymbol{X},t) = \frac{\partial \boldsymbol{x}}{\partial \boldsymbol{X}} \equiv \text{GRAD}\,\boldsymbol{x}, \quad J(\boldsymbol{X},t) = \det \boldsymbol{F}(\boldsymbol{X},t) \tag{4.5}$$

From $\boldsymbol{F}$, the right ($\boldsymbol{C}$) and left ($\boldsymbol{b}$) Cauchy-Green strain tensors are computed:

$$\boldsymbol{C} = \boldsymbol{F}^T \cdot \boldsymbol{F}; \quad \boldsymbol{b} = \boldsymbol{F} \cdot \boldsymbol{F}^T \tag{4.6}$$

Both tensors are symmetric: $C_{AB} = C_{BA}$ and $b_{ij} = b_{ji}$.

Different stress measures are needed: the first Piola-Kirchhoff (P-K) stress $\boldsymbol{P} = (P_{iA})$, whose transpose is the nominal stress $\boldsymbol{P}^n = \boldsymbol{P}^T$, the second P-K stress: $\boldsymbol{S} = (S_{AB})$, the Cauchy (true) stress: $\boldsymbol{\sigma} = (\sigma_{ij})$ and the Kirchhoff stress: $\boldsymbol{\tau} = (\tau_{ij})$. Stresses $\boldsymbol{S}$, $\boldsymbol{\sigma}$ and $\boldsymbol{\tau}$ are symmetric. The stress power per unit reference volume takes the equivalent expressions:

$$\boldsymbol{\tau} : \boldsymbol{d} = \boldsymbol{P}^n : \dot{\boldsymbol{F}} = \boldsymbol{S} : \frac{\dot{\boldsymbol{C}}}{2} \tag{4.7}$$

The following relations between the different stress measures hold:

$$\boldsymbol{P} = \boldsymbol{F} \cdot \boldsymbol{S}, \quad \boldsymbol{\tau} = J\boldsymbol{\sigma} = \boldsymbol{P} \cdot \boldsymbol{F}^T = \boldsymbol{F} \cdot \boldsymbol{P}^T = \boldsymbol{F} \cdot \boldsymbol{S} \cdot \boldsymbol{F}^T \tag{4.8}$$

4.3 Hyperelastic-plastic constituents

For homogeneous finite strain elasto(visco)plastic materials, there exists a formulation which is based on a multiplicative decomposition of the deformation gradient onto elastic and inelastic parts, and on hyperelastic stress-strain response. Although rather complicated, the formulation presents important advantages as compared to a more classical approach based on an additive decomposition of the rate of deformation tensor and on hypoelasticity. Indeed, the former is not restricted to small elastic strains (which makes it suitable for polymers), the hyperelastic stress-strain relation and the flow rule are derived from thermodynamic considerations, and there is no need to choose one objective stress rate over another (Jaumann, Green-Naghdi-Mc Innis, etc.) The following summary follows Simo (1992); see also Sect. 16.1 in Doghri (2000) for instance.

The multiplicative decomposition of $\boldsymbol{F}$ into elastic ($\boldsymbol{F}^e$) and inelastic ($\boldsymbol{F}^p$) parts reads (Fig. 4.1 presents a schematic illustration):

$$\boldsymbol{F}(\boldsymbol{X},t) = \boldsymbol{F}^e(\boldsymbol{X},t) \cdot \boldsymbol{F}^p(\boldsymbol{X},t) \tag{4.9}$$

Elastic left ($\boldsymbol{b}^e$) and plastic right ($\boldsymbol{C}^p$) Cauchy-Green strain tensors are defined as follows:

$$\boldsymbol{b}^e = \boldsymbol{F}^e \cdot \boldsymbol{F}^{eT}; \quad \boldsymbol{C}^p = \boldsymbol{F}^{pT} \cdot \boldsymbol{F}^p \tag{4.10}$$

It follows from the multiplicative decomposition (4.9)that:

$$\boldsymbol{b}^e = \boldsymbol{F} \cdot \boldsymbol{C}^{p^{-1}} \cdot \boldsymbol{F}^T \tag{4.11}$$

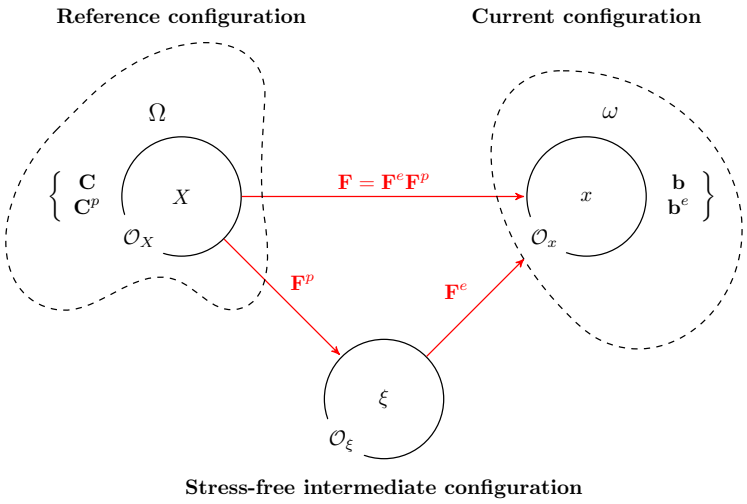

Figure 4.1: The multiplicative decomposition of the deformation gradient: $F^{e^{-1}}$ is interpreted as the local deformation that releases the stresses from each neighborhood O_x in the current configuration. Strain tensors associated with the reference or current configurations are schematically indicated.

For isotropic materials, there exists a specific free energy per unit reference volume $\psi(\boldsymbol{b}^e, \xi)$ which is an isotropic function of $\boldsymbol{b}^e$ and of an internal scalar variable ξ. The equations of state read:

$$\boldsymbol{\tau} = 2\frac{\partial \psi}{\partial \boldsymbol{b}^e} \cdot \boldsymbol{b}^e; \quad q \equiv \frac{\partial \psi}{\partial \xi} \tag{4.12}$$

The first equation is a hyperelastic relation between the Kirchhoff stress $\boldsymbol{\tau}$ and $\boldsymbol{b}^e$, while q is the thermodynamic force associated with ξ (typically, q is a hardening stress). The Clausis-Duhem inequality requiring the dissipation to be non-negative reads:

$$\mathcal{D} = \boldsymbol{\tau} : (-\frac{1}{2} \overset{L}{\boldsymbol{b}^e} \cdot \boldsymbol{b}^{e-1}) - q\dot{\xi} \geq 0 \tag{4.13}$$

where $\overset{L}{\boldsymbol{b}^e}$ is the Lie derivative of $\boldsymbol{b}^e$ and defined as :

$$\overset{L}{\boldsymbol{b}^e} = \dot{\boldsymbol{b}}^e - \boldsymbol{l} \cdot \boldsymbol{b}^e - \boldsymbol{b}^e \cdot \boldsymbol{l}^T \tag{4.14}$$

It is shown that the flow rules are:

$$-\frac{1}{2} \overset{L}{\boldsymbol{b}^e} \cdot \boldsymbol{b}^{e-1} = \dot{\gamma}\frac{\partial f}{\partial \boldsymbol{\tau}}(\boldsymbol{\tau}, q); \quad \dot{\xi} = -\dot{\gamma}\frac{\partial f}{\partial q}(\boldsymbol{\tau}, q); \tag{4.15}$$

where $f(\boldsymbol{\tau}, q)$ is an isotropic yield function. It is important to notice that what plays the role of "plastic strain rate" tensor in the theory is the left-hand-side of eq.(4.15-a), which can be rewritten as follows:

$$-\frac{1}{2} \overset{L}{\boldsymbol{b}^e} \cdot \boldsymbol{b}^{e-1} = \frac{1}{2}\boldsymbol{F} \cdot \boldsymbol{C}^{p-1} \cdot \dot{\boldsymbol{C}}^p \cdot \boldsymbol{F}^{-1} \tag{4.16}$$

For rate-independent hyperelastic-plastic models, the following conditions hold:

$$f(\boldsymbol{\tau}, q) \leq 0; \quad \dot{\gamma} \geq 0; \quad \dot{\gamma} f(\boldsymbol{\tau}, q) = 0 \tag{4.17}$$

The theory also applies to rate-dependent hyperelastic-viscoplastic models, with:

$$\dot{\gamma} \geq 0, \quad \dot{\gamma} > 0 \text{ if } f > 0, \dot{\gamma} = 0 \text{ if } f \leq 0, \tag{4.18}$$

where f is then seen as a viscous stress and $\dot{\gamma}$ a viscoplastic function.

4.4 Composites with hyperelastic-plastic constituents-Part I: An incremental tangent formulation

4.4.1 Mean-field homogenization (MFH)

A representative volume element (RVE) of the heterogeneous material occupies domains Ω_0 and ω_t in the reference and current configurations, respectively, with boundaries $\partial\Omega_0$ and $\partial\omega_t$. Consider the case of linear boundary displacements and velocities:

$$\boldsymbol{x} = \boldsymbol{F}^0 \cdot \boldsymbol{X}, \quad \dot{\boldsymbol{x}} = \dot{\boldsymbol{F}}^0 \cdot \boldsymbol{X}, \quad \boldsymbol{X} \in \partial\Omega_0 \tag{4.19}$$

with $\boldsymbol{F}^0$ and $\dot{\boldsymbol{F}}^0$ uniform on $\partial\Omega_0$. The following volume averaging results are found (e.g., Nemat-Nasser (1999))

$$< \boldsymbol{F} >_{\Omega_0} = \boldsymbol{F}^0, \quad < \dot{\boldsymbol{F}} >_{\Omega_0} = \dot{\boldsymbol{F}}^0 \tag{4.20}$$

Consider now the case of uniform boundary traction and traction rates:

$$\boldsymbol{T} = \boldsymbol{P}^0 \cdot \boldsymbol{N}, \quad \dot{\boldsymbol{T}} = \dot{\boldsymbol{P}}^0 \cdot \boldsymbol{N}, \quad \boldsymbol{X} \in \partial\Omega_0 \tag{4.21}$$

with $\boldsymbol{P}^0$ and $\dot{\boldsymbol{P}}^0$ uniform on $\partial\Omega_0$, and unit vector $\boldsymbol{N}$ the outer normal to $\partial\Omega_0$. The following stress averaging results hold (e.g., Nemat-Nasser (1999)):

$$< \boldsymbol{P}^n >_{\Omega_0} = \boldsymbol{P}^{0^T}, \quad < \dot{\boldsymbol{P}}^n >_{\Omega_0} = \dot{\boldsymbol{P}}^{0^T} \tag{4.22}$$

Let us consider a two-phase RVE, with a matrix and identical and aligned inclusions. Subscripts M and I designate the matrix and inclusion phases, resp., and $\alpha = M, I$. The initial volume fractions are f_{0_M} and $f_{0_I} = 1 - f_{0_M}$. The reference volume averages of the deformation gradients over each phase and the RVE are designated by $\boldsymbol{F}_\alpha(t)$ and $\boldsymbol{F}_{mac}(t)$, resp., so that:

$$\boldsymbol{F}_\alpha(t) \equiv < \boldsymbol{F}(\boldsymbol{X}, t) >_{\Omega_{0_\alpha}}, \quad \boldsymbol{F}_{mac}(t) \equiv < \boldsymbol{F}(\boldsymbol{X}, t) >_{\Omega_0} = \sum_\alpha f_{0_\alpha} \boldsymbol{F}_\alpha(t) \tag{4.23}$$

Consider rate-independent local material models which can be written in the following rate form:

$$\dot{\boldsymbol{P}}^n(\boldsymbol{X}, t) = \boldsymbol{\mathcal{A}}(\boldsymbol{X}, t) : \dot{\boldsymbol{F}}(\boldsymbol{X}, t) \tag{4.24}$$

where $\boldsymbol{\mathcal{A}} = (\mathcal{A}_{AiBj})$ is a so-called "nominal" tangent operator which possesses the major (diagonal) symmetries: $\mathcal{A}_{AiBj} = \mathcal{A}_{BjAi}$. For the homogenization of finite-strain rate-independent heterogeneous materials, a so-called incremental formulation was proposed by Hill (1970), Hill (1972), Hill (1984) and later completed and extended by Nemat-Nasser (1999). Accordingly, a linear comparison composite (LCC) is defined based on the association with each phase of a fictitious medium whose tangent operator is uniform,

$$\dot{\boldsymbol{P}}^n(\boldsymbol{X}, t) = \boldsymbol{\mathcal{A}}_\alpha(t) : \dot{\boldsymbol{F}}(\boldsymbol{X}, t); \ \boldsymbol{X} \in \Omega_{0_\alpha} \tag{4.25}$$

So-called strain rate concentration tensors $\boldsymbol{B}^\varepsilon$ and $\boldsymbol{A}^\varepsilon$ are defined as follows:

$$\dot{\boldsymbol{F}}_I(t) = \boldsymbol{B}^\varepsilon(t) : \dot{\boldsymbol{F}}_M(t) = \boldsymbol{A}^\varepsilon(t) : \dot{\boldsymbol{F}}_{mac}(t) \tag{4.26}$$

Tensors $\boldsymbol{B}^\varepsilon$ and $\boldsymbol{A}^\varepsilon$ are related:

$$\boldsymbol{A}^\varepsilon = \boldsymbol{B}^\varepsilon : \left[f_{0_I} \boldsymbol{B}^\varepsilon + (1 - f_{0_I}) \boldsymbol{\mathcal{I}} \right]^{-1} \tag{4.27}$$

where the fourth-rank identity tensor $\boldsymbol{\mathcal{I}}$ is non-symmetric and defined as follows using Kronecker's delta:

$$\boldsymbol{\mathcal{I}}_{iABj} = \delta_{ij}\delta_{AB} \quad \text{or} \quad \boldsymbol{\mathcal{I}}_{AijB} = \delta_{ij}\delta_{AB} \tag{4.28}$$

It is then possible to find a macro nominal tangent operator $\boldsymbol{\mathcal{A}}_{mac}(t)$ such that:

$$< \dot{\boldsymbol{P}}^n(\boldsymbol{X}, t) >_{\Omega_0} = \boldsymbol{\mathcal{A}}_{mac}(t) :< \dot{\boldsymbol{F}}(\boldsymbol{X}, t) >_{\Omega_0}, \ \text{i.e.} \ < \dot{P}^n_{Ai} >_{\Omega_0} = (\mathcal{A}_{mac})_{AiBj} < \dot{F}_{jB} >_{\Omega_0} \tag{4.29}$$

Using the above relations, a general expression is found:

$$\mathcal{A}_{mac}(t) = \left[f_{0_I}\mathcal{A}_I(t) : \boldsymbol{B}^{\varepsilon}(t) + (1 - f_{0_I})\mathcal{A}_M(t)\right] : \left[f_{0_I}\boldsymbol{B}^{\varepsilon}(t) + (1 - f_{0_I})\boldsymbol{\mathcal{I}}\right]^{-1} \tag{4.30}$$

With the LCC concept, Nemat-Nasser (1999) showed that it is possible to extend the results of Eshelby (1957) and MFH models from linear elasticity to the finite strain regime. Tensors of Eshelby ($\boldsymbol{\mathcal{S}}$) and Hill ($\boldsymbol{\mathcal{P}}$) are related as follows:

$$\boldsymbol{\mathcal{S}}(I, \mathcal{A}_M) = \boldsymbol{\mathcal{P}}(I, \mathcal{A}_M) : \mathcal{A}_M, \text{ i.e. } \mathcal{S}_{iABj} = \mathcal{P}_{iAkC}(\mathcal{A}_M)_{CkBj} \tag{4.31}$$

where argument I designates the geometry of an inclusion, assumed to be ellipsoidal. For the finite strain extension of the Mori and Tanaka (1973) model, strain concentration $\boldsymbol{B}^{\varepsilon}$ is given by:

$$\boldsymbol{B}^{\varepsilon} = \left[\boldsymbol{\mathcal{I}} + \boldsymbol{\mathcal{P}} : (\mathcal{A}_I - \mathcal{A}_M)\right]^{-1} \tag{4.32}$$

Within this MFH formulation, cavities in porous materials are considered as zero-stiffness inclusions. Therefore, the macro nominal tangent operator and nominal stress tensor become:

$$\mathcal{A}_{mac} = (1 - f_{0_I})\mathcal{A}_M : \left[f_{0_I}\boldsymbol{B}^{\varepsilon} + (1 - f_{0_I})\boldsymbol{\mathcal{I}}\right]^{-1}, \quad \boldsymbol{P}^n_{mac} = (1 - f_{0_I})\boldsymbol{P}^n_M \tag{4.33}$$

where for the Mori-Tanaka scheme,

$$\boldsymbol{B}^{\varepsilon} = (\boldsymbol{\mathcal{I}} - \boldsymbol{\mathcal{P}} : \mathcal{A}_M)^{-1} = (\boldsymbol{\mathcal{I}} - \boldsymbol{\mathcal{S}})^{-1} \tag{4.34}$$

4.4.2 Tangent operators

Tangent operators play an important role in MFH. In the incremental formulation of Section 4.4.1, a nominal tangent ($\mathcal{A}$) is used. However, other tangent operators are needed, either because they stem more naturally from the constitutive equations (e.g., hyperelastic-plastic or purely hyperelastic local models) or they are useful for linearizing equilibrium equations, imposing stress-constraint conditions or linking MFH to finite element (FE) solvers. The latter coupling enables two-scale simulations of heterogeneous solids and structures, with FE and MFH at the macro and micro scales, resp.

Assuming rate-independent material behavior, besides $\mathcal{A}$ of eq. (4.24), two other useful tangent operators are $\boldsymbol{C}$ and $\boldsymbol{c}$. The so-called "material" tangent operator $\boldsymbol{C} = (C_{ABCD})$ is defined as follows:

$$\dot{\boldsymbol{S}} = \boldsymbol{C} : \frac{\dot{\boldsymbol{C}}}{2}; \quad C_{ABCD} = C_{BACD} = C_{ABDC} = C_{CDAB} \tag{4.35}$$

The "spatial" tangent operator $\boldsymbol{c} = (c_{ijkl})$ is defined from:

$$\overset{L}{\boldsymbol{\tau}} = \boldsymbol{c} : \boldsymbol{d}; \quad c_{ijkl} = c_{jikl} = c_{ijlk} = c_{klij} \tag{4.36}$$

where $\overset{L}{\boldsymbol{\tau}}$ is the Lie derivative of $\boldsymbol{\tau}$ (an objective rate):

$$\overset{L}{\boldsymbol{\tau}} = \dot{\boldsymbol{\tau}} - \boldsymbol{l} \cdot \boldsymbol{\tau} - \boldsymbol{\tau} \cdot \boldsymbol{l}^T \tag{4.37}$$

Important remarks are that $\boldsymbol{C}$ is defined w.r.t. Ω_0, $\boldsymbol{c}$ w.r.t. ω_t, and both have minor and major (diagonal) symmetries, while $\boldsymbol{\mathcal{A}}$ has indices w.r.t. both Ω_0 and ω_t and possesses diagonal symmetry only.

After some algebra, the following relations between the tangent operators are found:

$$\begin{aligned} &c_{ijkl} = F_{iA}F_{jB}F_{kC}F_{lD}C_{ABCD}; \\ &\mathcal{A}_{AiBj} = F_{iC}F_{jD}C_{ACBD} + S_{AB}\delta_{ij} = (F^{-1})_{Ak}(F^{-1})_{Bl}c_{kilj} + S_{AB}\delta_{ij} \end{aligned} \tag{4.38}$$

Tangent operators appear in the linearization of the virtual work theorem (VWT). The VWT gives the following expressions for the work of stress in the gradient of an admissible variation $\delta\boldsymbol{\varphi}$:

$$G(\boldsymbol{\varphi}, \delta\boldsymbol{\varphi}) \equiv \int_{\Omega_0} \boldsymbol{P}^n : \mathrm{GRAD}(\delta\boldsymbol{\varphi})\, dV = \int_{\omega_t} \boldsymbol{\sigma} : \nabla(\delta\boldsymbol{\varphi})\, dv \tag{4.39}$$

The linearization of G in a direction $d\boldsymbol{\varphi}$ is defined as follows:

$$DG(\boldsymbol{\varphi}, \delta\boldsymbol{\varphi}) \cdot d\boldsymbol{\varphi} \equiv \frac{d}{d\varepsilon}_{(\varepsilon=0)} G(\boldsymbol{\varphi} + \varepsilon d\boldsymbol{\varphi}, \delta\boldsymbol{\varphi}) \tag{4.40}$$

The following two equivalent expressions are found:

$$DG(\boldsymbol{\varphi}, \delta\boldsymbol{\varphi}) \cdot d\boldsymbol{\varphi} = \int_{\Omega_0} \mathrm{GRAD}(\delta\boldsymbol{\varphi}) : \boldsymbol{\mathcal{A}} : \mathrm{GRAD}(d\boldsymbol{\varphi})\, dV = \int_{\omega_t} \nabla(\delta\boldsymbol{\varphi}) : \boldsymbol{c}^{lin} : \nabla(d\boldsymbol{\varphi})\, dv \tag{4.41}$$

where $\boldsymbol{c}^{lin}$ is a new spatial tangent operator which is related to the previously introduced ones as follows:

$$c^{lin}_{ijkl} = \frac{1}{J} F_{iA}F_{kB}\mathcal{A}_{AjBl} = \frac{1}{J} c_{ijkl} + \sigma_{ik}\delta_{jl} \tag{4.42}$$

4.4.3 Comments on the proposed MFH

Our objective is to develop MFH models where each solid phase can have any hyperelastic-plastic isotropic constitutive model. Since MFH does not use FE analysis or another direct full-field method at the micro level, it does not provide for detailed micro fields but only for average values of nominal stress and deformation gradient over each phase's reference configuration. In order to achieve the general objective within the restrictions imposed by MFH, some important assumptions were needed. However, it is crucial to keep in mind the following observations.

The response of fictitious comparison materials possessing uniform nominal tangent operators $\boldsymbol{\mathcal{A}}_\alpha(t) = \widehat{\boldsymbol{\mathcal{A}}}_\alpha(t)$ is computed from $\boldsymbol{F}_\alpha(t) =< \boldsymbol{F}(\boldsymbol{X}, t) >_{\Omega_{0_\alpha}}$ which are independent of position $\boldsymbol{X}$. However, this does not mean (and we do not assume) that the actual micro fields of deformation gradient, various stress measures, etc., are uniform, not even in the comparison material. Only the per-phase uniformity of $\widehat{\boldsymbol{\mathcal{A}}}_\alpha(t)$ is needed in order to generalize Eshelby's results and MFH models from the linear elastic regime to the inelastic one.

The incremental formalism is only used to compute compatible values of $\dot{\boldsymbol{F}}_I$ and $\dot{\boldsymbol{F}}_M$ (or

the increments $\Delta \boldsymbol{F}_I$ and $\Delta \boldsymbol{F}_M$ in the algorithm of section 4.4.4. However, the constitutive equations in each phase are satisfied rigorously by the comparison material (although not pointwise), i.e. hyperelastic-plastic model.

An important issue in the MFH of elasto(visco)plastic composites in the small strain regime is the computation of Eshelby's or Hill's tensors with isotropic projections of the matrix' instantaneous stiffness operator. For a discussion, see Chaboche et al. (2005) and Pierard and Doghri (2006). Recent proposals try to bypass the issue and construct LCCs which are naturally isotropic per phase, e.g. Brassart et al. (2011), Brassart et al. (2012), Lahellec and Suquet (2013), Wu et al. (2013a) and Wu et al. (2015). In the large deformation regime, the isotropisation issue becomes more difficult. Indeed, it is possible to define isotropic projections of spatial tangent operators, because although they are anisotropic, they are defined w.r.t. one configuration only (ω_t for both). However, trying an isotropisation of nominal tangent operator $\widehat{\boldsymbol{A}}_M$ does not make sense, because it has indices w.r.t. both configurations (Ω_0 and ω_t).

4.4.4 Proposed algorithm

Consider a time interval $[t_n, t_{n+1}]$. The data are: $\boldsymbol{F}_{mac}(t_n)$ and $\boldsymbol{F}_{mac}(t_{n+1})$, each phase's constitutive model and material parameters, the reference volume fractions f_{0_I} and $f_{0_M} = 1 - f_{0_I}$, the inclusions' shape and orientation at t_n. The problem is to compute the following macro variables at t_{n+1}: nominal stress $\boldsymbol{P}^n_{mac}(t_{n+1})$, Cauchy (true) stress $\boldsymbol{\sigma}_{mac}(t_{n+1})$, a nominal tangent operator $\widehat{\boldsymbol{\mathcal{A}}}_{mac}(t_{n+1})$ and a spatial tangent operator $\boldsymbol{c}^{lin}_{mac}(t_{n+1})$. In order to calculate the macro variables, we compute values of $\boldsymbol{F}_\alpha(t_{n+1})$ related by a homogenization model. In the following, Δ designates an increment, e.g.

$$\Delta \boldsymbol{F}_{mac} = \boldsymbol{F}_{mac}(t_{n+1}) - \boldsymbol{F}_{mac}(t_n) \tag{4.43}$$

In the algorithms, a fully implicit backward Euler scheme is used, so that rate equations are discretized over a time interval $[t_n, t_{n+1}]$ as follows:

$$\Delta \boldsymbol{F}_I = \boldsymbol{B}^\varepsilon(t_{n+1}) : \Delta \boldsymbol{F}_M = \boldsymbol{A}^\varepsilon(t_{n+1}) : \Delta \boldsymbol{F}_{mac} \tag{4.44}$$

The expression of $\boldsymbol{B}^\varepsilon$ depends on the homogenization model used; it is given for the Mori-Tanaka model hereafter. Note however that the expressions of $\boldsymbol{A}^\varepsilon$ and $\boldsymbol{\mathcal{A}}_{mac}$ are valid for any homogenization model.

For hyperelastic-plastic constituents, values at t_n of plastic right Cauchy-Green strain tensor $\boldsymbol{C}^p_\alpha(t_n)$ and internal variables $\xi_\alpha(t_n)$ are passed as input and need to be updated at t_{n+1}. They are approximate estimates of the mean values of the corresponding micro fields over each phase α.

- Initialize increment of average deformation gradient in inclusions' phase:

$$\Delta \boldsymbol{F}_I \longleftarrow \Delta \boldsymbol{F}_{mac}$$

- Iterations (i) (upper index (i) omitted for simplicity):

1. Compute average deformation gradient in matrix phase:

$$\boldsymbol{F}_M(t_{n+1}) = \frac{\boldsymbol{F}_{mac}(t_{n+1}) - f_{0_I}\boldsymbol{F}_I(t_{n+1})}{1 - f_{0_I}}$$

2. Compute each phase's $J_\alpha(t_{n+1}) = \det\boldsymbol{F}_\alpha(t_{n+1})$.
3. Call constitutive box of each phase's hyperelastic-plastic material with $\boldsymbol{F}_\alpha(t_{n+1})$, $\boldsymbol{C}^p_\alpha(t_n)$ and $\xi_\alpha(t_n)$as input. The output is a Cauchy stress $\boldsymbol{\sigma}_\alpha(t_{n+1})$, $\boldsymbol{C}^p_\alpha(t_{n+1})$, $\xi_\alpha(t_{n+1})$ and a spatial tangent operator $\boldsymbol{c}_\alpha(t_{n+1})$.
4. Compute nominal tangent operator $\mathcal{A}_M(t_{n+1})$- eq.(4.38) .
5. Update inclusions' shape and orientation at t_{n+1} using $\boldsymbol{F}_I(t_{n+1})$. The new geometry is designated by $I(t_{n+1})$.
6. Compute Hill's tensor $\mathcal{P}(t_{n+1})$ with $\mathcal{A}_M(t_{n+1})$ and $I(t_{n+1})$.
7. Compute strain concentration tensors $\boldsymbol{B}^\varepsilon$ (for Mori-Tanaka) and $\boldsymbol{A}^\varepsilon$: eqs. 4.32 and 4.27.
8. Check compatibility of assumed value of $\Delta\boldsymbol{F}_I$ by computing residual:

$$\boldsymbol{R} = \boldsymbol{A}^\varepsilon : \Delta\boldsymbol{F}_{mac} - \Delta\boldsymbol{F}_I$$

9. If $\|\boldsymbol{R}\| \leq$ TOL, then exit the loop.
10. Else: new iteration (go to step 1) with new $\Delta\boldsymbol{F}_I$:

$$\Delta\boldsymbol{F}_I \longleftarrow \Delta\boldsymbol{F}_I + \zeta\boldsymbol{R};\ \ \zeta \in]0, 1]$$

- After convergence:

11. Compute macro nominal tangent operator $\widehat{\mathcal{A}}_{mac}(t_{n+1})$: eq.(4.33).
12. Compute each phase's nominal stress $\widehat{\boldsymbol{P}}^n_\alpha(t_{n+1})$: eq.(4.8).
13. Compute macro nominal stress $\widehat{\boldsymbol{P}}^n_{mac}(t_{n+1})$:

$$\widehat{\boldsymbol{P}}^n_{mac}(t_{n+1}) = f_{0_I}\widehat{\boldsymbol{P}}^n_I(t_{n+1}) + (1 - f_{0_I})\widehat{\boldsymbol{P}}^n_M(t_{n+1})$$

14. Compute macro Cauchy stress from eq. (4.8):

$$\widehat{\boldsymbol{\sigma}}_{mac}(t_{n+1}) = \frac{1}{J_{mac}(t_{n+1})}\boldsymbol{F}_{mac}(t_{n+1}) \cdot \widehat{\boldsymbol{P}}^n_{mac}(t_{n+1})$$

In the algorithm as presented, it is $\Delta\boldsymbol{F}_I$ which is sought iteratively. It is also possible to iterate over $\Delta\boldsymbol{F}_M$ instead.

In step 13, the computation of the macro nominal stress $\widehat{\boldsymbol{P}}^n_{mac}$ is based on the following hypothesis:

$$\boldsymbol{F}_\alpha(t) =< \boldsymbol{F}(\boldsymbol{X}, t) >_{\Omega_{0_\alpha}} \overset{\text{hypo}}{\Longrightarrow} \widehat{\boldsymbol{P}}^n_\alpha(t) =< \widehat{\boldsymbol{P}}^n(\boldsymbol{X}, t) >_{\Omega_{0_\alpha}} \tag{4.45}$$

In step 5, inclusions' shape and orientation are updated at time t_{n+1}. It is assumed that initially, the inclusions are spheroids (that is ellipsoids of revolution). If linear

displacements are applied to the boundary of each ellipsoid, corresponding to the uniform deformation gradient $\boldsymbol{F}^0 = \boldsymbol{F}_I(t_{n+1})$ in eq. (4.19-a), then it is possible to show that the spheroid transforms into an ellipsoid (but generally not a spheroid). Solving a simple eigenvalue problem gives the lengths and the directions of the principal axes of the updated ellipsoid.

In step 10, ζ is a line search parameter; all the numerical simulations that we ran so far used a value of $\zeta = 1$.

4.4.5 Numerical simulations

The microstructure in this application is made up of initially spherical hyperelastic inclusions embedded in a hyperelastic-viscoplastic matrix. In order to reduce computational cost, we performed axisymmetric 2D FE simulations. The unit cell (see figure 4.2) is discretized with approximately 5400 elements. Again, FE computations were made with the commercial solver Abaqus and the model was meshed with 6-node modified, with hourglass control, hybrid with linear pressure axisymmetric elements (CAX6MH). The prescribed boundary conditions are as follows:

$$\begin{cases} u_r(r=0,z)=0, & 0 \le z \le H \\ u_z(r,z=0)=0, & 0 \le r \le R \\ u_z(r,z=H)=U_1, & 0 \le r \le R \\ u_r(r=R,z)=U_2, & 0 \le z \le H \end{cases} \tag{4.46}$$

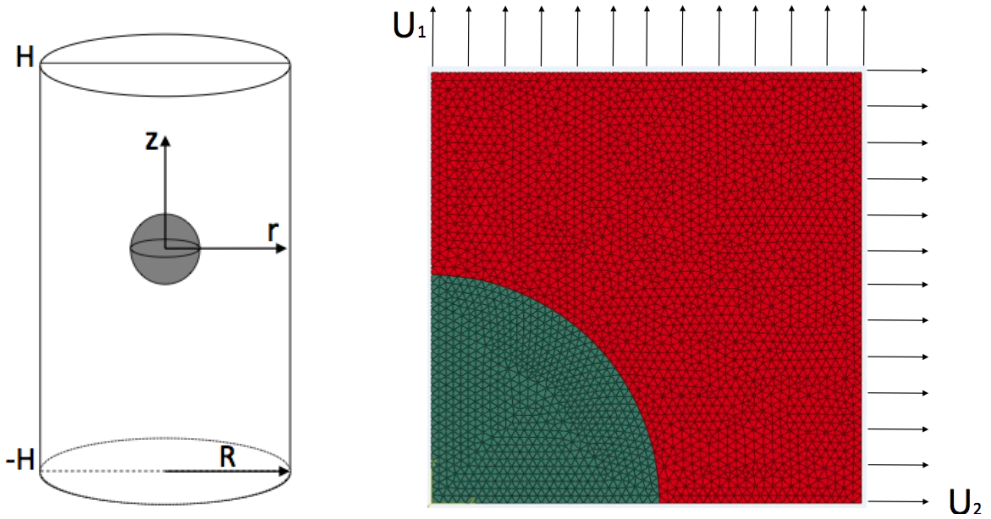

(a) Cylindrical unit cell

(b) 2D axisymmetric cell with displacement boundary conditions

Figure 4.2: Axisymmetric cell used for FE computations

In the following, uniaxial tests are performed using the described unit cell FE model. Thus, U_1 will be imposed depending on the desired elongation, and U_2 will come from

the resolution of the cell's equilibrium. The inclusions obey a quasi-incompressible neo-Hookean hyperelastic model:

$$W(F) = C_{10}\left(\tilde{I}_1 - 3\right) + \frac{\kappa}{2}(J-1)^2 . \tag{4.47}$$

where $\tilde{I}_1 = \mathrm{tr}(\widetilde{\boldsymbol{C}})$, with $\widetilde{\boldsymbol{C}} = \widetilde{\boldsymbol{F}}^T \cdot \widetilde{\boldsymbol{F}}$ being the isochoric part of the right Cauchy-Green strain $\boldsymbol{C}$. The isochoric (or deviatoric) part of the deformation gradient is defined as follows:

$$\widetilde{\boldsymbol{F}} = J^{-1/3}\boldsymbol{F}, \quad \det \boldsymbol{F} = J, \quad \det \widetilde{\boldsymbol{F}} = 1 \tag{4.48}$$

We have $\tilde{I}_1 = I_1 J^{-2/3}$ where $I_1 = \mathrm{tr}(\boldsymbol{C})$. Parameter κ is used to enforce incompressibility and C_{10} is a material constant. For this application, we choose the following material parameters for the Neo-Hookean potential: $C_{10} = 0.8$ MPa and $\kappa = 160$ MPa.

The matrix's hyperelastic-viscoplastic model is a simplified version of more complex models proposed for thermoplastic polymers by Klompen et al. (2005), Boyce et al. (1988) and Buckley (1995). Using the framework and notation of Sect.4.3, it is first supposed that the Kirchhoff stress follows the decomposition:

$$\boldsymbol{\tau} = GJ^{1/3}\mathrm{dev}\boldsymbol{b}^e + \boldsymbol{\tau}^{\mathrm{ins}} \tag{4.49}$$

where G is an elastic shear modulus, $\mathrm{dev}\boldsymbol{b}^e$ is the deviatoric part of the elastic left Cauchy-Green strain, $J = \det\boldsymbol{F}$, and $\boldsymbol{\tau}^{\mathrm{ins}}$ is an instantaneous Kirchhoff stress given by:

$$\boldsymbol{\tau}^{\mathrm{ins}} = KJ(J-1)\mathbf{1} + G_r J^{1/3}\mathrm{dev}\boldsymbol{b} \tag{4.50}$$

where K is an elastic bulk modulus, G_r is a hardening modulus and $\mathrm{dev}\boldsymbol{b}$ is the deviatoric part of the left Cauchy-Green strain.

The yield function takes the expression:

$$f = (\boldsymbol{\tau} - \boldsymbol{\tau}^{\mathrm{ins}})_{\mathrm{eq}} - \tau_Y \tag{4.51}$$

with $(\boldsymbol{\tau} - \boldsymbol{\tau}^{\mathrm{ins}})_{\mathrm{eq}}$ the von Mises measure of $(\boldsymbol{\tau} - \boldsymbol{\tau}^{\mathrm{ins}})$, and τ_Y a yield stress, which obeys the following model:

$$\tau_Y = \tau_0 \mathrm{sinh}^{-1}\left(\frac{\dot{\varepsilon}}{\dot{\varepsilon}_r}\right) \tag{4.52}$$

with τ_0 a characteristic stress, $\dot{\varepsilon}_r$ a reference strain rate, and $\dot{\varepsilon}$ a norm of $\mathrm{dev}\boldsymbol{d}$. Finally, the viscoplastic function is given by:

$$\dot{\gamma} = \frac{\tau_0}{\eta_r}\mathrm{sinh}\left(\frac{(\boldsymbol{\tau} - \boldsymbol{\tau}^{\mathrm{ins}})_{\mathrm{eq}}}{\tau_0\sqrt{3}}\right) > 0 \ \text{ if } f > 0, \dot{\gamma} = 0 \ \text{ if } f \leq 0, \tag{4.53}$$

where η_r is a material constant. In the following applications, the values of the matrix's material parameters are the following (which are typical of a thermoplastic polymer): $G = 321.4$ MPa, $K = 1500$ MPa, $G_r = 26$ MPa, $\tau_0 = 0.7$ MPa, $\eta_r = 3.6 \times 10^{11}$ MPa.s, $\dot{\varepsilon}_r = 7.8 \times 10^{-10}\mathrm{s}^{-1}$.

Two initial volume fractions for the hyperelastic inclusions are considered: 10% and 20% and the composites are subjected to various non-monotonic loadings. In the first test, we study monotonic loadings followed by unloadings until the initial undeformed state, i.e. $(F_{\text{mac}})_{11} = 1$. Two strain rates are simulated: 10^{-2} and $1\,\text{s}^{-1}$ which are imposed on the deformation gradient. For instance, for $1\,\text{s}^{-1}$, $(F_{\text{mac}})_{11}$ goes from 1 to 2 in 1 second.

The MFH results are plotted in figure 4.3 and superimposed to the FE simulations for strain rate $\pm 1\,\text{s}^{-1}$ in three cases: unreinforced matrix, and composite with two initial concentrations of inclusions. Since the particles are softer than the matrix, they do not reinforce it mechanically, but they may be useful for improving damping properties. The figure shows that the proposed MFH formulation and algorithm are able to simulate non-monotonic loadings under different concentrations. A good agreement between responses predicted by MFH and FE is observed for the considered volume fractions.

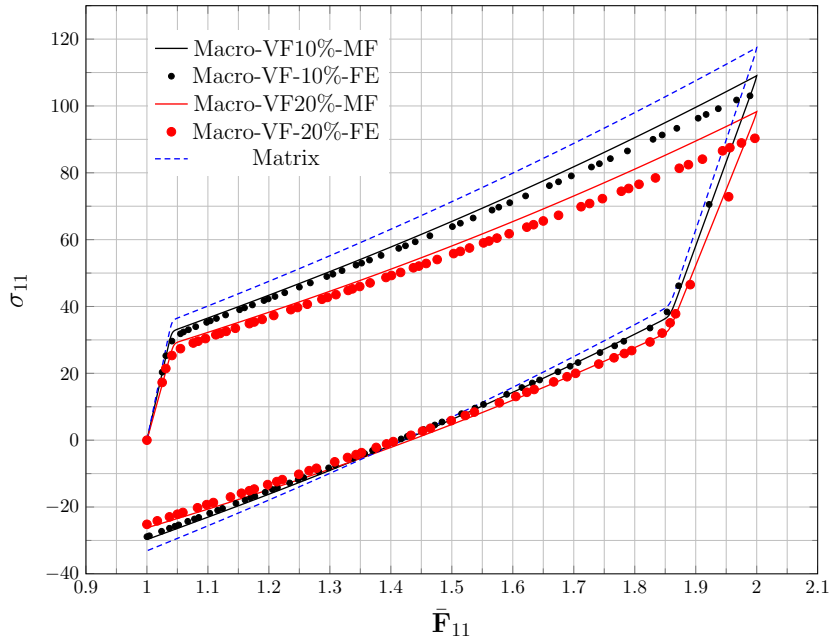

Figure 4.3: Hyperelastic-viscoplastic matrix with initially spherical hyperelastic inclusions under macro uniaxial load. Concentration effect. Strain rate : $\pm 1\,\text{s}^{-1}$. Macro Cauchy stress vs. macro deformation gradient. From top to bottom: (i) matrix alone, (ii) composite's response for 10% inclusions, (ii) composite's response for 20% inclusions.

In Fig. 4.4 are depicted the MFH and FE results for two strain rates: $\pm 1\,\text{s}^{-1}$ and $\pm 10^{-2}\,\text{s}^{-1}$, and two microstructures: unreinforced matrix, and composite with 20% initial concentration of inclusions. Again, MFH predictions agree quite well with FE results. The figure shows that the proposed MFH formulation and algorithm are able to simulate simultaneously the effects of strain rate, inclusions' concentration and non-monotonic loadings.

In a second example we simulate a cyclic uniaxial loading/unloading of the composite. The resulting macroscopic stress-deformation gradient curves are plotted in figure 4.5 together with matrix response and again we compare MFH results with those obtained by FE calculations. The MFH predictions are in good agreement with FE results up to

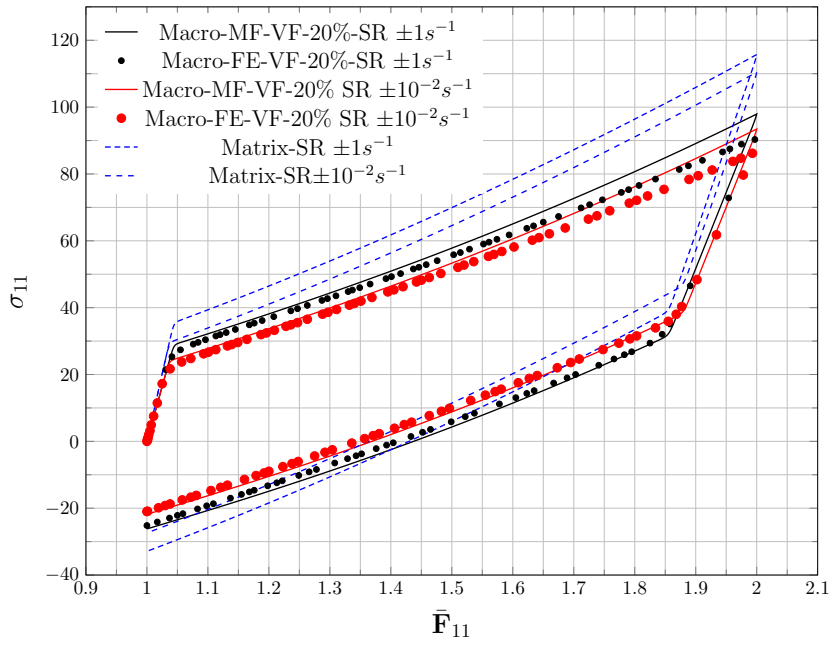

Figure 4.4: Hyperelastic-viscoplastic matrix with initially spherical hyperelastic inclusions under macro uniaxial load. Strain rate effect. Macro Cauchy stress vs. macro deformation gradient. From top to bottom: (i) matrix's behavior for $\pm 1\,\mathrm{s}^{-1}$, (i) matrix's behavior for $\pm 10^{-2}\,\mathrm{s}^{-1}$, (iii) composite's response for 20% inclusions and $\pm 1\,\mathrm{s}^{-1}$, (iv) composite's response for 20% inclusions and $\pm 10^{-2}\,\mathrm{s}^{-1}$.

50% of deformation then they slightly overestimate the effective response.

A third example of non-monotonic loading is presented in figure4.6 with consecutive steps of loading and partial unloading. The history of imposed macro deformation gradient is depicted in Fig. 4.6(a), and the MFH predictions are shown together with the FE results in Fig.4.6(b). Two initial volume fractions of inclusions are considered. The effective responses of the composites predicted by MFH compare well with the FE results.

Finally, a test with three steps of loading and partial relaxation is simulated. The history of prescribed macro deformation gradient is depicted in Fig.4.7(a), and both MF predictions and FE results are presented in Fig.4.7(b). Two initial concentrations of inclusions are considered. The MFH predictions reproduce the main trend of stress evolution, but fail to capture the slight stress relaxation. This shortcoming of MFH needs further investigation.

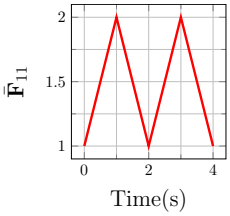

(a) Loading history

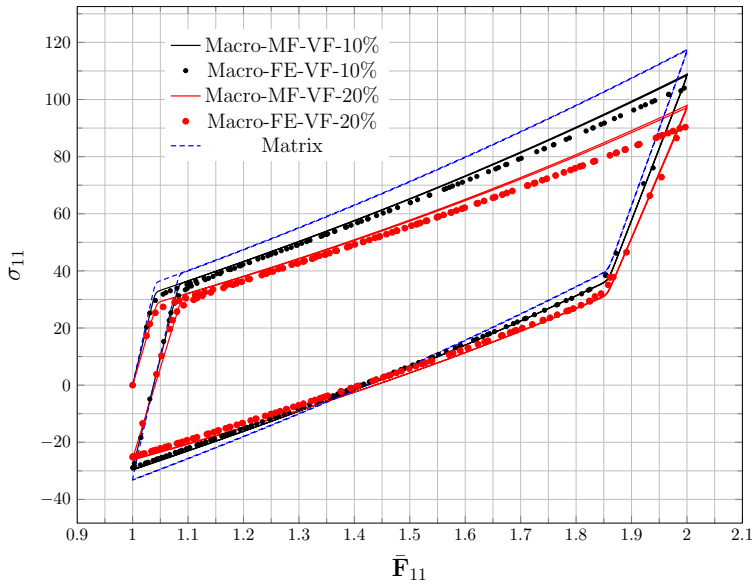

(b) Macro Cauchy stress vs. macro deformation gradient. From top to bottom: (i) matrix alone, (ii) composite's response for 10% inclusions, (ii) composite's response for 20% inclusions.

Figure 4.5: Hyperelastic-viscoplastic matrix with initially spherical hyperelastic inclusions under cyclic loading/unloading.

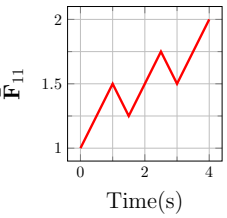

(a) Loading history

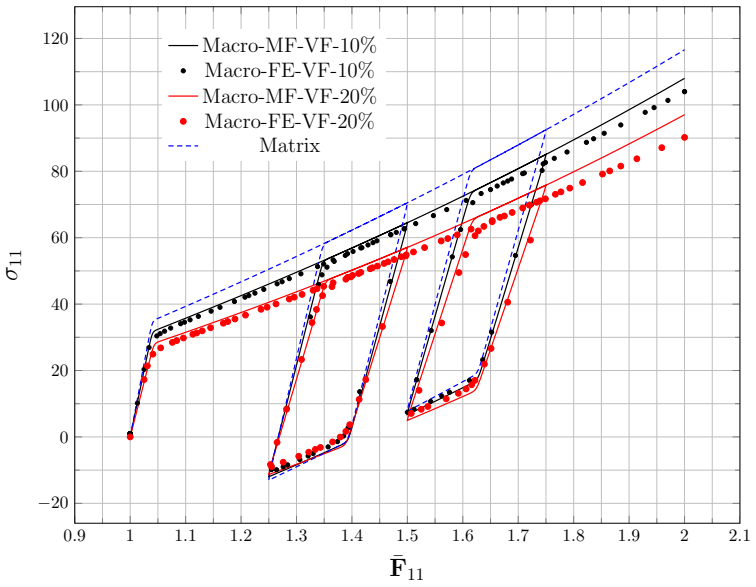

(b) Macro Cauchy stress vs. macro deformation gradient. From top to bottom: (i) matrix alone, (ii) composite's response for 10% inclusions, (ii) composite's response for 20% inclusions.

Figure 4.6: Hyperelastic-viscoplastic matrix with initially spherical hyperelastic inclusions under cyclic loading/partial unloading.

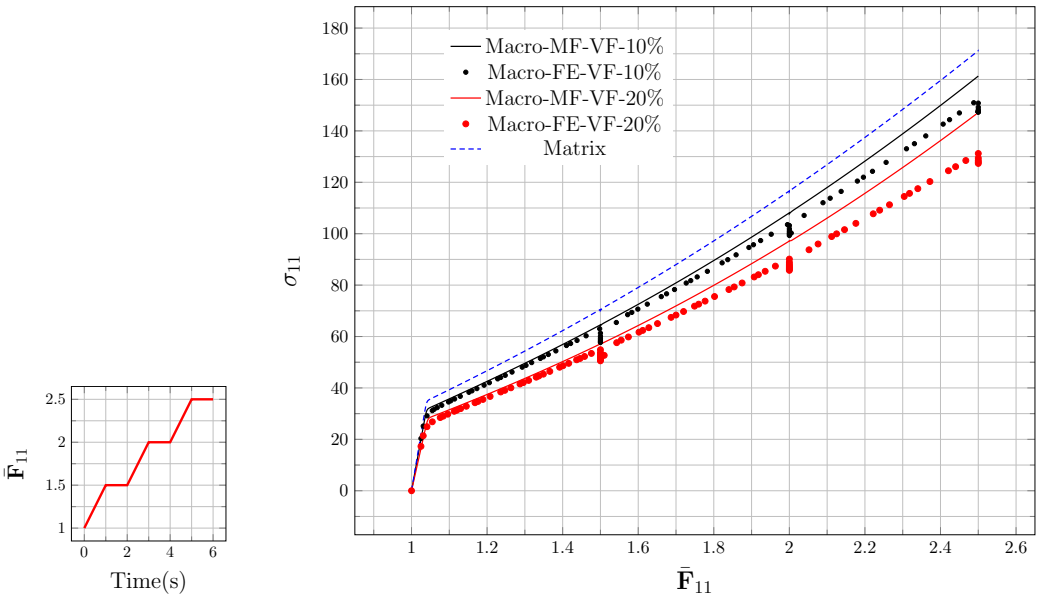

(a) Loading history

(b) Macro Cauchy stress vs. macro deformation gradient. From top to bottom: (i) matrix alone, (ii) composite's response for 10% inclusions, (ii) composite's response for 20% inclusions.

Figure 4.7: Hyperelastic-viscoplastic matrix with initially spherical hyperelastic inclusions under multiple steps of loading and partial relaxation.

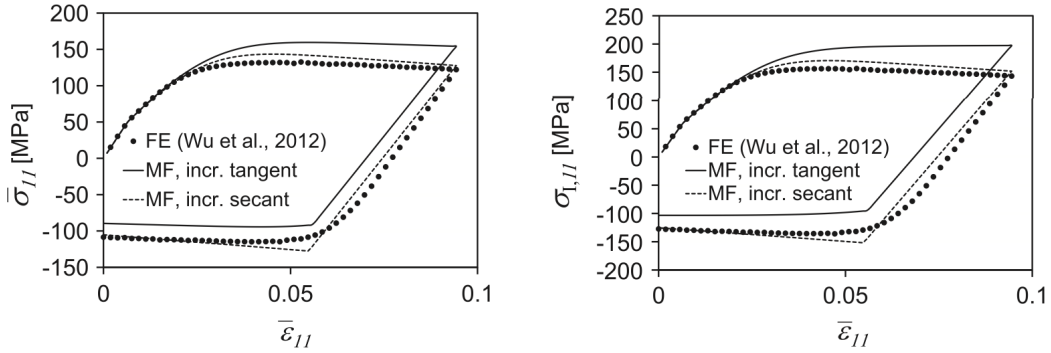

Figure 4.8: Stress evolution for elastic fibers embedded in a matrix following an elasto-plastic behavior with damage. (a) Average stress in the composite material along the loading direction. (b) Average stresses in the inclusion phases along the loading direction. Wu et al. (2013b)

4.5 Composites with hyperelastic-plastic constituents- Part II: An incremental secant formulation

Although the incremental tangent homogenization model presented in the previous section gives acceptable macroscopic predictions, one limitation of the incremental tangent formulation appears when considering damage. In fact, in the framework of small deformations, Wu et al. (2012) coupled a damage law in the constitutive model of the matrix phase for fiber-reinforced composites and showed that the incremental tangent formulation does not allow the fibers to see unloading during the softening stage of the matrix. This motivated the proposition of a new formulation: the incremental secant approach which accounts, by design, for resulting unloading of the fibers during strain softening of the matrix (see Wu et al. (2013a)). When damage in one phase is considered (Wu et al. (2013b)), the incremental secant approach improved considerably the accuracy of the predictions compared to the incremental tangent approach. As explained in Wu et al. (2013b) and illustrated in Fig.4.8-b, the average stress along the loading direction in the fibers keeps increasing as predicted by incremental-tangent model, however it should decrease after the damaging process in the matrix. This unloading is captured by the incremental secant model which leads to much better predictions at the macroscopic scale (see 4.8-a). The goal here is to construct in the finite strain regime a counterpart of the incremental-secant mean-field homogenization scheme Wu et al. (2013a) initially formulated for infinitesimal strains. This section presents the micromechanical model and the corresponding numerical algorithm for two-phase nonlinear composites. The local constitutive equations of each phase are based on the formulation of finite strain elastoplasticity based on a multiplicative decomposition of the deformation gradient as suggested by Simo (1992). The latter proposed algorithms which preserve the classical return mapping schemes of the infinitesimal theory by introducing spectral decompositions of the Kirchhoff stress and the left elastic Cauchy-Green tensors. In this work, we consider the specific case of a quadratic logarithmic free energy and J2 flow theory. We

show that the MFH technique used for infinitesimal elastoplasticity can still be used in this context.

Two main features distinguish the incremental-secant MFH scheme from the incremental tangent one. First, the residual stress and strain states in each phase are evaluated by applying a fictitious elastic unloading step. The mean stress fields in the phases are then computed using secant operators which are naturally isotropic. A Linear Comparison Composite is defined and is subjected to a strain increment deduced from the residual state. Numerical simulations of composite microstructures are verified against full-field finite element computations.

4.5.1 General return mapping algorithm in principal stresses

In this section, The essential ingredients of Simo's algorithm for multiplicative plasticity will be presented. The return mapping algorithm has a functional form identical to its infinitesimal theory counterpart. The key to this simplification, is to reformulate the governing equations (see section 4.3) in terms of the principal Kirchhoff stress and left Cauchy-Green tensors . The presentation proposed hereafter follows Simo (1992), see also Simo and Hughes (2000) and Doghri (2000).

Spectral decomposition

Similarly to section 4.3, we assume throughout that the material is isotropic and hence, $\psi(\boldsymbol{b}^e, \xi)$ and $f(\boldsymbol{\tau}, q)$ are isotropic functions of $\boldsymbol{b}^e$ and $\boldsymbol{\tau}$ respectively. Accordingly, $\boldsymbol{b}^e$ and $\frac{\partial \psi}{\partial \boldsymbol{b}^e}$ have the same eigenvectors and thus the principal directions of the Kirchhoff stress tensor $\boldsymbol{\tau}$ and the elastic left Cauchy-Green tensor coincide.

$$\boldsymbol{\tau} = \sum_{A=1}^{3} \boldsymbol{\beta}_A \boldsymbol{n}_t^{(A)} \otimes \boldsymbol{n}_t^{(A)}, \quad \boldsymbol{b}^e = \sum_{A=1}^{3} (\lambda_A^e)^2 \boldsymbol{n}_t^{(A)} \otimes \boldsymbol{n}_t^{(A)} \tag{4.54}$$

The restriction to isotropy also implies the existence of a function $\bar{\psi}$ such that $\psi(\boldsymbol{b}^e, \xi) = \bar{\psi}((\lambda_1^e)^2, (\lambda_2^e)^2, (\lambda_3^e)^2, \xi)$. Thus, using the the stress strain relation (4.12(a)), it is easily checked that the principal Khirchhoff stresses $\boldsymbol{\beta}_A$ are given by:

$$\boldsymbol{\beta}_A = 2(\lambda_A^e)^2 \frac{\partial \bar{\psi}}{\partial (\lambda_A^e)^2}. \tag{4.55}$$

The principal elastic logarithmic stretches are defined by the relation:

$$\boldsymbol{\varepsilon}_A^e = \ln(\lambda_A^e). \tag{4.56}$$

Introducing for convenience the following vector array notation:

$$\boldsymbol{\beta} = \begin{bmatrix} \beta_1 \\ \beta_2 \\ \beta_3 \end{bmatrix}; \quad \boldsymbol{\varepsilon}^e = \begin{bmatrix} \varepsilon_1^e \\ \varepsilon_2^e \\ \varepsilon_3^e \end{bmatrix}; \quad \mathbf{1} = \begin{bmatrix} 1 \\ 1 \\ 1 \end{bmatrix} \tag{4.57}$$

The isotropy assumption implies that the free energy ψ can be expressed as a function of the principal elastic stretches and, therefore, a function of the principal elastic logarithmic stretches: $\psi(\boldsymbol{b}^e, \xi) = \bar{\psi}((\lambda_1^e)^2, (\lambda_2^e)^2, (\lambda_3^e)^2, \xi) = \widehat{\psi}(\boldsymbol{\varepsilon}^e, \xi)$. With the preceding vector notation in hand, a straightforward manipulation of (4.55) gives the following stress-strain relations for the Kirchhoff principal stress which are form-identical to those of infinitesimal strain case:

$$\boldsymbol{\beta} = \frac{\partial \widehat{\psi}}{\partial \boldsymbol{\varepsilon}^e} \tag{4.58}$$

Trial elastic state

Analogously to the infinitesimal case, The first step in the return mapping algorithm is the "elastic predictor". It corresponds physically to a state obtained by "freezing" the evolution of plastic flow and assuming the increment to be purely elastic. Consequently, the intermediate configuration remains unchanged, i.e.,

$$(\boldsymbol{C}^{p^{tr}}_{n+1})^{-1} = \boldsymbol{C}^{p^{-1}}_{n} \tag{4.59}$$

Thus, with relationship (4.11) in hand, the trial elastic left Cauchy-Green strain is given by:

$$\boldsymbol{b}^{e^{tr}}_{t} = \boldsymbol{F}_t \cdot \boldsymbol{C}^{p^{-1}}_{n} \cdot \boldsymbol{F}^T_t \tag{4.60}$$

Where the subscript t refers to quantities evaluated within the time interval $[t_n, t_{n+1}]$. The Kirchhoff stress field and the stress-like internal variable are computed from the constitutive equations (4.12) as:

$$\boldsymbol{\tau}^{tr}_t = 2\frac{\partial \psi(\boldsymbol{b}^{e^{tr}}_t, \xi^{tr}_t)}{\partial \boldsymbol{b}^e} \cdot \boldsymbol{b}^{e^{tr}}_t; \quad q^{tr}_t = \frac{\partial \psi(\boldsymbol{b}^{e^{tr}}_t, \xi^{tr}_t)}{\partial \xi} \tag{4.61}$$

where $\xi^{tr}_t = \xi_n$. Using the vector notations, the trial elastic state can be expressed in the principal axes $\boldsymbol{n}^{tr}_A$ (associated to $\boldsymbol{b}^{e^{tr}}_t$) as:

$$\boldsymbol{\beta}_t = \frac{\partial \widehat{\psi}(\boldsymbol{\varepsilon}^{e^{tr}}_t, \xi^{tr}_t)}{\partial \boldsymbol{\varepsilon}^e}; \quad q^{tr}_t = \frac{\partial \widehat{\psi}(\boldsymbol{\varepsilon}^{e^{tr}}_t, \xi^{tr}_t)}{\partial \xi} \tag{4.62}$$

Two alternative situations may arise:

i The trial elastic state satisfies the yield condition (4.17), then the basic assumption is true and the trial elastic step is the solution at time t_{n+1}.

ii Alternatively, in the situation for which $f^{tr}(\boldsymbol{\tau}^{tr}_t, q^{tr}) > 0$, the trial stress $\boldsymbol{\tau}^{tr}_t$ is not admissible and plastic flow has occured during the increment. Thus, a correction is needed to bring the stress back onto the yield surface ($f(\boldsymbol{\tau}, q) = 0$) and the correct state at t_{n+1} has to be computed by performing the return mapping algorithm as will be explained in a subsequent section. In order to move to the next step of the algorithm, we need to time-discretize the plastic flow rules.

Exponential approximation of the flow rule

Recalling the evolution equations (4.15):

$$-\frac{1}{2}\overset{L}{\boldsymbol{b}^e}\cdot\boldsymbol{b}^{e-1}=\dot\gamma\frac{\partial f}{\partial\boldsymbol{\tau}}(\boldsymbol{\tau},q);\quad \dot\xi=-\dot\gamma\frac{\partial f}{\partial q}(\boldsymbol{\tau},q),$$

and using the relation (4.11) along with the Lie derivative definition (4.14), the flow rule can be rewritten in the material description as:

$$\left\{\begin{array}{l}\frac{d}{dt}(\boldsymbol{C}^{p^{-1}})=(-2\dot\gamma\boldsymbol{C}^{-1}.\boldsymbol{N}).\boldsymbol{C}^{p^{-1}}\\ \boldsymbol{N}:=\boldsymbol{F}^T.\frac{\partial f}{\partial\boldsymbol{\tau}}.\boldsymbol{F}\end{array}\right.\quad , \tag{4.63}$$

In geometric term, $\boldsymbol{N}$ is interpreted as the "pull-back" [1] of the normal $\frac{\partial f}{\partial\boldsymbol{\tau}}$ to the reference configuration. For the time discretization of the flow rule, Simo (1992) used an exponential approximation to the flow rule within the interval $[t_n,t]\subset[t_n,t_{n+1}]$ given by:

$$\tilde{\boldsymbol{C}}_t^{p^{-1}}=\exp(-2\Delta\gamma_t\boldsymbol{C}_t^{-1}\,.\,\tilde{\boldsymbol{N}}_t)\,.\,\boldsymbol{C}_n^{p^{-1}} \tag{4.64}$$

where ˜ refers to the algorithmic approximation and $\Delta\gamma_t=\gamma_t-\gamma_n$. This last result can be reformulated in a simpler form (making use of (4.60) and 4.11)) given by:

$$\tilde{\boldsymbol{b}}_t^e=\exp[-2\Delta\gamma_t\frac{\partial f}{\partial\boldsymbol{\tau}}]\cdot\boldsymbol{b}_t^{e^{tr}} \tag{4.65}$$

It is worth mentioning that this algorithm conserves exactly the plastic volume for pressure insensitive yield criteria (i.e. such that $tr(\frac{\partial f}{\partial\boldsymbol{\tau}})=0$).

Return mapping algorithm in principal stresses

The last equation (4.65) gives the spectral decomposition of $\boldsymbol{b}_t^{e^{tr}}$ as:

$$\begin{array}{rcl}\boldsymbol{b}_t^{e^{tr}} & = & \sum_{A=1}^3(\lambda_A^e)^2\exp[2\Delta\gamma_t\frac{\partial f(\boldsymbol{\tau},q)}{\partial\boldsymbol{\tau}}]\boldsymbol{n}_t^{(A)}\otimes\boldsymbol{n}_t^{(A)}\\ & = & \sum_{A=1}^3(\lambda_A^e)^2\exp[2\Delta\gamma_t\frac{\partial f(\beta_1,\beta_2,\beta_3,q)}{\partial\beta_A}]\boldsymbol{n}_t^{(A)}\otimes\boldsymbol{n}_t^{(A)}.\end{array} \tag{4.66}$$

By comparing (4.66) with the spectral decomposition of $\boldsymbol{b}_t^{e^{tr}}$ given by:

$$\boldsymbol{b}_t^{e^{tr}}=\sum_{A=1}^3(\lambda_A^{e^{tr}})^2\boldsymbol{n}_t^{tr(A)}\otimes\boldsymbol{n}_t^{tr(A)}, \tag{4.67}$$

[1] Following Simo (1992), a transformation of the formulation (involving the deformation gradient) of the evolution equations from the spatial description to the material description is referred to as a "pull-back". Reciprocally, the transformation of the discrete evolution equations back to the spatial description is refered to as a "push-forward". Figure 4.1 illustrates schematically the tensors associated to the reference and current configurations.

and from the uniqueness of the spectral decomposition, it is deduced that:

$$\begin{cases} \boldsymbol{n}_t^{(A)} = \boldsymbol{n}_t^{tr(A)} \\ (\lambda_A^{e^{tr}})^2 = \exp[2\Delta\gamma_t \dfrac{\partial \widehat{f}}{\partial \beta_A}](\lambda_A^e)^2 \end{cases} \tag{4.68}$$

This implies that the principal directions $\boldsymbol{n}_t^{(A)}$ associated with the final state coincide with the principal directions $\boldsymbol{n}_t^{tr(A)}$ defined by the trial elastic state. Taking the logarithm on both sides of (4.68-b) and using the vector notation, the algorithmic flow rule expressed in the principal axes $\boldsymbol{n}_t^{tr(A)}$ is rephrased under the following form which is identical to the return mapping algorithms for models of infinitesimal plasticity:

$$\begin{cases} \boldsymbol{\varepsilon}_t^e = \boldsymbol{\varepsilon}_t^{e^{tr}} - \Delta\gamma_t \dfrac{\partial \widehat{f}}{\partial \boldsymbol{\beta}}(\boldsymbol{\beta}_t, q_t) \\ \xi_t = \xi_n - \Delta\gamma_t \dfrac{\partial \widehat{f}}{\partial \boldsymbol{\beta}}(\boldsymbol{\beta}_t, q_t) \\ \widehat{f}(\boldsymbol{\beta}_t, q_t) = 0 \end{cases}, \tag{4.69}$$

4.5.2 Application to J2 flow theory

The previous section summarized Simo's algorithm formulated in the principal stresses and strains with a general free energy function $\widehat{\psi}(\boldsymbol{\varepsilon}^e, \xi)$. In this section, with the preceding developments in hand, we consider the formulation of $J2$ flow theory with isotropic hardening. It will be shown that in this particular context, the associated integration algorithm is exactly a straightforward extension of the radial return algorithm of infinitesimal $J2$ flow theory. We assume the following uncoupled form of the free energy function, quadratic in the principal elastic logarithmic stretches:

$$\widehat{\psi}(\boldsymbol{\varepsilon}^e, \xi) = \frac{1}{2}(k - \frac{2}{3}G)(\varepsilon_1^e + \varepsilon_2^e + \varepsilon_3^e)^2 + G[(\varepsilon_1^e)^2 + (\varepsilon_2^e)^2 + (\varepsilon_3^e)^2] + h(\xi) \tag{4.70}$$

were k and G are respectively the elastic bulk and shear moduli, and $h(\xi)$ is a function which characterizes isotropic hardening in the material.

Then, the stress-strain relations in principal axes are obtained by (4.58):

$$\boldsymbol{\beta} = \mathbf{a}\boldsymbol{\varepsilon}^e; \quad \boldsymbol{a} = k\mathbf{1}\otimes\mathbf{1} + 2G[\boldsymbol{I} - \frac{1}{3}\mathbf{1}\otimes\mathbf{1}] \tag{4.71}$$

We consider the classical Mises yield criterion formulated in terms of the Kirchhoff stress tensor as:

$$f(\boldsymbol{\tau}, q) = J_2(\boldsymbol{\tau}) - \sigma_Y - q(\xi) \leq 0 \tag{4.72}$$

where σ_Y is the flow stress, $q(\xi)$ is the hardening stress and $J_2(\boldsymbol{\tau}) = \sqrt{\frac{3}{2}\mathrm{dev}(\boldsymbol{\tau}) : \mathrm{dev}(\boldsymbol{\tau})}$ Equivalently, the yield criterion expressed in terms of principal stresses takes the form:

$$\widehat{f}(\boldsymbol{\beta}, q) = \|\mathrm{dev}(\boldsymbol{\beta})\| - \sigma_Y - q(\xi) \leq 0 \tag{4.73}$$

The unit normal to the Mises cylinder in principal stress space is given by:

$$\boldsymbol{\nu} = \frac{\partial \widehat{f}}{\partial \boldsymbol{\beta}}(\boldsymbol{\beta}, \xi) = \frac{3}{2}\frac{\mathrm{dev}(\boldsymbol{\beta})}{\|\mathrm{dev}(\boldsymbol{\beta})\|} \tag{4.74}$$

Premultiplying by $\mathbf{a}$ the algorithmic flow rule (4.69), and using (4.71) along with (4.74) leads to the following form of the return mapping algorithm in stress space:

$$\begin{cases} \boldsymbol{\beta}^{tr}_{n+1} = \mathbf{a}\boldsymbol{\varepsilon}^{e^{tr}}_{n+1} \\ \boldsymbol{\beta}_{n+1} = \boldsymbol{\beta}^{tr}_{n+1} - 2G\Delta\gamma\boldsymbol{\nu}(\boldsymbol{\beta}_{n+1}) \\ \xi_{n+1} = \xi_n + \Delta\gamma \\ \boldsymbol{\varepsilon}^{e}_{n+1} = \boldsymbol{\varepsilon}^{e^{tr}}_{n+1} - \Delta\xi\boldsymbol{\nu}(\boldsymbol{\beta}_{n+1}) \\ \Delta\gamma\widehat{f}_{n+1} = 0, \quad \Delta\gamma \geq 0, \quad \widehat{f}_{n+1} \leq 0 \end{cases} \tag{4.75}$$

Analogously to the infinitesimal theory, it is shown that the normals to the yield surface associated with the final state coincide with the normal defined by the trial state (i.e: $\boldsymbol{\nu}(\boldsymbol{\beta}_{n+1}) = \boldsymbol{\nu}(\boldsymbol{\beta}^{tr}_{n+1})$)and the plastic correction step boils down to resolving the following familiar equation with the single scalar unknown $\Delta\xi$:

$$3G\Delta\xi + q(\xi_n + \Delta\xi) + \sigma_Y - \|\mathrm{dev}(\boldsymbol{\beta})\| = 0 \tag{4.76}$$

4.5.3 Mean-field homogenization (MFH)

Our approach for the homogenization of a nonlinear composite at finite strains involves two key ingredients:

(i) First, we make use of the previous developments in order to bring the present finite deformation problem into the framework of the infinitesimal theory.

(ii) Second, we transform the homogenization problem of the nonlinear composite into that of a Linear Comparison Composite and subsequently make use of classical results for linear composites. Our approach in this second step is based on a direct linearization of the constitutive behavior. Several linearization techniques were developed in order to define the LCC. Among them, the secant formulation determines for each phase a secant operator which links the total strain to the total stress. This method is limited to monotonic and proportional loadings. The incremental approaches are based on a rate formulation of the local problem Hill (1965b). The linearization is carried out by a time discretization over each time interval via an algorithmic tangent operator relating the stress and strain increments. Affine method also uses tangent moduli in a non-incremental way by introducing a polarization stress. Both the incremental-tangent method and the affine method need isotropic projections of the tangent operators in the homogenisation process otherwise they yield too stiff estimates. The adopted approach in the present work combines both incremental and secant methods following the work of Wu et al. (2013a) and enables to deal with a wide range of loading paths (e.g.: non monotonic and non-proportional loadings) while avoiding an isotropization step. The main ideas and steps of the incremental secant formulation are recalled hereafter following the presentation of Wu et al. (2013a) with adaptation to the context of finite strain regime.

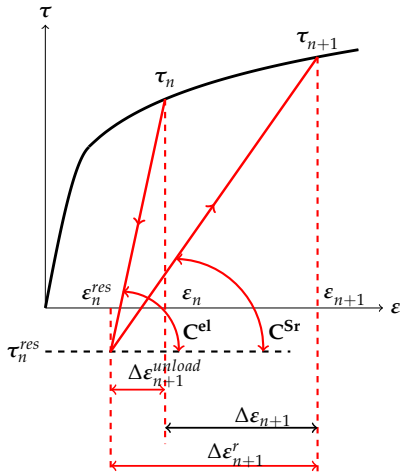

Figure 4.9: Schematics of the incremental-secant formulations adapted from Wu et al. (2013a). The residual-incremental-secant operator linearly relates the strain increment to the stress increment from an unloaded state.

4.5.3.1 Linearization procedure: Incremental secant approach

We are concerned in this section with the local stress-strain relations in each phase ω_i of the composite. The incremental secant formulation recently developed by Wu et al. (2013a) determines for each phase and at each increment a secant operator which links the strain increment to the stress increment from a virtually unloaded state. In our description of the secant approach, we use the logarithmic strain ε and the Kirchhoff stress τ in order to transform the original description from the infinitesimal theory to the finite strain framework. Detailed pre-processings and post processings needed to deal with two different frameworks will be presented and discussed in a subsequent section 4.5.3.2.
Considering a time interval $[t_n, t_{n+1}]$, we suppose that total strain tensor $\boldsymbol{\varepsilon}_n$, the stress tensor $\boldsymbol{\tau}_n$ and all needed variables to be known at the beginning of the time interval. A virtual elastic unloading step from the stress state $\boldsymbol{\tau}_n$ to a stress state $\boldsymbol{\tau}_n^{res}$ is applied at t_n,to which a residual strain tensor $\boldsymbol{\varepsilon}_n^{res}$ is associated, see Fig. 4.9.

Residual state

The residual state in the composite and per phase is obtained by assuming a purely elastic process and solving the following system of equations:

$$\bar{\boldsymbol{\varepsilon}}_n^{res} = \bar{\boldsymbol{\varepsilon}}_n - \Delta\bar{\boldsymbol{\varepsilon}}_n^{unload} = \bar{\boldsymbol{\varepsilon}}_n - (\bar{\boldsymbol{C}}^{el})^{-1} : \bar{\boldsymbol{\tau}}_n^{res}, \tag{4.77}$$

$$\bar{\boldsymbol{\tau}}_n^{res} = 0 = \bar{\boldsymbol{\sigma}}_n^{res} = f_{n_M}\boldsymbol{\sigma}_{n_M}^{res} + f_{n_I}\boldsymbol{\sigma}_{n_I}^{res} = f_{n_M}\frac{\boldsymbol{\tau}_{n_M}^{res}}{J_{n_M}} + f_{n_I}\frac{\boldsymbol{\tau}_{n_I}^{res}}{J_{n_I}}, \tag{4.78}$$

with:

$$\boldsymbol{\tau}_{n_\alpha}^{res} = \boldsymbol{\tau}_{n_\alpha} - \boldsymbol{C}_\alpha^{el} : \Delta\boldsymbol{\varepsilon}_{n_\alpha}^{unload} \tag{4.79}$$

At this point, a modelling assumption must be clarified which consists in applying the averaging rules of the MFH on the logarithmic strain increments and not on the deformation gradient increments as in the incremental tangent model presented in the section 4.4. This assumption is not supported theoretically but despite its apparent roughness, it will be shown that the obtained results at least at the macroscopic scale are very satisfying. This assumption allows to write:

$$\Delta\bar{\boldsymbol{\varepsilon}}_n^{unload} = f_{n_M}\Delta\boldsymbol{\varepsilon}_{n_M}^{unload} + f_{n_I}\Delta\boldsymbol{\varepsilon}_{n_I}^{unload} \tag{4.80}$$

with the relation between the unloading strain increments per phase:

$$\Delta\boldsymbol{\varepsilon}_{n_I}^{unload} = \boldsymbol{B}^{\varepsilon}(\boldsymbol{\mathcal{I}}, \boldsymbol{C}_M^{el}, \boldsymbol{C}_I^{el}) : \Delta\boldsymbol{\varepsilon}_{n_M}^{unload} \tag{4.81}$$

which allows to compute the residual strains in the inclusions and matrix phases from:

$$\begin{aligned} \boldsymbol{\varepsilon}_{n_I}^{res} &= \boldsymbol{\varepsilon}_{n_I} - \Delta\boldsymbol{\varepsilon}_{n_I}^{unload} = \boldsymbol{\varepsilon}_{n_I} - \boldsymbol{B}^{\varepsilon} : [f_{n_I}\boldsymbol{B}^{\varepsilon} + f_{n_M}\boldsymbol{\mathcal{I}}]^{-1} : \Delta\bar{\boldsymbol{\varepsilon}}_n^{unload}, \\ \boldsymbol{\varepsilon}_{n_M}^{res} &= \boldsymbol{\varepsilon}_{n_M} - \Delta\boldsymbol{\varepsilon}_{n_M}^{unload} = \boldsymbol{\varepsilon}_{n_M} - [f_{n_I}\boldsymbol{B}^{\varepsilon} + f_{n_M}\boldsymbol{\mathcal{I}}]^{-1} : \Delta\bar{\boldsymbol{\varepsilon}}_n^{unload} \end{aligned} \tag{4.82}$$

The predictor-corrector and return mapping schemes

The strain and stress updates at time t_{n+1} are defined from the virtually unloaded state[2] (as pictured in Fig.4.9 such that:

$$\begin{aligned} \boldsymbol{\varepsilon}_{n+1_\alpha} &= \boldsymbol{\varepsilon}_{n_\alpha}^{res} + \Delta\boldsymbol{\varepsilon}_{n+1_\alpha}^{r}, \\ \boldsymbol{\tau}_{n+1_\alpha} &= \boldsymbol{\tau}_{n_\alpha}^{res} + \Delta\boldsymbol{\tau}_{n+1_\alpha}^{r} \end{aligned} \tag{4.83}$$

where

$$\Delta\boldsymbol{\tau}_{n+1_\alpha}^{r} = \boldsymbol{C}_\alpha^{Sr} : \Delta\boldsymbol{\varepsilon}_{n+1_\alpha}^{r} \tag{4.84}$$

In the last equation, $\boldsymbol{C}_\alpha^{Sr}$ is the residual-incremental-secant operator of the linear comparison material.
Practically, the stress is updated following a predictor-corrector scheme (see Fig4.10). First, a trial stress is computed in each phase from the unloaded state using the elastic tensor $\boldsymbol{C}^{el}$ as follows:

$$\boldsymbol{\tau}_{n+1_\alpha}^{tr} = \boldsymbol{\tau}_{n_\alpha}^{res} + \boldsymbol{C}_\alpha^{el} : \Delta\boldsymbol{\varepsilon}_{n+1_\alpha}^{r} \tag{4.85}$$

If the trial stress satisfies the yielding condition:

$$f_{n+1}^{trial}(\boldsymbol{\tau}_{n+1}^{tr}, q_n) \leq 0, \tag{4.86}$$

then the actual increment is fully elastic and the trial state is indeed the solution(i.e.: $\boldsymbol{\tau}_{n+1_\alpha} = \boldsymbol{\tau}_{n+1_\alpha}^{tr}$ and $\boldsymbol{C}_\alpha^{Sr} = \boldsymbol{C}_\alpha^{el}$ Otherwise, a plastic correction is applied on the trial elastic estimate to bring the stress back onto the yield surface.

$$\boldsymbol{\tau}_{n+1_\alpha} = \boldsymbol{\tau}_{n+1_\alpha}^{tr} - 2G\Delta\gamma_\alpha\boldsymbol{N}_{n+1_\alpha} \tag{4.87}$$

[2]Equations such eq.(4.83) and similar equations such as eq.(4.85) need a more rigorous mathematical treatment because they involve tensors which are computed on different configurations. This is left for future work.

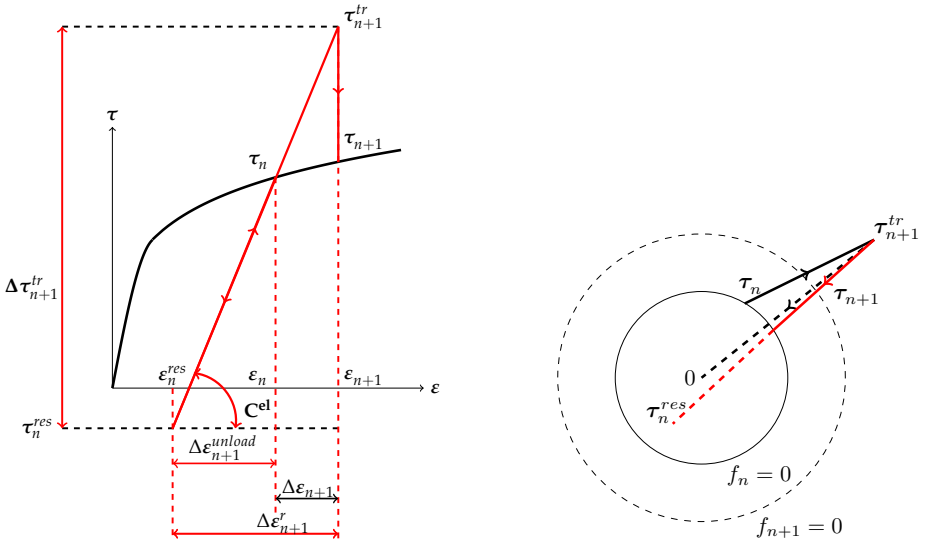

Figure 4.10: The predictor-corrector scheme: the trial stress is computed from an elastic increment (a) (i.e.: $\boldsymbol{C}^{Sr} = \boldsymbol{C}^{el}$), the plastic correction brings the stress back to the yield surface ($f_{n+1} = 0$): both the classical radial return mapping and the modified direction of the plastic flow adopted in this model are presented (b).

Following Wu et al. (2013a), we choose a modified plastic flow direction given by:

$$\boldsymbol{N}_{n+1_\alpha} = \frac{3}{2}\frac{\mathrm{dev}(\boldsymbol{\tau}_{n+1_\alpha} - \boldsymbol{\tau}^{res}_{n_\alpha})}{J_2(\boldsymbol{\tau}_{n+1_\alpha} - \boldsymbol{\tau}^{res}_{n_\alpha})} = \frac{3}{2}\frac{\mathrm{dev}(\boldsymbol{C}^{Sr} : \Delta\boldsymbol{\varepsilon}^{r}_{n+1_\alpha})}{J_2(\boldsymbol{C}^{Sr} : \Delta\boldsymbol{\varepsilon}^{r}_{n+1_\alpha})} \tag{4.88}$$

which satisfies $\boldsymbol{N} : \boldsymbol{N} = \frac{3}{2}$. This implies that the plastic correction is directed along $\Delta\boldsymbol{\tau}^{r}_{\alpha}$ and not along $\boldsymbol{\tau}_\alpha$ as in the classical relation (eq. (4.74)). However, when $\mathrm{dev}(\boldsymbol{\tau}^{res}) = 0$, the classical case is retrieved. The approximation used in the calculation of $\boldsymbol{N}$ is schematically depicted in Fig (4.10-(b)). It will be shown later that this approximation allows to directly obtain an isotropic incremental-secant operator. The trial flow direction is also introduced as:

$$\boldsymbol{N}^{tr}_{n+1_\alpha} = \frac{3}{2}\frac{\mathrm{dev}(\boldsymbol{\tau}^{tr}_{n+1_\alpha} - \boldsymbol{\tau}^{res}_{n_\alpha})}{J_2(\boldsymbol{\tau}^{tr}_{n+1_\alpha} - \boldsymbol{\tau}^{res}_{n_\alpha})} = \frac{3}{2}\frac{\mathrm{dev}(\boldsymbol{C}^{el} : \Delta\boldsymbol{\varepsilon}^{r}_{n+1_\alpha})}{J_2(\boldsymbol{C}^{el} : \Delta\boldsymbol{\varepsilon}^{r}_{n+1_\alpha})} \tag{4.89}$$

and it was shown (see Wu et al. (2013a)) that $\boldsymbol{N}^{tr}_{n+1_\alpha} = \boldsymbol{N}_{n+1_\alpha}$. This leads to the following result (from definitions (4.88) and (4.89)):

$$J_2((\boldsymbol{\tau}_{n+1_\alpha} - \boldsymbol{\tau}^{res}_{n_\alpha})) + 3G\Delta\gamma = J_2((\boldsymbol{\tau}^{tr}_{n+1_\alpha} - \boldsymbol{\tau}^{res}_{n_\alpha})) \tag{4.90}$$

The plastic correction consists in solving the last equation together with $f(\boldsymbol{\tau}_{n+1}, q_{n+1}) = 0$. The stress increment $\Delta\boldsymbol{\tau}^{r}_{n+1_\alpha}$ evaluated from the residual state can be obtained combining equations (4.83-b), (4.87) and (4.85):

$$\Delta\boldsymbol{\tau}^{r}_{n+1_\alpha} = \boldsymbol{C}^{el} : \Delta\boldsymbol{\varepsilon}^{r}_{n+1_\alpha} - 2G\Delta\gamma\boldsymbol{N}_{n+1_\alpha} \tag{4.91}$$

Substituting (4.91) into (4.84) and using (4.89) yield the following explicit expression of the incremental-secant operator:

$$\boldsymbol{C}_\alpha^{Sr} = \boldsymbol{C}_\alpha^{el} - 3G\Delta\gamma \frac{\boldsymbol{\mathcal{I}}^{\text{dev}} : \boldsymbol{C}_\alpha^{el}}{J_2(\boldsymbol{C}_\alpha^{el} : \Delta\boldsymbol{\varepsilon}^r_{n+1_\alpha})} \tag{4.92}$$

Since $\boldsymbol{C}_\alpha^{el}$ is isotropic, the residual-incremental-secant operator $\boldsymbol{C}_\alpha^{Sr}$ of the linear comparison material is also isotropic and can be recast as:

$$\boldsymbol{C}_\alpha^{Sr} = 3k^{Sr}\boldsymbol{\mathcal{I}}^{vol} + 2G^{Sr}\boldsymbol{\mathcal{I}}^{\text{dev}}, \tag{4.93}$$

with

$$k_\alpha^{Sr} = k_\alpha^{el}, \tag{4.94}$$

$$G_\alpha^{Sr} = G_\alpha^{el} - \frac{3(G_\alpha^{el})^2\Delta\gamma}{J_2(\Delta\boldsymbol{\tau}^{tr}_{n+1_\alpha})} \tag{4.95}$$

In the particular case of an elastic loading in the phase α, it is seen from (4.94) and (4.95) that the incremental secant operator reduces to the elastic tensor.

4.5.3.2 Homogenization procedure

Consider now a two-phase composite made of at least one hyperelastic-plastic phase. The so-called Linear Comparison Composite is defined through the residual-incremental-secant operators which are chosen by design uniform per phase α and will be denoted $\bar{\boldsymbol{C}}_\alpha^{Sr}$. It is also assumed that this fictitious composite has a spatial distribution of the phases and geometries that coincides with those of the actual non-linear composite. On a time interval $[t_n, t_{n+1}]$, the data are the macroscopic deformation gradient $\bar{\boldsymbol{F}}$ and $\Delta\bar{\boldsymbol{F}}$. All history variables at t_n are also known for both the composite and each phase α including the residual variables obtained from the virtual elastic unloading of the LCC. It is also assumed that the LCC is subjected to a strain increment $\Delta\bar{\boldsymbol{\varepsilon}}^r_{n+1}$ which is deduced from the unloaded residual state and which is different from the actual strain increment $\Delta\bar{\boldsymbol{\varepsilon}}_{n+1}$ applied to the actual RVE. This macroscopic strain increment is computed from:

$$\Delta\bar{\boldsymbol{\varepsilon}}^r_{n+1} = \bar{\boldsymbol{\varepsilon}}_n + \Delta\bar{\boldsymbol{\varepsilon}}_{n+1} - \bar{\boldsymbol{\varepsilon}}^{res}_{n+1} \tag{4.96}$$

The strain partitioning between the two phases is governed by the strain concentration tensor evaluated from the virtual elastic operators of the LCC and which corresponds in our secant approach to the secant moduli:

$$\Delta\boldsymbol{\varepsilon}^r_{n+1_I} = \boldsymbol{B}^\varepsilon(\boldsymbol{\mathcal{I}}, \boldsymbol{C}_M^{Sr}, \boldsymbol{C}_I^{Sr}) : \Delta\boldsymbol{\varepsilon}^r_{n+1_M} \tag{4.97}$$

The expression of $\boldsymbol{B}^\varepsilon$ corresponds in this work to the one for Mori-Tanaka model and reads:

$$\boldsymbol{B}^\varepsilon = \boldsymbol{\mathcal{I}} + \boldsymbol{\mathcal{S}} : [(\boldsymbol{C}_M^{Sr})^{-1} : \boldsymbol{C}_I^{Sr} - \boldsymbol{\mathcal{I}}]^{-1} \tag{4.98}$$

The homogenization procedure which allows to update the macroscopic stress is described in the following:

- Compute the macroscopic left Cauchy Green strain tensor:

$$\bar{\boldsymbol{b}}_{n+1} = \bar{\boldsymbol{F}}_{n+1} \cdot \bar{\boldsymbol{F}}_{n+1}^{T}$$

- Make the spectral decomposition of $\bar{\boldsymbol{b}}$ from which eigenvalues are denoted $(\lambda_A)^2$ and principal directions $\boldsymbol{e}^{(A)}$.

- Compute the macroscopic logarithmic strain at t_{n+1}:

$$\bar{\boldsymbol{\varepsilon}}_{n+1} = \sum_{A=1}^{3} \ln(\lambda_A) \boldsymbol{e}^{(A)} \otimes \boldsymbol{e}^{(A)}$$

- Compute the macroscopic strain increment to be applied on the LCC from eq. (4.96)

- **Initialization** : the strain increment in the inclusion phase is initialized from the macroscopic one:

$$\Delta\boldsymbol{\varepsilon}^{r}_{n+1_I} \leftarrow \Delta\bar{\boldsymbol{\varepsilon}}^{r}_{n+1}$$

- **Iteration** (i): A Newton-Raphson iterative process is applied over the strain increment in the inclusions phase (upper indices (i) are omitted for simplicity)

  1) Compute the strain increment in the matrix phase:

$$\Delta\boldsymbol{\varepsilon}^{r}_{n+1_M} = \frac{\Delta\bar{\boldsymbol{\varepsilon}}^{r}_{n+1} - f_{n_I}\Delta\boldsymbol{\varepsilon}^{r}_{n+1_I}}{f_{n_M}}$$

  2) Trial elastic state (for each phase $\alpha = I, M$):

  i Compute the trial elastic left Cauchy-Green strain at t_{n+1}:

$$\boldsymbol{b}^{e^{tr}}_{n+1_\alpha} = \boldsymbol{F}^{r}_{n+1_\alpha} \cdot \boldsymbol{C}^{p^{-1}}_{n_\alpha} \cdot \boldsymbol{F}^{r^{T}}_{n+1_\alpha}$$

  where the update of $\boldsymbol{F}^{r}_{n+1_\alpha}$ from $\Delta\boldsymbol{\varepsilon}^{r}_{n+1_\alpha}$ is detailed in Appendix A.

  ii Compute the trial principal elastic logarithmic stretches in the phase α $\bar{\boldsymbol{\varepsilon}}^{e^{tr}}_{n+1_\alpha}$ from (4.67) and (4.56).

  iii Compute the trial principal Kirchhoff stresses $\boldsymbol{\beta}^{tr}_{n+1_\alpha}$ from (4.71).

  iv Compute Kirchhoff trial stress $\boldsymbol{\tau}^{tr}_{n+1_\alpha}$ from (4.54-a)

  3) Call the constitutive box of each phase α (described in the previous section) with $\Delta\boldsymbol{\varepsilon}^{r}_{n+1_\alpha}$ and $\boldsymbol{\tau}^{tr}_{n+1_\alpha}$. The output is the updated stress $\boldsymbol{\tau}_{n+1_\alpha}$, the internal variables at t_{n+1} and the incremental secant operator $\boldsymbol{C}^{Sr}_{\alpha}$.

  4) Compute Eshelby's tensor $\boldsymbol{\mathcal{S}}_{n+1}$ with $\boldsymbol{C}^{Sr}_{n+1_M}$.

  5) Check compatibility of the strain increment in the matrix $\Delta\boldsymbol{\varepsilon}^{r}_{n+1_M}$. In order to solve these MFH iterations, eq.(4.97) is rewritten as $\boldsymbol{R} = 0$ where $\boldsymbol{R}$ is the stress residual in the inclusion phase. During the time step $[t_n; t_{n+1}]$, the strain increment $\Delta\bar{\boldsymbol{\varepsilon}}^{r}_{n+1}$ is constant and the stress residual can be evaluated as:

$$\boldsymbol{R} = \boldsymbol{C}^{Sr}_{n+1_M} : [\Delta\boldsymbol{\varepsilon}^{r}_{n+1_I} - \frac{1}{f_{n_M}} \boldsymbol{\mathcal{S}}^{-1}_{n+1} : (\Delta\boldsymbol{\varepsilon}^{r}_{n+1_I} - \Delta\bar{\boldsymbol{\varepsilon}}^{r}_{n+1})] - \boldsymbol{C}^{Sr}_{n+1_I} : \Delta\boldsymbol{\varepsilon}^{r}_{n+1_I}$$

- If $\|\boldsymbol{R}\| \leq \text{TOL}$, then exit the loop.
- Else: a new iteration has to be performed (go to step 1) and the strain increment in the inclusions phase is corrected following:

$$\Delta\boldsymbol{\varepsilon}^{r}_{n+1_I} \leftarrow \Delta\boldsymbol{\varepsilon}^{r}_{n+1_I} - \boldsymbol{J}^{-1} : \boldsymbol{R}$$

The Jacobian $\boldsymbol{J}$ matrix is computed at constant $\Delta\bar{\boldsymbol{\varepsilon}}^{r}_{n+1}$, such that $\delta\boldsymbol{R} = \boldsymbol{J} : \delta\Delta\boldsymbol{\varepsilon}^{r}_{I}$. The details about the Newton-Raphson procedure and the computations of the Jacobian matrix are given in Appendix B.

After convergence:

- Compute the principal elastic logarithmic stretches in the different phases $\boldsymbol{\varepsilon}^{e}_{\alpha}$ at t_{n+1} from eq.(4.75-d).
- Compute the inverse of elastic left Cauchy-Green strain in both phases α:

$$(\boldsymbol{b}^{e}_{n+1_\alpha})^{-1} = \sum_{A=1}^{3} \exp[-2\varepsilon^{e}_{n+1_\alpha}]\boldsymbol{n}^{tr}_{n+1} \otimes \boldsymbol{n}^{tr}_{n+1}$$

- Compute plastic right Cauchy-Green strain:

$$\boldsymbol{C}^{p}_{n+1_\alpha} = \boldsymbol{F}^{r^T}_{n+1_\alpha} \cdot (\boldsymbol{b}^{e}_{n+1_\alpha})^{-1} \cdot \boldsymbol{F}^{r}_{n+1_\alpha}$$

- Update Green-Lagrange plastic strain at t_{n+1}:

$$\boldsymbol{\varepsilon}^{p}_{n+1_\alpha} = \frac{1}{2}(\boldsymbol{C}^{p}_{n+1_\alpha} - I)$$

- Update inclusions' shape and orientation at t_{n+1} using $\boldsymbol{F}^{r}_{n+1_I}$. The new geometry is designated by I_{n+1}.
- Update each phase's volume fractions:

$$f_{n+1_\alpha} = \frac{J_{n+1_\alpha} f_{0_\alpha}}{J_{n+1_M} f_{0_M} + J_{n+1_I} f_{0_I}}$$

with : $J_{n+1_\alpha} = \det\boldsymbol{F}^{r}_{n+1_\alpha}$

- Compute the macroscopic stress update:

$$\begin{cases} \bar{\boldsymbol{\sigma}}_{n+1} = f_{n+1_M} \dfrac{\boldsymbol{\tau}_{n+1_M}}{J_{n+1_M}} + f_{n+1_I} \dfrac{\boldsymbol{\tau}_{n+1_I}}{J_{n+1_I}} \\ \bar{\boldsymbol{\tau}} = \bar{J}\bar{\boldsymbol{\sigma}} \end{cases},$$

- **Unloading step**: A virtual elastic unloading is applied at the composite material level and the set of equations (4.77)-(4.82) needs to be solved in order to update the residual variables $\boldsymbol{\varepsilon}^{res}_{n+1_\alpha}, \boldsymbol{\varepsilon}^{\bar{res}}_{n+1}, \boldsymbol{\tau}^{res}_{n+1_\alpha}$.

4.5.4 Microstructure evolution

In the presented MFH model, the information of the microstructure that is taken into account are the volume fraction of each phase, the shape and orientations of the inclusions. It is assumed that initially, the inclusions are spheroids (that is ellipsoids of revolution) [3]. Note that due to the Eshelby's hypothesis, the inclusions must have the same aspect ratio and orientation. Those geometrical properties are described by the following set of internal variables:

- f_α: volume fraction of phase α
- $Ar_1 = \frac{a}{b}, Ar_2 = \frac{c}{b}$: two aspect ratios (constrained to be equal), with a, b and c are half the lengths of the principal axes of the ellipsoid.
- Euler angles to describe the orientation of the inclusions with respect to the global frame axes $\boldsymbol{e}_i$.

In the proposed algorithm, the volume fraction of the phase α is updated as follows: As for the entire RVE, we can define its macro volume change as follows:

$$J_{mac}(t) = \det \ < \boldsymbol{F}(\boldsymbol{X}, t) >_{\Omega_0} = \frac{V(t)}{V_0} \tag{4.99}$$

Each phase's initial volume fraction is defined as follows:

$$f_{0_\alpha} = \frac{V_{0_\alpha}}{V_0} \tag{4.100}$$

From the different definitions, the following equalities hold:

$$V(t) = \sum_\alpha V_\alpha(t) = V_0 J_{mac}(t) \tag{4.101}$$

The above results allow to update each phase's current volume fraction:

$$f_\alpha(t) = \frac{V_\alpha(t)}{V(t)} = \frac{J_\alpha(t)}{f_{0_M} J_M(t) + f_{0_I} J_I(t)} f_{0_\alpha} \quad \text{(no sum)} \tag{4.102}$$

Besides the volume fraction evolution, inclusions' (and more significantly cavities') shape and orientation evolve during the deformation process. An example of the evolution of the initially spherical inclusions into ellipsoids under large deformation is shown in figure 4.11.

[3] This restriction is motivated by the fact that Analytical formulae of the Eshelby's tensor are limited to the case of spheroids. Later, Withers (1989) extended this result to transversely isotropic medium, with the restriction that the direction of anisotropy is aligned with the revolution direction of the spheroid . In the other cases, a numerical evaluation of the tensor is necessary and was implemented by Gavazzi and Lagoudas (1990).

Figure 4.11: Hyperelastic matrix with initially spherical hyperelastic inclusions under uniaxial tension along direction 1. Evolution of inclusions' shape: superposition of the deformed and undeformed microstructures of the RVE.

If linear displacements are applied to the boundary of each ellipsoid, corresponding to the uniform deformation gradient $\boldsymbol{F}^0 = \boldsymbol{F}_I(t_{n+1})$, then it is possible to show that the spheroid transforms into an ellipsoid (but generally not a spheroid).
Solving the eigenvalue problem described below gives the lengths and the directions of the principal axes of the updated ellipsoid.
At t_n, the implicit ellipsoid equation has the following form:

$$\frac{x_n^2}{a_n^2} + \frac{y_n^2}{b_n^2} + \frac{z_n^2}{c_n^2} = 1 \tag{4.103}$$

where a Cartesian coordinate system is used, in which the origin is the center of the ellipsoid and the coordinate axes are aligned with the axes of the ellipsoid (see figure 4.12 for an illustration). The last equation can be written in a matrix equation:

$$\{\boldsymbol{X}_n\}^T[\boldsymbol{A}_n]\{X_n\} = 1, \text{ on } \partial(I) \tag{4.104}$$

with:

$$\{\boldsymbol{X}_n\} = \begin{bmatrix} x_n \\ y_n \\ z_n \end{bmatrix}; \quad [\boldsymbol{A}_n] = \begin{bmatrix} \frac{1}{a_n^2} & 0 & 0 \\ 0 & \frac{1}{b_n^2} & 0 \\ 0 & 0 & \frac{1}{c_n^2} \end{bmatrix}$$

At t_{n+1}, on $\partial(I)$ we have:

$$\boldsymbol{X}_{n+1} = \boldsymbol{F}_{n+1_I}.\boldsymbol{X}_0 = \boldsymbol{F}_{n+1_I} \,.\, \boldsymbol{F}_{n_I}^{-1} \,.\, \boldsymbol{X}_n \tag{4.105}$$

or equivalently:

$$\boldsymbol{X}_n = \boldsymbol{F}_{n_I}.\, \boldsymbol{F}_{n+1_I}^{-1} \,.\, \boldsymbol{X}_{n+1} \tag{4.106}$$

Using this last relation combined with eq.(4.104), the ellipsoid's equation at t_{n+1} becomes:

$$\{\boldsymbol{X}_{n+1}\}^T[\boldsymbol{F}_{n+1_I}]^{-T}[\boldsymbol{F}_{n_I}]^T[\boldsymbol{A}_n][\boldsymbol{F}_{n_I}][\boldsymbol{F}_{n+1_I}]^{-1}\{X_{n+1}\} = 1, \text{ on } \partial(I) \tag{4.107}$$

or equivalently:

$$\{\boldsymbol{X}_{n+1}\}^T[\boldsymbol{A}_{n+1}]\{X_{n+1}\} \;=\; 1 \tag{4.108}$$

The eigendecomposition of the matrix $\boldsymbol{A}_{n+1}$ provides the new principal directions of the ellipsoid and the new lengths of the principal semi-axes.
In a last step, we approximate the ellipsoid by a spheroid by constraining the two aspect ratios to be equal while conserving the "true" volume fraction and the longest semi-axe.

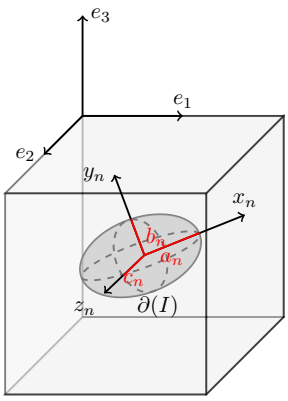

Figure 4.12: Semi-principal axes and principal axes of the ellipsoid at a given time t_n.

4.5.5 Assessment of the model

The MFH incremental-secant formulation presented in the previous section is tested for several two-phase particulate composites and porous materials. We compare its predictions to reference results obtained from FE simulations.

Composites with spherical inclusions

We consider first periodic composites made of an hexagonal array of spherical inclusions. Such composites can be approximated by cylindrical unit cells allowing full-field computations at low computational cost using axisymmetric elements (see 4.4.5).

- **Metal matrix composites**

The MFH incremental secant procedure is first assessed for a metal matrix composite (MMC) which is made of a J_2 elasto-plastic matrix reinforced by stiffer elastic inclusions. The matrix phase presents isotropic hardening described by a power law: $q(\xi) = h\xi^n$.
The material parameters for the matrix and the inclusions' phases are:

- Inclusions: E= 400 GPa, ν =0.2;
- Matrix: E= 75 GPa, ν = 0.3,σ_Y=75 MPa, h=416 MPa, n=0.3895.

These parameters correspond to an aluminum alloy reinforced with stiff ceramic particles. Two initial inclusions' volume fractions are considered: f_{0_I}=0.1 and f_{0_I}=0.2. Fig.4.13 shows the effective response of the two considered metal matrix composites as well as the

response of the matrix without reinforcement (i.e f_{0_I}=0). Predictions of the macroscopic response delivered by the MFH-incremental-secant formulation are in a good agreement with the reference results from FE computations.

The phases' responses predicted by the MF model and FE analysis are also presented in Fig.4.14. One could notice that the phase responses are fairly captured by the mean-field model for the composite containing 10% of inclusions. However inaccuracies are related to the prediction of the inclusion response for the composite comprising 20% of inclusions. The stress in the inclusion phase is underestimated but compensated by a slight overestimation of the matrix stress thus this inaccuracy does not affect the macroscopic behavior as seen in Fig.4.13.

- **Dual-phase steel**

As a second illustration, we consider a dual-phase steel consisting in 20% of spherical elastic inclusions dispersed in a ferrite-based matrix. We consider the following materials properties:

- Inclusions: E= 200 GPa, ν =0.3;
- Matrix: E= 220 GPa, ν = 0.3,σ_Y=300 MPa, h=1130 MPa, n=0.31.

The microstructure is subjected to uniaxial tension followed by compression until the initial undeformed state. The macroscopic response of the composite as predicted by MF model is confronted to results obtained from FE computations. Fig.4.15 illustrates the different predictions. At the first stage of the loading (tensile part), MF predictions and FE results are almost superposed. Elastic unloading is also well predicted by our MF model. However, for the compression stage, the elasto-plastic transition is not accurately captured by MF model and at the final stage of compression the stress level is moderately overestimated. Nevertheless, the mismatch between the different predictions does not exceed 10%.

Composites with ellipsoidal inclusions

We consider again the same materials properties as the the dual-phase steel considered previously and we aim to assess the capability of the model to capture the effect of the morphology of the inclusion phase on the effective behavior of the composite. As an illustration, we consider ellipsoidal inclusions with aspect ratio of 3, the long diameter is aligned with the direction of traction. For the FE analysis, we considered two different models. The first model consists in an axisymmetric unit cell and presents the advantage of low computational cost. In order to attain the desired volume fraction 20%, it was necessary to consider an aspect ratio of the unit cell $\frac{R}{H} \neq 1$. In our model (see fig.4.16), $\frac{R}{H} = 0.25$. The second model is a 3D periodic unit cell (see Fig.4.17) representative of a periodic regular array of short fibers. Periodic boundary conditions are applied to the prism faces. The unit cell was meshed using modified 10-node tetrahedra with hour-glass control (C3D10M in Abaqus) for the elastic (stiff) inclusions and hybrid with linear pressure(C3D10MH) for the metallic matrix phase. The obtained results are reported in Fig.4.18 and they correspond to the longitudinal stress. It is expected that this composite made with ellipsoids (Aspect ratio=3) has a better resistance in the longitudinal direction

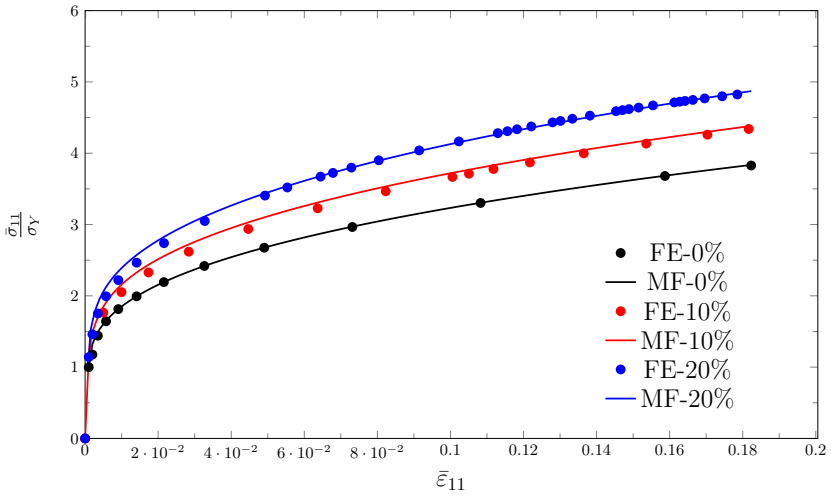

Figure 4.13: Effective response of three MMCs (0%, 10% and 20% of stiff inclusions embedded in an elasto-plastic matrix): simulation of uniaxial tension.

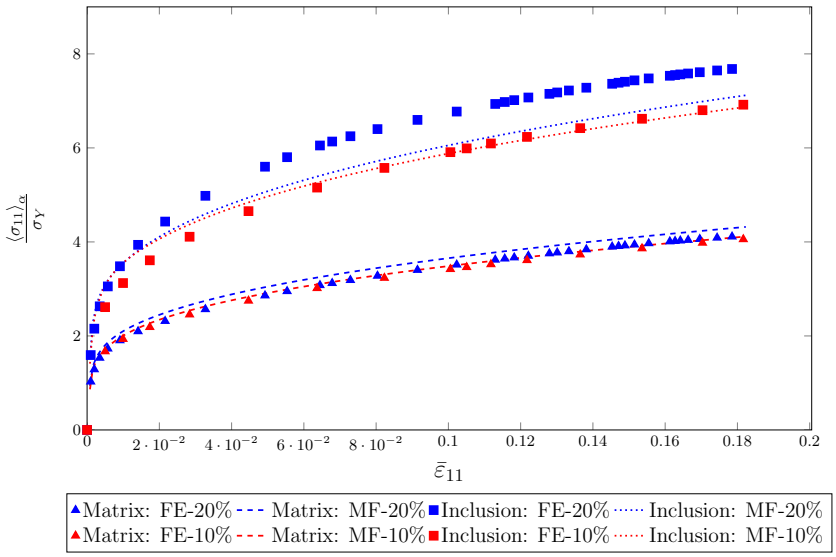

Figure 4.14: Prediction of the per-phase response of two MMCs made of 10% and 20% of stiff inclusions embedded in an elasto-plastic matrix.

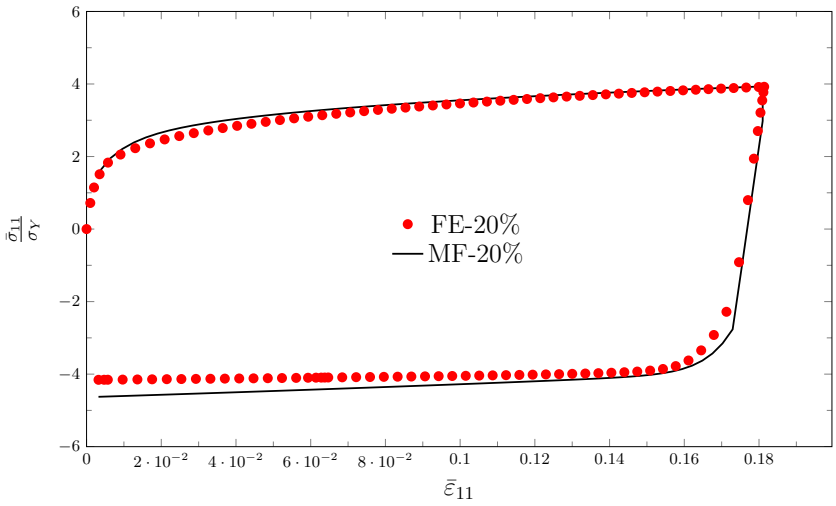

Figure 4.15: Macroscopic response of a dual-phase steel under uniaxial tension followed by uniaxial compression: a comparison between FE analysis of axisymmetric unit cell and MFH-incremental secant formulation

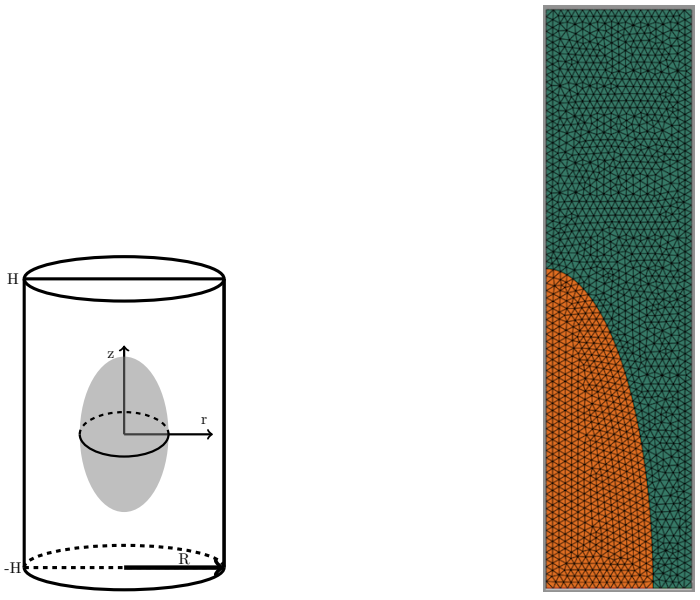

Figure 4.16: Axisymmetric cell used to model a MMC reinforced by ellipsoidal inclusions for FE computations: (a)Cylindrical unit cell, (b) 2D axisymmetric cell for spheroidal inclusions

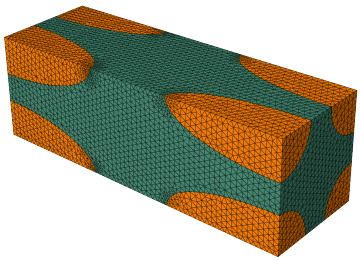

Figure 4.17: 3D unit cell used for FE computation: ellipsoidal particles are aligned and periodic boundary conditions are applied.

than the composite reinforced by spheres (see Fig.4.15 for comparison). This was the case with a different degrees of strengthening according to the different used approaches. The two different models used for FE computations give the same stress-strain curve for the linear elasticity zone and quite different results for the plastic regime. Axisymmetric model predicts higher composite strengthening than full 3D model. The stiffer response given by the hexagonal array (obtained from the axisymmetric cell) probably occur because the geometrical constraints (unit cell low aspect ratio) needed for forming the unit cell lead to neighbouring particles which are close to each other, and this overestimates the coupling between the particles. This scatter between the FE results obtained from 3D and axisymmetric calculations was already pointed out by Saraev and Schmauder (2003). The authors explain the higher stress-strain curves obtained from axisymmetric unit cell by the fact that the particle in cylindrical cell is influenced by a higher number of neighbourhing particles in the transverse direction around its circumference compared to the particles in the 3D cell. Fig.4.18 shows that the predictions with the MFH-incremental secant model are closer to 3D FE results. Note that the MF model assumes aligned randomly distributed ellipsoidal inclusions.

Porous material

A porous metallic matrix is considered now. The matrix has the same material properties as the aluminium alloy considered previously for the MMC. In stead of reinforcements, we consider initially spherical voids dispersed in the matrix phase with initially 25% of porosity.
The FE simulations performed in this study are based on cubic RVEs consisting of a random dispersion of about 50 initially spherical cavities and having different sizes embedded in a continuum matrix. The RVE microstructure is periodic along the cube axes allowing to apply periodic boundary conditions (PBCs) written as:

$$\boldsymbol{x}^{+} - \boldsymbol{x}^{-} = \boldsymbol{F}_{mac}.(\boldsymbol{X}^{+} - \boldsymbol{X}^{-}) \tag{4.109}$$

where symbols + and − designate opposite faces of the RVE boundary. In fact, it has been shown that PBCs lead to the best predictions and a faster convergence rate of the overall properties as the size of the RVE increases compared to prescribed displacements and tractions, e.g. van der Sluis et al. (2000) and Terada et al. (2000) The RVEs were meshed

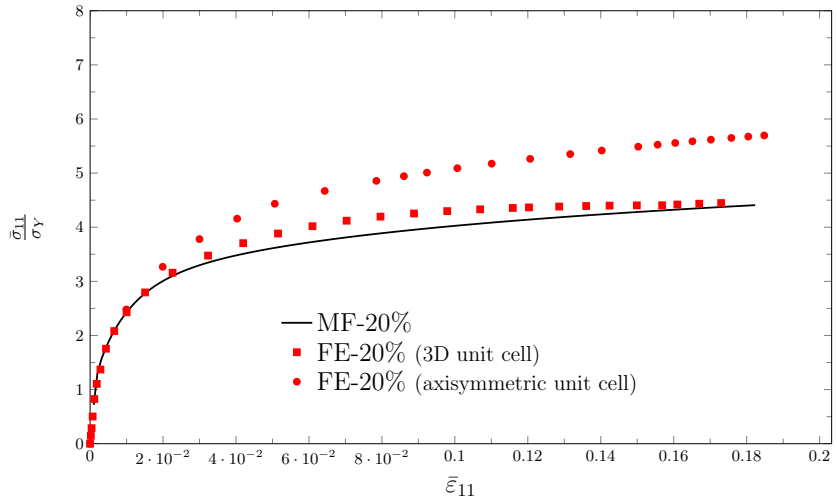

Figure 4.18: Results for the composite with 20% of ellipsoidal reinforcements loaded in the longitudinal direction.

using modified 10-node tetrahedra hybrid elements with linear pressure (C3D10MH). For the simulations three different cases were generated: a "reference" one with a fine mesh comprising approximately 3×10^5 elements and 4×10^5 nodes and two other ones comprising typically 1.6×10^5 elements. Each of the three cases corresponds to a different random realization of the microstructure, and it was checked that the scatter in the macroscopic responses is negligible (less than 2% in all studied cases).

The predictions of the effective response for a tension test are reported on Fig.4.19. The response of the matrix material without cavities is also presented to give an impression of the influence of the holes. The figure shows that the MFH-incremental secant model is able to reproduce fairly well the stress-strain curve.

4.6 Conclusions

We proposed two finite strain MFH formulations: incremental - tangent and incremental - secant which both present several original features with respect to the existing literature. Microstructures such that multiple solid inclusions or cavities of ellipsoidal shapes are embedded in a continuum matrix can be studied. For hyperelastic-plastic constituents, the local models follow the framework of the thermodynamics of irreversible processes and are based on two main assumptions: a multiplicative decomposition of the deformation gradient into elastic and inelastic parts, and a hyperelastic relation between the Kirchhoff stress and the left Cauchy-Green strain tensors. Special emphasis was put on proper definition of macro stress measures and tangent operators. Computational algorithms were developed for a finite strain version of the Mori-Tanaka MFH model and numerically implemented.

The proposed MFH formulations and algorithms were extensively tested under various loadings. Different microstructures were considered: hyperelastic-viscoplastic ma-

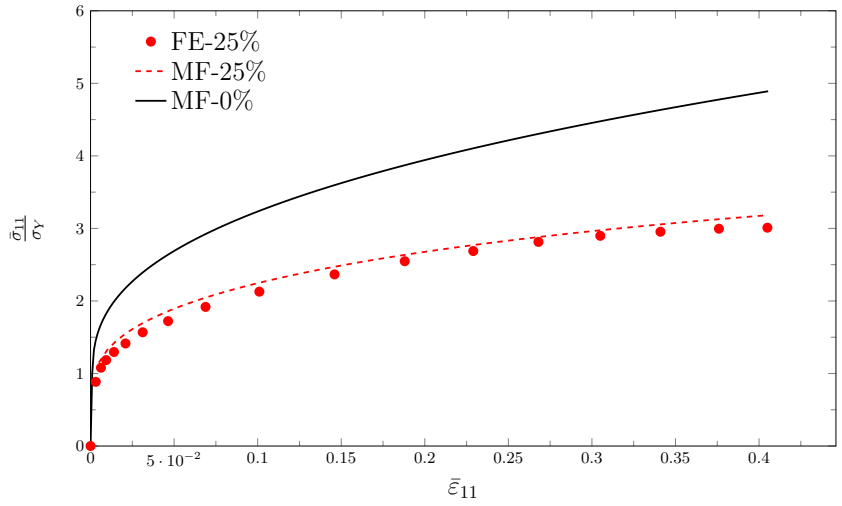

Figure 4.19: Effective response of a porous metallic matrix containing 25% of initially spherical cavities. The response of the matrix without cavities is also provided for comparison.

trix with hyperelastic inclusions and porous hyperelastoplastic matrix. Different values of initial volume fraction of solid inclusions were considered. The MFH predictions were compared against direct full-field FE simulations on RVEs or unit cells and found to be accurate.

For the hyperelastic-viscoplastic model of Sect4.4.5 , the incremental-tangent formulation of Sect. 4.4.1 was used. However, since the latter supposes rate-independent materials, the partition of mean deformation gradient values between matrix and inclusions' phases may not be accurate enough. For that application, one should use a MFH based on an affine linearization of the local rate-dependent models, e.g. extend to the finite strain regime the incrementally affine method of Doghri et al. (2010).

The MFH methods proposed in this chapter are based on first statistical moments, i.e. only the mean values (volume averages) of the per-phase deformation gradient are used to compute an approximation of the mean nominal stresses in the phases. Better predictions are obtained by using a richer information, namely the second statistical moments, which enable to measure the variance of the micro fields. For hyperelastic constituents, such MFH formulations, based on variational theorems, have been proposed by Ponte Castañeda, Suquet and their co-workers. For elasto(visco)plastic composites, the challenge is to include field fluctuations while having truly history-dependent material models in each phase, and being able to simulate non-monotonic and non-proportional loadings. This has been achieved in the small-strain regime by the recent formulations of Doghri et al. (2011), Wu et al. (2015), Brassart et al. (2011), Brassart et al. (2012) and Lahellec and Suquet (2013), each based on a different approach. It remains to extend those formulations to the finite strain regime.

Under large deformation, moderate or severe strain localizations can occur. For the former case, strain heterogeneity is pronounced within each phase and our first-moment MFH formulations are expected to lead to poor predictions. Presumably, better results

could be obtained with MFH theories using both first and second statistical moments per phase. The more severe case is that of strain localization within thin bands. As shown by Hill (1962), Rice (1976) and many others, rate-independent (e.g., elasto-plastic) models for homogeneous materials can exhibit strain localization in the large deformation regime. Actually, even under infinitesimal strains, strain-softening rate-independent homogeneous material models also exhibit strain localization, typically due to the coupling with a damage evolution law, e.g. Doghri and Billardon (1995). The effect of heterogeneous micro-structures (e.g., porous or composite materials) has also been studied, e.g. Danas and Ponte Castañeda (2012) and Tvergaard (2014). One important consequence of localization is the loss of uniqueness of the initial boundary value problem. Therefore, even a full-field FE resolution becomes unreliable as it leads to severe mesh-sensitive post-localization predictions. The issue has been debated extensively in the literature, for homogeneous and heterogeneous materials, and various constitutive models. Numerous authors have proposed various solutions, typically involving viscous regularization, non-local material modeling or higher order continuum theories, and FE procedures have been designed to deal with the proposed regularizations. For a review, see for instance Petryk (1997). Some generalized MFH methods have also been proposed in order to address the issue of strain localization in heterogeneous materials, e.g. Wu et al. (2013b).

Appendix A

Update of the deformation gradient in phase α from Mori-Tanaka iterations

In the described homogenization algorithm (section 4.5.3.2), iterations are needed to ensure the compatibility of mean strain increments in the different phases. The iterations allow to update the mean strain increment $\Delta\varepsilon^r_\alpha$. However, for the update of the trial stress and the plastic right Cauchy Green strain in the phase α, the updated deformation gradient per phase $\boldsymbol{F}^r_\alpha$ is needed. From the polar decomposition of $\boldsymbol{F}$ we have:

$$\boldsymbol{F} = \boldsymbol{V} \cdot \boldsymbol{R} \tag{4.110}$$

where $\boldsymbol{R}$ is the rotation tensor and $\boldsymbol{V}$ is the left stretch tensor. We need to update those tensors from the knowledge of $\Delta\boldsymbol{\varepsilon}^r_\alpha$ at each iteration (i). This can be done by means of an approximation consisting in calling in every iteration the rotation tensor of the previous iteration as follows:

- Initialization:
  - Set $\boldsymbol{R}^{(i)}_{(t=0)_\alpha} = \mathbf{1}$,
  - $\boldsymbol{R}^{(0)}_{n+1_\alpha} = \boldsymbol{R}_{n_\alpha}$.
- For iteration $(i) \geq 1$:
  - Spectral decomposition of the logarithmic strain $\boldsymbol{\varepsilon}^{(i)}_{n+1_\alpha}$ which is updated from $\Delta\boldsymbol{\varepsilon}^{r^{(i)}}_\alpha$ (see eq. (4.83-a)):

$$\boldsymbol{\varepsilon}^{(i)}_{n+1_\alpha} = \sum_{A=1}^{3} \ln(\lambda^{(i)}_{A_\alpha}) \boldsymbol{e}^{(A)^{(i)}}_\alpha \otimes \boldsymbol{e}^{(A)^{(i)}}_\alpha \tag{4.111}$$

  - The eigenvectors of the right Cauchy-Green strain can be approximated from

$$\boldsymbol{E}^{(A)^{(i)}}_{n+1_\alpha} \simeq (\boldsymbol{R}^{(i-1)}_{n+1_\alpha})^T \cdot \boldsymbol{e}^{(A)^{(i)}}_\alpha \tag{4.112}$$

  - Inverse of left stretch tensor:

$$(\boldsymbol{V}^{(i)}_{n+1_\alpha})^{-1} = \sum_{A=1}^{3} \frac{1}{\lambda^{(i)}_{A_\alpha}} \boldsymbol{e}^{(A)^{(i)}}_\alpha \otimes \boldsymbol{e}^{(A)^{(i)}}_\alpha \tag{4.113}$$

  - Spectral decomposition of deformation gradient:

$$\boldsymbol{F}^{r^{(i)}}_{n+1_\alpha} \simeq \sum_{A=1}^{3} \lambda^{(i)}_{A_\alpha} \boldsymbol{e}^{(A)^{(i)}}_\alpha \otimes \boldsymbol{E}^{(A)^{(i)}}_{n+1_\alpha} \tag{4.114}$$

  - Update the rotation tensor to be used in the next iteration:

$$\boldsymbol{R}^{(i)}_{n+1_\alpha} \simeq (\boldsymbol{V}^{(i)}_{n+1_\alpha})^{-1} \cdot \boldsymbol{F}^{r^{(i)}}_{n+1_\alpha} \tag{4.115}$$

Appendix B

Numerical resolution of the localization equations: Newton-Raphson scheme

Derivation of the secant operator

The evaluation of $\frac{\partial \boldsymbol{C}^{Sr}}{\partial \boldsymbol{\varepsilon}}$, follows from

$$\frac{\partial \boldsymbol{C}^{Sr}}{\partial \boldsymbol{\varepsilon}} = \frac{\partial}{\partial \Delta \boldsymbol{\varepsilon}^r}\left(3\kappa^{Sr}\boldsymbol{I}^{vol} + 2G^{Sr}\boldsymbol{I}^{\mathrm{dev}}\right) : \frac{\partial \Delta \boldsymbol{\varepsilon}^r}{\partial \boldsymbol{\varepsilon}} = 2\boldsymbol{I}^{\mathrm{dev}} \otimes \frac{\partial G_s^r}{\partial \Delta \boldsymbol{\varepsilon}^r} \tag{4.116}$$

Using, $\frac{\partial J_2(\Delta\boldsymbol{\tau})}{\partial \Delta \boldsymbol{\tau}^r} = \frac{3}{2}\frac{\partial \Delta \boldsymbol{\tau}}{\partial \Delta \boldsymbol{\tau}^r}$, $\frac{\partial \Delta \mathrm{dev}(\boldsymbol{\tau})}{\partial \Delta \boldsymbol{\tau}^r} = \boldsymbol{I}^{\mathrm{dev}}$, $\frac{\partial \Delta \boldsymbol{\varepsilon}^{eq}}{\partial \Delta \boldsymbol{\varepsilon}^r} = \frac{2}{3}\frac{\partial \Delta \boldsymbol{\varepsilon}}{\partial \Delta \boldsymbol{\varepsilon}^r}$, and equation 4.95 this last relation becomes

$$\frac{\partial \boldsymbol{C}^{Sr}}{\partial \boldsymbol{\varepsilon}} = 2\boldsymbol{I}^{\mathrm{dev}} \otimes \left[\frac{1}{6G_s^r(\Delta\varepsilon^{eq})^2}\Delta \mathrm{dev}(\boldsymbol{\tau}) : \boldsymbol{C}^{alg} - \frac{2}{3}G_s^r\frac{\Delta \boldsymbol{e}}{(\Delta\varepsilon^{eq})^2}\right] \tag{4.117}$$

where the increments of the stress and strain tensors are decomposed into their hydrostatic and deviatoric parts:

$$\Delta\boldsymbol{\tau}^r = \Delta\boldsymbol{\tau}^m\mathbf{1} + \Delta \mathrm{dev}(\boldsymbol{\tau}) \text{ and } \Delta\boldsymbol{\varepsilon}^r = \Delta\boldsymbol{\varepsilon}^m\mathbf{1} + \Delta\boldsymbol{e} \tag{4.118}$$

with $\Delta\boldsymbol{\tau}^m = \frac{1}{3}tr(\Delta\boldsymbol{\tau})$, $\Delta\boldsymbol{\varepsilon}^m = \frac{1}{3}tr(\Delta\boldsymbol{\varepsilon})$, and $\Delta\boldsymbol{e} = \Delta\boldsymbol{\varepsilon} - \Delta\boldsymbol{\varepsilon}^m\mathbf{1}$.
In Eq.(4.117), $\boldsymbol{C}^{alg}$ is the derivative of the stress increment with respect to the strain increment, which is obtained from the constitutive law of the material. Due to the modification of the return mapping algorithm, this expression is slightly changed compared to the usual one and reads

$$\boldsymbol{C}^{alg} = \boldsymbol{C}^{el} - \frac{\left(2G^{el}\right)^2}{h}\boldsymbol{N}\otimes\boldsymbol{N} - \frac{\left(2G^{el}\right)^2\Delta\xi}{\left(\boldsymbol{\tau}_{n+1}^{tr} - \boldsymbol{\tau}_n^{res}\right)^{eq}}\left(\frac{2}{3}\boldsymbol{I}^{\mathrm{dev}} - \boldsymbol{N}\otimes\boldsymbol{N}\right) \tag{4.119}$$

with $h = \frac{1}{3}\boldsymbol{N} : \left(\frac{3}{2}\frac{\mathrm{dev}(\boldsymbol{\tau}_{n+1})}{J_2(\boldsymbol{\tau})}\right)^{-1}\frac{\partial q}{\partial \xi} + 3G^{el}$

Residual stress vector and Jacobian evaluation

The equation to be satisfied at the end of the MFH procedure is Eq.(4.97). The averaging rule is applied in this work to the residual strains increments as:

$$\Delta\bar{\boldsymbol{\varepsilon}}_{n+1}^r = f_M\Delta\boldsymbol{\varepsilon}_{n+1_M}^r + f_I\Delta\boldsymbol{\varepsilon}_{n+1_I}^r \tag{4.120}$$

Multiplying Eq.(4.120) by $\boldsymbol{B}^{\epsilon}(\boldsymbol{I}, \boldsymbol{C}_0^{Sr}, \boldsymbol{C}_I^{Sr})$ and using Eq.(4.97) lead to:

$$f_M\Delta\boldsymbol{\varepsilon}_{n+1_I}^r + f_I\boldsymbol{B}^{\epsilon}(\boldsymbol{I}, \boldsymbol{C}_0^{Sr}, \boldsymbol{C}_I^{Sr}) : \Delta\boldsymbol{\varepsilon}_{n+1_I}^r = \boldsymbol{B}^{\epsilon}(\boldsymbol{I}, \boldsymbol{C}_0^{Sr}, \boldsymbol{C}_I^{Sr}) : \Delta\bar{\boldsymbol{\varepsilon}}_{n+1}^r \tag{4.121}$$

With M-T assumption, the strain concentration tensor follows from Eq.(4.98) and Eq. (4.121) reads

$$\Delta\boldsymbol{\varepsilon}^r_{n+1_I} + f_0\boldsymbol{\mathcal{S}} : \left[(\boldsymbol{C}^{Sr}_M)^{-1} : \boldsymbol{C}^{Sr}_I - \boldsymbol{I}\right] : \Delta\boldsymbol{\varepsilon}^r_{n+1_I} = \Delta\bar{\boldsymbol{\varepsilon}}^r_{n+1} \tag{4.122}$$

or again $\boldsymbol{F} = 0$ with

$$\boldsymbol{F} = \boldsymbol{C}^{Sr}_M : \left[\Delta\boldsymbol{\varepsilon}^r_{n+1_I} - \frac{1}{f_M}\boldsymbol{\mathcal{S}}^{-1} : (\Delta\boldsymbol{\varepsilon}^r_{n+1_I} - \Delta\bar{\boldsymbol{\varepsilon}}^r_{n+1})\right] - \boldsymbol{C}^{Sr}_I : \Delta\boldsymbol{\varepsilon}^r_{n+1_I} \tag{4.123}$$

In order to satisfy $\boldsymbol{F} = 0$, Eq. (4.123) is linearized as

$$d\boldsymbol{F} = \frac{\partial \boldsymbol{F}}{\partial \boldsymbol{\varepsilon}_I} : d\Delta\boldsymbol{\varepsilon}^r_I + \frac{\partial \boldsymbol{F}}{\partial \boldsymbol{\varepsilon}_M} : d\Delta\boldsymbol{\varepsilon}^r_M + \frac{\partial \boldsymbol{F}}{\partial \bar{\boldsymbol{\varepsilon}}} : d\Delta\bar{\boldsymbol{\varepsilon}}^r \tag{4.124}$$

When solving $\boldsymbol{F} = 0$ at constant $\Delta\bar{\boldsymbol{\varepsilon}}^r$, as $f_M\Delta\boldsymbol{\varepsilon}^r_{n+1_M} + f_I\Delta\boldsymbol{\varepsilon}^r_{n+1_I}$ is also a constant, the iteration process relies on $d\boldsymbol{F} = \boldsymbol{J} : d\boldsymbol{\varepsilon}_I$

$$\begin{aligned}
\boldsymbol{J} &= \tfrac{\partial \boldsymbol{F}}{\partial \boldsymbol{\varepsilon}_I} + \tfrac{\partial \boldsymbol{F}}{\partial \boldsymbol{\varepsilon}_M} : \tfrac{\partial \boldsymbol{\varepsilon}_M}{\partial \boldsymbol{\varepsilon}_I} \\
&= \boldsymbol{C}^{Sr}_{n+1_M} : \left[\boldsymbol{I} - \boldsymbol{\mathcal{S}}^{-1}\right] - \boldsymbol{C}^{Sr}_{n+1_I}\frac{\partial \boldsymbol{C}^{Sr}_{n+1_I}}{\partial \boldsymbol{\varepsilon}_I} : \Delta\boldsymbol{\varepsilon}^r_{n+1_I} - \tfrac{f_I}{f_M}\frac{\partial \boldsymbol{C}^{Sr}_{n+1_M}}{\partial \boldsymbol{\varepsilon}_M} \\
&: \left[\Delta\boldsymbol{\varepsilon}^r_{n+1_I} - \boldsymbol{\mathcal{S}}^{-1} : \frac{\Delta\boldsymbol{\varepsilon}^r_{n+1_I} - \Delta\bar{\boldsymbol{\varepsilon}}^r_{n+1_I}}{f_M}\right] - \tfrac{f_I}{f_M}\boldsymbol{C}^{Sr}_{n+1_M} \otimes (\Delta\boldsymbol{\varepsilon}^r_{n+1_I} - \Delta\bar{\boldsymbol{\varepsilon}}^r_{n+1}) \\
&:: (\boldsymbol{\mathcal{S}}^{-1} \otimes \boldsymbol{\mathcal{S}}^{-1}) :: \frac{\partial \boldsymbol{\mathcal{S}}}{\partial \boldsymbol{\varepsilon}_M} - \tfrac{f_I}{f_M}\boldsymbol{C}^{Sr}_{n+1_M} : \boldsymbol{\mathcal{S}}^{-1}
\end{aligned} \tag{4.125}$$

where $\frac{\partial \boldsymbol{C}^{Sr}_r}{\partial \boldsymbol{\varepsilon}_r}$ results from Eq4.117.
The derivative of Eshleby tensor is given by:

$$\frac{\partial \boldsymbol{\mathcal{S}}}{\partial \Delta\boldsymbol{\varepsilon}^r} = \frac{\partial \boldsymbol{\mathcal{S}}}{\partial \nu} \otimes \left(\frac{\partial \nu}{\partial \kappa}\frac{\partial \kappa}{\partial \Delta\boldsymbol{\varepsilon}^r} + \frac{\partial \nu}{\partial G^r_s}\frac{\partial G^{Sr}}{\partial \Delta\boldsymbol{\varepsilon}^r}\right) \tag{4.126}$$

One directly has

$$\frac{\partial \kappa}{\partial \Delta\boldsymbol{\varepsilon}^r} = 0 \tag{4.127}$$

and therefore

$$\frac{\partial \boldsymbol{\mathcal{S}}}{\partial \Delta\boldsymbol{\varepsilon}^r} = \frac{\partial \boldsymbol{\mathcal{S}}}{\partial \nu} \otimes \left(\frac{\partial \nu}{\partial G^{Sr}}\frac{\partial G^{Sr}}{\partial \Delta\boldsymbol{\varepsilon}^r}\right) \tag{4.128}$$

Once $\boldsymbol{F} = 0$ is satisfied, the effect on the strain increment in each phase of a variation $d\Delta\bar{\boldsymbol{\varepsilon}}^r$ can directly be obtained by constraining $d\boldsymbol{F} = 0$, and Eq(4.124) leads to [4]

$$0 = \frac{\partial \boldsymbol{F}}{\partial \boldsymbol{\varepsilon}_I} : d\Delta\boldsymbol{\varepsilon}^r_I + \frac{\partial \boldsymbol{F}}{\partial \boldsymbol{\varepsilon}_M} : d\Delta\boldsymbol{\varepsilon}^r_M + \frac{\partial \boldsymbol{F}}{\partial \bar{\boldsymbol{\varepsilon}}} : d\Delta\bar{\boldsymbol{\varepsilon}}^r \tag{4.129}$$

or again

[4] Note that the derivative with respect to $\Delta\boldsymbol{\varepsilon}^r_\alpha$ has the same expression as the derivative with respect to $\boldsymbol{\varepsilon}_\alpha$.

$$\frac{\partial \boldsymbol{\varepsilon}_I}{\partial \bar{\boldsymbol{\varepsilon}}} = -\boldsymbol{J}^{-1} : \frac{\partial \boldsymbol{F}}{\partial \bar{\boldsymbol{\varepsilon}}} \tag{4.130}$$

As under these circumstances $d\bar{\boldsymbol{\varepsilon}}^r = f_M d\boldsymbol{\varepsilon}_M^r + f_I d\boldsymbol{\varepsilon}_I^r$, this last equation is completed by

$$\frac{\partial \boldsymbol{\varepsilon}_M}{\partial \bar{\boldsymbol{\varepsilon}}} = \frac{1}{f_M}\left(\boldsymbol{\mathcal{I}} - f_I \frac{\partial \boldsymbol{\varepsilon}_I}{\partial \bar{\boldsymbol{\varepsilon}}}\right) \tag{4.131}$$

Conclusions

In the context of an increasing need for predictive modeling tools that accurately describe and allow to optimize the complex micro-macro mechanical relations of multi-phase materials, continuous efforts have been devoted to mean-field homogenization (MFH) approaches in order to enhance the accuracy of their predictions and the range of their applicability. In this line, this thesis aimed at shedding light upon some issues related to the homogenization of composite and porous materials.

In the first chapter, we investigated the potential of some mean-field (MF) models to predict the elastic and linear viscoelastic response of highly porous solids and pushed forward this investigation to the limiting case of cellular materials. We started from existing models in linear elasticity and via the correspondence principle, we made extensions to the linear viscoelastic behavior. We have first studied several micromechanical models for the prediction of the properties of open cell solids. The accuracy of their predictions were assessed by comparing them to FE computations on unit cells under periodic boundary conditions. It was found that for low relative density R, the analytical predictions of Young's and shear moduli were close to those of FE but discrepancy was observed for higher values of R and for the estimation of Poisson's ratio. In the second part of the chapter, some MF models were examined for the homogenization of porous solids and were confronted to FE simulations made on numerous RVEs for a la. It was found that for low concentration of dispersed impenetrable spherical voids, MF models yield good predictions. But when increasing the porosity and the pores become macroscopically interconnected only the differential scheme based on Mori-Tanaka (MT) model at each iteration succeeded to follow the variation of the effective elastic moduli for the entire range of porosity. We also tested Torquato's Three Point Estimates (see Torquato (2002) and Torquato (1998)). Their estimates are close to FE results for porous solids involving both microgeometries of "hard" and overlapping spherical cavities and to DM predictions for the latter morphology.
In a third part of the study, we tested the adequacy of some MF models to reproduce the behavior of low density open cell solids. It was concluded that some MF models give results comparable to those of beam theory models devoted to cellular solids in linear elasticity and viscoelasticity.

While in the current study we modeled open cell cellular solids by a periodic model of tetrakaidecahedral cell, the cells of a real material have irregular shapes and dimensions and the actual microstructure is more complex. The limitation of this study is that the models considered do not account for the irregularities due to imperfect geometry or/and irregular arrangement of cells. Among future improvements of the present study of low density materials (foam) is considering irregular cell structures. Such analysis of the effect of cell irregularities on the overall mechanical behavior does exist in Zhu et al. (2000), Bart-Smith et al. (2002),Li et al. (2006), Jeon and Asahina (2005) andLuxner et al. (2007) for instance.
Also, our approach does not predict size effects at it assumes a scale separation, i.e. the ratio of the sample size to the cell size is high. In some engineering applications, size effects are present, with or without scale separation. For instance, the specimen size might be of the order of the length scale of the cell. Trends of the stiffness and strength as function of the sample size are identified both experimentally (e.g. Anderson and

Lakes (1994), Andrews et al. (2001) and Jeon and Asahina (2005)) and numerically (see for instance Onck et al. (2001) and Tekoglu et al. (2011)).

Now, as regards the application of MF models to cellular materials, the former cannot be expected to capture aspects such as considerable changes of shape or buckling of cell struts or walls under compression.

Extending the MF scheme to the nonlinear regime for porous solids, especially under hydrostatic or high triaxiality loadings remains a challenging task. One step toward this objective has been achieved in the second chapter. In the pioneering model of Gurson (1977), only a single cavity embedded in a rigid plastic matrix was considered. Thus, the model did not incorporate interaction effects between cavities and therefore when dealing with moderate to high porosities, needs additional parameters in the macroscopic yield criterion to account for such effects. We proposed an original coupling between MFH and Gurson's solution. Alternative multiple cavities microstructures were considered and homogenized using the generalized self consistent (GSC) or the MT models based on secant formulations. Second statistical moment versions of secant GSC and MT were developed, which enabled to take into account the variance of the strain fields in each phase. When compared to full-field FE results for a large range of porosities (from 1% to 50%), it was found that the GSC model gives rather excellent predictions, except when both the porosity and the stress triaxiality are small. For the MT model, some predictions are good, especially at high porosities, while some others are not, especially at low porosities. A future work might consist in devising a predictive interpolative model between the proposed GSC at high porosities and the Gurson solution for dilute porosity. However, the interpolation should be predictive with no fitting parameters. Another important aspect that has to be considered for an improvement of the presently proposed model is the effect of the Lode parameter (which is a function of the third invariant J_3 of stress deviator). 3D numerical analysis by Zhang et al. (2001) and Gao and Kim (2006) who considered 3D loadings showed that this parameter has a significant effect on void growth and coalescence (see also Benzerga and Besson (2001) who investigated this effect under axisymmetric loadings).

Another direction was also pursued in this thesis in the perspective of accounting for more realistic constitutive behavior for ductile porous materials. In the framework of a static limit-analysis approach, and following the modelling strategy developped by Cheng et al. (2014), a new macroscopic criterion for porous ductile metals accounting for plastic anisotropy of the matrix phase was derived. Interestingly, the proposed procedure delivered an anisotropic macroscopic strength criterion which is not only pressure dependent, but exhibits an original sensitivity to the sign of the third invariant of the stress deviator.

At this stage, some additional partial conclusions as regards modelling of non linear porous materials need to be stated:

- First, MF models developed within our research group, namely the incremental tangent model Doghri and Ouaar (2003), Pierard and Doghri (2006), the variational model Brassart et al. (2011) and the incremental secant model Wu et al. (2013a) are not able in their current status to predict pressure sensitivity of the macroscopic response which is an important feature of porous materials. Also, since those models

extensively rely on the J2 plasticity model, considering other constitutive models with different flow rules for the matrix phase is not a straightforward modification. In addition, for perfectly plastic porous matrix, first order estimates of the MF models lead systematically to a macroscopic equivalent stress proportional to the one of the matrix phase which in this specific case remains constant for all the loading conditions. Therefore, MF models are not reliable for predicting yield surfaces of plastic porous materials.

- In the same line as the model developed within the second chapter and which couples MF models to Gurson's solution, one could explore more realistic material constitutive models which include more ingredients such as elasticity, viscosity, anisotropy and hardening effects. Another extension could concern the void shape effects by considering general ellipsoidal cavities with different aspect ratios. Practically, this implies the use of one of the extensions of the Gurson model according to the effect to be considered. A survey of these different extensions can be found in the review paper of Pineau and Pardoen (2007).

The second part of the thesis was dedicated to the extension of MFH to finite deformations. Local constitutive equations of each solid phase are based on a multiplicative decomposition of the deformation gradient onto elastic and inelastic parts and hyperelastic-plastic stress strain relations. Starting from the established MFH schemes in linear elasticity, the extension to finite strains framework was achieved through the definition of a Linear Comparison Composite (LCC). Two formulations were proposed throughout the fourth chapter. In a first attempt, an incremental approach was presented which is based on a rate formulation of the constitutive equations. This first formulation builds on the earlier finite strain homogenization framework of Nemat-Nasser (1999). The latter showed how to generalize Eshelby's results as well as MFH schemes, provided that we consider tangent operators which are uniform per phase. Evolving microstructure was accounted for by computing in each time step the new geometry parameters of inclusions phase or cavities (i.e.: volume fraction, aspect ratio and orientation) through the average deformation gradient applied to the inclusions / cavities while assuming the shape of inclusions / cavities to remain ellipsoidal. In order to validate the finite strain version of the incremental tangent scheme, its predictions were extensively tested against direct FE simulations of unit cells and representative volume elements.

The comparative study revealed that the MF model captures fairly well the macroscopic response for moderate deformations but tends to overestimate the stress for higher strains. The gap increases with inclusions / cavities volume fraction. This trend of predicting stiffer response is documented (see Chaboche et al. (2005) and Pierard and Doghri (2006)) in the small strain regime and thus was expected. Several stiffness reduction methods were suggested and the idea revolves around the computation of Eshelby's or Hill's tensors with isotropic projections of the matrix's instantaneous stiffness operator. However, in the large deformation regime, the isotropisation issue becomes more difficult. Indeed, trying an isotropisation of nominal tangent operator is not conceivable, because it has indices with respect to both reference and current configurations. In small strain regime, recent proposals try to bypass the issue and construct LCCs which are naturally isotropic per phase, e.g. Brassart et al. (2011) Brassart et al. (2012), Lahellec and Suquet

(2013), Wu et al. (2013a) and Wu et al. (2015).

This partially motivated the proposal of a second finite strain formulation based on the incremental secant method and which preserves the isotropy of the secant operators. A second feature that distinguishes the incremental-secant MFH scheme from an incremental tangent one is the fact that the LCC is defined and is subjected to a strain increment deduced from the residual state evaluated from a fictitious elastic unloading step. This provided the second motivation for incremental-secant MFH which is the ability to predict unloading of solid fibers or inclusions upon macro unloading of the composite. So far, this second formulation performed well for the overall response but still presents some inaccuracies at the phase level. In fact, under large deformations, strain heterogeneity is pronounced within each phase and first-moment formulation does not allow to account for intra-phase field fluctuations. One possible way to increase the quality of the microscopic predictions is to take into account second order moments of fields (i.e. their variances).

Undoubtedly, and in addition to to the future work options mentioned hereinabove this thesis still leaves several open issues and other aspects which need to be further explored. Among them:

- One possible improvement that emanates directly from the previous observations consists in making use of higher order moments of mechanical fields which hopefully will help in better capturing of the per-phase response in finite strain MFH. The accuracy of the predicted per phase stress and strain fields is very important when accounting for material degradation, through damage or fracture models. Second-statistical moment MFH methods were already treated in the literature for the secant formulations by Suquet (1995), for the variational formulations by Ponte Castañeda and Suquet (1997), Ponte Castañeda (2002), Danas and Ponte Castañeda (2009a) and Brassart et al. (2011), for the incremental tangent formulation by Doghri et al. (2011) and more recently for the incremental-secant procedure by Wu et al. (2015). However, introducing second-statistical moments in the finite strain formulation of the incremental tangent or the incremental secant methods for elasto(visco)plastic composites is still an open area.

- Dealing with the thermo-mechanical coupling: as temperature has an important effect on the materials properties (hardening, yield strength, etc.), accounting for thermal effects in the constitutive equations is necessary specially when dealing with polymers. Particularly, self-heating during large deformation in thermoplastic polymers might induce a significant temperature increase and thus affect the mechanical response (see Billon and Bikard (2013)).

- Another direction that could be explored naturally after dealing with composites and porous media separately, is to consider the three phase material: cavities, inclusions and a matrix phase. As mentioned in the introduction, three phase materials are not uncommon. For instance initial voids may be present in metal matrix composites: they form during eutectic solidification and grow further by elasto-plastic flow of the matrix during cooling as reported by Schöbel et al. (2014). Also, in fiber

reinforced composites, voids form during the melt-compounding process because of entrapment of air. Several studies have addressed the causes of void formation during the manufacturing processes of composites (e.g. Vaxman et al. (2011) reviews theoretical and experimental studies dealing with void formation in fiber-reinforced thermoplastic composites, Koushyar et al. (2012) addressed the influence of some manufacturing parameters on initial porosity in carbon fiber/epoxy composites, see also Lundstrom et al. (1993) and Campbell et al. (1995)). Moreover, voids may nucleate at inclusions by particle-matrix interface decohesion, by particle cracking, or also by particle fragmentation for elongated inclusions loaded along their length (e.g. Beremin (1981); Roy et al. (1981); Babout et al. (2004)).
Elasto-plastic three-phase materials could be treated in two different ways:

- As a two-phase composite material (i.e. inclusions embedded in a porous matrix) while considering a damage model for the matrix phase (see figure 4.20 for an illustration). For the behavior of the homogenized porous matrix, one could consider a Gurson like model which accounts for initial porosity. This porosity will be seen as the damage variable whose evolution is controlled by the plastic flow. Void nucleation should be also accounted for by considering a criterion taking as parameter stress measure in the particles. Therefore, the total porosity evolution will be the sum of these two contributions (i.e. existing voids' growth and nucleation rate). Void coalescence criterion jointly with the model for the growth of cavities have to be incorporated into the Gurson-like model. Once a tangent operator for the elasto-plastic porous matrix is computed [5], the homogenization of the elasto-plastic composite could be accomplished relying on one of the incremental tangent or incremental secant MFH formulations.

  This first approach presents some common features with the two-level homogenization approach. Indeed, as in the latter approach, in the deep level, matrix containing cavities is first homogenized. In the upper level, inclusions are added to the homogenized material from the deep level and a second homogenization is carried out. For multiphase linear visco-elastic composites, accurate results were obtained by this strategy (see Friebel et al. (2006)). However, the novelty with respect to the latter approach is twofold: first, in the deep level an elasto-plastic porous matrix is treated by a Gurson like damage model (or could also for high porosities be homogenized via a coupled MF/Gurson model similar to the one developed in the second chapter). In addition, in the high level, an nonlinear MFH model have to be applied.
- Alternatively, as a composite matrix containing voids (see figure 4.21). The elasto-plastic inclusions within the elasto-plastic matrix are first homogenized via an adequate MFH model and the effective properties (elastic and plastic) are then transmitted to the Gurson like model as parameters for its associated matrix. As for the first approach, the Gurson like model should take into ac-

[5] The derivation of the consistent tangent moduli could be difficult because of the complicated forms of the constitutive equations to be considered for the porous plastic matrix. For instance, one may consider the consistent tangent moduli derived by Kim and Gao (2005).

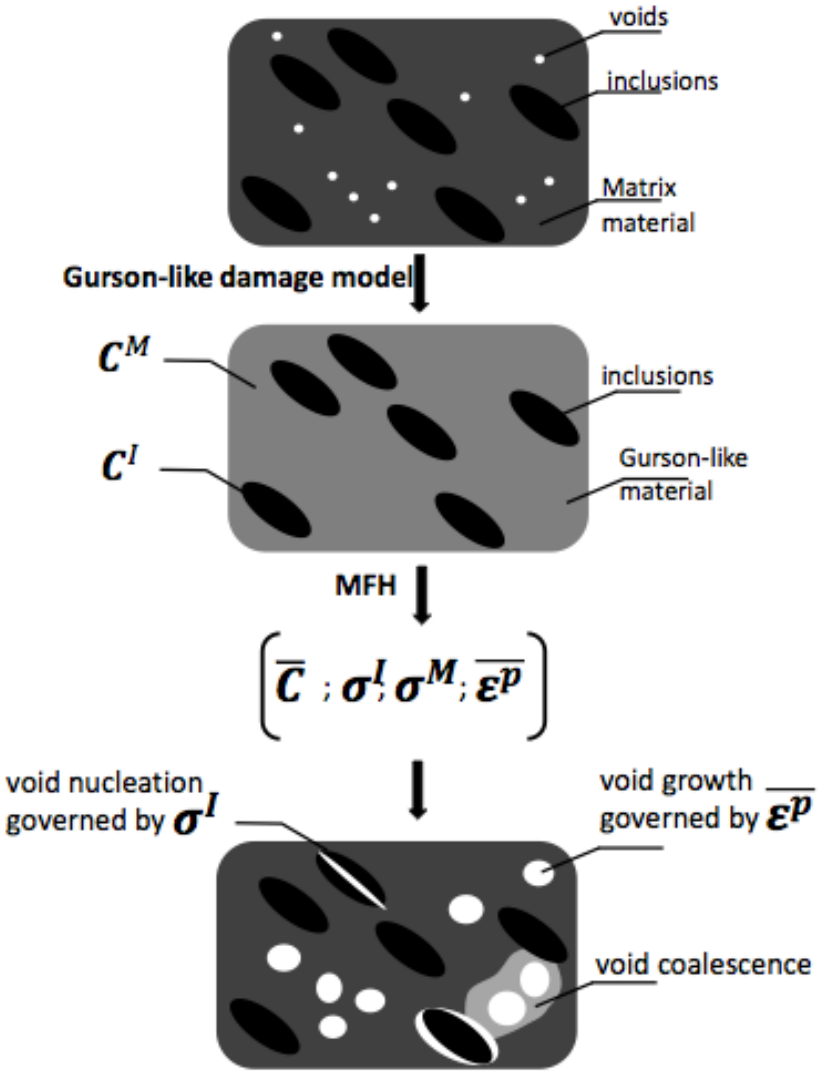

Figure 4.20: Schematic illustration of the first strategy proposed to micro-mechanically model a three phase composite material. The porous elasto-plastic matrix is first treated by a Gurson type damage model and tangent operator C^M has to be derived. A nonlinear MFH scheme is then applied which allows to evaluate the stress field in the inclusion phase σ^I to be transmitted to the nucleation model.

count both the elasticity and the hardening effect. It should also account for the nucleation of voids that occurs from the particle cracking and/or decohesion. This second strategy was already applied by Tekoglu and Pardoen (2010) by coupling a damage model based on the Gologanu-Leblond-Devaux constitutive behavior with an incremental tangent MT scheme. Potentially, better predictions could be achieved when considering the incremental secant formulation with second statistical moments version of Wu et al. (2015). Indeed, the incremental tangent formulation suffers from an over-stiff predictions limitation. Tekoglu and Pardoen (2010) bypassed this limitation by dividing the composite into two subsystems: in the first subsystem, the homogenization is carried out with an isotropization step for the tangent operator and in the second subsystem the Eshelby tensor is computed with the anisotropic tangent operator without invoking the isotropization step.Wu et al. (2013b) used a coupled (first moment) incremental secant MFH formulation with a non local damage model for the elasto-plastic matrix. Improvement of the prediction accuracy compared to the incremental-tangent scheme was noted. It is expected that a second moment procedure improves the accuracy even further.

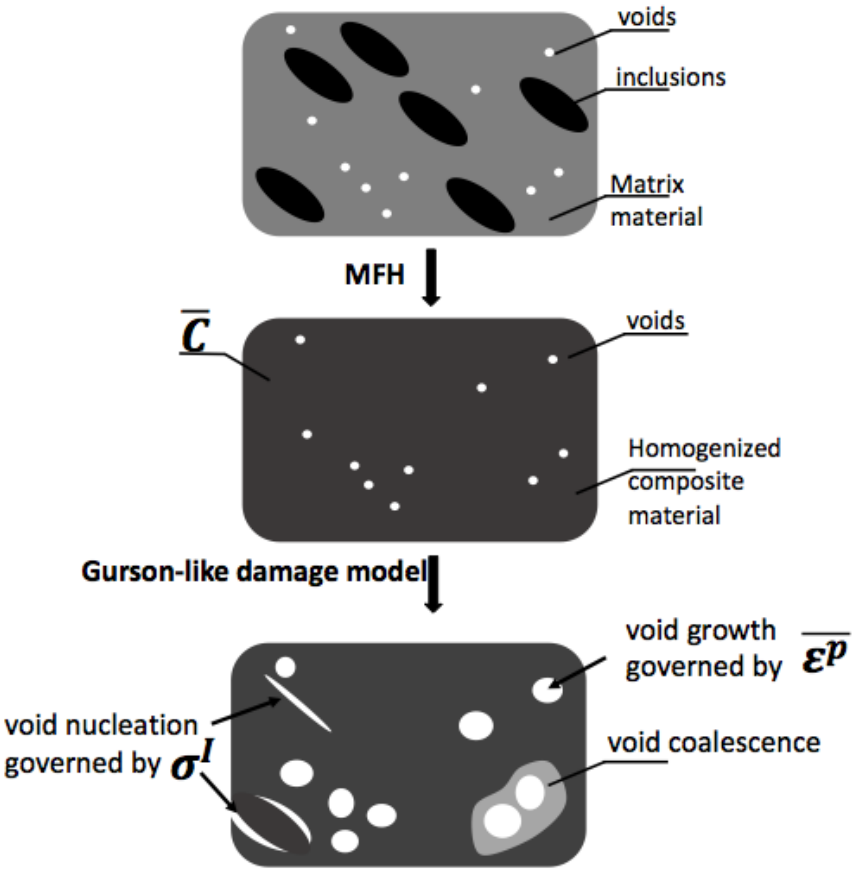

Figure 4.21: Schematic illustration of the second strategy proposed to micro-mechanically model a three phase composite material. First, the inclusions and matrix phases are homogenized using a nonlinear MFH scheme (preferably using second moments). The effective properties are affected to the matrix phase of the Gurson-like damage model. The stress field in the inclusion phase σ^I will be the parameter controlling the nucleation of voids.

Bibliography

Abaqus. 2014. A general purpose FE program. Dassault Systèmes, Providence, Rhode Island, U.S.A.

Anderson, W. B. and Lakes, R. S. 1994. Size effects due to Cosserat elasticity and surface damage in closed-cell polymethacrylimide foam. Journal of Materials Science, 29(24):6413–6419.

Andrews, E., Gioux, G., Onck, P., and Gibson, L. 2001. Size effects in ductile cellular solids. Part II: experimental results. International Journal of Mechanical Sciences, 43(3):701 – 713.

Aravas, N. and Ponte Castañeda, P. 2004. Numerical methods for porous metals with deformation-induced anisotropy. Computer Methods in Applied Mechanics and Engineering, 193:3767–3805.

Babout, L., Brechet, Y., Maire, E., and Fougres, R. 2004. On the competition between particle fracture and particle decohesion in metal matrix composites. Acta Materialia, 52(15):4517 – 4525.

Bart-Smith, H., Hutchinson, J., Fleck, N., and Evans, A. 2002. Influence of imperfections on the performance of metal foam core sandwich panels. International Journal of Solids and Structures, 39(19):4999 – 5012.

Benallal, A., Desmorat, R., and Fournage, M. 2014. An assessment of the role of the third stress invariant in the Gurson approach for ductile fracture. European Journal of Mechanics - A/Solids, 47:400 – 414.

Bensoussan, A., Lions, J., and Papanicolaou, G. 1978. Asymptotic analysis for periodic structures. North Holland, Amsterdam.

Benveniste, Y. 1987. A new approach to the application of Mori-Tanaka's theory in composite materials. Mechanics of Materials, 6(2):147 – 157.

Benzerga, A. 2000. Rupture ductile des tôles anisotropes. Thèse de Doctorat, Ecole Nationale Supérieure des Mines de Paris.

Benzerga, A. and Leblond, J. 2010. Ductile fracture by void growth to coalescence. Advances in Applied Mechanics.

Benzerga, A. A. and Besson, J. 2001. Plastic potentials for anisotropic porous solids. European Journal of Mechanics - A/Solids, 20(3):397–434.

Beremin, F. M. 1981. Cavity formation from inclusions in ductile fracture of A508 steel. Metallurgical Transactions A, 12(5):723–731.

Bilger, N., Auslender, F., Bornert, M., Michel, J.-C., Moulinec, H., Suquet, P., and Zaoui, A. 2005. Effect of a nonuniform distribution of voids on the plastic response of voided materials: a computational and statistical analysis. International Journal of Solids and Structures, 42(2):517 – 538.

Bilger, N., Auslender, F., Bornert, M., Moulinec, H., and Zaoui, A. 2007. Bounds and estimates for the effective yield surface of porous media with a uniform or a nonuniform distribution of voids. European Journal of Mechanics - A/Solids, 26(5):810 – 836.

Billon, N. and Bikard, J. 2013. A new frame for constitutive modeling of visco elastic polymers; Accounting thermal effects and strain induced crystallization. In 5th International Conference on Computational Methods for Coupled Problems in Science and Engineering, COUPLED PROBLEMS 2013, pages 151–158. International Center for Numerical Methods in Engineering, Santa Eulalia, Ibiza Island, Spain.

Bobeth, M. and Diener, G. 1987. Static elastic and thermoelastic field fluctuations in multiphase composites. Journal of the Mechanics and Physics of Solids, 35(2):137 – 149.

Böhm, H. J. 2012. A short introduction to basic aspects of continuum micromechanics.

Bornert, M., Bretheau, T., and Gilormini, P. 2001. Homogénéisation en mécanique des matériaux. Hermes Science Europe, Stanmore, UK.

Bourih, A., Kaddouri, W., Kanit, T., Madani, S., and Imad, A. 2017. Effective yield surface of porous media with random overlapping identical spherical voids. Journal of Materials Research and Technology.

Boyce, M. C., Parks, D. M., and Argon, A. S. 1988. Large inelastic deformation of glassy polymers. part I: rate dependent constitutive model. Mechanics of Materials, 7(1):15–33.

Brassart, L., Doghri, I., and Delannay, L. 2010. Homogenization of elasto-plastic composites coupled with a nonlinear finite element analysis of the equivalent inclusion problem. International Journal of Solids and Structures, 47(5):716 – 729.

Brassart, L., Stainier, L., Doghri, I., and Delannay, L. 2011. A variational formulation for the incremental homogenization of elasto-plastic composites. Journal of the Mechanics and Physics of Solids, 59(12):2455–2475.

Brassart, L., Stainier, L., Doghri, I., and Delannay, L. 2012. Homogenization of elasto-(visco) plastic composites based on an incremental variational principle. International Journal of Plasticity, 36:86–112.

Buckley, C. 1995. Glass-rubber constitutive model for amorphous polymers near the glass transition. Polymer, 36(17):3301–3312.

Brvik, T., Hopperstad, O. S., and Pedersen, K. O. 2010. Quasi-brittle fracture during structural impact of AA7075-T651 aluminium plates. International Journal of Impact Engineering, 37(5):537 – 551.

Campbell, F., Mallow, A., and Browning, C. 1995. Porosity in carbon fiber composites: an overview of causes. J Adv Mater, pages 18–33.

Cazacu, O., Revil-Baudard, B., Lebensohn, R. a., and Grjeu, M. 2013. On the Combined Effect of Pressure and Third Invariant on Yielding of Porous Solids With von Mises Matrix. Journal of Applied Mechanics, 80(6):064501.

Chaboche, J. L., Kanouté, P., and Roos, a. 2005. On the capabilities of mean-field approaches for the description of plasticity in metal matrix composites. International Journal of Plasticity, 21(7):1409–1434.

Chawla, N., Deng, X., and Schnell, D. 2006. Thermal expansion anisotropy in extruded SiC particle reinforced 2080 aluminum alloy matrix composites. Materials Science and Engineering: A, 426(1):314 – 322.

Cheng, L. and Guo, T. 2007. Void interaction and coalescence in polymeric materials. International Journal of Solids and Structures, 44(6):1787 – 1808. Physics and Mechanics of Advanced Materials.

Cheng, L., de Saxc, G., and Kondo, D. 2014. A stress-based variational model for ductile porous materials. International Journal of Plasticity, 55:133 – 151.

Cheng, L., Monchiet, V., Morin, L., de Saxc, G., and Kondo, D. 2015. An analytical Lode angle dependent damage model for ductile porous materials. Engineering Fracture Mechanics, 149:119 – 133.

Chew, H., Guo, T., and Cheng, L. 2006. Effects of pressure-sensitivity and plastic dilatancy on void growth and interaction. International Journal of Solids and Structures, 43(21):6380 – 6397.

Christensen, R. 1979. Mechanics of Composite Materials. A WILEY-Inter-science Publication.

Christensen, R. 1998. Two Theoretical Elasticity Micromechanics Models. Journal of Elasticity, 50(1):15–25.

Christensen, R. and Lo, K. 1979. Solutions for effective shear properties in three phase sphere and cylinder models. Journal of the Mechanics and Physics of Solids, 27(4):315 – 330.

Christensen, R. M. 1990. A critical evaluation for a class of micro-mechanics models. Journal of the Mechanics and Physics of Solids, 38(3):379 – 404.

Danas, K. and Aravas, N. 2012. Numerical modeling of elasto-plastic porous materials with void shape effects at finite deformations. Composites Part B: Engineering, 43(6):2544–2559.

Danas, K. and Ponte Castañeda, P. 2009a. A finite-strain model for anisotropic viscoplastic porous media: II - Applications. European Journal of Mechanics, A/Solids, 28(3):402 – 416.

Danas, K. and Ponte Castañeda, P. 2009b. A finite-strain model for anisotropic viscoplastic porous media: I Theory. European Journal of Mechanics - A/Solids, 28(3):387 – 401.

Danas, K. and Ponte Castañeda, P. 2012. Influence of the Lode parameter and the stress triaxiality on the failure of elasto-plastic porous materials. International Journal of Solids and Structures, 49(11-12):1325–1342.

Danas, K., Idiart, M., and Ponte Castañeda, P. 2008. A homogenization-based constitutive model for isotropic viscoplastic porous media. International Journal of Solids and Structures, 45(1112):3392 – 3409.

Dang, N. 1976. Direct limit analysis via rigid-plastic finite elements. Computer Methods in Applied Mechanics and Engineering, 8(1):81–116.

Dement'ev, A. G. and Tarakanov, O. G. 1970a. Effect of cellular structure on the mechanical properties of plastic foams. Polymer Mechanics, 6(4):519–525.

Dement'ev, A. G. and Tarakanov, O. G. 1970b. Model analysis of the cellular structure of plastic foams of the polyurethane type. Polymer Mechanics, 6(5):744–749.

Digimat. 2011. A software for the linear and nonlinear multi-scale modeling of heterogeneous materials. e-Xstream engineering, Louvain-la-Neuve, Belgium (www.e-xstream.com).

Digimat. 2014. Linear and nonlinear multi-scale material modeling software. e-Xstream engineering SA (http://www.e-Xstream.com),Louvain-la-Neuve, Belgium.

Doghri, I. 2000. Mechanics of deformable solids: linear and nonlinear, analytical and computational aspects. Springer.

Doghri, I. and Billardon, R. 1995. Investigation of localization due to damage in elasto-plastic materials. Mechanics of Materials, 19(2-3):129–149.

Doghri, I. and Ouaar, A. 2003. Homogenization of two-phase elasto-plastic composite materials and structures: study of tangent operators, cyclic plasticity and numerical algorithms. Int. J. Solids Struct., 40:1681–1712.

Doghri, I., Adam, L., and Bilger, N. 2010. Mean-field homogenization of elasto-viscoplastic composites based on a general incrementally affine linearization method. International Journal of Plasticity, 26(2):219–238.

Doghri, I., Brassart, L., Adam, L., and Gérard, J. S. 2011. A second-moment incremental formulation for the mean-field homogenization of elasto-plastic composites. International Journal of Plasticity, 27(3):352–371.

Doghri, I., El Ghezal, M., and Adam, L. 2016. Finite strain mean-field homogenization of composite materials with hyperelastic-plastic constituents. International Journal of Plasticity, 81:40 – 62.

Dormieux, L., Lemarchand, E., Kondo, D., and Brach, S. 2017. Strength criterion of porous media: Application of homogenization techniques. Journal of Rock Mechanics and Geotechnical Engineering, 9(1):62–73.

Drucker, D. C., Prager, W., and Greenberg, H. J. 1952. Extended limit design theorems for continuousmedia. Quarterly of Applied Mathematics, 9(4):381–389.

El Ghezal, M. I. and Doghri, I. Under review. Predictive second moment homogenization models coupled with Gurson's solution.

El Ghezal, M. I., Maalej, Y., and Doghri, I. 2013. Micromechanical models for porous and cellular materials in linear elasticity and viscoelasticity. Computational Materials Science, 70:51 – 70.

El Ghezal, M. I., Doghri, I., and Kondo, D. 2017. Static limit analysis and strength of porous solids with Hill orthotropic matrix. International Journal of Solids and Structures, 109:63 – 71.

El Ghezal, M. I., Wu, L., Doghri, I., and Noels, L. in preparation. A finite strain incremental-secant homogenization model for elasto-plastic composites.

Eshelby, J. D. 1957. The Determination of the Elastic Field of an Ellipsoidal Inclusion, and Related Problems. Proceedings of the Royal Society A: Mathematical, Physical and Engineering Sciences, 241(1226):376–396.

Fourmeau, M., Brvik, T., Benallal, A., Lademo, O., and Hopperstad, O. 2011. On the plastic anisotropy of an aluminium alloy and its influence on constrained multiaxial flow. International Journal of Plasticity, 27(12):2005 – 2025. Special Issue In Honor of Nobutada Ohno.

Friebel, C., Doghri, I., and Legat, V. 2006. General mean-field homogenization schemes for viscoelastic composites containing multiple phases of coated inclusions. International Journal of Solids and Structures, 43(9):2513 – 2541.

Fritzen, F., Forest, S., Böhlke, T., Kondo, D., and Kanit, T. 2012. Computational homogenization of elasto-plastic porous metals. International Journal of Plasticity, 29(1):102–119.

Gao, X. and Kim, J. 2006. Modeling of ductile fracture: Significance of void coalescence. International Journal of Solids and Structures, 43(20):6277 – 6293.

Garajeu, M. 1995. Contribution à l'étude du comportement non linéaire de milieux poreux avec ou sans renfort. Thèse de Doctorat, Université de la Méditerranée.

Garajeu, M. and Suquet, P. 1997. Effective properties of porous ideally plastic or viscoplastic materials containing rigid particles. Journal of the Mechanics and Physics of Solids, 45(6):873–902.

Garajeu, M., Michel, J., and Suquet, P. 2000. A micromechanical approach of damage in viscoplastic materials by evolution in size, shape and distribution of voids. Computer Methods in Applied Mechanics and Engineering, 183(34):223 – 246.

Gavazzi, A. C. and Lagoudas, D. C. 1990. On the numerical evaluation of Eshelby's tensor and its application to elastoplastic fibrous composites. Computational Mechanics, 7(1):13–19.

Geers, M. G. D., Kouznetsova, V. G., and Brekelmans, W. A. M. 2010. Multi-scale computational homogenization: Trends and challenges. In Journal of Computational and Applied Mathematics, volume 234, pages 2175–2182.

Gibson, L. and Ashby, M. 1999. Cellular Solids: Structure and Properties. Cambridge Solid State Science Series. Cambridge University Press.

Gibson, L. J. 2005. Biomechanics of cellular solids. Journal of Biomechanics, 38(3):377 – 399.

Gologanu, M., Leblond, J. B., and Devaux, J. 1993. Approximate models for ductile metals containing non-spherical voids-Case of axisymmetric prolate ellipsoidal cavities. Journal of the Mechanics and Physics of Solids, 41(11):1723–1754.

Gologanu, M., Leblond, J. B., and Devaux, J. 1994. Approximate models for ductile metals containing non spherical voids - case of axisymmetric oblate ellipsoidal cavities. ASME. J. Eng. Mater. Technol, 116:290–297.

Gologanu, M., Leblond, J.-B., Perrin, G., and Devaux, J. 1997. Recent Extensions of Gurson's Model for Porous Ductile Metals, pages 61–130. Springer Vienna, Vienna.

Guo, T., Faleskog, J., and Shih, C. 2008. Continuum modeling of a porous solid with pressure-sensitive dilatant matrix. Journal of the Mechanics and Physics of Solids, 56(6):2188–2212.

Gurson, A. 1977. continium theory of ductile rupture by void nucleation and growth: Part I- yield criteria and flow rules for porous ductile media. Journal of Engineering Materials and Technology, 99(1):2–15.

Gvozdev, A.-A. 1938. The determination of the value of the collapse load for statically indeterminate systems undergoing plastic deformation. Proceedings of the Conference on Plastic DeformationsAkademiia Nauk SSSR, Moscow, pages 19 –33.

Hashin, Z. 1962. The Elastic Moduli of Heterogeneous Materials. Journal of Applied Mechanics, 29:143.

Hashin, Z. 1988. The differential scheme and its application to cracked materials. Journal of the Mechanics and Physics of Solids, 36(6):719 – 734.

Hashin, Z. and Shtrikman, S. 1963. A variational approach to the theory of the elastic behaviour of multiphase materials. Journal of the Mechanics and Physics of Solids, 11(2):127 – 140.

Hill, R. 1948. A theory of the yielding and plastic flow of anisotropic metals. Proceedings of the Royal Society of London A: Mathematical, Physical and Engineering Sciences, 193(1033):281–297.

Hill, R. 1950. The mathematical Theory of Plasticity. Oxford University Press.

Hill, R. 1962. Acceleration waves in solids. Journal of the Mechanics and Physics of Solids, 10(1):1–16.

Hill, R. 1965a. A self-consistent mechanics of composite materials. Journal of the Mechanics and Physics of Solids, 13(March 1962):213–222.

Hill, R. 1965b. Continuum micro-mechanics of elastoplastic polycrystals. J. Mech. Phys. Solids, 13:89–101.

Hill, R. 1967. The essential structure of constitutive laws for metal composites and polycrystals. J. Mech. Phys. Solids, 17:79–95.

Hill, R. 1970. Constitutive inequalities for isotropic elastic solids under finite strain. Proceedings of the Royal Society of London. Series A, Mathematical and Physical, 314(1519):457–472.

Hill, R. 1972. On constitutive macro-variables for heterogeneous solids at finite strain. Proceedings of the Royal Society A: Mathematical, Physical and Engineering Sciences, 326:131–147.

Hill, R. 1984. On macroscopic effects of heterogeneity in elastoplastic media at finite strain. Mathematical Proceedings of the Cambridge Philosophical Society, 95(03):481–494.

Hom, C. L. and McMeeking, R. 1989. Void Growth in Elastic-Plastic Materials. ASME. J. Appl. Mech, 56(2):309 – 317.

Huang, J. S. and Gibson, L. J. 1991. Creep of polymer foams. Journal of Materials Science, 26(3):637–647.

Huang, Y. 1993. The role of nonuniform particle distribution in plastic flow localization. Mechanics of Materials, 16(3):265 – 279.

Huang, Z., Yuan, X., Wang, R., and Ning, J. 1996. Dynamic yield loci of a porous visco-plastic material by using a lower bound approach. IUTAM Symposia, pages 155–162.

Huber, A. and Gibson, L. 1988. Anisotropy of foams. Journal of Materials Science, 23(8):3031–3040.

Idiart, M. I., Danas, K., and Ponte Castañeda, P. 2006. Second-order theory for nonlinear composites and application to isotropic constituents. Comptes Rendus - Mecanique, 334(10):575–581.

Jeon, I. and Asahina, T. 2005. The effect of structural defects on the compressive behavior of closed-cell Al foam. Acta Materialia, 53(12):3415 – 3423.

Jeong, H.-Y. 2002. A new yield function and a hydrostatic stress-controlled void nucleation model for porous solids with pressure-sensitive matrices. International Journal of Solids and Structures, 39(5):1385 – 1403.

Jeong, H.-Y. and Pan, J. 1995. A macroscopic constitutive law for porous solids with pressure-sensitive matrices and its implications to plastic flow localization. International Journal of Solids and Structures, 32(24):3669 – 3691.

Ji, S. 2004. Generalized means as an approach for predicting Youngs moduli of multiphase materials. Materials Science and Engineering: A, 366(1):195 – 201.

Ji, S., Gu, Q., and Xia, B. 2006. Porosity dependence of mechanical properties of solid materials. Journal of Materials Science, 41(6):1757–1768.

Kanouté, P., Boso, D. P., Chaboche, J. L., and Schrefler, B. a. 2009. Multiscale methods for composites: A review. Archives of Computational Methods in Engineering, 16(1):31–75.

Kastner, J., Plank, B., Salaberger, D., and Sekelja, J. 2010. Defect and Porosity Determination of Fibre Reinforced Polymers by X-ray Computed Tomography. 2nd Int. Symposium on NDT in Aerospace, Hamburg, D, Germany.

Keralavarma, S. and a.a. Benzerga. 2010. A constitutive model for plastically anisotropic solids with non-spherical voids. Journal of the Mechanics and Physics of Solids, 58(6):874–901.

Kim, H. and Al-Hassani, S. 2001. A morphological elastic model of general hexagonal columnar structures. International Journal of Mechanical Sciences, 43(4):1027 – 1060.

Kim, J. and Gao, X. 2005. A generalized approach to formulate the consistent tangent stiffness in plasticity with application to the GLD porous material model. International Journal of Solids and Structures, 42(1):103 – 122.

Klompen, E. T. J., Engels, T. a. P., Govaert, L. E., and Meijer, H. E. H. 2005. Modeling of the postyield response of glassy polymers: Influence of thermomechanical history. Macromolecules, 38(16):6997–7008.

Ko, W. 1965. Deformations of Foamed Elastomers. Journal of Cellular Plastics, 1(1):45–50.

Koplik, J. and Needleman, A. 1988. Void growth and coalescence in porous plastic solids. Int. J. Solids Structures, 24:835–853.

Koushyar, H., Alavi-Soltani, S., Minaie, B., and Violette, M. 2012. Effects of variation in autoclave pressure, temperature, and vacuum-application time on porosity and mechanical properties of a carbon fiber/epoxy composite. Journal of Composite Materials, 46(16):1985–2004.

Kouznetsova, V. 2004. Computational homogenization. Lecture notes, Micromechanics graduate course. T. U. Eindhoven.

Kröner, E. 1958. Berechnung der elastischen Konstanten des Vielkristalls aus den Konstanten des Einkristalls. Zeitschrift für Physik, 151(4):504–518.

Kröner, E. 1961. Zur plastischen verformung des vielkristalls. Acta Metall. Mater., 9:155–161.

Lahellec, N. and Suquet, P. 2013. Effective response and field statistics in elasto-plastic and elasto-viscoplastic composites under radial and non-radial loadings. International Journal of Plasticity, 42:1–30.

Leblond, J.-B. 2003. Mécanique de la rupture fragile et ductile. Hermes Science Publications,Lavoisier.

Leblond, J.-B., Perrin, G., and Devaux, J. 1995. An improved Gurson-type model for hardenable ductile metals. European journal of mechanics. A. Solids, 14(4):499–527.

Leblond, J.-B., Morin, L., and Cazacu, O. 2014. An Improved Description of Spherical Void Growth in Plastic Porous Materials with Finite Porosities. Procedia Materials Science, 3:1232 – 1237.

Li, K., Gao, X.-L., and Roy, A. 2003. Micromechanics model for three-dimensional open-cell foams using a tetrakaidecahedral unit cell and Castigliano's second theorem. Composites Science and Technology, 63(12):1769 – 1781.

Li, K., Gao, X.-L., and Subhash, G. 2006. Effects of cell shape and strut cross-sectional area variations on the elastic properties of three-dimensional open-cell foams. Journal of the Mechanics and Physics of Solids, 54(4):783 – 806.

Lundstrom, T., Gebart, B., and Lundemo, C. 1993. Void Formation in RTM. Journal of Reinforced Plastics and Composites, 12(12):1339–1349.

Luxner, M. H., Stampfl, J., and Pettermann, H. E. 2007. Numerical simulations of 3D open cell structures influence of structural irregularities on elasto-plasticity and deformation localization. International Journal of Solids and Structures, 44(9):2990 – 3003.

Matous, K. and Maniatty, A. 2009. Multiscale modeling of elasto-viscoplastic polycrystals subjected to finite deformations. Interaction and Multiscale Mechanics, 2:375–396.

McClintock, F. A. 1968. A Criterion for Ductile Fracture by the Growth of Holes. Journal of Applied Mechanics, 35(2):363 – 371.

Michel, J. and Suquet, P. 1992. The constitutive law of nonlinear viscous and porous materials. Journal of the Mechanics and Physics of Solids, 40(4):783 – 812.

Michel, J., Moulinec, H., and Suquet, P. 1999. Effective properties of composite materials with periodic microstructure: a computational approach. Computer Methods in Applied Mechanics and Engineering, 172(1):109 – 143.

Miehe, C., Schröder, J., and Schotte, J. 1999. Computational homogenization analysis in finite plasticity Simulation of texture development in polycrystalline materials. Computer Methods in Applied Mechanics and Engineering, 171(3-4):387–418.

Miled, K., Sab, K., and Roy, R. L. 2011. Effective elastic properties of porous materials: Homogenization schemes vs experimental data. Mechanics Research Communications, 38(2):131 – 135.

Mills, N. J. 2006. Finite element models for the viscoelasticity of open-cell polyurethane foam. Cellular Polymers, 25.

Miserez, A., Rossoll, A., and Mortensen, A. 2004. Investigation of crack-tip plasticity in high volume fraction particulate metal matrix composites. Engineering Fracture Mechanics, 71(16):2385 – 2406.

Monchiet, V., Cazacu, O., Charkaluk, E., and Kondo, D. 2008. Macroscopic yield criteria for plastic anisotropic materials containing spheroidal voids. International Journal of Plasticity, 24(7):1158–1189.

Monchiet, V., Charkaluk, E., and Kondo, D. 2011. A micromechanics-based modification of the Gurson criterion by using Eshelby-like velocity fields. European Journal of Mechanics - A/Solids, 30(6):940–949.

Monchiet, V., Charkaluk, E., and Kondo, D. 2014. Macroscopic yield criteria for ductile materials containing spheroidal voids: An Eshelby-like velocity fields approach. Mechanics of Materials, 72:1 – 18.

Mondal, D., Ramakrishnan, N., Suresh, K., and Das, S. 2007. On the moduli of closed-cell aluminum foam. Scripta Materialia, 57(10):929 – 932.

Mori, T. and Tanaka, K. 1973. Average stress in matrix and average elastic energy of materials with misfitting inclusions. Acta Metallurgica, 21(5):571 – 574.

Morin, L., Madou, K., Leblond, J.-B., and Kondo, D. 2014. A new technique for finite element limit-analysis of Hill materials, with an application to the assessment of criteria for anisotropic plastic porous solids. International Journal of Engineering Science, 74:65–79.

Morin, L., Leblond, J.-B., and Kondo, D. 2015. A Gurson-type criterion for plastically anisotropic solids containing arbitrary ellipsoidal voids. International Journal of Solids and Structures, 77:86 – 101.

Moulinec, H. and Suquet, P. 1998. A numerical method for computing the overall response of nonlinear composites with complex microstructure. Computer Methods in Applied Mechanics and Engineering, 157(1):69 – 94.

Needleman, A. 1972a. A numerical study of necking in circular cylindrical bar. Journal of the Mechanics and Physics of Solids, 20(2):111 – 127.

Needleman, A. 1972b. Void Growth in an Elastic-Plastic Medium. ASME. J. Appl. Mech., 39(4):964 – 970.

Nemat-Nasser, S. 1999. Averaging theorems in finite deformation plasticity. Mechanics of Materials, 31:493–523.

Nemat-Nasser, S. and Hori, M. 1999. Micromechanics: overall properties of heterogeneous materials. Elsevier North-Holland.

Nemat-Nasser, S. and Obata, M. 1986. Rate-Dependent, Finite Elasto-Plastic Deformation of Polycrystals. Proceedings of the Royal Society, A 407(1833):343–375.

Norris, A. 1985. A differential scheme for the effective moduli of composites. Mechanics of Materials, 4(1):1 – 16.

Onck, P., Andrews, E., and Gibson, L. 2001. Size effects in ductile cellular solids. Part I: modeling. International Journal of Mechanical Sciences, 43(3):681 – 699.

Onck, P. R. 2008. Cellular Solids. Lecture notes, Micromechanics graduate course. T. U. Eindhoven.

Pabst, W., Gregorov, E., and Tich, G. 2006. Elasticity of porous ceramicsA critical study of modulusporosity relations. Journal of the European Ceramic Society, 26(7):1085 – 1097.

Pardoen, T. and Hutchinson, J. 2000. An extended model for void growth and coalescence. Journal of the Mechanics and Physics of Solids, 48(12):2467 – 2512.

Pastor, F., Pastor, J., and Kondo, D. 2012. Limit analysis of hollow spheres or spheroids with Hill orthotropic matrix. Comptes Rendus Mécanique, 340(3):120–129.

Pastor, F., Kondo, D., and Pastor, J. 2013. 3D-FEM formulations of limit analysis methods for porous pressure-sensitive materials. International Journal for Numerical Methods in Engineering, 95(10):847–870.

Perrin, G. 1992. Contribution à l'étude théorique et numérique de la rupture ductile des métaux. Ph.D. Thesis, Ecole Polytechnique.

Perrin, G. and Leblond, J. B. 1990. Analytical study of a hollow sphere made of plastic porous material and subjected to hydrostatic tension- application to some problems in ductile fracture of metals. Int. J. Plasticity, 6:677–699.

Petryk, H. 1997. Plastic instability: Criteria and computational approaches. Archives of Computational Methods in Engineering, 4(2):111–151.

Pettermann, H. E., Huber, C. O., Luxner, M. H., Nogales, S., and Böhm, H. J. 2010. An Incremental Mori-Tanaka Homogenization Scheme for Finite Strain Thermoelastoplasticity of MMCs. Materials, 3(1):434–451.

Pierard, O. and Doghri, I. 2006. Study of various estimates of the macroscopic tangent operator in the incremental homogenization of elasto-plastic composites. International Journal for Multiscale Computational Engineering, 4:521–543.

Pierard, O., Friebel, C., and Doghri, I. 2004. Mean-field homogenization of multi-phase thermo-elastic composites: a general framework and its validation. Composites Science and Technology, 64(10):1587 – 1603.

Pineau, A. and Pardoen, T. 2007. 2.06 - Failure of Metals. In Milne, I., Ritchie, R., and Karihaloo, B., editors, Comprehensive Structural Integrity, pages 684 – 797. Pergamon, Oxford.

Pineau, A., Benzerga, A., and Pardoen, T. 2016. Failure of metals I: Brittle and ductile fracture. Acta Materialia, 107:424 – 483.

Plateau, J. A. F. 1873. Statique expérimentale et théorique des liquides soumis aux seules forces moléculaires. Gauthier-Villars, Paris.

Ponte Castañeda, P. 1991. The effective mechanical properties of nonlinear isotropic composites. Journal of the Mechanics and Physics of Solids, 39(1):45 – 71.

Ponte Castañeda, P. 2002. Second-order homogenization estimates for nonlinear composites incorporating field fluctuations: I-theory. Journal of the Mechanics and Physics of Solids, 50(4):737–757.

Ponte Castañeda, P. 2012. Bounds for nonlinear composites via iterated homogenization. Journal of the Mechanics and Physics of Solids, 60(9):1583 – 1604.

Ponte Castañeda, P. and Suquet, P. 1997. Nonlinear Composites. Advances in Applied Mechanics, 34:171 – 302.

Ponte Castañeda, P. and Suquet, P. 2002. Nonlinear Composites and Microstructure Evolution. In Aref, H. and Phillips, J., editors, Mechanics for a New Mellennium, pages 253–274. Springer Netherlands.

Ponte Castañeda, P. and Tiberio, E. 2000. Second-order homogenization method in finite elasticity and applications to black-filled elastomers. Journal of the Mechanics and Physics of Solids, 48(6):1389–1411.

Ponte Castañeda, P. and Zaidman, M. 1994. Constitutive models for porous materials with evolving microstructure. Journal of the Mechanics and Physics of Solids, 42(9):1459 – 1497.

Ramakrishnan, N. and Arunachalam, V. S. 1990. Effective elastic moduli of porous solids. Journal of Materials Science, 25(9):3930–3937.

Ramakrishnan, N. and Arunachalam, V. S. 1993. Effective Elastic Moduli of Porous Ceramic Materials. Journal of the American Ceramic Society, 76(11):2745–2752.

Reuss, A. 1929. Berechnung der Fliessgrenze von Mischkristallen auf Grund der Plastizitätsbedingung für Einkristalle. Z. Angew. Math. Mech., 9:49–58.

Revil-Baudard, B. and Cazacu, O. 2014. New three-dimensional strain-rate potentials for isotropic porous metals: Role of the plastic flow of the matrix. International Journal of Plasticity, 60:101 – 117.

Rice, J. and Tracey, D. 1969. On the ductile enlargement of voids in triaxial stress fields. Journal of the Mechanics and Physics of Solids, 17(3):201 – 217.

Rice, J. R. 1976. The localization of plastic deformation. 14th International Congress on Theoratical and Applied Mechanics, pages 207–220.

Richelsen, A. and Tvergaard, V. 1994. Dilatant plasticity or upper bound estimates for porous ductile solids. Acta Metallurgica et Materialia, 42(8):2561 – 2577.

Roberts, A. and Garboczi, E. 2002. Elastic properties of model random three-dimensional open-cell solids. Journal of the Mechanics and Physics of Solids, 50(1):33 – 55.

Roberts, A. P. and Garboczi, E. J. 2000. Elastic Properties of Model Porous Ceramics. Journal of the American Ceramic Society, 83(12):3041–3048.

Roscoe, R. 1973. Isotropic composites with elastic or viscoelastic phases: General bounds for the moduli and solutions for special geometries. Rheologica Acta, 12(3):404–411.

Roy, G. L., Embury, J., Edwards, G., and Ashby, M. 1981. A model of ductile fracture based on the nucleation and growth of voids. Acta Metallurgica, 29(8):1509 – 1522.

Salençon, J. 1983. Viscoélasticité. Presses de l'École Nationale des Ponts et Chaussées.

Saraev, D. and Schmauder, S. 2003. Finite element modelling of Al/SiCp metal matrix composites with particles aligned in stripes-a 2D-3D comparison. International Journal of Plasticity, 19(6):733 – 747.

Save, M., Massonnet, C., and de Saxce, G. 1997. Plastic limit analysis of plates, shells and disks. North Holland.

Sawada, T. and Kusaka, T. 2017. Strength predictions by applied effective volume theory in short-glass-fibre-reinforced plastics. Polymer Testing, 62(Supplement C):143 – 153.

Schöbel, M., Requena, G., Fiedler, G., Tolnai, D., Vaucher, S., and Degischer, H. 2014. Void formation in metal matrix composites by solidification and shrinkage of an AlSi7 matrix between densely packed particles. Composites Part A: Applied Science and Manufacturing, 66(Supplement C):103 – 108.

Segurado, J., Parteder, E., Plankensteiner, A., and Böhm, H. 2002. Micromechanical studies of the densification of porous molybdenum. Materials Science and Engineering: A, 333(1):270 – 278.

Segurado, J., Lebensohn, R. A., Llorca, J., and Tomé, C. N. 2012. Multiscale modeling of plasticity based on embedding the viscoplastic self-consistent formulation in implicit finite elements. International Journal of Plasticity, 28(1):124–140.

Simo, J. 1992. Algorithms for static and dynamic multiplicative plasticity that preserve the classical return mapping schemes of the infinitesimal theory. Computer Methods in Applied Mechanics and Engineering, 99(1):61–112.

Simo, J. and Hughes, T. 2000. Computational Inelasticity. Interdisciplinary Applied Mathematics. Springer New York.

Soppa, E., Schmauder, S., Fischer, G., Thesing, J., and Ritter, R. 1999. Influence of the microstructure on the deformation behaviour of metal-matrix composites. Computational Materials Science, 16(1):323 – 332.

Suquet, P. 1995. Overall properties of nonlinear composites: a modified secant moduli theory and its link with Ponte Castañeda's nonlinear variational procedure. C. R. Acad. Sci. Paris, 320 (Série IIb):563–571.

Talbot, D. R. S. and Willis, J. R. 1985. Variational Principles for Inhomogeneous Non-linear Media. IMA Journal of Applied Mathematics, 35(1):39–54.

Tekoglu, C. and Pardoen, T. 2010. A micromechanics based damage model for composite materials. International Journal of Plasticity, 26(4):549 – 569.

Tekoglu, C., Gibson, L., Pardoen, T., and Onck, P. 2011. Size effects in foams: Experiments and modeling. Progress in Materials Science, 56(2):109 – 138.

Terada, K., Hori, M., Kyoya, T., and Kikuchi, N. 2000. Simulation of the multi-scale convergence in computational homogenization approaches. International Journal of Solids and Structures, 37(16):2285 – 2311.

Thomson, C., Worswick, M., Pilkey, A., and Lloyd, D. 2003. Void coalescence within periodic clusters of particles. Journal of the Mechanics and Physics of Solids, 51(1):127 – 146.

Torquato, S. 1998. Effective stiffness tensor of composite media : II. Applications to isotropic dispersions. Journal of the Mechanics and Physics of Solids, 46(8):1411 – 1440.

Torquato, S. 2002. Random Heterogeneous Materials: Microstructure and Macroscopic properties. Springer.

Torquato, S., Stell, G., and Beasley, J. 1985. Third-order bounds on the effective bulk and shear modulus of a dispersion of fully penetrable spheres. International Journal of Engineering Science, 23(3):385 – 392.

Tvergaard, V. 1981. Influence of voids on shear band instabilities under plane strain conditions. Int. J. Frac, 17:389–407.

Tvergaard, V. 1982. On localization in ductile materials containing spherical voids. International Journal of Fracture, 18(4):237–252.

Tvergaard, V. 2014. Bifurcation into a localized mode from non-uniform periodic deformations around a periodic pattern of voids. Journal of the Mechanics and Physics of Solids, 69:112 – 122.

van der Sluis, O., Schreurs, P., and Brekelmans, H., W.A.M.and Meijer. 2000. Overall behavior of heterogeneous elastoviscoplastic materials: effect of microstructural modelling. Mechanics of Materials, 32:449–462.

Vaxman, A., Narkis, M., Segmann, A., and Kenig, S. 2011. Discontinuous Fiber Thermoplastic Composites: Void Formation During Melt Processing. John Wiley & Sons, Inc.

Vladimirov, I. N., Pietryga, M. P., and Reese, S. 2010. Anisotropic finite elastoplasticity with nonlinear kinematic and isotropic hardening and application to sheet metal forming. International Journal of Plasticity, 26(5):659–687.

Voigt, W. 1889. Ueber die Bezienhung zwischen den beiden Elasticitätsconstanten isotroper Körper. Ann. Phys., 38:573–587.

Warren, W. and Kraynik, A. 1988. The linear elastic properties of open-cell foams. Journal of Applied Mechanics, 55(2):341–346.

Warren, W. and Kraynik, A. 1997. Linear elastic behavior of a low-density Kelvin foam with open cells. TRANSACTIONS-AMERICAN SOCIETY OF MECHANICAL ENGINEERS JOURNAL OF APPLIED MECHANICS, 64:787–794.

Willis, J. R. 1983. The overall response of composite materials. ASME J. Appl. Mech., 50(23):1202–1209.

Wineman, A. S. and Rajagopal, K. R. 2000. Mechanical response of polymers - An introduction. Cambridge University Press.

Withers, P. J. 1989. The determination of the elastic field of an ellipsoidal inclusion in a transversely isotropic medium, and its relevance to composite materials. Philosophical Magazine A, 59(4):759–781.

Worswick, M. and Pick, R. 1990. Void growth and constitutive softening in a periodically voided solid. Journal of the Mechanics and Physics of Solids, 38(5):601 – 625.

Wu, L., Noels, L., Adam, L., and Doghri, I. 2012. A multiscale mean-field homogenization method for fiber-reinforced composites with gradient-enhanced damage models. Computer Methods in Applied Mechanics and Engineering, 233-236:164 – 179.

Wu, L., Noels, L., Adam, L., and Doghri, I. 2013a. A combined incremental-secant mean-field homogenization scheme with per-phase residual strains for elasto-plastic composites. International Journal of Plasticity, 51:80–102.

Wu, L., Noels, L., Adam, L., and Doghri, I. 2013b. An implicit-gradient-enhanced incremental-secant mean-field homogenization scheme for elasto-plastic composites with damage. International Journal of Solids and Structures, 50(24):3843 – 3860.

Wu, L., Doghri, I., and Noels, L. 2015. An incremental-secant mean-field homogenization method with second statistical moments for elasto-plastic composite materials. Philosophical Magazine, 95(28-30):3348–3384.

Xu, F., Aravas, N., and Sofronis, P. 2008. Constitutive modeling of solid propellant materials with evolving microstructural damage. Journal of the Mechanics and Physics of Solids, 56(5):2050–2073.

Zhai, W., Yu, X., Song, X., Ang, L. Y. L., Cui, F., Lee, H. P., and Li, T. 2018. Microstructure-based experimental and numerical investigations on the sound absorption property of open-cell metallic foams manufactured by a template replication technique. Materials & Design, 137(Supplement C):108 – 116.

Zhang, K., Bai, J., and François, D. 2001. Numerical analysis of the influence of the Lode parameter on void growth. International Journal of Solids and Structures, 38(32):5847 – 5856.

Zhu, H. and Mills, N. 1999. Modelling the creep of open-cell polymer foams. Journal of the Mechanics and Physics of Solids, 47(7):1437 – 1457.

Zhu, H., Knott, J., and Mills, N. 1997. Analysis of the elastic properties of open-cell foams with tetrakaidecahedral cells. Journal of the Mechanics and Physics of Solids, 45(3):319 – 343.

Zhu, H., Hobdell, J., and Windle, A. 2000. Effects of cell irregularity on the elastic properties of open-cell foams. Acta Materialia, 48(20):4893 – 4900.

Zimmerman, R. W. 1991. Elastic moduli of a solid containing spherical inclusions. Mechanics of Materials, 12(1):17 – 24.

Zimmerman, R. W. 1996. Effective conductivity of a two-dimensional medium containing elliptical inhomogeneities. Proceedings of the Royal Society of London A: Mathematical, Physical and Engineering Sciences, 452(1950):1713–1727.